



ATLAS NOTE

SUSY-2015-09

8th February 2016



Draft version 2.1

Search for strongly produced superpartners in final states with same-sign leptons or three leptons and jets in $p p$ collisions at $\sqrt{s} = 13$ TeV (Supporting note)

B. Abbott¹, J.-F. Arguin², S. Berlendis³, F. Cardillo⁴, G. Carrillo-Montoya⁵, A. Di Simone⁴, O. Ducu^{6,7}, D. Gerbaudo⁸, F. Hubaut⁷, G. Herten⁴, S. Kahn⁷, A. Lleres³, J. Maurer⁶, E. Monnier⁷, T. Nguyen², A. Paramonov⁹, J. Poveda⁵, P. Pralavorio⁷, H. Ren^{10,7}, O. Rifki¹, Y.-T. Shen¹, P. Skubic¹, A. Taffard⁸, P. Tornambé⁴, H. Trépanier², X. Zhuang¹⁰

¹University of Oklahoma

²Université de Montréal

³Laboratoire de Physique Subatomique et de Cosmologie de Grenoble (LPSC)

⁴Albert-Ludwigs-Universität Freiburg

⁵European Laboratory for Particle Physics, CERN

⁶Horia Hulubei National Institute for R&D in Physics and Nuclear Engineering (IFIN-HH) Bucharest

⁷Centre de Physique des Particules de Marseille (CPPM)

⁸University of California, Irvine

⁹Argonne National Laboratory

¹⁰Institute of High Energy Physics, Chinese Academy of Sciences, Beijing

Abstract

A search for strongly produced supersymmetric particles is conducted using signatures involving multiple energetic jets and either two isolated leptons (e or μ) with the same electric charge, or at least three isolated leptons. The search also utilises jets originating from b -quarks, missing transverse momentum and other observables to extend its sensitivity. The analysis uses a data sample corresponding to a total integrated luminosity of XX fb^{-1} of $\sqrt{s} = 13$ TeV proton-proton collisions recorded with the ATLAS detector at the Large Hadron Collider in 2015. (Add results).

28 **Contents**

29	1	Introduction	6
30	2	Signal models	7
31	2.1	Signal models considered in this analysis	7
32	3	MC samples	10
33	3.1	Derivation versions and analysis model	10
34	3.2	Signal Samples	11
35	3.3	Background Samples	11
36	3.4	Detector simulation	12
37	3.5	Pileup reweighting	12
38	3.6	Data samples	17
39	4	Object definition	17
40	4.1	Jets	17
41	4.1.1	<i>b</i> -tagging	17
42	4.2	Leptons	19
43	4.2.1	Electrons	20
44	4.2.2	Muons	21
45	4.2.3	Lepton isolation	21
46	4.2.4	Electron acceptance	22
47	4.3	Overlap removal	22
48	4.4	Missing transverse energy	23
49	4.5	Lepton truth matching	23
50	5	Event selection	24
51	5.1	Trigger studies	24
52	5.1.1	Final trigger strategy	24
53	5.1.2	Detailed trigger studies (DC14, MC15)	24
54	5.2	Event pre-selection	27
55	5.2.1	Optimisation of lepton pairing selection	28
56	5.2.2	Validation of the p_T cuts for the leading, sub-leading and 3rd lepton	30
57	5.3	Data-MC comparisons	30
58	6	Signal region definition	37
59	6.1	Optimization procedure and results	38
60	6.2	Signal regions	38
61	6.3	“Auxiliary” signal regions	39
62	6.4	Validation of the jet p_T requirements in signal regions with a <i>b</i> veto	40
63	7	Background estimation	45
64	7.1	Backgrounds with prompt SS dilepton or three leptons	45
65	7.2	Charge flip leptons	46
66	7.2.1	Systematics	55
67	7.3	Backgrounds with fake leptons: general information	56
68	7.3.1	Fake lepton sources close to the signal regions	57

69	7.4	Backgrounds with fake leptons: the matrix method	58
70	7.4.1	Measurement of the ϵ probabilities (prompt leptons)	63
71	7.4.2	Measurement of the ζ probabilities (fake leptons)	66
72	7.5	Neglected backgrounds	78
73	7.5.1	Double-parton scattering	78
74	8	Alternative methods for background estimates	81
75	8.1	Backgrounds with fake leptons: the MC template method	81
76	8.2	Backgrounds with fake leptons and ≥ 3 b -jets: the ABCD method	88
77	8.3	Backgrounds with fake b -jets	89
78	9	Validation of the background estimates	90
79	9.1	Validation of the data-driven estimates	90
80	9.2	Validation regions	113
81	9.3	Results in the auxiliary signal regions	116
82	10	Systematic Uncertainties	117
83	10.1	Experimental systematics	117
84	10.2	Theoretical systematics	119
85	11	Simultaneous fit method and results	119
86	11.1	Non-combination of signal regions	120
87	11.2	Background-only fits	120
88	11.3	Discovery fits	121
89	11.4	Model-independent upper limits	121
90	11.5	Exclusion plots	135
91	12	Conclusion	138
92	Appendix		143
93	13	Details on the overlap removal comparisons of rel19 and rel20	144
94	14	Details about the isolation thresholds in IsolationSelectionTool	146
95	15	Charge flip details	148
96	15.1	Comparison of charge flip rates in different MC productions	148
97	15.2	Charge flip rates plots: MC12 vs. DC14 vs. MC15	152
98	15.3	Charge flip rates plots: MC12 vs. MC15 vs. MC12r20	155
99	15.4	Charge flip rates plots using variables z_0 , $ptvarcone20/pT$ or $topoETcone20/pT$ as signal selection cuts	157
100			
101	16	Real leptons efficiencies	158
102	16.1	Description of the real lepton efficiencies	158
103	16.2	Real leptons efficiency measured using Z events	160
104	16.3	Z tag-and-probe systematics uncertainties	164
105	16.4	Real leptons efficiency measured using $t\bar{t}$ events	170

106	17 Further details on background estimation	176
107	18 MC closure test for detector backgrounds	184
108	19 Studies on the excess observed in $t\bar{t} + X$ validation regions	188
109	20 Updated study on E_T^{miss} trigger	198
110	20.0.1 Dependency on jet requirements	198
111	20.0.2 Inefficiency issues of E_T^{miss} triggers	199
112	21 Selected events and efficiency plot for E_T^{miss} trigger	202
113	22 Further details on the MC template method	204
114	23 Details on the study of the theoretical uncertainties for simulated samples	205
115	24 Detailed isolation studies	206
116	25 Additional checks	211
117	26 List/details of candidate events in the SRs	217
118	27 HEPData material	221

¹¹⁹ List of contributions

B. Abbott	Supervision of students
J.-F. Arguin	Charge flip studies, supervision of students
S. Berlendis	Generation of background MC
F. Cardillo	Event selection (lepton pairing), trigger strategy, MC15 signal region optimization, tree production with experimental systematic uncertainties, HistFitter statistical interpretation, production of exclusion plots
G. Carrillo-Montoya	Event selection (<i>b</i> -tagging, overlap removal), DPS cross-checks
A. Di Simone	HistFitter statistical interpretation, production of exclusion plots, supervision of students
O. Ducu	Event selection (electron acceptance), DC14 signal regions optimization, fake-lepton background estimation and composition studies, validation regions definitions, data/MC comparisons
D. Gerbaudo	Generation of background MC, theory uncertainties
F. Hubaut	Supervision of students
G. Herten	Supervision of students
S. Kahn	Real lepton efficiency studies, study of pMSSM models
A. Lleres	Supervision of students
J. Maurer	Analysis coordination, editor of supporting note, CONF note and paper; signal sample generation, background estimation cross-checks
E. Monnier	Supervision of students
T. Nguyen	Charge flip background estimation
A. Paramonov	Rare processes evaluation, supervision of students
J. Poveda	Analysis coordination, editor of supporting note, CONF note and paper; ntuple production, event selection (lepton isolation), data/MC comparisons, MC15 signal region optimization
P. Pralavorio	Supervision of students
H. Ren	Fake lepton background estimation
O. Rifki	MC template method, data/MC comparisons, background estimation cross-checks
Y.-T. Shen	25/50ns MC comparisons, isolation SF studies
P. Skubic	Supervision of students
A. Taffard	Supervision of students
P. Tornambé	Event selection (lepton pairing), MC15 signal region optimization, tree production with experimental systematic uncertainties, HistFitter statistical interpretation, production of exclusion plots
H. Trépanier	Charge flip background
X. Zhuang	Supervision of students

¹²⁰

122 1 Introduction

123 Supersymmetry (SUSY) [1–9] is a theoretically favoured extension of the Standard Model (SM), which
 124 for each degree of freedom of the SM predicts another degree of freedom with a different spin. These
 125 degrees of freedom combine into physical superpartners of the SM particles: scalar partners of quarks and
 126 leptons (squarks (\tilde{q}) and sleptons), fermionic partners of gauge and Higgs bosons (gluinos (\tilde{g}), charginos
 127 ($\tilde{\chi}_i^{\pm}$, with $i = 1,2$) and neutralinos ($\tilde{\chi}_i^0$ with $i = 1,2,3,4$)), all with identical quantum numbers to their SM
 128 partners, except spin. Since no superpartner of any of the SM particles has been observed yet, SUSY must
 129 be a broken symmetry at some higher energy scale.

130 The discovery (or exclusion) of weak-scale SUSY is one of the highest physics priorities for the LHC.
 131 The primary target for early supersymmetry searches in proton-proton (pp) collisions at a centre-of-mass
 132 energy of 13 TeV at the LHC, given their large expected cross-section, is the strong production of gluinos
 133 and squarks. In order for supersymmetry to provide a solution to the hierarchy problem of the SM, the
 134 supersymmetric partners of the top and bottom quarks are expected to be light and within reach of the
 135 LHC.

136 Under the hypothesis of R -parity conservation [10–13], SUSY partners are produced in pairs and decay
 137 to the Lightest Supersymmetric Particle (LSP) which is stable and, in large variety of models, is assumed
 138 to be the lightest neutralino ($\tilde{\chi}_1^0$) which escapes detection. The undetected $\tilde{\chi}_1^0$ would result in substantial
 139 missing transverse momentum (E_T^{miss}), while the rest of the cascade, originating from the decays of squarks
 140 and gluinos, would yield final states with multiple jets and possibly leptons.

141 In this analysis, events containing multiple jets and either two leptons (electrons or muons) of the same
 142 electric charge (same-sign leptons, SS) or at least three leptons (3L) are used to search for strongly
 143 produced supersymmetric particles. Signatures with SS or 3L are predicted in many SUSY scenarios.
 144 Gluinos produced in pairs or in association with a squark can lead to SS signatures when decaying to any
 145 final state that includes leptons because gluinos are Majorana fermions. Squark production, directly in
 146 pairs or through $\tilde{g}\tilde{g}$ or $\tilde{g}\tilde{q}$ production with subsequent $\tilde{g} \rightarrow q\tilde{q}$ decay, can also lead to SS or 3L signatures
 147 when the squarks decay in cascades involving top quarks (t), charginos, neutralinos or sleptons, which
 148 subsequently decay as $t \rightarrow bW$, $\tilde{\chi}_i^{\pm} \rightarrow W^{\pm(*)}\tilde{\chi}_j^0$, $\tilde{\chi}_i^0 \rightarrow h/Z^{(*)}\tilde{\chi}_j^0$, or $\tilde{\ell} \rightarrow \ell\tilde{\chi}_1^0$, respectively. Since this
 149 search benefits from low SM backgrounds, it allows the use of relatively loose kinematic requirements
 150 on E_T^{miss} , increasing the sensitivity to scenarios with small mass differences between SUSY particles
 151 (compressed scenarios) or where R -parity is violated. This search is thus sensitive to a wide variety of
 152 models based on very different assumptions.

153 This note presents the analysis of the 2015 dataset. Previous Run-2 preparation studies performed with
 154 DC14 samples can be found in [14]. The Run-1 search for strongly produced SUSY particles with SS/3L
 155 was conducted using data from the full 2012 data-taking period (20.3 fb^{-1} at $\sqrt{s}=8 \text{ TeV}$) [15, 16]. In
 156 that result, exclusion limits were placed on 15 different models. Gluino-mediated top squark scenarios,
 157 favoured by naturalness arguments, were excluded for $m_{\tilde{g}} < [600\text{--}1000] \text{ GeV}$, largely independently of
 158 the top squark mass and decay mode. Similar limits were placed on gluino-mediated production of first-
 159 and second-generation quarks for $m_{\tilde{\chi}_1^0} < [300\text{--}600] \text{ GeV}$. Limits were also placed on pair-production of
 160 bottom squarks and sleptons of the first and second generations decaying in long cascades. In this new set
 161 of results using 2015 data, no significant excess is observed, and we extend the Run-1 exclusion limits for
 162 several SUSY models.

163 2 Signal models

164 2.1 Signal models considered in this analysis

165 Final states with two same-sign leptons and multiple jets are sensitive to a variety of new physics
 166 scenarios. In supersymmetric models in particular, such final states can be produced in the decays of
 167 heavy superpartners involving massive gauge bosons, sleptons or top quarks. We list in this section the
 168 different simplified models which we used as benchmarks to define our signal regions.

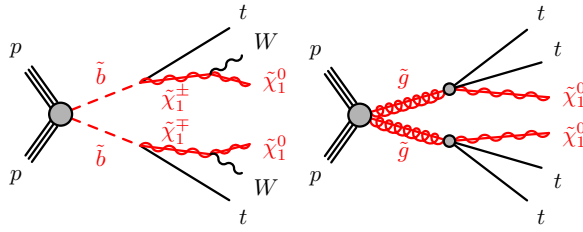


Figure 1: SUSY signal benchmarks leading to multiple b -jets : direct sbottom pair production decaying to top + chargino (left), and gluino decay via offshell stop (right).

169 Direct sbottom $\tilde{b}_1 \rightarrow t\tilde{\chi}_1^\pm$

170 In this model, bottom squarks are rather light and assumed to decay in a top quark and a chargino $\tilde{\chi}_1^\pm$
 171 (Fig. 1), providing complementarity to the mainstream search which focuses on the channel $\tilde{b}_1 \rightarrow b\tilde{\chi}_1^0$.
 172 The final state resulting from the production of a sbottom pair contains pairs of top quarks, of W bosons
 173 and of neutralinos. While this final state may lead to various experimental signatures, the model was
 174 considered in Run-1 [17] only by the same-sign leptons and jets search, leading to the exclusion limits
 175 presented in Fig. 2. The signal grid generated with the MC15 configurations adopts different hypotheses
 176 on the SUSY mass spectrum than what was retained for Run-1: in the latter case two grids were proposed
 177 with either a fixed neutralino mass (60 GeV) or a fixed chargino-to-neutralino mass ratio (2:1). The MC15
 178 grid fixes the chargino-neutralino mass difference to 100 GeV, always allowing on-shell W bosons in
 179 the $\tilde{\chi}_1^\pm \rightarrow W\tilde{\chi}_1^0$ decay. The reduced chargino-neutralino mass gap compared to the MC12 grids allows
 180 to study signal scenarios with heavy neutralinos, which were not considered previously. Only pair pro-
 181 duction of the lightest sbottom is considered, followed by an exclusive decay in the aforementioned channel.
 182

183 Gluino-stop offshell $\tilde{g} \rightarrow t\bar{t}\tilde{\chi}_1^0$

184 In this model inspired by naturalness arguments, gluinos are coupling preferentially to stops which are
 185 lighter than the other squarks. Gluinos are however considered lighter than stops, and decay directly into a
 186 $t\bar{t}\tilde{\chi}_1^0$ triplet via a virtual stop (Fig. 1). The pair production of gluinos leads to a final state containing four
 187 top quarks and two neutralinos. This characteristic final state is accessible through various experimental
 188 signatures, which is why this model is commonly used as a benchmark to compare analyses sensitivities.
 189 The searches performed with Run-1 data [17], summarized in Fig. 2, showed that the same-sign leptons
 190 final state is competitive only at large neutralino mass. This region of the phase space is consequently
 191 given a particular attention in the choice of signal regions described further on. In the signal samples
 192 referenced in this document, the mass of the lightest stop is fixed to 10 TeV and is mostly a \tilde{t}_R state. Only
 193 gluino pair production is considered, followed by an exclusive decay in the aforementioned channel.

194

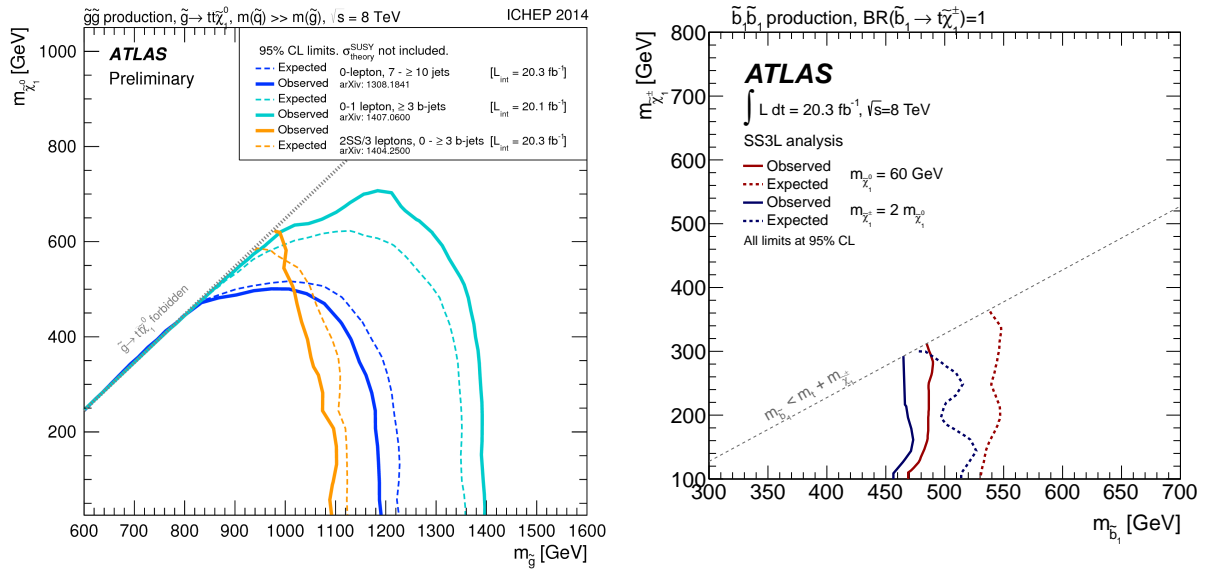


Figure 2: Exclusion limits on the gluino-stop offshell (left) and direct sbottom (right) scenarios set by ATLAS with the 2012 dataset [17].



Figure 3: SUSY signal benchmarks leading to no or few b -jets : gluino pair production followed by two-step decays via heavy bosons or sleptons.

195 Gluinos decays via gauginos

196 These scenarios feature a less oriented search for gluinos, in the cases when they decay through gauginos
 197 in two steps, either via W and Z bosons ($\tilde{g} \rightarrow q\bar{q}'\tilde{\chi}_1^\pm \rightarrow q\bar{q}'W\tilde{\chi}_2^0 \rightarrow q\bar{q}'WZ\tilde{\chi}_1^0$) or sleptons ($\tilde{g} \rightarrow$
 198 $q\bar{q}'\tilde{\chi}_2^0 \rightarrow q\bar{q}'\tilde{\ell}/\tilde{\nu} \rightarrow q\bar{q}'\ell\ell/\nu\nu\tilde{\chi}_1^0$). The b -jet multiplicity in these scenarios is low and they are used as
 199 benchmarks to define signal regions with b -jet vetoes.

200 In the first scenario, the final state is made of two W and two Z bosons (including offshell contributions),
 201 four additional jets and invisible particles (neutrinos and neutralinos). This generally leads to events with
 202 large jet multiplicities and a fair branching ratio for dileptonic final states. The exclusion limits obtained
 203 in run-1 indeed illustrate the competitiveness of the SS/3L+jets search (Fig. 4 left). The signal grid is
 204 built with variable gluino and LSP masses, and the chargino and neutralino 2 masses are set such that the
 205 former lies half-way between the gluino and LSP masses, and the latter half-way between the chargino
 206 and LSP masses.

207 In the second scenario, the final state is made of charged leptons, four additional jets and invisible particles
 208 (neutrinos and neutralinos). The average jet multiplicity per event is smaller than in the previous scenario;

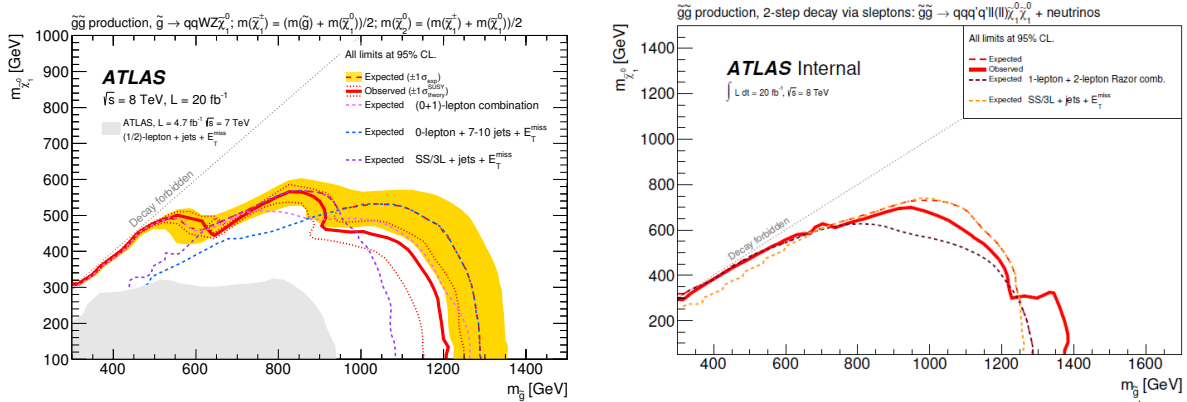


Figure 4: Exclusion limits on scenarios featuring gluino pair production followed by two-step decays via heavy gauge bosons or sleptons, set by ATLAS with the 2012 dataset [17].

another characteristic is the large fraction of events with several leptons, unlike most of the other scenarios that have a rather low acceptance due to the branching ratios of $W \rightarrow \ell\nu$ or $Z \rightarrow \ell\ell$. The exclusion limits obtained in run-1 (Fig. 4 right) show again that the SS/3L+jets final state is very competitive to probe those models. The signal grid is built with variable gluino and LSP masses; the $\tilde{\chi}_2^0$ mass is chosen half-way between the gluino and LSP masses, and the sleptons masses are also set equal and half-way between the $\tilde{\chi}_2^0$ and LSP masses. The $\tilde{\chi}_2^0$ may decay to any of the six sleptons ($\tilde{\ell}, \tilde{\nu}$) with equal probability. Noticeable changes have been introduced with respect to the run-1 grid. First, bottom squarks are no longer decoupled but are assumed to be mass-degenerate with the light-flavor squarks, opening the decay mode $\tilde{g} \rightarrow b\bar{b}\tilde{\chi}_2^0$ with 20% branching ratio. However, to simplify the model description we do not consider these decay modes; this translates concretely into vetoing events with $\tilde{g} \rightarrow b\bar{b}\tilde{\chi}_2^0$ decays and weighting the remaining events by a factor $1/(2 * 0.2 * 0.8 + 0.2^2)$ to readjust the branching ratios. Another more important change is that only gluino decays through $\tilde{\chi}_2^0$ are now considered in the model generation, while in the run-1 model decays via charginos $\tilde{g} \rightarrow q\bar{q}'\tilde{\chi}_1^\pm$ (followed by $\tilde{\chi}_1^\pm \rightarrow \tilde{\ell}\nu/\ell\tilde{\nu}$) were also considered with a 50% branching ratio. The consequences of the latter change are quite important for this analysis, reducing the acceptance of inclusive trilepton selections by $\sim 30\%$.

Since both scenarios include non-resonant $W^* \rightarrow \ell\nu$ and $Z^* \rightarrow \ell\ell$ contributions, they also provide motivated benchmarks to gauge the analysis sensitivity for softer leptons p_T spectra, unlike the $\tilde{g} \rightarrow t\bar{t}\tilde{\chi}_1^0$ and $\tilde{b}_1 \rightarrow t\tilde{\chi}_1^\pm$ scenarios in which leptons always originate from on-shell W bosons hence can't be arbitrarily soft.

Models not considered for the moment

In the publications [15, 17] of the analysis results obtained with Run-1 data, exclusion limits were also provided for other signal models. These scenarios included notably simplified models such as $\tilde{g} \rightarrow tbW\tilde{\chi}_1^0$, $\tilde{g} \rightarrow tcW\tilde{\chi}_1^0$, squark pair production with similar decay modes as in the previous paragraph, as well as minimal models featuring R -parity violation through bilinear terms, gauge-mediated SUSY breaking, or universal extra dimensions. These models are not considered for the moment, although interpretations might be proposed for them again in the future.

Gluino mass (GeV)	500	550	600	650	700
Cross section (pb)	$27.4 \pm 14\%$	$15.6 \pm 14\%$	$9.20 \pm 14\%$	$5.60 \pm 14\%$	$3.53 \pm 14\%$
750	800	850	900	950	1000
$2.27 \pm 14\%$	$1.49 \pm 15\%$	$0.996 \pm 15\%$	$0.677 \pm 16\%$	$0.466 \pm 16\%$	$0.325 \pm 17\%$
1050	1100	1150	1200	1250	1300
$0.229 \pm 17\%$	$0.163 \pm 18\%$	$0.118 \pm 18\%$	$0.0856 \pm 18\%$	$0.0627 \pm 19\%$	$0.0461 \pm 20\%$
1350	1400	1450	1500	1550	1600
$0.0340 \pm 20\%$	$0.0253 \pm 21\%$	$0.0189 \pm 22\%$	$0.0142 \pm 23\%$	$0.0107 \pm 23\%$	$0.00810 \pm 24\%$
Sbottom mass (GeV)	400	450	500	550	
Cross section (pb)	$1.84 \pm 14\%$	$0.948 \pm 13\%$	$0.518 \pm 13\%$	$0.296 \pm 13\%$	
600	650	700	750	800	
$0.175 \pm 13\%$	$0.107 \pm 13\%$	$0.0670 \pm 13\%$	$0.0431 \pm 14\%$	$0.0283 \pm 14\%$	

Table 1: Signal cross-sections and related uncertainties for scenarios featuring gluino (top table) or sbottom (bottom table) pair production, as a function of the pair-produced superpartner mass, computed in [18].

235 3 MC samples

236 This section summarizes the signal and background samples used for the studies presented in this note, as
 237 well some details about the Monte Carlo production and analysis framework. Unless otherwise stated, all
 238 samples were produced as part of the MC15 Monte-Carlo campaign.

239 3.1 Derivation versions and analysis model

240 We relied without exception on the SUSY2 DxAOD derivations. For the final results, the data samples
 241 were produced with the derivation tag p2425. For the MC samples we used a mix of MC15a and MC15b
 242 samples (details in sections 3.2 and 3.3), derivations were produced with tags p2419/p2421 (20.1.7.1
 243 cache) or later (up to p2470). These derivation tag were not affected by the CutBookkepper bug the could
 244 potentially lead to problems in MC normalization.

245 Most of the studies shown in this note were performed using flat ROOT ntuples produced on the grid using
 246 code based on the SUSYAnalysisExample EventLoop package and various tags of SUSYTools up to
 247 00-07-17 (for the final results). They contained basic object information, although no overlap removal or
 248 isolation cuts were applied to allow flexibility for optimization studies. No systematic uncertainties were
 249 included. The total size of these ntuples is 40 GB (data as well as MC background and signal samples).
 250 These files were shared among the groups participating in the analysis.

251 In addition, dedicated flat ROOT ntuples with all the systematic variations included in the SUSYTools
 252 getSystInfoList() method were also produced for the samples containing prompt SS/3L ($t\bar{t} + V$, $t\bar{t} + h$,
 253 diboson, signals). To reduce the size of the output files, only events that contained in any of the systematic
 254 variations at least 2 leptons with $p_T > 10$ GeV, and either $E_T > 100$ GeV or at least 3 b-tagged jets
 255 ($p_T > 20$ GeV) or $H_T > 300$ GeV were kept. These ntuples were not used in the results presented here,
 256 however.

Signal scenario	dataset IDs	N_{gen}	ϵ_{filter}
$\tilde{b}_1 \rightarrow t\tilde{\chi}_1^\pm$	372300-372369	10000	$\sim 10\%$
$\tilde{g} \rightarrow t\bar{t}\tilde{\chi}_1^0$	370100-370187	20000	100%
$\tilde{g} \rightarrow q\bar{q}'WZ\tilde{\chi}_1^0$	371200-371349	20000	100%
$\tilde{g} \rightarrow q\bar{q}\ell\ell\tilde{\chi}_1^0$	372450-372511	20000	$\sim 30\%$

Table 2: List of simulated samples for SUSY signal model grids. The range of dataset IDs, the typical number of generated events N_{gen} per sample and the typical generator filter efficiency are shown.

257 Some of the groups in the analysis team used other frameworks to analyze the data, also relying on the
 258 same input SUSY2 Dx AOD samples and SUSYTools tag, which served as cross-check of the results, and
 259 provided the experimental sources of systematic uncertainties.

260 3.2 Signal Samples

261 The baseline signal models correspond to the different scenarios described in Section 2. The signal
 262 processes are generated from leading order (LO) matrix elements with up to two extra partons, using
 263 the MADGRAPH v5.2.2.3 generator [19] interfaced to PYTHIA 8.186 [20] with the ATLAS 14 tune [21]
 264 for the modelling of the SUSY decay chain, parton showering, hadronisation and the description of the
 265 underlying event. Parton luminosities are provided by the NNPDF23LO [22] set of parton distribution
 266 functions. Jet-parton matching is realized following the CKKW-L prescription [23], with a matching
 267 scale set to one quarter of the pair-produced superpartner mass. The signal samples are normalised to the
 268 next-to-next-to-leading order cross-section including the resummation of soft gluon emission at next-to-
 269 next-to-leading-logarithmic accuracy (NLO+NLL), as detailed in Ref. [18]. All the signal MC samples
 270 were generated using a 25-ns bunch spacing configuration, with the MC15b configuration.

271 The dataset IDs are listed in Table 2, together with the number of generated events and the filter efficiency.

272 3.3 Background Samples

273 The background samples used are listed in Tables 3-4. They were generated using a 25-ns bunch spacing
 274 configuration and either MC15a or MC15b (cf tables).

275 Simulated $t\bar{t}$ events are generated using the PowHEG generator [24–26], interfaced to PYTHIA 6 [27]
 276 and using the Perugia2012 tune [28]. The $t\bar{t}$ samples are normalised to their next-to-next-to-leading-
 277 order (NNLO) cross-section including the resummation of soft gluon emission at next-to-next-to-leading-
 278 logarithmic (NNLL) accuracy using Top++2.0 [29].

279 Samples of single top quark backgrounds corresponding to the t -, s - and Wt production mechanisms
 280 are generated with PowHEG interfaced to PYTHIA 6. The leading-order cross-sections obtained from the
 281 generator is used for these samples.

282 The processes of $t\bar{t} + V$ production are generated at LO with MADGRAPH [19] interfaced to PYTHIA 8,
 283 with up to two (ttW), one ($ttZ^{(*)}$ -including on-shell and off-shell contributions-) or no ($ttWW$) extra
 284 parton included in the matrix elements. The samples are normalised to their NLO cross-sections using

appropriate k -factors [19]. The development of more accurate samples (NLO matrix elements, spin correlations) is still ongoing and they are not part of these results.

Simulated $W/Z+jets$ samples are produced using either Powheg interfaced to Pythia 8 [27] or Sherpa 2.1.1 [30] with massive b -, c -quarks with up to four additional partons in the matrix element and parton shower and are normalised to their NNLO QCD theoretical cross sections [31].

Simulated samples for diboson processes with the two vector bosons decaying leptonically (to ℓ or ν_ℓ) are produced with Sherpa, including dedicated samples for the electroweak (VBS, such as $W^\pm W^\pm jj$) and loop-induced gluon-gluon production (including the $gg \rightarrow h \rightarrow WW, ZZ$ contributions). Note that these samples include the contributions from tri-boson production with one of the vector bosons decaying hadronically and separate Sherpa samples are simulated for the tri-lepton production with fully leptonic decays.

Simulated samples of Higgs boson production are produced using Powheg interfaced to Pythia 8 for gluon fusion with $H \rightarrow 4\ell$. Production of a Higgs boson in association with a $t\bar{t}$ pair is simulated using MadGraph5_AMC@NLO [19] interfaced to Herwig. Higgs boson production in association with a W or Z boson is simulated with Pythia 8. In fact, the contribution from $WH \rightarrow WWW \rightarrow \ell^\pm \nu q \bar{q} \ell^\pm \nu$ is also included in the same-sign diboson samples and that of VBF production of $H \rightarrow ZZ$ is included in the EW6 diboson samples, so there is some partial double-counting of these processes. However, their contribution is negligible to both validation and signal regions, therefore no correction is applied. Only the contributions from $gg \rightarrow ZH$ and $WH \rightarrow \ell\nu\tau\tau$ are not covered with the current set of samples, but they are respectively only 10% of the total $pp \rightarrow ZH$ cross section, and smaller than $WH \rightarrow WWW$.

QCD multijets are not included in this study since these backgrounds are expected to be very small.

3.4 Detector simulation

The detector simulation is performed with either full ATLAS detector simulation [32] based on Geant4 [33] or a fast simulation using a parameterisation of the performance of the electromagnetic and hadronic calorimeters and Geant4 for the other parts of the detector [34], and are reconstructed in the same manner as the data. All simulated samples are generated with a range of minimum-bias interactions using Pythia 8 [20] with the MSTW2008LO PDF set [35] and the A2 tune overlaid on the hard-scattering event to account for the multiple pp interactions in the same bunch crossing (in-time pileup) and neighbouring bunch crossing (out-of-time pileup). A bunch spacing of 25 ns is used, and the distribution for the average number of interactions per bunch crossing is assumed with values ranging from 0 to 50, with more events generated with values between 15 to 30 for MC15a [36], while the distribution in MC15b [37] is closer to that observed in data.

3.5 Pileup reweighting

For comparisons with data, the MC is reweighted to reproduce the observed distribution of the average number of collisions per bunch crossing (μ) using the official PileupReweightingTool. Following the current recommendations, the μ value in data is scaled by 1/1.16 (assessing the cases of 1/1.23 and 1 as uncertainty on that value) based on studies of the number of vertices as a function of μ as well as the results from inelastic cross section measurement.

Table 3: List of simulated samples for top-related background processes, and Sherpa di- and tri-boson production. The dataset ID, the generator cross-section σ , the k -Factor, the generator filter efficiency ϵ_{filter} , the total number of generated events N_{gen} , the equivalent luminosity ($L_{equival}$) and pile-up configuration (mc15a or mc15b) are shown.

datasetID	Sample name	$\sigma \times BR$ [pb]	k-Factor	ϵ_{filter}	N_{gen}	L_{equiv}	PU settings
361100	mcl5_13TeV_361100.PowhegPythia8EvtGen_AZNLOCTEQ6L1_Wplusenu.merge.AOD.e3601_s2576_s2132_r6765_r6282/	11306.0000	1.02	1.	29914098	2.6	mc15a
361101	mcl5_13TeV_361101.PowhegPythia8EvtGen_AZNLOCTEQ6L1_Wplusmu.merge.AOD.e3601_s2576_s2132_r6725_r6282/	11306.0000	1.02	1.	27951402	2.4	mc15a
361102	mcl5_13TeV_361102.PowhegPythia8EvtGen_AZNLOCTEQ6L1_Wplustau.merge.AOD.e3601_s2576_s2132_r6725_r6282/	11306.0000	1.02	1.	29908753	2.6	mc15a
361103	mcl5_13TeV_361103.PowhegPythia8EvtGen_AZNLOCTEQ6L1_Wminusenu.merge.AOD.e3601_s2576_s2132_r6765_r6282/	8282.6000	1.04	1.	19916972	2.3	mc15a
361104	mcl5_13TeV_361104.PowhegPythia8EvtGen_AZNLOCTEQ6L1_Wminusmu.merge.AOD.e3601_s2576_s2132_r6725_r6282/	8282.6000	1.04	1.	19965914	2.3	mc15a
361105	mcl5_13TeV_361105.PowhegPythia8EvtGen_AZNLOCTEQ6L1_Wminustau.merge.AOD.e3601_s2576_s2132_r6725_r6282/	8282.6000	1.04	1.	19952348	2.3	mc15a
361106	mcl5_13TeV_361106.PowhegPythia8EvtGen_AZNLOCTEQ6L1_Zee.merge.AOD.e3601_s2576_s2132_r6765_r6282/	1901.2000	1.03	1.	19916520	10.2	mc15a
361107	mcl5_13TeV_361107.PowhegPythia8EvtGen_AZNLOCTEQ6L1_Ztautau.merge.AOD.e3601_s2576_s2132_r6765_r6282/	1901.2000	1.03	1.	19942848	10.2	mc15a
361108	mcl5_13TeV_361108.PowhegPythia8EvtGen_AZNLOCTEQ6L1_Zbottom.merge.AOD.e3601_s2576_s2132_r6765_r6282/	1901.2000	1.03	1.	19197457	9.8	mc15a
361468	mcl5_13TeV_361468.Sherpa_CTI0_Zee_M11 0 0 40_Pt0_70_BFilter.merge.AOD.e4198_s2608_s2183_r6869_r6282/	2256.1000	1.00	0.95157	2493800	1.2	mc15a
361469	mcl5_13TeV_361469.Sherpa_CTI0_Zee_M11 0 0 40_Pt0_70_BFilter.merge.AOD.e4198_s2608_s2183_r6869_r6282/	2252.9000	1.00	0.947153	499000	4.7	mc15a
361470	mcl5_13TeV_361470.Sherpa_CTI0_Zee_M11 0 0 40_Pt0_140_BFilter.merge.AOD.e4198_s2608_s2183_r6869_r6282/	7.7821	1.00	0.89335	598800	86.0	mc15a
361471	mcl5_13TeV_361471.Sherpa_CTI0_Zee_M11 0 0 40_Pt0_140_BFilter.merge.AOD.e4198_s2608_s2183_r6869_r6282/	7.8015	1.00	0.099233	99600	128.7	mc15a
361472	mcl5_13TeV_361472.Sherpa_CTI0_Zee_M11 0 0 40_Pt140_400_BFilter.merge.AOD.e4198_s2608_s2183_r6869_r6282/	0.7101	1.00	0.86947	299000	484.3	mc15a
361473	mcl5_13TeV_361473.Sherpa_CTI0_Zee_M11 0 0 40_Pt140_400_BFilter.merge.AOD.e4198_s2608_s2183_r6869_r6282/	0.7067	1.00	0.10501	99200	1336.7	mc15a
361474	mcl5_13TeV_361474.Sherpa_CTI0_Zee_M11 0 0 40_Pt400_E_CMS_BVeto.merge.AOD.e4198_s2608_s2183_r6869_r6282/	0.0073	1.00	0.82797	99600	16478.7	mc15a
361475	mcl5_13TeV_361475.Sherpa_CTI0_Zee_M11 0 0 40_Pt400_E_CMS_BFilter.merge.AOD.e4198_s2608_s2183_r6869_r6282/	0.0075	1.00	0.17203	49940	450E06	mc15a
361476	mcl5_13TeV_361476.Sherpa_CTI0_Zumu_M11 0 0 40_Pt0_70_BFilter.merge.AOD.e4198_s2608_s2183_r6869_r6282/	2251.1000	1.00	0.95124	2491200	1.2	mc15a
361477	mcl5_13TeV_361477.Sherpa_CTI0_Zumu_M11 0 0 40_Pt0_70_BFilter.merge.AOD.e4198_s2608_s2183_r6869_r6282/	2250.0000	1.00	0.047227	496500	4.7	mc15a
361479	mcl5_13TeV_361479.Sherpa_CTI0_Zumu_M11 0 0 40_Pt0_70_BFilter.merge.AOD.e4198_s2608_s2183_r6869_r6282/	7.7840	1.00	0.10194	99800	125.8	mc15a
361480	mcl5_13TeV_361480.Sherpa_CTI0_Zumu_M11 0 0 40_Pt140_400_BFilter.merge.AOD.e4198_s2608_s2183_r6869_r6282/	0.7142	1.00	0.87022	298800	480.8	mc15a
361481	mcl5_13TeV_361481.Sherpa_CTI0_Zumu_M11 0 0 40_Pt400_E_CMS_BVeto.merge.AOD.e4198_s2608_s2183_r6869_r6282/	0.0073	1.00	0.11674	99800	1209.2	mc15a
361482	mcl5_13TeV_361482.Sherpa_CTI0_Zumu_M11 0 0 40_Pt400_E_CMS_BFilter.merge.AOD.e4198_s2608_s2183_r6869_r6282/	0.0075	1.00	0.84321	99800	15781.0	mc15a
361483	mcl5_13TeV_361483.Sherpa_CTI0_Zumu_M11 0 0 40_Pt0_70_BFilter.merge.AOD.e4198_s2608_s2183_r6869_r6282/	0.0075	1.00	0.15679	49320	450E06	mc15a
361485	mcl5_13TeV_361485.Sherpa_CTI0_Zumu_M11 0 0 40_Pt0_70_BFilter.merge.AOD.e4198_s2608_s2183_r6869_r6282/	2254.2000	1.00	0.046987	497000	4.7	mc15a
361486	mcl5_13TeV_361486.Sherpa_CTI0_Zumu_M11 0 0 40_Pt0_70_BFilter.merge.AOD.e4198_s2608_s2183_r6869_r6282/	7.7699	1.00	0.89210	598200	86.3	mc15a
361487	mcl5_13TeV_361487.Sherpa_CTI0_Zumu_M11 0 0 40_Pt70_140_BFilter.merge.AOD.e4198_s2608_s2183_r6869_r6282/	7.8242	1.00	0.10367	100000	123.3	mc15a
361488	mcl5_13TeV_361488.Sherpa_CTI0_Zumu_M11 0 0 40_Pt140_400_BFilter.merge.AOD.e4198_s2608_s2183_r6869_r6282/	0.7097	1.00	0.87013	299400	484.8	mc15a
361489	mcl5_13TeV_361489.Sherpa_CTI0_Zumu_M11 0 0 40_Pt140_BFilter.merge.AOD.e4198_s2608_s2183_r6869_r6282/	0.7068	1.00	0.11787	99800	1197.9	mc15a
361490	mcl5_13TeV_361490.Sherpa_CTI0_Zumu_M11 0 0 40_Pt400_E_CMS_BFilter.merge.AOD.e4198_s2608_s2183_r6869_r6282/	0.0074	1.00	0.94162	99600	14293.9	mc15a
361491	mcl5_13TeV_361491.Sherpa_CTI0_Zumu_M11 0 0 40_Pt400_E_CMS_BFilter.merge.AOD.e4198_s2608_s2183_r6869_r6282/	0.0074	1.00	0.05838	49980	115E06	mc15a
361372	mcl5_13TeV_361372.Sherpa_CTI0_Zee_Pt0_70_CVetoBVeto.merge.AOD.e3651_s2586_s2174_r6869_r6282/	2205.0000	0.90	0.7785	1993200	1.3	mc15a
361373	mcl5_13TeV_361373.Sherpa_CTI0_Zee_Pt0_70_CVetoBVeto.merge.AOD.e3651_s2586_s2174_r6869_r6282/	2205.0000	0.90	0.1422	1198000	4.2	mc15a
361374	mcl5_13TeV_361374.Sherpa_CTI0_Zee_Pt0_70_CVetoBVeto.merge.AOD.e3651_s2586_s2174_r6869_r6282/	2205.0000	0.90	0.0795	2452200	15.5	mc15a
361375	mcl5_13TeV_361375.Sherpa_CTI0_Zee_Pt70_140_CVetoBVeto.merge.AOD.e3651_s2586_s2174_r6869_r6282/	76.0300	0.90	0.6480	1223400	27.6	mc15a
361376	mcl5_13TeV_361376.Sherpa_CTI0_Zee_Pt70_140_CFilterBVeto.merge.AOD.e3651_s2586_s2174_r6869_r6282/	76.0300	0.90	0.2198	493900	32.8	mc15a
361377	mcl5_13TeV_361377.Sherpa_CTI0_Zee_Pt70_140_CFilterBVeto.merge.AOD.e3651_s2586_s2174_r6869_r6282/	76.0300	0.90	0.1309	873700	97.5	mc15a
361378	mcl5_13TeV_361378.Sherpa_CTI0_Zee_Pt140_280_CVetoBVeto.merge.AOD.e3651_s2586_s2174_r6869_r6282/	11.6400	0.90	0.6139	376400	58.5	mc15a
361379	mcl5_13TeV_361379.Sherpa_CTI0_Zee_Pt140_280_CFilterBVeto.merge.AOD.e3651_s2586_s2174_r6869_r6282/	11.6400	0.90	0.2426	473000	186.1	mc15a
361380	mcl5_13TeV_361380.Sherpa_CTI0_Zee_Pt140_280_CFilterBVeto.merge.AOD.e3651_s2586_s2174_r6869_r6282/	11.6400	0.90	0.1468	633.4	mc15a	
361381	mcl5_13TeV_361381.Sherpa_CTI0_Zee_Pt280_500_CVetoBVeto.merge.AOD.e4133_s2608_s2183_r6869_r6282/	0.7646	0.90	0.5836	498600	1241.5	mc15a
361382	mcl5_13TeV_361382.Sherpa_CTI0_Zee_Pt280_500_CFilterBVeto.merge.AOD.e4133_s2608_s2183_r6869_r6282/	0.7646	0.90	0.2632	299800	1655.3	mc15a
361383	mcl5_13TeV_361383.Sherpa_CTI0_Zee_Pt280_500_CFilterBVeto.merge.AOD.e4133_s2608_s2183_r6869_r6282/	0.0081	0.90	0.1594	299700	2732.3	mc15a
361384	mcl5_13TeV_361384.Sherpa_CTI0_Zee_Pt500_700_CVetoBVeto.merge.AOD.e4133_s2608_s2183_r6869_r6282/	0.0081	0.90	0.5499	30000	12631.5	mc15a
361385	mcl5_13TeV_361385.Sherpa_CTI0_Zee_Pt500_700_CFilterBVeto.merge.AOD.e4133_s2608_s2183_r6869_r6282/	0.0043	0.90	0.2692	200000	17829.2	mc15a
361386	mcl5_13TeV_361386.Sherpa_CTI0_Zee_Pt500_700_CFilterBVeto.merge.AOD.e4133_s2608_s2183_r6869_r6282/	0.0043	0.90	0.1718	199800	27909.3	mc15a
361387	mcl5_13TeV_361387.Sherpa_CTI0_Zee_Pt700_1000_CVetoBVeto.merge.AOD.e4133_s2608_s2183_r6869_r6282/	0.0081	0.90	0.5625	50000	12193.3	mc15a
361388	mcl5_13TeV_361388.Sherpa_CTI0_Zee_Pt700_1000_CFilterBVeto.merge.AOD.e4133_s2608_s2183_r6869_r6282/	0.0081	0.90	0.2958	30000	13912.2	mc15a
361389	mcl5_13TeV_361389.Sherpa_CTI0_Zee_Pt700_1000_CFilterBVeto.merge.AOD.e4133_s2608_s2183_r6869_r6282/	0.0081	0.90	0.1806	29800	26345.5	mc15a
361390	mcl5_13TeV_361390.Sherpa_CTI0_Zee_Pt1000_2000_CVetoBVeto.merge.AOD.e4133_s2608_s2183_r6869_r6282/	0.0011	0.90	0.5499	64440.3	mc15a	
361391	mcl5_13TeV_361391.Sherpa_CTI0_Zee_Pt1000_2000_CFilterBVeto.merge.AOD.e4133_s2608_s2183_r6869_r6282/	0.0011	0.90	0.3135	20000	108554.6	mc15a
361392	mcl5_13TeV_361392.Sherpa_CTI0_Zee_Pt1000_2000_CFilterBVeto.merge.AOD.e4133_s2608_s2183_r6869_r6282/	0.0001	0.90	0.1861	20000	108554.6	mc15a
361393	mcl5_13TeV_361393.Sherpa_CTI0_Zee_Pt2000_E_CMS_CVetoBVeto.merge.AOD.e4133_s2608_s2183_r6869_r6282/	0.0000	0.90	0.4874	19800	mc15a	
361394	mcl5_13TeV_361394.Sherpa_CTI0_Zee_Pt2000_E_CMS_CFilterBVeto.merge.AOD.e4133_s2608_s2183_r6869_r6282/	0.0000	0.90	0.3078	10000	mc15a	
361395	mcl5_13TeV_361395.Sherpa_CTI0_Zee_Pt2000_E_CMS_BFilter.merge.AOD.e4133_s2608_s2183_r6869_r6282/	0.0000	0.90	0.2048	9980	mc15a	

Table 4: List of simulated samples for Powheg W/Z+jets, Sherpa low-mass Drell-Yan and $Z \rightarrow ee$ -jets production. The dataset ID, the generator cross-section σ , the k-Factor, the generator filter efficiency ϵ_{filter} , the total number of generated events N_{gen} , the equivalent luminosity (L_{equiv}) and pile-up configuration (mc15a or mc15b) are shown.

datasetID	Sample name	$\sigma \times BR$ [pb]	k-Factor	ϵ_{filter}	N_{gen}	L_{equiv}	PU settings
361396	mc15_1.3TeV_361396.Sherpa_CTI0_Zinmu_Pt0_70_CVetoBVeto.merge.AOD.e3651_s2586_s2174_r6869_r6282/	2205.0000	0.90	0.7785	1997600	1.3	mc15a
361397	mc15_1.3TeV_361397.Sherpa_CTI0_Zinmu_Pt0_70_CFilterBVeto.merge.AOD.e3651_s2586_s2174_r6869_r6282/	2205.0000	0.90	0.1422	1173000	4.2	mc15a
361398	mc15_1.3TeV_361398.Sherpa_CTI0_Zinmu_Pt0_70_BFilter.merge.AOD.e3651_s2586_s2174_r6869_r6282/	2205.0000	0.90	0.0795	1965400	12.5	mc15a
361399	mc15_1.3TeV_361399.Sherpa_CTI0_Zinmu_Pt0_70_CVetoBVeto.merge.AOD.e3651_s2586_s2174_r6869_r6282/	76.0300	0.90	0.6480	1237400	27.9	mc15a
361400	mc15_1.3TeV_361400.Sherpa_CTI0_Zinmu_Pt70_140_CFilterBVeto.merge.AOD.e3651_s2586_s2174_r6869_r6282/	76.0300	0.90	0.2198	487000	32.4	mc15a
361401	mc15_1.3TeV_361401.Sherpa_CTI0_Zinmu_Pt70_140_BFilter.merge.AOD.e3651_s2586_s2174_r6869_r6282/	76.0300	0.90	0.1309	1096000	122.4	mc15a
361402	mc15_1.3TeV_361402.Sherpa_CTI0_Zinmu_Pt140_280_CVetoBVeto.merge.AOD.e3651_s2608_s2183_r6869_r6282/	11.6400	0.90	0.6139	197400	30.7	mc15a
361403	mc15_1.3TeV_361403.Sherpa_CTI0_Zinmu_Pt140_280_CFilterBVeto.merge.AOD.e3651_s2586_s2174_r6869_r6282/	11.6400	0.90	0.2426	450200	177.1	mc15a
361404	mc15_1.3TeV_361404.Sherpa_CTI0_Zinmu_Pt140_280_BFilter.merge.AOD.e3651_s2586_s2174_r6869_r6282/	11.6400	0.90	0.1468	530.5	30.5	mc15a
361405	mc15_1.3TeV_361405.Sherpa_CTI0_Zinmu_Pt280_500_CVetoBVeto.merge.AOD.e4133_s2608_s2183_r6869_r6282/	0.7646	0.90	0.5836	499000	1242.5	mc15a
361406	mc15_1.3TeV_361406.Sherpa_CTI0_Zinmu_Pt280_500_CFilterBVeto.merge.AOD.e4133_s2608_s2183_r6869_r6282/	0.7646	0.90	0.2632	299000	1650.9	mc15a
361407	mc15_1.3TeV_361407.Sherpa_CTI0_Zinmu_Pt280_500_BFilter.merge.AOD.e4133_s2608_s2183_r6869_r6282/	0.7646	0.90	0.1594	299800	2733.2	mc15a
361408	mc15_1.3TeV_361408.Sherpa_CTI0_Zinmu_Pt500_700_CVetoBVeto.merge.AOD.e4133_s2608_s2183_r6869_r6282/	0.0463	0.90	0.5692	299200	12614.6	mc15a
361409	mc15_1.3TeV_361409.Sherpa_CTI0_Zinmu_Pt500_700_CFilterBVeto.merge.AOD.e4133_s2608_s2183_r6869_r6282/	0.0463	0.90	0.2692	199600	1793.5	mc15a
361410	mc15_1.3TeV_361410.Sherpa_CTI0_Zinmu_Pt500_700_BFilter.merge.AOD.e4133_s2608_s2183_r6869_r6282/	0.0463	0.90	0.1718	199400	27853.4	mc15a
361411	mc15_1.3TeV_361411.Sherpa_CTI0_Zinmu_Pt70_1000_CVetoBVeto.merge.AOD.e4133_s2608_s2183_r6869_r6282/	0.0081	0.90	0.5625	50000	12193.3	mc15a
361412	mc15_1.3TeV_361412.Sherpa_CTI0_Zinmu_Pt70_1000_CFilterBVeto.merge.AOD.e4133_s2608_s2183_r6869_r6282/	0.0081	0.90	0.2958	30000	13912.2	mc15a
361413	mc15_1.3TeV_361413.Sherpa_CTI0_Zinmu_Pt70_1000_BFilter.merge.AOD.e4133_s2608_s2183_r6869_r6282/	0.0081	0.90	0.1806	30000	22786.4	mc15a
361414	mc15_1.3TeV_361414.Sherpa_CTI0_Zinmu_Pt1000_2000_CVetoBVeto.merge.AOD.e4133_s2608_s2183_r6869_r6282/	0.0011	0.90	0.5499	30000	55106.4	mc15a
361415	mc15_1.3TeV_361415.Sherpa_CTI0_Zinmu_Pt1000_2000_CFilterBVeto.merge.AOD.e4133_s2608_s2183_r6869_r6282/	0.0011	0.90	0.3135	19800	63795.9	mc15a
361416	mc15_1.3TeV_361416.Sherpa_CTI0_Zinmu_Pt70_1000_CVetoBVeto.merge.AOD.e4133_s2608_s2183_r6869_r6282/	0.0011	0.90	0.1861	19240	1044296	mc15a
361417	mc15_1.3TeV_361417.Sherpa_CTI0_Zinmu_Pt70_1000_ECMS_CVetoBVeto.merge.AOD.e4133_s2608_s2183_r6869_r6282/	0.0000	0.90	0.4874	20000	mc15a	
361418	mc15_1.3TeV_361418.Sherpa_CTI0_Zinmu_Pt2000_E_ECMS_CFilterBVeto.merge.AOD.e4133_s2608_s2183_r6869_r6282/	0.0000	0.90	0.3078	9980	mc15a	
361419	mc15_1.3TeV_361419.Sherpa_CTI0_Zinmu_Pt1000_2000_ECMS_BFilter.merge.AOD.e4133_s2608_s2183_r6869_r6282/	0.0000	0.90	0.2048	9790	0.0	mc15a
361420	mc15_1.3TeV_361420.Sherpa_CTI0_Zinmu_Pt70_1000_CVetoBVeto.merge.AOD.e3733_s2608_s2183_r6869_r6282/	2205.0000	0.90	0.7785	1995200	1.3	mc15a
361421	mc15_1.3TeV_361421.Sherpa_CTI0_Zinmu_Pt70_1000_CFilterBVeto.merge.AOD.e3733_s2608_s2183_r6869_r6282/	2205.0000	0.90	0.1422	1189000	4.2	mc15a
361422	mc15_1.3TeV_361422.Sherpa_CTI0_Zinmu_Pt70_1000_BFilter.merge.AOD.e3733_s2608_s2183_r6869_r6282/	2205.0000	0.90	0.0795	2215600	14.0	mc15a
361423	mc15_1.3TeV_361423.Sherpa_CTI0_Zinmu_Pt70_1000_CVetoBVeto.merge.AOD.e3733_s2608_s2183_r6869_r6282/	76.0300	0.90	0.6480	1242000	28.0	mc15a
361424	mc15_1.3TeV_361424.Sherpa_CTI0_Zinmu_Pt70_140_CFilterBVeto.merge.AOD.e3733_s2608_s2183_r6869_r6282/	76.0300	0.90	0.2198	497900	33.1	mc15a
361425	mc15_1.3TeV_361425.Sherpa_CTI0_Zinmu_Pt70_140_BFilter.merge.AOD.e3733_s2608_s2183_r6869_r6282/	76.0300	0.90	0.1309	1105600	123.4	mc15a
361426	mc15_1.3TeV_361426.Sherpa_CTI0_Zinmu_Pt70_1000_CVetoBVeto.merge.AOD.e3733_s2608_s2183_r6869_r6282/	11.6400	0.90	0.7785	263000	40.9	mc15a
361427	mc15_1.3TeV_361427.Sherpa_CTI0_Zinmu_Pt70_140_CFilterBVeto.merge.AOD.e3733_s2608_s2183_r6869_r6282/	11.6400	0.90	0.2426	468200	184.2	mc15a
361428	mc15_1.3TeV_361428.Sherpa_CTI0_Zinmu_Pt70_140_BFilter.merge.AOD.e3733_s2608_s2183_r6869_r6282/	11.6400	0.90	0.1468	964600	627.2	mc15a
361429	mc15_1.3TeV_361429.Sherpa_CTI0_Zinmu_Pt70_140_CVetoBVeto.merge.AOD.e4133_s2608_s2183_r6869_r6282/	0.7646	0.90	0.5836	499000	1242.5	mc15a
361430	mc15_1.3TeV_361430.Sherpa_CTI0_Zinmu_Pt70_140_BFilter.merge.AOD.e4133_s2608_s2183_r6869_r6282/	0.7646	0.90	0.2632	299100	1651.4	mc15a
361431	mc15_1.3TeV_361431.Sherpa_CTI0_Zinmu_Pt70_140_CVetoBVeto.merge.AOD.e4133_s2608_s2183_r6869_r6282/	0.7646	0.90	0.1594	300000	2735.0	mc15a
361432	mc15_1.3TeV_361432.Sherpa_CTI0_Zinmu_Pt500_1000_CFilterBVeto.merge.AOD.e4133_s2608_s2183_r6869_r6282/	0.0463	0.90	0.5692	299600	12631.5	mc15a
361433	mc15_1.3TeV_361433.Sherpa_CTI0_Zinmu_Pt500_1000_BFilter.merge.AOD.e4133_s2608_s2183_r6869_r6282/	0.0463	0.90	0.2692	199000	17740.0	mc15a
361434	mc15_1.3TeV_361434.Sherpa_CTI0_Zinmu_Pt500_1000_CVetoBVeto.merge.AOD.e4133_s2608_s2183_r6869_r6282/	0.0463	0.90	0.1718	199180	27822.7	mc15a
361435	mc15_1.3TeV_361435.Sherpa_CTI0_Zinmu_Pt500_1000_BFilter.merge.AOD.e4133_s2608_s2183_r6869_r6282/	0.0463	0.90	0.5625	49800	12144.5	mc15a
361436	mc15_1.3TeV_361436.Sherpa_CTI0_Zinmu_Pt700_1000_CFilterBVeto.merge.AOD.e4133_s2608_s2183_r6869_r6282/	0.0081	0.90	0.2958	300000	13912.2	mc15a
361437	mc15_1.3TeV_361437.Sherpa_CTI0_Zinmu_Pt700_1000_CFilterBVeto.merge.AOD.e4133_s2608_s2183_r6869_r6282/	0.0081	0.90	0.1806	300000	22786.4	mc15a
361438	mc15_1.3TeV_361438.Sherpa_CTI0_Zinmu_Pt1000_2000_CVetoBVeto.merge.AOD.e4133_s2608_s2183_r6869_r6282/	0.0011	0.90	0.5499	300000	55106.4	mc15a
361439	mc15_1.3TeV_361439.Sherpa_CTI0_Zinmu_Pt1000_2000_CFilterBVeto.merge.AOD.e4133_s2608_s2183_r6869_r6282/	0.0011	0.90	0.3135	200000	64440.3	mc15a
361440	mc15_1.3TeV_361440.Sherpa_CTI0_Zinmu_Pt1000_2000_BFilter.merge.AOD.e4133_s2608_s2183_r6869_r6282/	0.0011	0.90	0.1861	200000	108554.6	mc15a
361441	mc15_1.3TeV_361441.Sherpa_CTI0_Zinmu_Pt2000_E_CMS_CVetoBVeto.merge.AOD.e4133_s2608_s2183_r6869_r6282/	0.0000	0.90	0.4874	200000	mc15a	
361442	mc15_1.3TeV_361442.Sherpa_CTI0_Zinmu_Pt2000_E_CMS_CFilterBVeto.merge.AOD.e4133_s2608_s2183_r6869_r6282/	0.0000	0.90	0.3078	9980	mc15a	
361443	mc15_1.3TeV_361443.Sherpa_CTI0_Zinmu_Pt2000_E_CMS_BFilter.merge.AOD.e4133_s2608_s2183_r6869_r6282/	0.0000	0.90	0.2048	9360	mc15a	

Table 5: List of simulated samples for $Z \rightarrow \mu\mu/\tau\tau$ -jets using Sherpa. The dataset ID, the generator cross-section σ , the k -Factor, the generator filter efficiency ϵ_{filter} , the total number of generated events N_{gen} , the equivalent luminosity (L_{equiv}) and pile-up configuration (mc15a or mc15b) are shown.

datasetID	Sample name	$\sigma \times BR [\text{pb}]$	$k\text{-Factor}$	ϵ_{filter}	N_{gen}	L_{event}	PU settings
341177	mc1.5_13TeV.341177.amcAtNloHewigggEvtGen_UEEFS_CTEQ6L1_CT10ME_iH125_inc.merge.AOD.e3921_s2608_s2183_r6869_r6282/	0.5085	1.00	0.10554	1951000	36553.8	mc1.5a
341270	mc1.5_13TeV.341270.amcAtNloHewigggEvtGen_UEEFS_CTEQ6L1_CT10ME_iH125_inc.semilegmerge.AOD.e3921_s2608_s2183_r6869_r6282/	0.5085	1.00	0.43929	976000	4369.3	mc1.5a
341271	mc1.5_13TeV.341271.amcAtNloHewigggEvtGen_UEEFS_CTEQ6L1_CT10ME_iH125_inc.allmerge.AOD.e3921_s2608_s2183_r6869_r6282/	0.5085	1.00	0.45517	976000	4216.8	mc1.5a
342284	mc1.5_13TeV.342284.Pythia8EvtGen_A14NNPDF23LO.WH125_inc.merge.AOD.e4246_s2608_s2183_r6869_r6282/	1.1021	1.25	1.0	99400	72.2	mc1.5a
342285	mc1.5_13TeV.342285.Pythia8EvtGen_A14NNPDF23LO.ZH125_inc.merge.AOD.e4246_s2608_s2183_r6869_r6282/	0.6007	1.45	1.0	99200	113.9	mc1.5a
341471	mc1.5_13TeV.341471.PowhegPythia8EvtGen_C10_AZNLOCTE150.i.geh1.25_ZZ4pi_mergemerge.AOD.e3952_s2608_s2183_r6869_r6282/	0.0081	1.45	1.0	289600	24657.3	mc1.5a
301891	mc1.5_13TeV.301891.Sherpa_C10_leugammamP70_i40.merge.AOD.e3952_s2608_s2183_r6793_r6264/	1.2822	1.00	1.	250000	163.6	mc1.5a
301892	mc1.5_13TeV.301892.Sherpa_C10_leugammamP70_i40.merge.AOD.e3952_s2608_s2183_r6793_r6264/	0.2415	1.00	1.	249800	1034.4	mc1.5a
301893	mc1.5_13TeV.301893.Sherpa_C10_muungammamP35_i70.merge.AOD.e3952_s2608_s2183_r6630_r6264/	1.27270	1.00	1.	498476	32.6	mc1.5a
301894	mc1.5_13TeV.301894.Sherpa_C10_muungammamP35_i70.merge.AOD.e3952_s2608_s2183_r6630_r6264/	1.3235	1.00	1.	249400	163.7	mc1.5a
301895	mc1.5_13TeV.301895.Sherpa_C10_muungammamP40.merge.AOD.e3952_s2608_s2183_r6630_r6264/	0.2418	1.00	1.	248900	1029.4	mc1.5a
301896	mc1.5_13TeV.301896.Sherpa_C10_tauungammamP35_i70.merge.AOD.e3952_s2608_s2183_r6793_r6264/	1.2970	1.00	1.	498200	32.6	mc1.5a
301897	mc1.5_13TeV.301897.Sherpa_C10_tauungammamP70_i40.merge.AOD.e3952_s2608_s2183_r6793_r6264/	1.3290	1.00	1.	249600	163.2	mc1.5a
301898	mc1.5_13TeV.301898.Sherpa_C10_tauungammamP70_i40.merge.AOD.e3952_s2608_s2183_r6793_r6264/	0.2426	1.00	1.	249580	1028.8	mc1.5a
301899	mc1.5_13TeV.301899.Sherpa_C10_leugammamP35_i70.merge.AOD.e3952_s2608_s2183_r6793_r6264/	0.2420	1.00	1.	50000	95.4	mc1.5a
301900	mc1.5_13TeV.301900.Sherpa_C10_leugammamP70_i40.merge.AOD.e3952_s2608_s2183_r6793_r6264/	0.3846	1.00	1.	246400	640.7	mc1.5a
301901	mc1.5_13TeV.301901.Sherpa_C10_leugammamP70_i40.merge.AOD.e3952_s2608_s2183_r6793_r6264/	0.0472	1.00	1.	250000	5296.6	mc1.5a
301902	mc1.5_13TeV.301902.Sherpa_C10_muungammamP35_i70.merge.AOD.e3952_s2608_s2183_r6630_r6264/	0.5245	1.00	1.	498042	94.9	mc1.5a
301903	mc1.5_13TeV.301903.Sherpa_C10_muungammamP70_i40.merge.AOD.e3952_s2608_s2183_r6630_r6264/	0.3855	1.00	1.	248800	645.4	mc1.5a
301904	mc1.5_13TeV.301904.Sherpa_C10_muungammamP70_i40.merge.AOD.e3952_s2608_s2183_r6630_r6264/	0.0472	1.00	1.	248700	5269.1	mc1.5a
301907	mc1.5_13TeV.301907.Sherpa_C10_tautauungammamP35_i70.merge.AOD.e3952_s2608_s2183_r6793_r6264/	0.0470	1.00	1.	249000	5297.9	mc1.5a
301908	mc1.5_13TeV.301908.Sherpa_C10_muungammamP35_i70.merge.AOD.e3952_s2608_s2183_r6793_r6264/	0.4365	1.00	1.	498400	123.5	mc1.5a
301910	mc1.5_13TeV.301910.Sherpa_C10_muungammamP70_i40.merge.AOD.e3952_s2608_s2183_r6630_r6264/	0.0715	1.00	1.	248995	256.3	mc1.5a
301911	mc1.5_13TeV.301911.Sherpa_C10_muungammamP70_i40.merge.AOD.e3952_s2608_s2183_r6630_r6264/	0.0711	1.00	1.	248600	1453.0	mc1.5a

Table 6: List of simulated samples for $W + \gamma$ and Higgs processes. The dataset ID, the generator cross-section σ , the k -Factor, the generator filter efficiency ϵ_{filter} , the total number of generated events N_{gen} , the equivalent luminosity (L_{equiv}) and pile-up configuration (mc15a or mc15b) are shown.

323 3.6 Data samples

324 The data used in this note was collected in pp collisions at $\sqrt{s} = 13$ TeV during 2015 in data-taking periods
 325 D-J6 (runs 276262-284484, corresponding to a total integrated luminosity of 3.21 fb^{-1} after GoodRunList
 326 selection) unless otherwise stated. Note that these periods are not affected by L1Calo saturation problems
 327 found at the beginning of the 2015 run, and the runs with the IBL detector switched off are not used for this
 328 analysis. The officially recommended GoodRunLists were used to select only events within luminosity
 329 blocks with good beam, detector and data quality. Note that period A was not considered due to its low
 330 integrated luminosity and known problems in some of the detectors. The uncertainty on the integrated
 331 luminosity is $\pm 5\%$. It was derived, following the same methodology as that detailed in Ref. [38], from
 332 a preliminary calibration of the luminosity scale using a pair of x - y beam separation scans performed in
 333 June 2015.

334 4 Object definition

355 This section presents the definitions of the objects used in the analysis: jets, electrons, muons and E_T^{miss} .
 356 Unless otherwise stated, the recommendations implemented in SUSYTools-00-07-17 tag and analysis
 357 release SUSY,2.3.38b are used for all the objects; most of the studies that led to these definitions were
 358 however performed with earlier tags. Note that the electron identification scale factors released on
 359 15/01/16 within the ElectronEfficiencyCorrection-00-01-39 package are used for AtlFast2 samples in the
 360 final results since they differ by up to 10% in the barrel region with respect to those included in analysis
 361 release SUSY,2.3.38b.

342 4.1 Jets

343 The jet selection is summarized in Table 7. Jets are reconstructed using the anti- k_t jet algorithm [39] with
 344 the distance parameter R set to 0.4 and topological clusters as input. Jets are calibrated with the EMTopo
 345 scheme applying the jet area pile up corrections. The jets are kept only if they have $p_T > 20$ GeV and lie
 346 within $|\eta| < 2.8$. To mitigate the effects of pileup, Jet Vertex Tagger (JVT) [40] requirements are applied
 347 to the selected jets as recommended by the JetEtMiss group (reject jets after the overlap removal procedure
 348 with $p_T < 50$ GeV, $|\eta| < 2.4$ and JVT<0.64). The gain in stability with respect to pile-up after applying
 349 this set of cut is illustrated in Figure 5. In order to remove events with fake E_T^{miss} , an event is vetoed when
 350 a jet ($|\eta| < 4.9$) with quality judged as bad according to the VeryLoose criterion is present.

351 4.1.1 b -tagging

352 Tagging of b -jets is done using the MV2c20 algorithm with the 70% efficiency operating point. This
 353 algorithm is based on a neural network using the output weights of the JetFitter+IP3D, IP3D and SV1
 354 algorithms as input. This efficiency working point was favored by optimisation studies performed with
 355 MC15 simulated signal and background samples as described below. Figure 6 shows the b -jet multiplicity
 356 for the three tagging efficiency working points. Monte Carlo background distributions are shown after
 357 same-sign lepton pair requirement.

Table 7: Summary of the jet selection criteria.

Pre-selected jet	
Collection	AntiKt4EMTopo
Acceptance	$p_T > 20 \text{ GeV}, \eta < 2.8$
Overlap	see section 4.3
Jet vertex tagger	reject jets with $p_T < 50 \text{ GeV}, \eta < 2.4$ and $\text{JVT} < 0.64$ after overlap removal
b-jets	
Acceptance	$p_T > 20 \text{ GeV}, \eta < 2.5$
b -tagging	MV2c20 algorithm 70% OP MV2c20 algorithm 80% OP for overlap removal

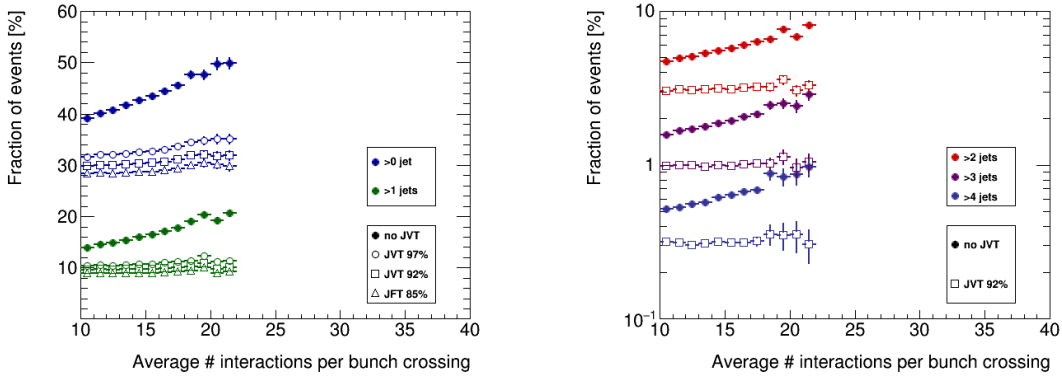


Figure 5: Fraction of events [%] in data with at least 1 or 2 jets (left) and with at least 3, 4 or 5 jets (right) with respect to average number of interactions per bunch crossing with and without a cut on the JVT. Event selection requires a pair of leptons, and all jets have $p_T > 25 \text{ GeV}$. $L = 3.2 \text{ fb}^{-1}$ and $\sqrt{s} = 13 \text{ TeV}$.

358 Different signal models described earlier on this document are expected to contain different heavy flavour
 359 jet multiplicities. Therefore the choice of the most performant b -jet tagging efficiency working point was
 360 made by looking into regions that emulate the signal regions that would eventually be used in the analysis.
 361 Table 8 describes the six different signal-like regions used on this optimisation.

362 Figure 7 shows the discovery signal significance using a simple Gaussian approximation ($S/\sqrt{S + (\Delta B)^2}$)
 363 for different choices of the b -tagging working point (60%, 70%, 77% and 85%) with a flat assumption on
 364 the background uncertainty of 40%. The signal region for each of the models was chosen based on the
 365 highest sensitivity. The 3 b Soft signal-like region was found to be the most performant for the gluino-stop
 366 off-shell production, and the 0 b -5j signal-like region for the gluino production mediated by charginos as
 367 well as the 2-step gluino production mediated by gauginos. The 70% b -tagging efficiency working point
 368 is chosen since it is the best compromise allowing to reach good sensitivity in the different tested signal
 369 models.

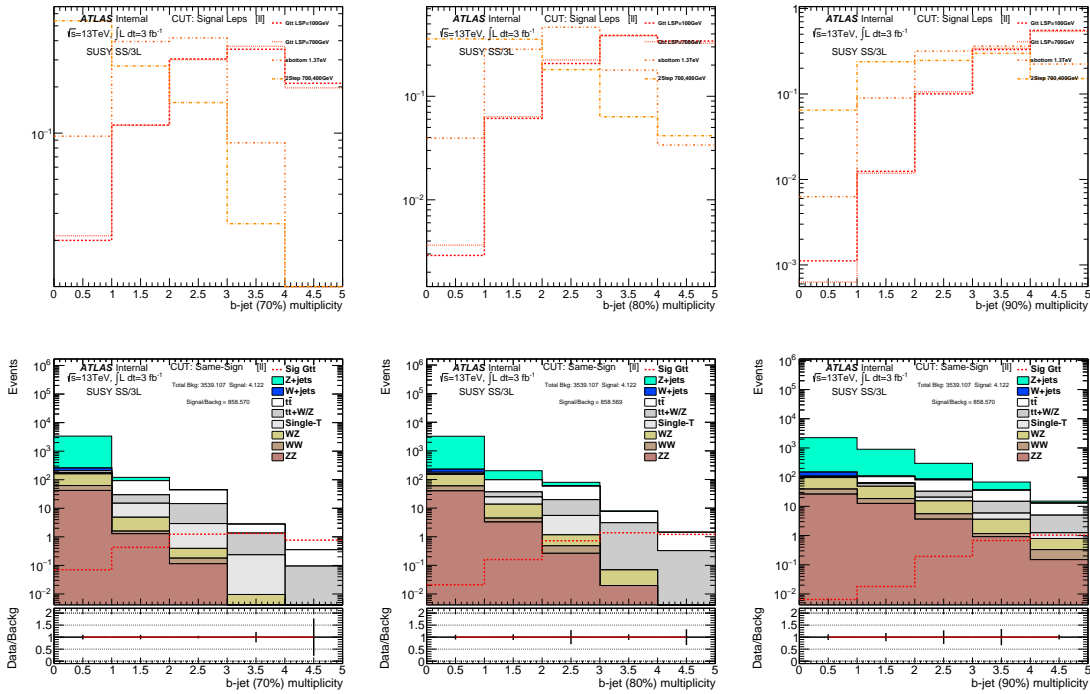


Figure 6: b -jet multiplicity for three different tagging efficiency working points, left 70%, center 80%, right 90%. Signals shapes are shown on the top figures, and stacked background expectations for an integrated luminosity of 3 fb^{-1} are shown on the bottom plots.

Table 8: Signal-like region selections used for the b -jet efficiency working point optimisation.

	# ℓ	# b -jets	Other cuts
SR-3 b	≥ 2	≥ 3	$N_j^{40} \geq 6$
SR-3 b Soft	≥ 2	≥ 3	$N_j^{20} \geq 7 \ \&\& \text{MET} > 150 \text{ GeV}$
SR-1 b	≥ 2	≥ 1	$N_j^{50} \geq 4 \ \&\& \text{MET} > 150 \text{ GeV} (\text{!SR3}b)$
SR-1 b Incl	≥ 2	≥ 1	$N_j^{40} \geq 4 \ \&\& \text{MET} > 150 \text{ GeV}$
SR-0 b - 5j	≥ 2	$= 0$	$N_j^{50} \geq 5 \ \&\& \text{MET} > 100 \text{ GeV}$
SR-0 b - 3j	≥ 2	$= 0$	$N_j^{40} \geq 3 \ \&\& \text{MET} > 200 \text{ GeV}$

4.2 Leptons

This section summarizes the electron and muon object selection, as well as developments done in the optimization of the lepton isolation and electron acceptance cuts.

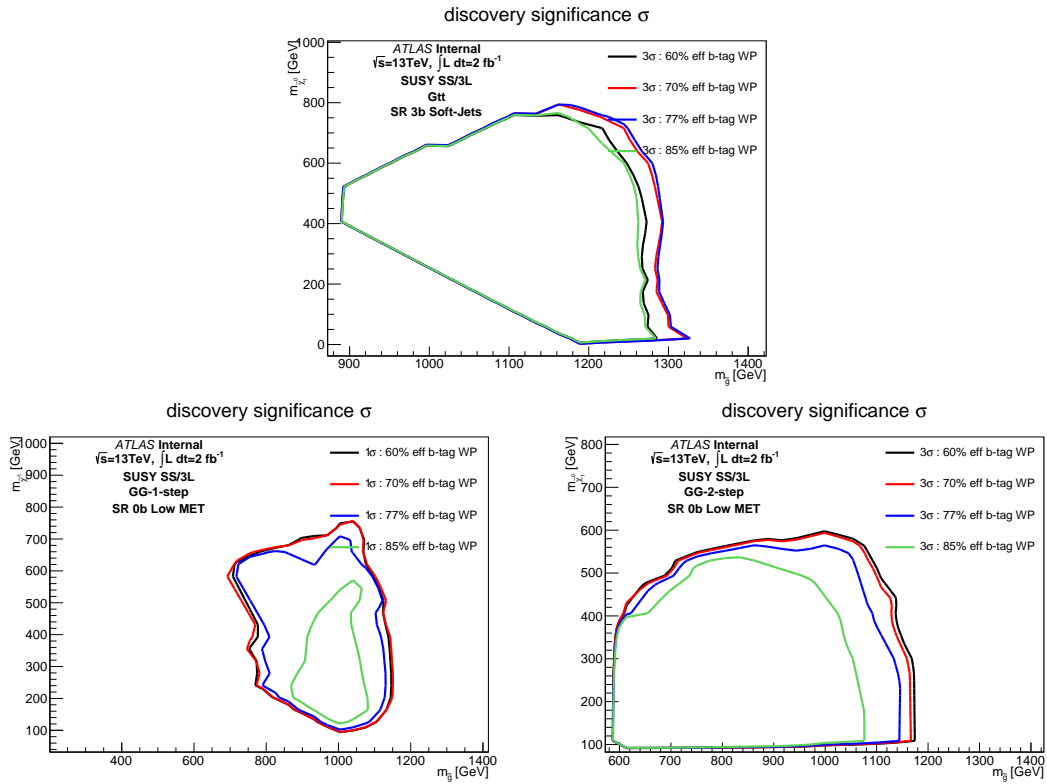


Figure 7: Gaussian discovery signal significance for the various signal-like regions where the different models are sensitive. Three signal models are tested: the gluino-stop off-shell (top), the gluino production mediated by charginos (bottom left) and the 2-step gluinos via charginos (bottom right). b -jet tagging efficiency working points supported by the heavy flavour working group are 60%(black), 70%(red), 77%(blue) and 85%(green). Expectations are estimated assuming an integrated luminosity of 2 fb^{-1} of 13 TeV.

373 4.2.1 Electrons

374 The electron selection is summarized in Table 9. The Egamma CP group recommends the likelihood-based
 375 electron identification [41] for Run-2, since it provides a factor of two better background rejection
 376 than the cut-based identification. Four working points (VeryLooseLH, LooseLH, MediumLH, TightLH)
 377 are available for LH electrons.

378 Pre-selected electrons must satisfy the LooseLH requirements and have $E_T > 10 \text{ GeV}$ and $|\eta| < 2.47$.
 379 Electrons in the LAr crack region ($1.37 < |\eta| < 1.52$) are rejected to reduce the contribution from non-prompt
 380 electrons. A requirement on the transverse impact parameter of $|d_0/\sigma(d_0)| < 5$ (as recommended
 381 by TrackingCP) is also applied to pre-selected electrons and helps reducing the contribution from charge
 382 mis-identification. Signal electrons are additionally required to pass the isolation cuts defined in 4.2.3 as
 383 well as the TightLH identification criteria and standard requirements of the longitudinal impact parameter
 384 ($|z_0 \cdot \sin(\theta)| < 0.5 \text{ mm}$, as recommended by TrackingCP).

385 A multiplicative event weight is applied for each signal electron in MC to the overall event weight in order
 386 to correct for differences in efficiency between data and MC as recommended by the Egamma group.

387 4.2.2 Muons

388 The muon selection is summarized in Table 9. The Run-2 muon reconstruction is performed by the
 389 so-called *third chain*: it has been designed to combine the best features of the Run-1 STACO and MUID
 390 chains to provide the best performance. The following muon selection working points are supported:
 391 **Tight**, **Medium**, **Loose** and **VeryLoose**.

392 Pre-selected muon candidates must pass the **Medium** muon quality cuts and have $p_T > 10 \text{ GeV}$ and
 393 $|\eta| < 2.4$. A smearing procedure is applied to the muon p_T . A multiplicative event weight is applied
 394 for each selected muon in MC to the overall event weight in order to correct for differences in efficiency
 395 between data and MC as recommended by the Muon CP group.

396 Finally, signal muon candidates are required to pass the isolation cuts defined in 4.2.3 as well as the
 397 requirements on the impact parameter of $|d_0/\sigma(d_0)| < 3$ and $|z_0 \cdot \sin(\theta)| < 0.5 \text{ mm}$, as recommended by
 398 TrackingCP.

399 Note that events with “cosmic” muons, or “Bad” muon are vetoed as described in Section 5.2.

Table 9: Summary of the electron and muon selection criteria. The signal selection requirements are applied on top of the preselection. The lepton-jet isolation requirement is applied after electron-jet overlap removal.

	Pre-selected Electron	Pre-selected Muon
Acceptance	$p_T > 10 \text{ GeV}, \eta^{\text{clust}} < 2.47$ except $1.37 < \eta^{\text{clust}} < 1.52$	$p_T > 10 \text{ GeV}, \eta < 2.5$
Quality	LooseLLH	xAOD::Muon::Medium
ℓ -jet Isolation	$\Delta R(e, \text{jet}) > 0.4$	$\Delta R(\mu, \text{jet}) > 0.4$
Impact parameter	$ d_0/\sigma(d_0) < 5.0$	
	Signal Electron	Signal Muon
Quality	TightLLH $ \eta < 2.0$	- -
Isolation	“ FixedCutTight ”	“ FixedCutTightTrackOnly ”
Impact parameter	$ z_0 \cdot \sin(\theta) < 0.5 \text{ mm}$	$ z_0 \cdot \sin(\theta) < 0.5 \text{ mm}$ $ d_0/\sigma(d_0) < 3.0$

400 4.2.3 Lepton isolation

401 The isolation working points proposed from this analysis were accepted by the ATLAS Isolation forum and
 402 implemented as officially supported working points in the `IsolationSelectionTool`. Unless otherwise
 403 stated, the following isolation working points are used in the analysis:

- 404 • Electrons: `TightLLH`, $\text{ptvarcone}20/p_T < 0.06$ and $\text{topoetcone}20/p_T < 0.06$ (“`FixedCutTight`”)
 405 • Muons: $\text{ptvarcone}30/p_T < 0.06$ (“`FixedCutTightTrackOnly`”)

406 Isolation scale factors determined by the CP groups for these working points are applied.
 407 More details on the isolation studies performed in the context of this analysis can be found in Ap-
 408 pendix 24.

409 **4.2.4 Electron acceptance**

410 Dedicated studies have been conducted to evaluate the impact of a reduction of the $|\eta|$ coverage for
 411 electrons. This is motivated by the fact that the largest contributions from charge-flip and fake lepton
 412 backgrounds are observed at $|\eta| > 2$ and in the LAr crack region ($1.37 < |\eta| < 1.52$), due to poorer
 413 detector resolution or increased amount of material in these regions.

414 Table 10 shows the impact on the expected event yields when reducing the electron $|\eta|$ acceptance for the
 415 two leading electrons (taking a reference the case of $|\eta| < 2.3$). The event selection applied to compute
 416 those numbers requires SS/3L, at least 3 jets with $p_T > 30$ GeV and m_{ee} outside the 84-98 GeV range to
 417 reduce the contribution from charge flips.

Table 10: Relative decrease in the event yield when reducing the $|\eta|$ acceptance for the two leading electrons with respect to $|\eta| < 2.3$. The reference is considered to be $|\eta| < 2.47$, and the crack region is excluded in all the cases. Numbers are shown for the event selection described in the text and separately for events with 1 or more b -jets.

	Prompt SS	$t\bar{t} + W$	Gtt (G900_L100)	Non-prompt leptons	Charge flip
$\leq 1b, \eta < 1.37$	14%	16%	12%	28%	69%
$\leq 1b, \eta < 2.0$	5.4%	6%	7%	11%	37%
$\leq 1b, \eta < 2.3$	0.4%	1.5%	4.7%	3.6%	11%
$> 1b, \eta < 1.37$	13%	18%	10%	44%	66%
$> 1b, \eta < 2.0$	4.3%	6.5%	2.9%	21%	30%
$> 1b, \eta < 2.3$	1.3%	1.5%	0.3%	8%	5.8%

418 As shown, reducing the acceptance to $|\eta| < 2.0$ would reduce the contribution from processes with prompt
 419 SS/3L by 6.5% or less, but the reduction in non-prompt leptons (11-21%) and charge flip (30-37%) is
 420 quite larger. Reducing the acceptance more severely for the two leading electrons to $|\eta| < 1.37$ would
 421 reduce the non-prompt and charge flip components by 28-44% and ~69%, respectively, with a reduction
 422 of only 13-18% for prompt SS/3L processes.

423 Therefore, this study proves that additional rejection against some of the main backgrounds affecting the
 424 analysis can be achieved by reducing the $|\eta|$ acceptance of the electrons. As illustrated in Table 9 we chose
 425 in conclusion to reject electrons with $|\eta| > 2.0$ or in the EM calorimeter cracks ($1.37 < |\eta_{\text{cluster}}| < 1.52$).
 426 Note that these requirements are applied to electrons regardless of the lepton multiplicity of the event.

427 **4.3 Overlap removal**

428 According to the above definitions, one single final state object may fall in more than one category, being
 429 therefore effectively double-counted. For example, one isolated electron is typically reconstructed both as
 430 an electron and as a jet. A procedure to remove overlaps between final state objects was therefore put in

place, and applied on pre-selected objects. For this iteration, recommendations from the Harmonization effort [42] have been fully adopted.

The procedure performed is described as follows:

- First, jets that are angularly close (cone of $\Delta R_y < 0.2$, note the usage of rapidity instead of pseudo-rapidity) to a pre-selected (non-isolated) electron are removed from the jet list, except if the *b*-tagging weight satisfies the 80% working point (the electron is then likely coming from a semileptonic *b*-quark decay, so it is removed and the jet is kept).
- Following this, pre-selected electrons are removed if their distance to the closest jet is $\Delta R_y < 0.4$. Then if the ΔR_y between a jet and a muon is less than 0.4, one looks at the number of tracks associated to the jet (`xAOD::JetAttribute::NumTrkPt500`): if strictly less than 3 the jet is removed (and the muon is kept), otherwise the muon is removed (and the jet is kept).
- If there are an electron and a muon with $\Delta R_y < 0.01$, the former is likely to originate from a bremsstrahlung of the muon. Such a muon momentum is not measured correctly so that in this case, both the electron and the muon are removed.
- Finally, if there are two electrons with $\Delta R_y < 0.05$, the electron with the highest p_T is kept and the other one is discarded.

Note that preliminary studies with DC14 data showed a few percent gain in sensitivity if using a narrower cone for the muon-jet overlap removal ($\Delta R_y < 0.2$), but this was found to introduce features in the muon real and fake efficiency used in the matrix method (see Appendix 16). Therefore, for simplicity and robustness in the analysis, it was decided to used the default value of $\Delta R_y < 0.4$.

4.4 Missing transverse energy

The missing transverse energy (E_T^{miss}) is rebuilt using the xAOD container “MET_RefFinal” as input and using the calibrated electron, muon and jet objects (and baseline taus and photons according to SUSYTools definitions). In this version of the analysis, the track soft term is used for building the E_T^{miss} following the defaults in SUSYTools-00-07-17.

4.5 Lepton truth matching

In several studies presented in this document, a lepton truth matching strategy is applied to distinguish the lepton originating from prompt decays of gauge boson or SUSY particles from non-prompt leptons originating from semileptonic *b*-decays, photon conversions or fakes. This strategy largely relies on the information from the `MCTruthClassifier` tool. However, the latter does not always allow to properly classify electrons originating from a photon conversion, where it is important to fully understand the origin of the photon and its possible proximity to a prompt electron (FSR, bremsstrahlung, which is the main mechanism leading to charge-flip electrons). In these cases, we complete this information by a matching within a cone of $\Delta R < 0.1$ with truth prompt electrons, which are identified as the decays of heavy bosons (W , Z , h) or SUSY particles. This is however only possible in MC generators storing intermediate resonances in the event record, i.e. notably MC samples in which decay chains are handled by Pythia.

468 5 Event selection

469 5.1 Trigger studies

470 5.1.1 Final trigger strategy

471 Based on the studies and efficiency measurements detailed in the rest of this section, the following trigger
 472 strategy is used in the analysis:

- 473 • If $E_T^{\text{miss}} < 250$ GeV, only an OR combination of the following di-lepton triggers is used:
 474 HLT_2e12_lhloose_L12EM10VH, HLT_e17_lhloose_mu14, HLT_mu18_mu8noL1.
- 475 • If $E_T^{\text{miss}} > 250$ GeV, an OR between the di-lepton triggers and HLT_xe70 is used.

476 Trigger matching is applied as follows:

- 477 • only signal leptons with $p_T > 20$ GeV are considered
- 478 • for technical reasons, matching to muon triggers is performed only on the corresponding level-1
 479 item (L1_MU10 and L1_MU15)
- 480 • trigger matching for HLT_mu18_mu8noL1 is performed only on the mu18 leg; however, the
 481 presence of another signal muon in the event is required.

482 5.1.2 Detailed trigger studies (DC14, MC15)

483 The trigger strategy for the analysis in Run-2 is similar to the one used in the Run-1 version. There, a
 484 combination of E_T^{miss} , single-lepton and di-lepton triggers was used for the selection of events in the signal
 485 regions as well as for background estimations. The triggers were checked consecutively starting with the
 486 E_T^{miss} trigger, followed by the single-lepton trigger and the di-lepton triggers, until one of the triggers is
 487 passed by the event. Offline cuts on the missing energy and the p_T of the triggered objects were applied
 488 to ensure to be on the efficiency plateau of the corresponding trigger.

489 For Run-2, the triggers to be considered are single-lepton, di-lepton triggers and a E_T^{miss} trigger. The
 490 lepton trigger menu includes di-lepton triggers selecting same-flavour and mixed-flavour lepton events.
 491 Some single-lepton triggers have additional requirements on the isolation of the triggered lepton. The
 492 following triggers have been regarded as important for this analysis and were used for further studies on
 493 performance and efficiency:

- 494 • Single-lepton triggers: HLT_mu26, HLT_mu50, HLT_mu24_imedium, HLT_mu26_imedium,
 495 HLT_e20_medium, HLT_e60_medium, HLT_e24_tight_iloose, HLT_e26_tight_iloose
- 496 • Di-lepton triggers: HLT_2e12_loose_L12EM10VH, HLT_2e12_lhloose_L12EM10VH
 497 HLT_e17_loose_mu14, HLT_e17_lhloose_mu14, HLT_mu18_mu8noL1
- 498 • E_T^{miss} trigger: HLT_xe100

499 Note that the low- p_T single-lepton triggers which would be run un-prescaled in 2015 contain requirements
500 on the lepton isolation (`iLoose`, `iMedium`) and/or more stringent electron identification requirements
501 (`medium`) than those used in the baseline lepton definition. Therefore we can't rely on these chains to
502 select the sample of event to be used for fake-lepton background estimation, although they might still be
503 useful for signal region selection.

504 The performance of these triggers has been investigated by running the analysis on dedicated Monte Carlo
505 samples. For each object triggered, an offline cut on the object p_T or the E_T^{miss} is applied to ensure the full
506 efficiency of the trigger in the selected event. We ensure that the tested trigger was activated by one of the
507 signal leptons found in the analysis, by requiring a geometrical ΔR matching between these signal leptons
508 and the leptons reconstructed by the online version of the software, responsible for the trigger decision.

509 **Monte Carlo samples and software framework** The analysis code was setup with the `AnalysisBase`
510 framework (2.3.8 branch for rel.20 ATLAS software). The object selection was done by using the
511 `SUSYTools-00-06-03` package which the recommended selections of signal and baseline objects at the
512 time of the study.

513 The Monte Carlo samples used for these studies are validation samples produced with the 20.1.4.3 MC15
514 ATLAS software release.

- 515 • $t\bar{t}$ sample:

516 `valid3.110401.PowhegPythia_P2012_ttbar_nonallhad.recon.AOD.e3099_s2578_r6540`

- 517 • $Z \rightarrow \mu\mu$ sample:

518 `valid3.167826.Sherpa_CT10_ZmumuMassiveCBPt280_500_CVetoBVeto.recon.AOD.e3099_s2578_r6540`

- 519 • $Z \rightarrow ee$ sample:

520 `valid3.147406.PowhegPythia8_AZNLO_Zee.recon.AOD.e3099_s2578_r6540`

521 **Total event yields** The total event yields for the test Monte Carlo samples and different trigger configura-
522 tions were investigated in order to understand the gain of the several trigger types and their combinations.
523 The yields are measured in a $t\bar{t}$ Monte Carlo sample and for different trigger applications applied. The
524 three configuration tested were:

- 525 1. Applying only di-lepton triggers (`HLT_2e12_loose_L12EM10VH`, `HLT_2e12_lhloose_L12EM10VH`,
526 `HLT_mu18_mu8noL1`, `HLT_e17_loose_mu14`, `HLT_e17_lhloose_mu14`)
- 527 2. Applying a logical OR between di-lepton triggers and the E_T^{miss} trigger (`HLT_xe100`)
- 528 3. Applying a logical OR between di-lepton, E_T^{miss} , and single-lepton triggers without explicit isolation
529 requirements (`HLT_e60_lhmedium`, `HLT_mu50`)

530 The results are shown in Figure 8, separately for events with $E_T^{\text{miss}} < 200$ GeV and $E_T^{\text{miss}} > 200$ GeV.
531 While for the low- E_T^{miss} events, the single-lepton triggers induce a enhancement on the yields of about
532 1.5%, the measurement for high- E_T^{miss} events shows only a negligible gain by adding single-lepton triggers
533 to the configuration. The most significant increase is induced by adding the E_T^{miss} trigger to the di-lepton
534 trigger chain for events with $E_T^{\text{miss}} > 200$ GeV, with a 6% increase in the event yields. Therefore, the

logical OR of di-lepton and E_T^{miss} triggers will be used in the analysis. For simplicity and due to the small improvement they could provide, single-lepton triggers will not be used in the following.

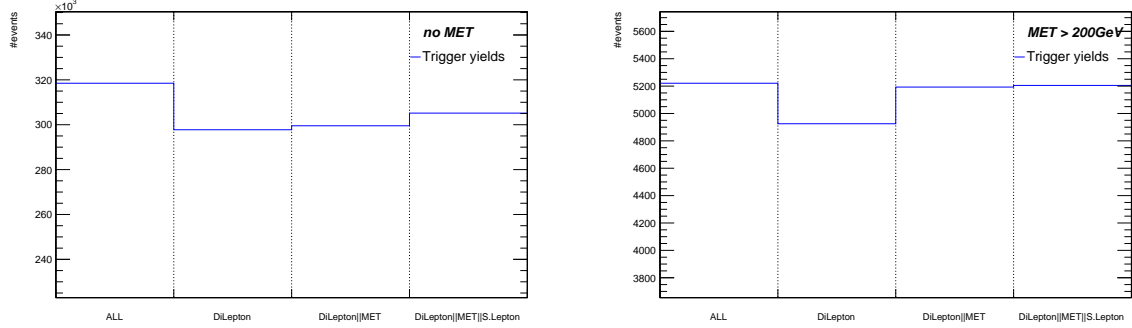


Figure 8: Total events yields of the $t\bar{t}$ sample for several trigger configurations. The yields are measured for events with $E_T^{\text{miss}} < 200 \text{ GeV}$ (left) and $E_T^{\text{miss}} > 200 \text{ GeV}$ (right) independently.

Efficiencies The trigger efficiency in Monte Carlo can be obtained by dividing the number of triggered events by the total number of events. The generic cleaning cuts are applied in both cases.

The efficiencies have been calculated separately for single-lepton, di-lepton triggers and for E_T^{miss} triggers. The results for some examples are shown in Fig. 9 for di-lepton and E_T^{miss} triggers. The turn-on curve for the E_T^{miss} trigger shows the expected evolution. The efficiency plateau is reached for $E_T^{\text{miss}} > 150 - 200 \text{ GeV}$. At the trigger plateau, the efficiency is reaching $> 99\%$. The combination of di-lepton and missing energy trigger shows an efficiency of $> 90\%$ for di-muon events.

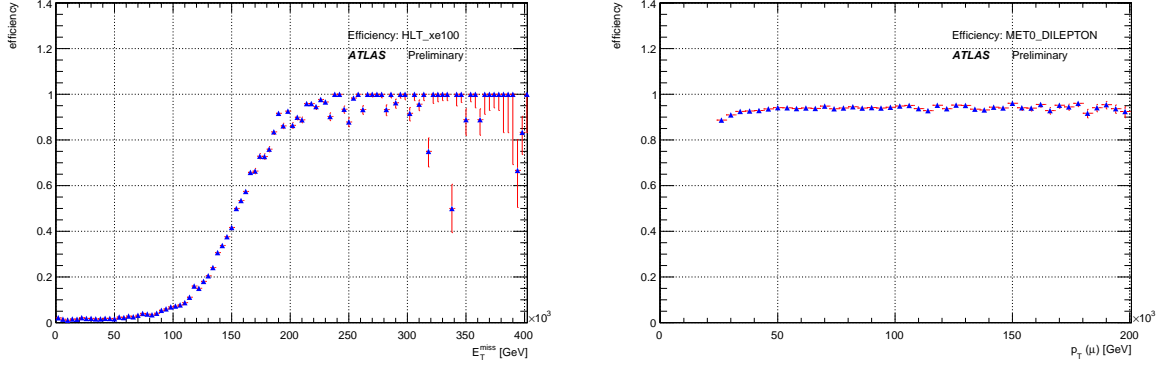


Figure 9: Trigger efficiencies for HLT_xe100 (left) versus the missing energy and for the combination of di-lepton and E_T^{miss} -triggers (right) versus the p_T of the leading triggered muon.

Choice of E_T^{miss} trigger During the review of this analysis, it was pointed out that xe_70 trigger will be unprescaled during the 2015. Figure 10 shows the turn-on curves of this trigger item for different requirements in the jet multiplicity, and compared with xe_80 items. In all cases, the plateau of these trigger is reached at a E_T^{miss} value of 250 GeV. More details can be found in App. 20.

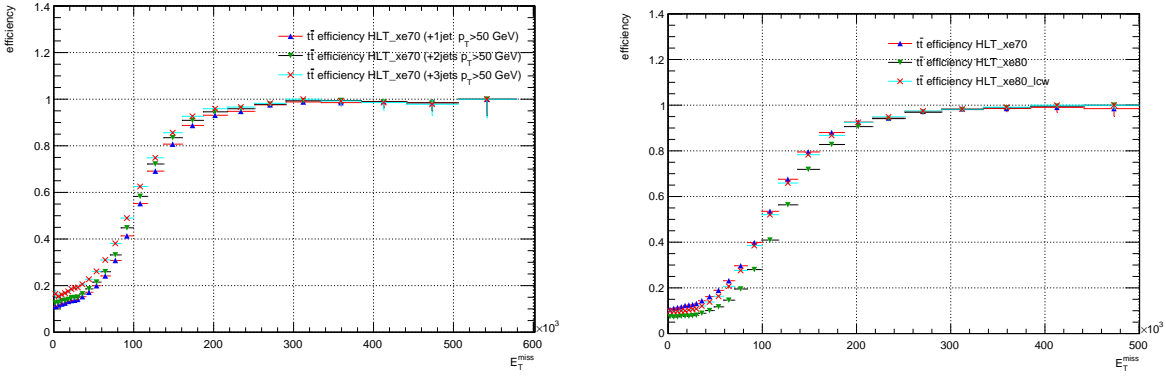


Figure 10: Trigger efficiencies in data for HLT_xe70 (left) and HLT_xe80, HLT_xe80_tc_lcw (right) versus E_T^{miss} . The different curves show the efficiency for events containing a di-lepton pair.

548 Based on these studies and efficiency measurements, a preliminary decision for the trigger selection has
549 been made.

- 550 • If $E_T^{\text{miss}} < 250$ GeV, only an OR combination of di-lepton triggers is used.
551 • If $E_T^{\text{miss}} > 250$ GeV, an OR between the di-lepton triggers and HLT_xe70 is used.

552 5.2 Event pre-selection

553 A sample of two same-sign or three leptons is selected applying the following criteria:

- 554 • **Jet Cleaning:** Events are required to pass the VeryLooseBad set of cleaning requirements re-
555 commended by Jet- E_T^{miss} group [43] and implemented in the JetCleaningTool. An event is
556 rejected if at least one of the pre-selected jets (thus after jet-electron overlap removal) fails the jet
557 quality criteria. The cleaning requirements are intended to remove events where significant energy
558 was deposited in the calorimeters due to instrumental effects such as cosmic rays, beam-induced
559 (non-collision) particles, and noise.
- 560 • **Primary Vertex:** events are required to have a primary vertex, that is, one of the reconstructed
561 vertices must be labeled as `xAOD::VxType::PriVtx`. No additional requirements on the number
562 of tracks in the vertex should be applied as recommended by the Tracking CP group [44].
- 563 • **Bad Muon Veto:** Events containing at least one pre-selected muon satisfying $\sigma(q/p)/|q/p| > 0.2$
564 before the overlap removal are rejected.
- 565 • **Cosmic Muon Veto:** Events containing a cosmic muon candidate are rejected. Cosmic muon
566 candidates are selected among pre-selected muons, if they fail the requirements $|z_0| < 1.0$ mm and
567 $|d_0| < 0.2$ mm, where the longitudinal and transverse impact parameters z_0 and d_0 are calculated
568 with respect to the primary vertex.
- 569 • **At least two leptons:** Events are required to contain at least two signal leptons (see Section 4 and
570 Table 9) with $p_T > 20$ GeV for the two leading leptons. If the event contains a third signal lepton
571 with $p_T > 10$ GeV the event is regarded as three-lepton event otherwise as a two-lepton event. Two

of the leptons in the event are matched to the trigger objects if the event is classified as passing a dilepton trigger (i.e. in the low- E_T^{miss} region). The data sample obtained is then divided into three channels depending on the flavor of the two leptons forming a same-sign pair (ee , $\mu\mu$, $e\mu$). If more than one same-sign pairs can be built, the one involving the leading lepton will be considered for the channel selection.

- **Same sign:** If the event is a two-lepton event the two leading leptons have to be of same charge (same-sign).

The following event variables are also used in the definition of the signal and validation regions in the analysis:

- The inclusive effective mass m_{eff} defined as the scalar sum of the signal leptons p_T (see Table 9), all signal jets p_T (see Table 7) and E_T^{miss} ;
- The transverse mass m_T computed from the leading lepton and E_T^{miss} as

$$m_T = \sqrt{2 \cdot p_T^\ell \cdot E_T^{\text{miss}} \cdot (1 - \cos(\Delta\phi(\ell, E_T^{\text{miss}})))}.$$

5.2.1 Optimisation of lepton pairing selection

In the previous version of this analysis performed during Run-1, different strategies have been used to select same-sign lepton pairs in an event. In order to optimize the event selection of the analysis, different types of lepton pairing selections were compared in terms of their sensitivity to the proposed signal regions:

- **Inclusive 2 Leptons:** Two same-sign leptons with $p_T > 20$ GeV are required, no cuts are applied on an eventual third lepton;
- **Inclusive 2 Leptons + 1:** Two same-sign leptons with $p_T > 20$ GeV are required. A p_T cut of 10 GeV is applied to an eventual third lepton. If there are three leptons in the event the two leading leptons can also have opposite sign.
- **Inclusive 3 Leptons:** At least three leptons are required to be in the event. The two leading leptons need to have a p_T of 20 GeV while the third lepton needs to have at least 10 GeV.
- **Exclusive 2 Leptons:** Exactly two same-sign leptons are required with a $p_T > 20$ GeV. If a third lepton occurs in the event, the event is vetoed.

The background estimation for these optimization studies is purely Monte Carlo driven. In every Signal Region has been studied the related benchmark signal model. For this study, the object selection was done by using the SUSYTools-00-06-24-01 package and release 2.3.28 of the AnalysisBase software framework.

Studies were performed on several grid points (varying gluino and neutralino masses). All background and signal samples were scaled according to their cross-sections and the number of generated Monte Carlo events to an integrated luminosity of 4 fb^{-1} . The significance has been estimated using RooStats::NumberCountingUtils::BinomialObsZ, assuming 40% of background uncertainty, while the error on the significance is evaluated with 100 MC toys.

The different lepton pairing selections are tested on Run1-like Signal Regions.

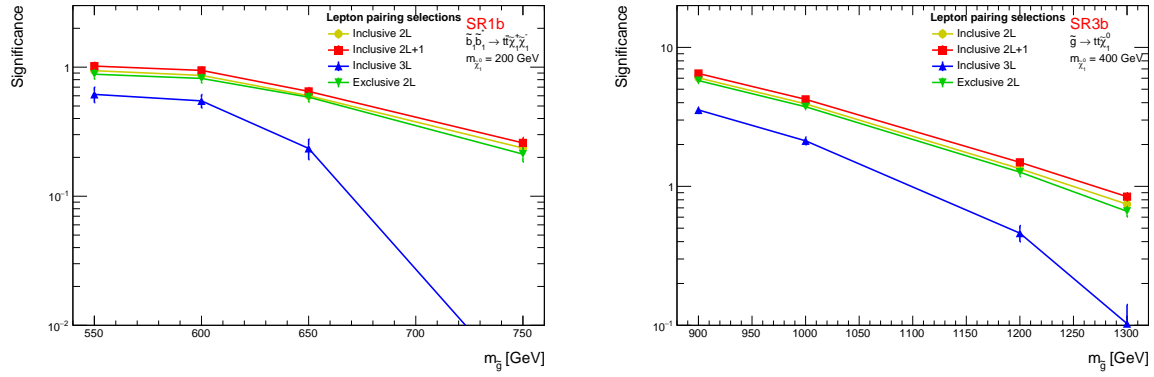


Figure 11: Left: Signal significances for a “SR1b-like” selection (cf text), for several $\tilde{b}_1\tilde{b}_1^* \rightarrow t\bar{t}\tilde{\chi}_1^+\tilde{\chi}_1^-$ models with variable $m_{\tilde{g}}$ and fixed $m_{\tilde{\chi}} = 200$ GeV. Right: Signal significances for a “SR3b-like” selection (cf text), for several $\tilde{g} \rightarrow t\bar{t}\tilde{\chi}_1^0$ models with variable $m_{\tilde{g}}$ and fixed $m_{\tilde{\chi}} = 400$ GeV. The significance is computed for different lepton pair selection strategies which are drawn in different colors in the plot.

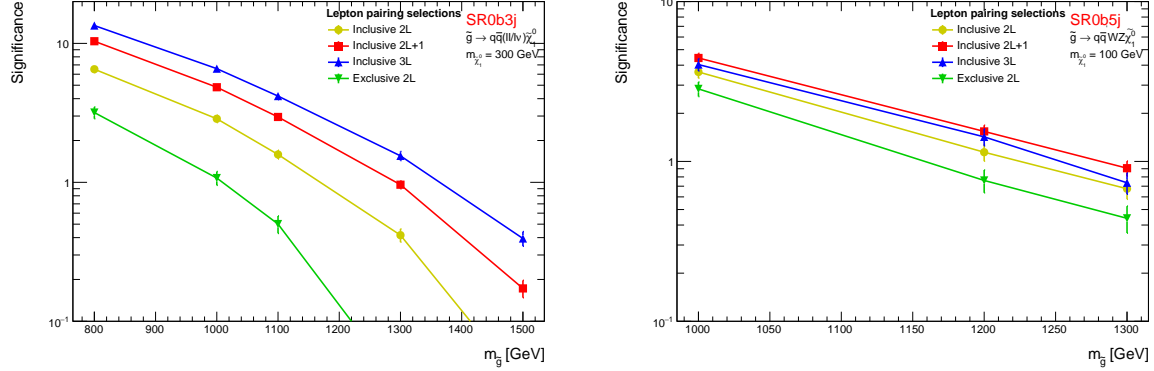


Figure 12: Left: Signal significances for a “SR0b3j-like” selection (cf text) for several $\tilde{g} \rightarrow q\bar{q}(ll/l\nu)\tilde{\chi}_1^0$ models with variable $m_{\tilde{g}}$ and fixed $m_{\tilde{\chi}} = 300$ GeV. Right: Signal significances for a “SR0b5j-like” selection (cf text) for several $\tilde{g} \rightarrow q\bar{q}WZ\tilde{\chi}_1^0$ models with variable $m_{\tilde{g}}$ and fixed $m_{\tilde{\chi}} = 100$ GeV. The significance is computed for different lepton pair selection strategies which are drawn in different colors in the plot.

Figure 11 and 12 show the signal significance for event selections ¹ close to the final signal regions definitions (cf section 6), for the four different lepton pairing selections varying the gluino mass and a fixed neutralino mass. The “inclusive 2L+1” option shows the highest significance for almost all of the mass points investigated. Since this pairing option is the most inclusive one in all signal regions, the event yields are higher with respect to the other options leading to a better exclusion strength for most signal scenarios.

The only exception is in SR0b3j where the Inclusive 3L is more efficient. This motivates the final decision of requiring at least 3 leptons in this signal region (cf section refsec:SignalRegDef).

618

¹ All regions require ≥ 2 same-sign leptons; SR3b = ≥ 3 b-jets + ≥ 6 jets, SR1b = ≥ 1 b-jet + ≥ 4 jets + $E_T^{\text{miss}} > 150$ GeV + $m_{\text{eff}} > 500$ GeV, SR0b3j = b-jet veto + ≥ 3 jets + $E_T^{\text{miss}} > 200$ GeV + $m_{\text{eff}} > 400$ GeV, SR0b5j = b-jet veto + ≥ 5 jets + $E_T^{\text{miss}} > 100$ GeV + $m_{\text{eff}} > 400$ GeV.

619 **5.2.2 Validation of the p_T cuts for the leading, sub-leading and 3rd lepton**

620 Since the “inclusive 2L+1” lepton pairing selection turned out to be the most significant one in most
 621 scenarios, this configuration has been used to investigate also the impact of changes in the p_T cuts of
 622 the lepton on the analysis sensitivity. Therefore several p_T cuts for the signal leptons have been tested
 623 independently. One additional configuration which was also tested in which is to apply only the baseline
 624 requirements on the third lepton if already two signal leptons have been found in the event.

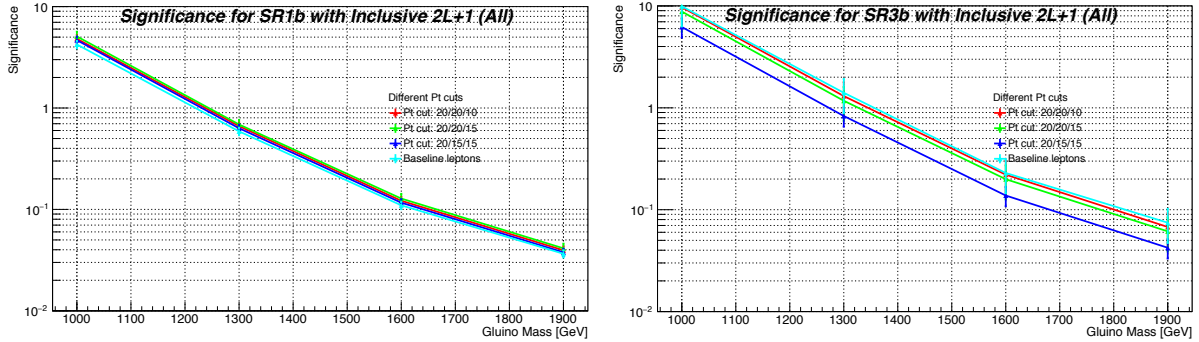


Figure 13: Significances of the signal region SR1b and SR3b for $\tilde{g} \rightarrow t\bar{t}\chi_1$ models with variable $m_{\tilde{g}}$ and fixed m_{χ} of 100 GeV. The significances are computed for different p_T cuts on 1st, 2nd and 3rd lepton. The significances are also shown for $p_T(1st, 2nd, 3rd) = 20, 20, 10$ GeV, relaxing the requirements on the third lepton to baseline-cuts.

625 Figure 13 shows the significances of SR1b and SR3b (as defined in previous section) for different p_T cuts
 626 on first, second and third leptons. The significances are also shown for $p_T(1st, 2nd, 3rd) = 20, 20, 10$
 627 GeV but relaxing the requirements on the third lepton to baseline-cuts. The observed significances show
 628 only small dependencies on changes of the p_T cuts. Also relaxing the requirements of the third lepton to
 629 the baseline definition has no big impact on the sensitivity of the analysis. Therefore a modification of the
 630 nominal lepton selection criteria would not bring a substantial benefit to the analysis sensitivity.

631 **5.3 Data-MC comparisons**

632 In order to validate the various choices made regarding the object definitions and event selection, check
 633 their sensible behavior and their reasonable modelling in the simulations, we looked at the distributions
 634 of several kinematic variables obtained with the available 13 TeV data. Figures 14-19 show such selected
 635 distributions in data compared to MC. The background distributions are taken directly from MC with no
 636 data-driven estimation of the charge flip or non-prompt lepton backgrounds.

637 Figure 14 shows the dilepton invariant mass distributions for both OS and SS dilepton events, computed
 638 with the two leading p_T leptons. A very good agreement with MC is observed in the OS channels, with
 639 a clear Z-boson mass peak in the ee and $\mu\mu$ channels. In the SS channels, the Z-boson mass peak is
 640 also observed in the ee channel due to electron charge mis-identification, with MC overestimating data by
 641 20-30%. An accumulation of events at the Z-boson mass is also observed in the SS $e\mu$ and $\mu\mu$ channels
 642 due to three-lepton events from either Z+jets with a fake lepton or from WZ production.

643 Lepton distributions are shown in Figures 15-16, with a reasonable data-MC agreement except at low
 644 lepton p_T where some discrepancies and accumulation of events involving fake leptons ($Z+jets$, $W+jets$,
 645 $t\bar{t}$) are observed. Jet and b -jet distributions are shown in Figures 17-18 and Figure 19 shows the E_T^{miss} and
 646 m_{eff} distributions.

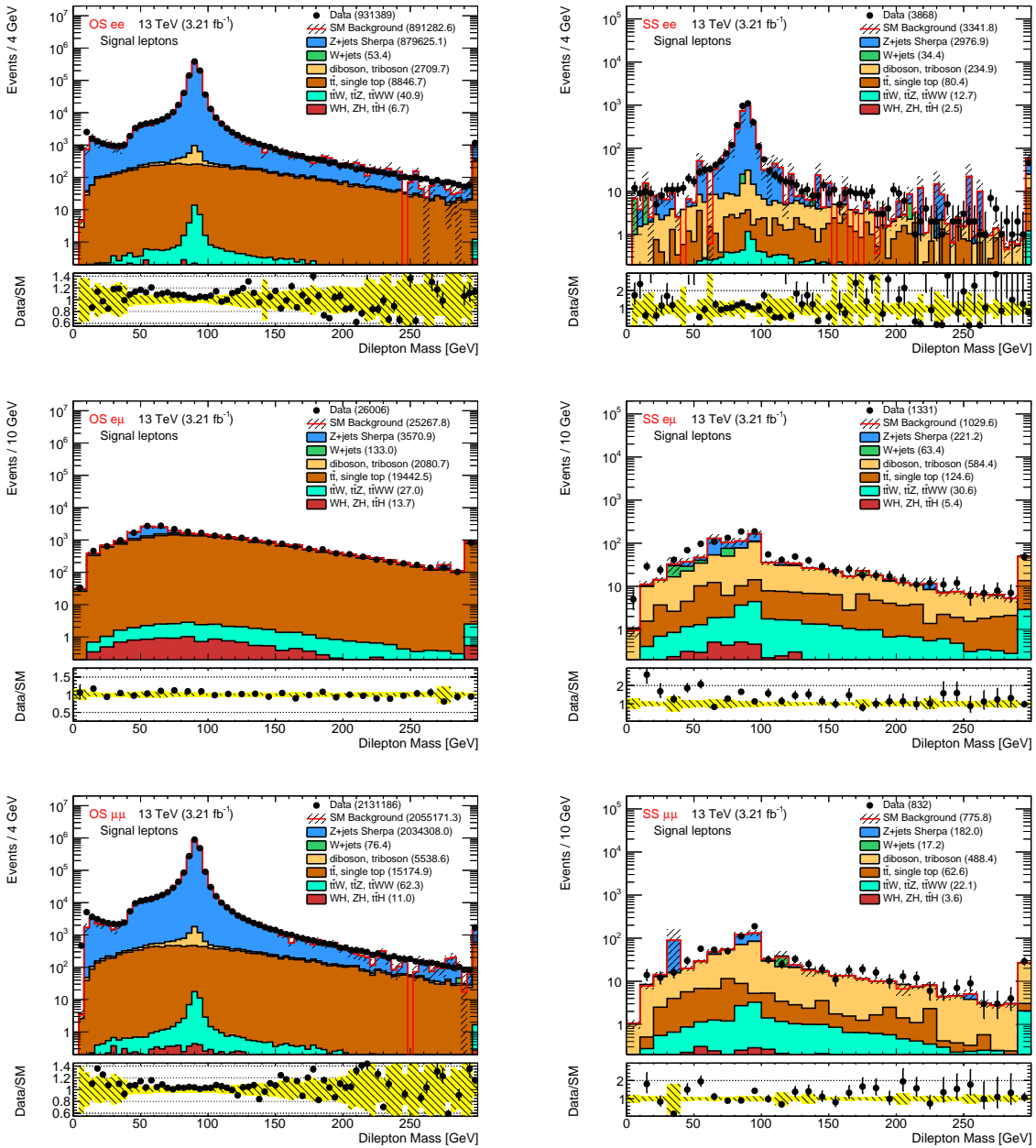


Figure 14: Dilepton invariant mass distributions for opposite-sign (left) and same-sign (right) pairs for events selected in the ee (top), $e\mu$ (center) and $\mu\mu$ (bottom) channels, computed with the two leading p_T leptons. The background contribution is taken directly from MC with no data-driven estimation of the background with fake and non-prompt leptons or charge mis-identification. No low-mass Drell-Yan sample is included. Only luminosity and MC statistical uncertainties are included.

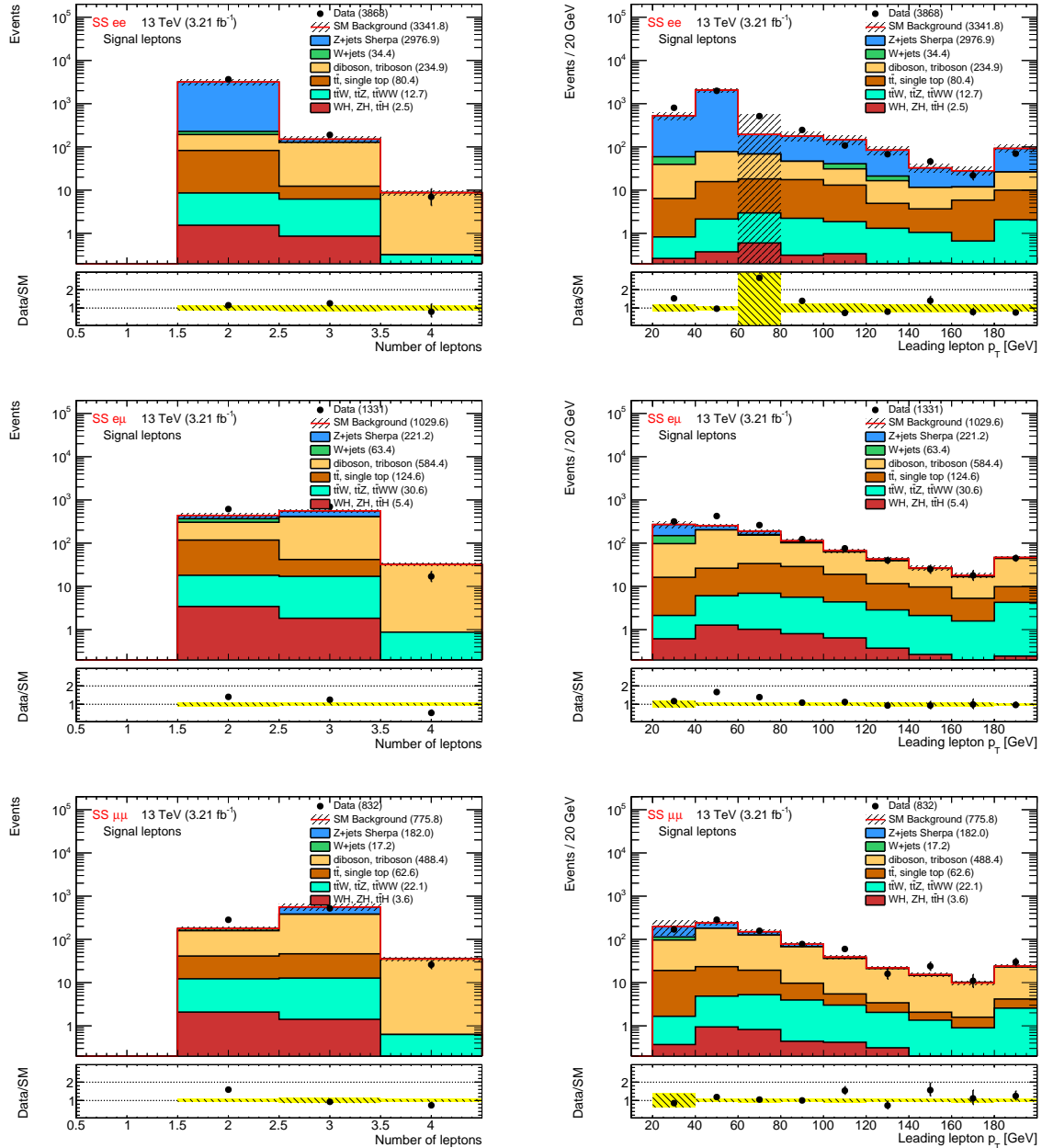


Figure 15: Lepton multiplicity (left) and leading lepton p_T (right) for events selected in the ee (top), $e\mu$ (center) and $\mu\mu$ (bottom) channels. The background contribution is taken directly from MC with no data-driven estimation of the background with fake and non-prompt leptons or charge mis-identification. Only luminosity and MC statistical uncertainties are included.

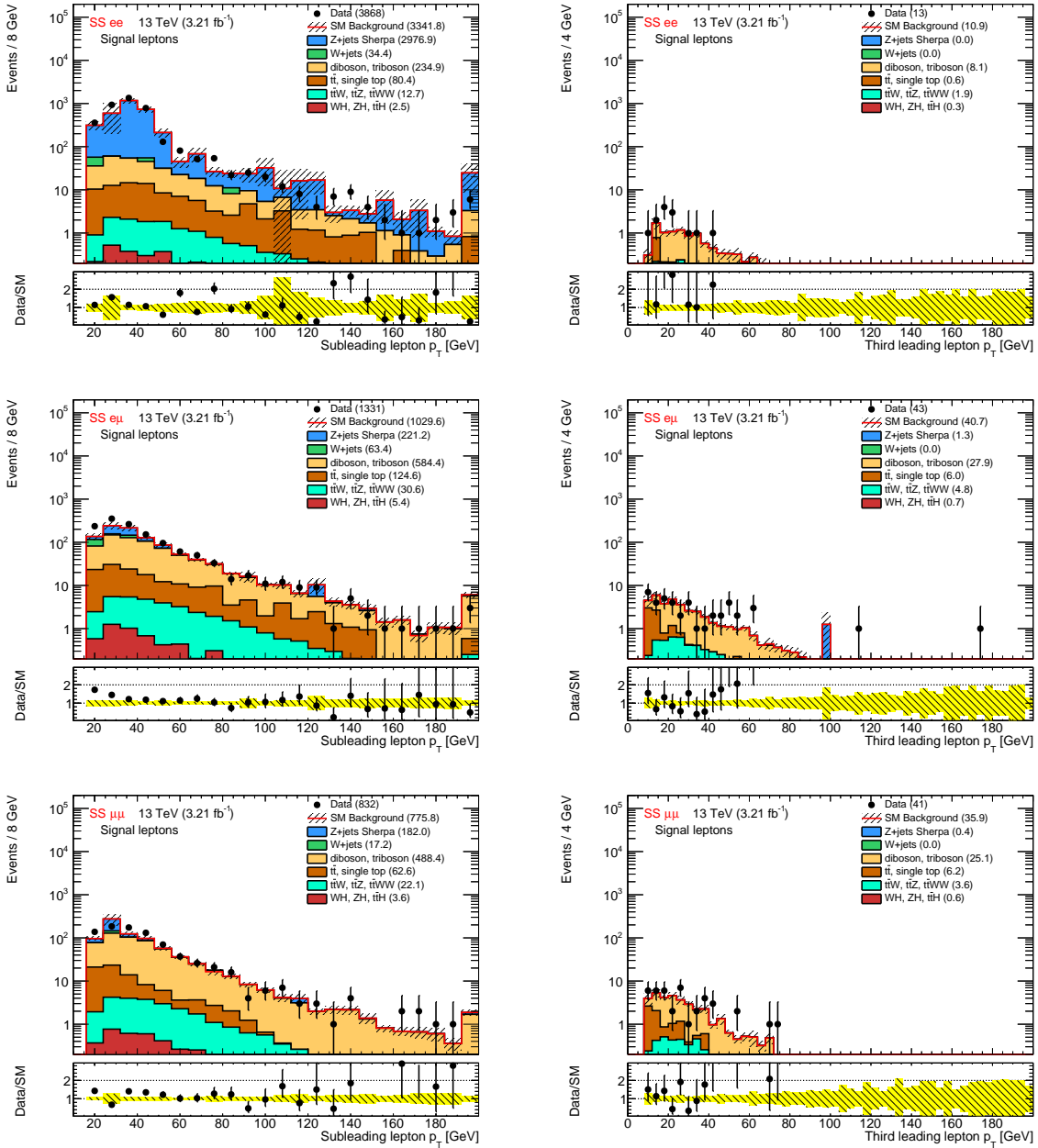


Figure 16: Sub-leading (left) and third leading lepton p_T (right) for events selected in the ee (top), $e\mu$ (center) and $\mu\mu$ (bottom) channels. The background contribution is taken directly from MC with no data-driven estimation of the background with fake and non-prompt leptons or charge mis-identification. Only luminosity and MC statistical uncertainties are included.

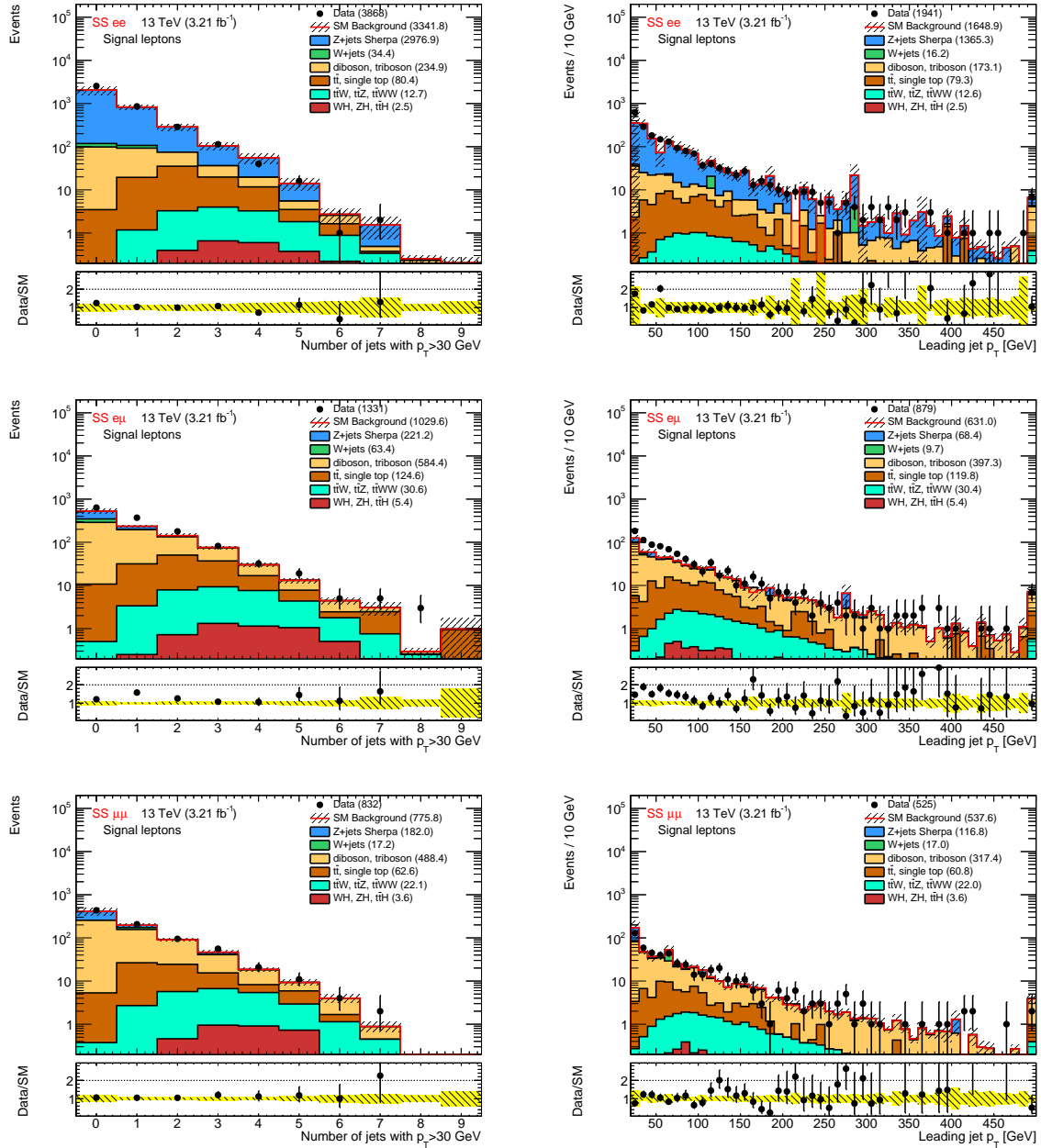


Figure 17: Number of jets (left) and leading jet p_T (right) for events selected in the ee (top), $e\mu$ (center) and $\mu\mu$ (bottom) channels. The background contribution is taken directly from MC with no data-driven estimation of the background with fake and non-prompt leptons or charge mis-identification. Only luminosity and MC statistical uncertainties are included.

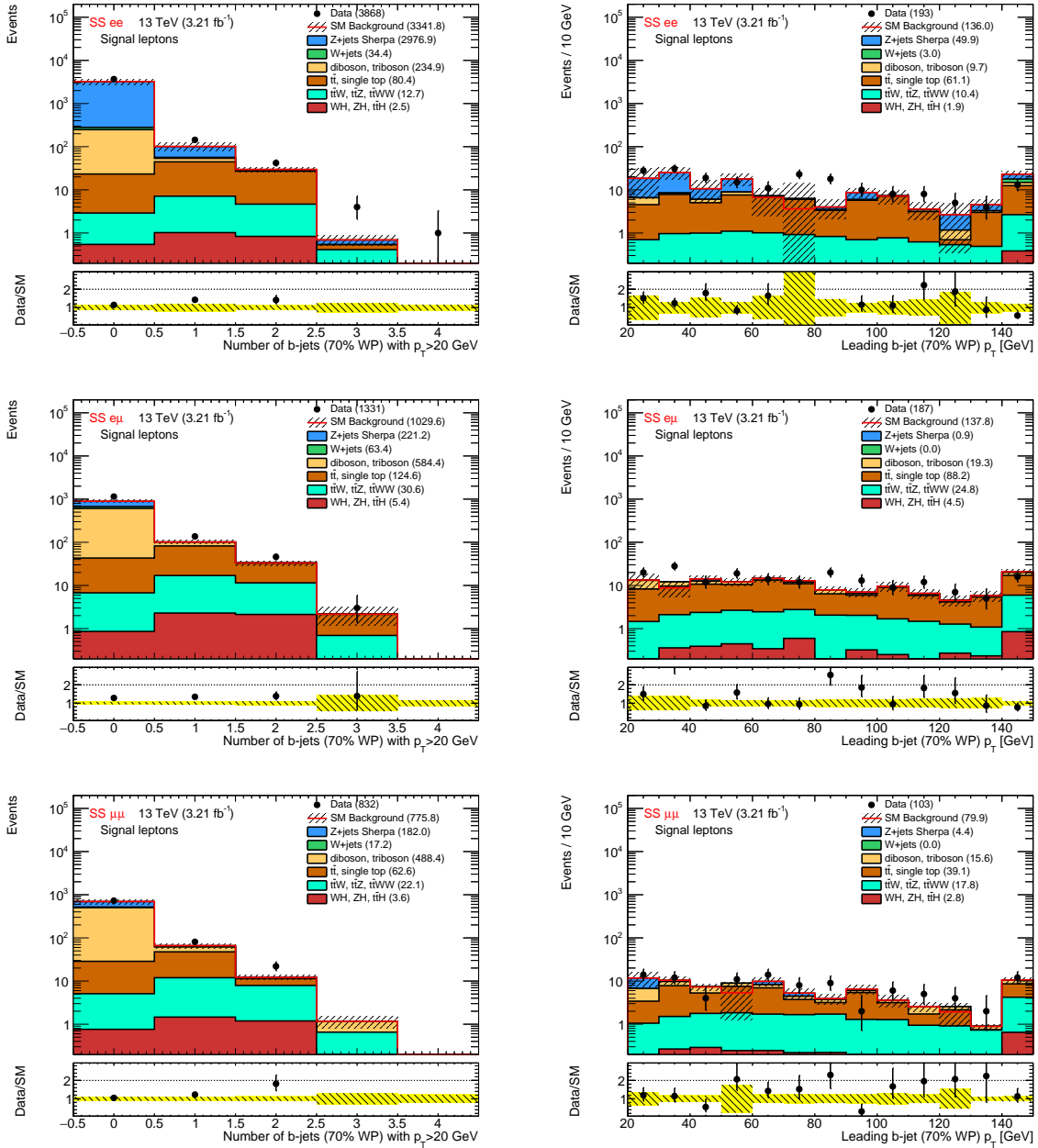


Figure 18: Number of b -jets (left) and leading b -jet p_T (right) for events selected in the ee (top), $e\mu$ (center) and $\mu\mu$ (bottom) channels. The background contribution is taken directly from MC with no data-driven estimation of the background with fake and non-prompt leptons or charge mis-identification. Only luminosity and MC statistical uncertainties are included.

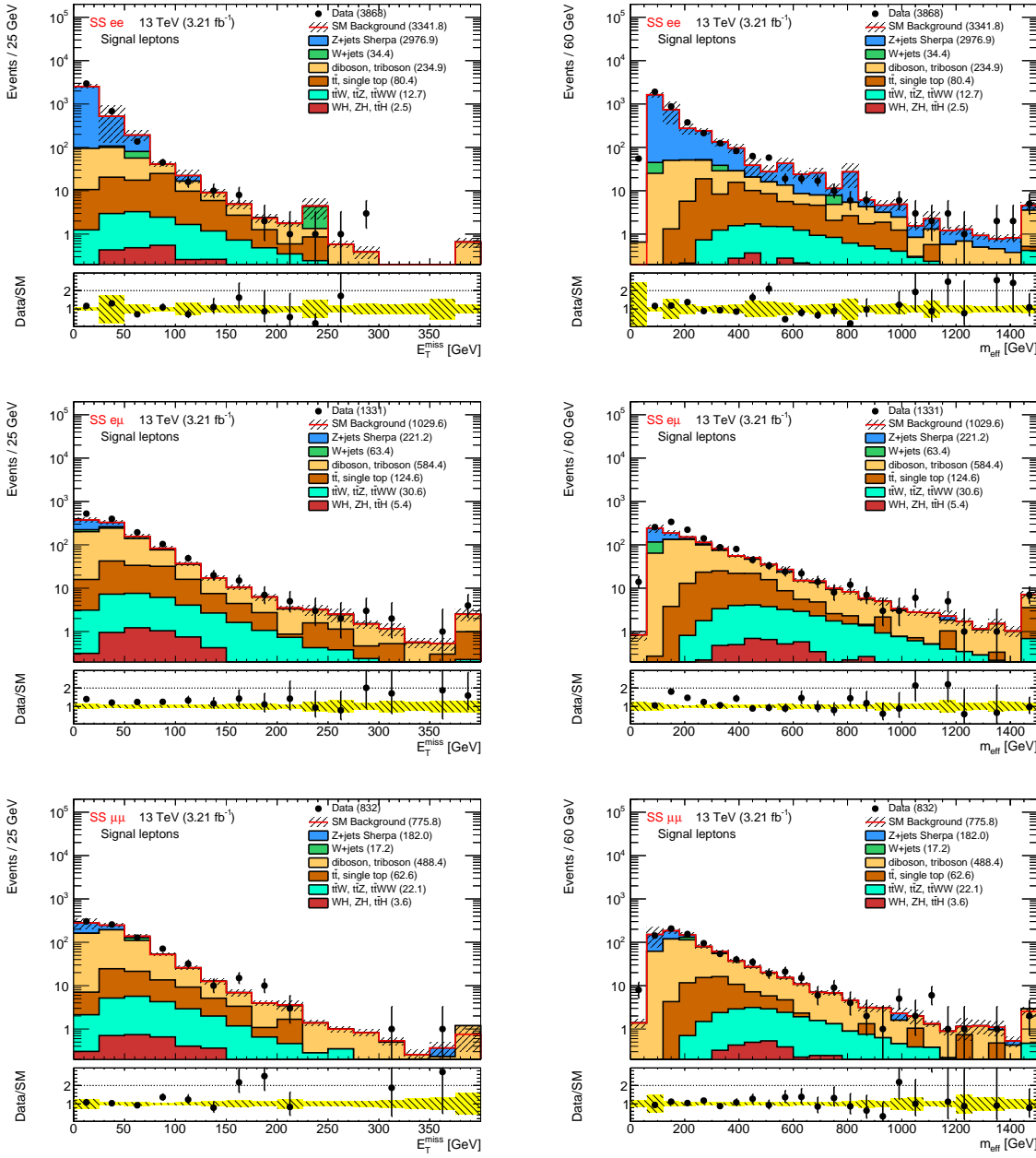


Figure 19: Distributions of the E_T^{miss} (left) and effective mass (right) for events selected in the ee (top), $e\mu$ (center) and $\mu\mu$ (bottom) channels. The background contribution is taken directly from MC with no data-driven estimation of the background with fake and non-prompt leptons or charge mis-identification. Only luminosity and MC statistical uncertainties are included.

6 Signal region definition

The definitions of the signal regions have been studied to provide an optimal performance for $\sqrt{s} = 13$ TeV collisions and a low integrated luminosity ($2\text{-}4 \text{ fb}^{-1}$). This optimization process was first performed with DC14 MC samples, and was then refined with the more accurate MC15 samples and close-to-final object definitions. We chose to categorize the signal regions based on their b -jet multiplicity, in continuation of the approach sustained in the Run-1 analysis:

- Signal region(s) with at least one b -jet (“SR1b”): these selections target signal scenarios involving top or bottom quarks, mostly related to third-generation squarks, such as the benchmark process $\tilde{b}_1 \tilde{b}_1^* \rightarrow t\bar{t} \tilde{\chi}_1^+ \tilde{\chi}_1^-$.
- Signal region(s) with at least three b -jets (“SR3b”): these selections target signal scenarios involving many top or bottom quarks, such as the benchmark process $\tilde{g}\tilde{g} \rightarrow t\bar{t}t\bar{t} \tilde{\chi}_1^0 \tilde{\chi}_1^0$, and with their intrinsically very low background are particularly well suited for scenarios with compressed mass spectra.
- Signal region(s) with a b -jet veto (“SR0b”): these selections allow to increase the sensitivity to signal scenarios without bottom quarks, by suppressing most of the top background – the selections are then dominated by diboson background.

One can notice that there is no dedicated selection for final states with ≥ 2 b -jets: it is found to not be particularly useful, as the background is generally dominated by $t\bar{t} + X$ processes, which does not change substantially between ≥ 1 and ≥ 2 b -jets selections. By contrast the difference between ≥ 1 and ≥ 3 b -jets selections is very important.

To this first classification we add minimal requirements on the inclusive jet multiplicity:

Signal region(s)	SR0b		SR1b	SR3b
Jets req.	$\geq 3 (p_T > 50 \text{ GeV})$	$\geq 5 (p_T > 50 \text{ GeV})$	$\geq 4 (p_T > 50 \text{ GeV})$	–

As one can see, the SR0b selections were subdivided into two overlapping selections (≥ 3 or ≥ 5 jets, also denoted as SR0b5j and SR0b3j) to cover various signal scenarios that lead to differently jet-enriched final states. The optimal minimal number of jets and the jet p_T thresholds were defined as part of the DC14-based optimization, through a (m_{eff} , $E_{\text{T}}^{\text{miss}}$, #jets, jet p_T) scan similar to the one described below and focused on the few benchmark signal scenarios that were produced for DC14 studies. Only the p_T threshold for SR0b3j was raised from 40 to 50 GeV for homogenization among the SRs since this change had very small impact in the sensitivity.

All these selections are inclusive in terms of leptons (“at least two same-sign leptons”, see Section 5.2.1), it was found that for these early results no substantial gain would be achieved by considering trilepton final states separately (as was done in the Run-1 analysis) except for SR0b3j, where a ≥ 3 lepton requirement was found to improve the sensitivity to slepton-mediated signals ($\tilde{g} \rightarrow q\bar{q}(\ell\ell/\ell\nu)\tilde{\chi}_1^0$).

To complete the definition of the signal regions, we added requirements on the effective mass m_{eff} and missing transverse momentum $E_{\text{T}}^{\text{miss}}$. We rely only on these two discriminant variables, well suited for generic SUSY searches, as one of the analysis strengths is to be sensitive to a broad range of BSM scenarios and we do not want to overrule it to a restricted set of benchmarks.

684 6.1 Optimization procedure and results

685 The optimization of the signal region definitions was carried on with the MC15 samples. We scanned
 686 the $(m_{\text{eff}}, E_{\text{T}}^{\text{miss}})$ plane for the four selections detailed above, looking at the impact of the cuts on vari-
 687 ous signal benchmarks. We used as figure of merit the signal discovery significance (Z_n), calculated
 688 with `RooStats::NumberCountingUtils::BinomialObsZ` assuming an overall 40% systematic un-
 689 certainty on the background prediction (as a compromise to the 50% expected uncertainty on the fake-
 690 lepton background and 30% on the prompt-lepton background). We discarded the cut configurations
 691 where the background projection was too imprecise, due to limited MC statistics; more precisely when
 692 the statistical error on the projected background exceeded 30%. We also focused on signal benchmarks
 693 that would provide at least 2 signal events for the considered luminosity.

694 Figure 20 shows as an example the $(m_{\text{eff}}, E_{\text{T}}^{\text{miss}})$ planes for two different signal regions and models. The
 695 resulting maximum discovery significance across the signal grids and the corresponding $(m_{\text{eff}}, E_{\text{T}}^{\text{miss}})$
 696 configurations are shown in Figure 21 for SR1b, SR3b and SR0b5j. As shown, with 2 fb^{-1} of data we can
 697 have sensitivity beyond the existing Run-1 limits in some of the models. Note that the Run-1 limits shown
 698 in the figures correspond to the best ATLAS limit, not necessarily obtained by the SS/3L analysis.

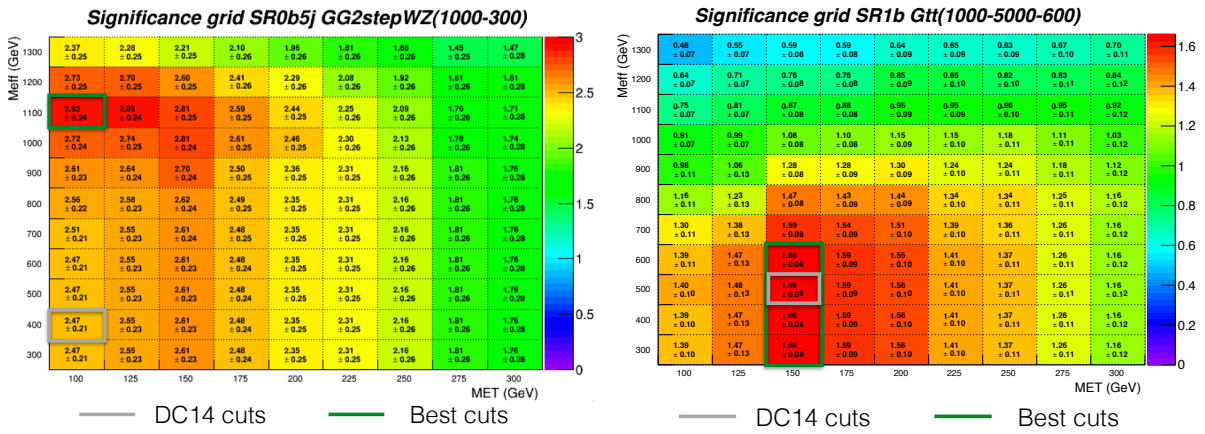


Figure 20: Example of $(E_{\text{T}}^{\text{miss}}, m_{\text{eff}})$ scans for SR0b5j (left) and SR3b (right). The configurations with maximum significance are highlighted as well as the outcome of the DC14 optimization studies.

699 6.2 Signal regions

700 The definition of the exact SR was done as a good compromise across the signal grids shown in Figure 21
 701 with a single $(E_{\text{T}}^{\text{miss}}, m_{\text{eff}})$ configuration. Tables 11–13 show the optimized signal region definitions for
 702 scenarios with $2, 3$ and 4 fb^{-1} respectively. The final SR to be used for the 2015 analysis was determined
 703 by the luminosity available at the end of the data-taking period: if less than 2.5 fb^{-1} had been available
 704 for analysis after GRL, we would have used the SRs for the 2 fb^{-1} scenario; if more than 3.5 fb^{-1} had
 705 been available, we would have used the SRs for the 4 fb^{-1} scenario. But with the 3.2 fb^{-1} eventually
 706 collected, we used the definitions corresponding to the intermediate scenario of 3 fb^{-1} . Figures 22 and
 707 23 show the significance values obtained for those signal regions in the SUSY models considered, with
 708 the 1.64σ discovery contours extending beyond the Run-1 exclusions, even achieving a 3σ sensitivity in
 709 certain regions of the mass parameter space.

Table 11: Signal regions definition for the 2 fb^{-1} scenario (to be used for $L < 2.5 \text{ fb}^{-1}$). The two leading leptons are required to have $p_T > 20 \text{ GeV}$.

Signal region	N_{lept}	$N_{b\text{-jets}}^{20}$	N_{jets}^{50}	$E_T^{\text{miss}} [\text{GeV}]$	$m_{\text{eff}} [\text{GeV}]$
SR3b	≥ 2	≥ 3	-	> 100	> 600
SR1b	≥ 2	≥ 1	≥ 4	> 125	> 500
SR0b5j	≥ 2	$== 0$	≥ 5	> 100	> 600
SR0b3j	≥ 3	$== 0$	≥ 3	> 150	> 500

Table 12: Signal regions definition for the 3 fb^{-1} scenario (to be used for $2.5 \leq L < 3.5 \text{ fb}^{-1}$), the one eventually used in this analysis. The two leading leptons are required to have $p_T > 20 \text{ GeV}$.

Signal region	N_{lept}	$N_{b\text{-jets}}^{20}$	N_{jets}^{50}	$E_T^{\text{miss}} [\text{GeV}]$	$m_{\text{eff}} [\text{GeV}]$
SR3b	≥ 2	≥ 3	-	> 125	> 650
SR1b	≥ 2	≥ 1	≥ 4	> 150	> 550
SR0b5j	≥ 2	$== 0$	≥ 5	> 125	> 650
SR0b3j	≥ 3	$== 0$	≥ 3	> 200	> 550

Table 13: Signal regions definition for the 4 fb^{-1} scenario (to be used for $L \geq 3.5 \text{ fb}^{-1}$). The two leading leptons are required to have $p_T > 20 \text{ GeV}$.

Signal region	N_{lept}	$N_{b\text{-jets}}^{20}$	N_{jets}^{50}	$E_T^{\text{miss}} [\text{GeV}]$	$m_{\text{eff}} [\text{GeV}]$
SR3b	≥ 2	≥ 3	-	> 125	> 700
SR1b	≥ 2	≥ 1	≥ 4	> 150	> 600
SR0b5j	≥ 2	$== 0$	≥ 5	> 125	> 700
SR0b3j	≥ 3	$== 0$	≥ 3	> 200	> 600

6.3 “Auxiliary” signal regions

In addition to the signal regions defined above, used for the final results, two more regions are defined as shown in Table 14. SR2b has the same kinematic requirements as SR3b but at least 2 b -jets are required instead of at least 3. This region is used to check the background estimates and data close to SR3b but with larger statistics available. SR3L3b is defined with the exact same kinematic requirements as the $3\ell+3b$ -jet excess observed in 2012 data [45].

Table 14: Auxiliary signal regions definition. The two leading leptons are required to have $p_T > 20 \text{ GeV}$.

Signal region	N_{lept}	$N_{b\text{-jets}}^{20}$	N_{jets}^{50}	$E_T^{\text{miss}} [\text{GeV}]$	$m_{\text{eff}} [\text{GeV}]$	Other
SR2b ($< 3.5 \text{ fb}^{-1}$)	≥ 2	≥ 2	-	> 125	> 650	-
SR3L3b	$== 3$	≥ 3	-	> 50	-	Veto $81.2 < m_{\ell\ell}^{\text{SFOS}} < 101.2 \text{ GeV}$ Veto $81.2 < m_{\ell\ell\ell} < 101.2 \text{ GeV}$

716 **6.4 Validation of the jet p_T requirements in signal regions with a b veto**

717 In SR0b3j and SR0b5j it is important to verify which is the best cut on the p_T of the jets. In the analysis
718 performed for RunI the cut was set to 40 GeV. It was decided to perform a comparison with a higher cut
719 (50 GeV) and a lower cut (30 GeV) to check if it would improve the sensitivity of the analysis in those
720 signal regions.

721 The significance calculation is performed as in the studies shown in section 5.2.1 and the background
722 estimation is purely Monte Carlo driven. The study was performed on the benchmark models for the two
723 signal regions with a fixed Neutralino mass. All samples are rescaled to 4 fb^{-1}

724 Figure 24 and 25 show the comparison between the three different p_T jet thresholds in the two signal
725 regions. A jet p_T cut of 50 GeV performs better for each signal point in both the signal regions.

726 The right plot in Figure 25 shows the behavior in a compressed scenario, in this case a cut of 30 GeV is
727 more efficient for low gluino masses.

728 In conclusion, even though in a compressed scenario a lower jet p_T cut would perform better, the decision
729 is to apply a jet p_T cut of 50 GeV which gives an higher sensitivity to the analysis in a wider spectra of
730 signal masses.

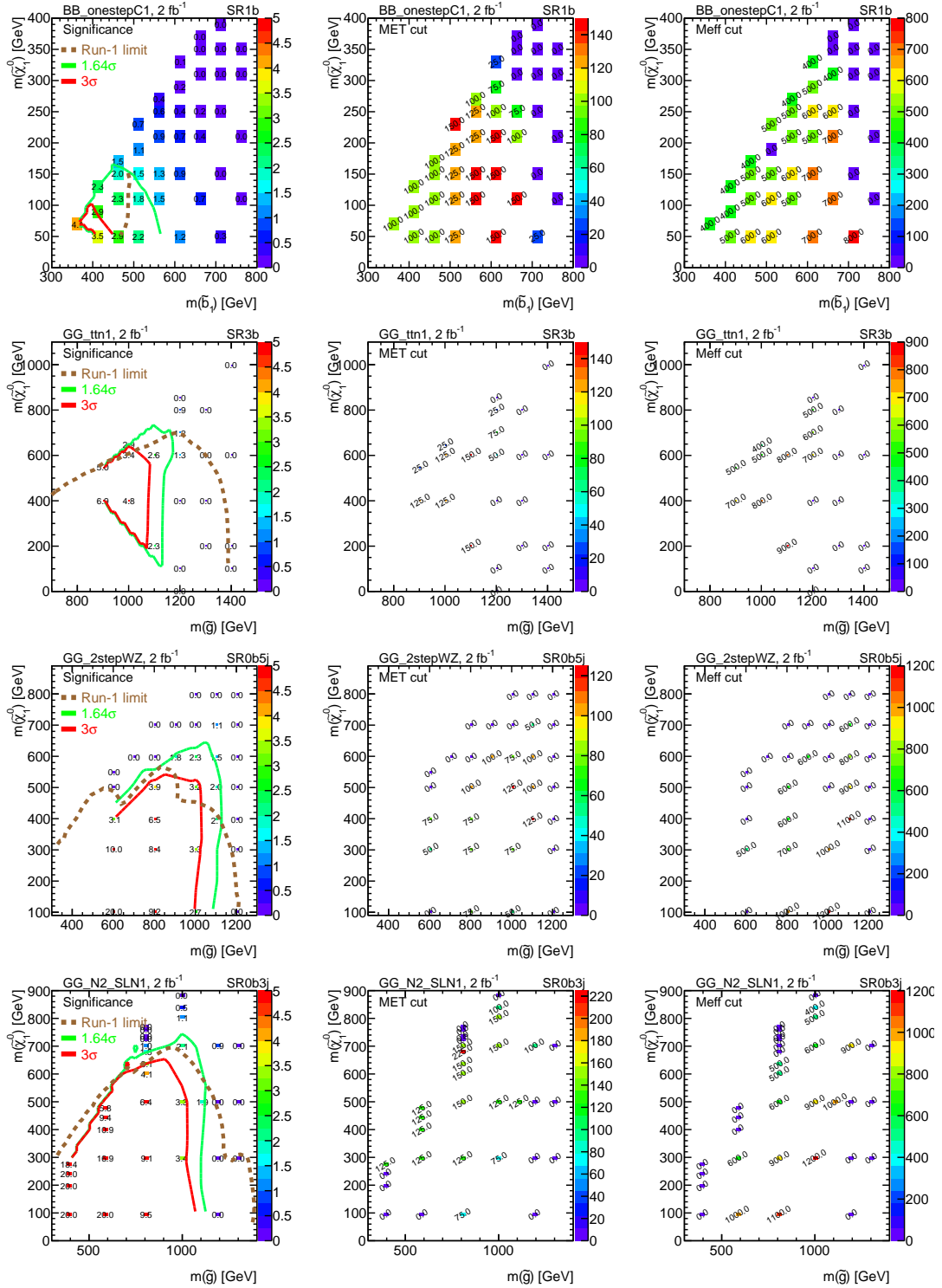


Figure 21: Maximum discovery significance (left) for 2 fb^{-1} , as well as the E_T^{miss} (center) and m_{eff} (right) cuts needed to maximize the significance for: (from top to bottom) SR1b in the $\tilde{b}_1 \tilde{b}_1^* \rightarrow t \bar{t} \tilde{\chi}_1^+ \tilde{\chi}_1^-$ grid, SR3b in the $\tilde{g} \tilde{g} \rightarrow t \bar{t} t \bar{t} \tilde{\chi}_1^0 \tilde{\chi}_1^0$ grid, SR0b5j in the $\tilde{g} \tilde{g} \rightarrow q \bar{q}' W Z \tilde{\chi}_1^0$ grid and SR0b3j in the $\tilde{g} \tilde{g} \rightarrow q \bar{q} (\ell \ell / \ell \nu) \tilde{\chi}_1^0$ grid. The Run-1 limits in those models are shown with a brown line, and the 1.64σ and 3σ discovery contours from the proposed signal regions are shown in green and red, respectively.

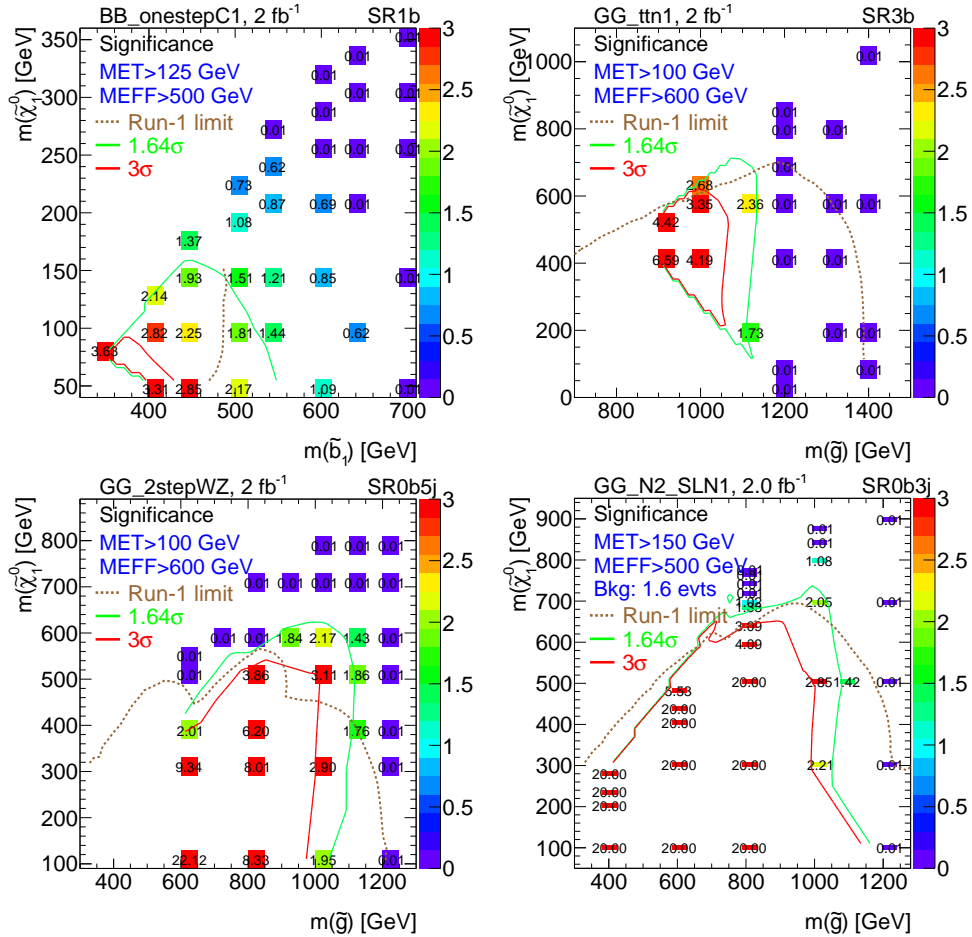


Figure 22: Discovery significance for the SRs defined in Table 11 (2 fb^{-1}) for SR1b in the $\tilde{b}_1 \tilde{b}_1^* \rightarrow t \bar{t} \tilde{\chi}_1^+ \tilde{\chi}_1^-$ grid (top left), SR3b in the $\tilde{g} \tilde{g} \rightarrow t \bar{t} t \bar{t} \tilde{\chi}_1^0 \tilde{\chi}_1^0$ grid (top right), SR0b5j in the $\tilde{g} \tilde{g}$ with $\tilde{g} \rightarrow q \bar{q}' W Z \tilde{\chi}_1^0$ grid (bottom left) and SR0b3j in the $\tilde{g} \tilde{g}$ with $\tilde{g} \rightarrow q \bar{q} (\ell \ell / \ell \nu) \tilde{\chi}_1^0$ grid (bottom right). The Run-1 limits in those models are shown with a brown line, and the 1.64σ and 3σ discovery contours from the proposed signal regions are shown in green and red, respectively.

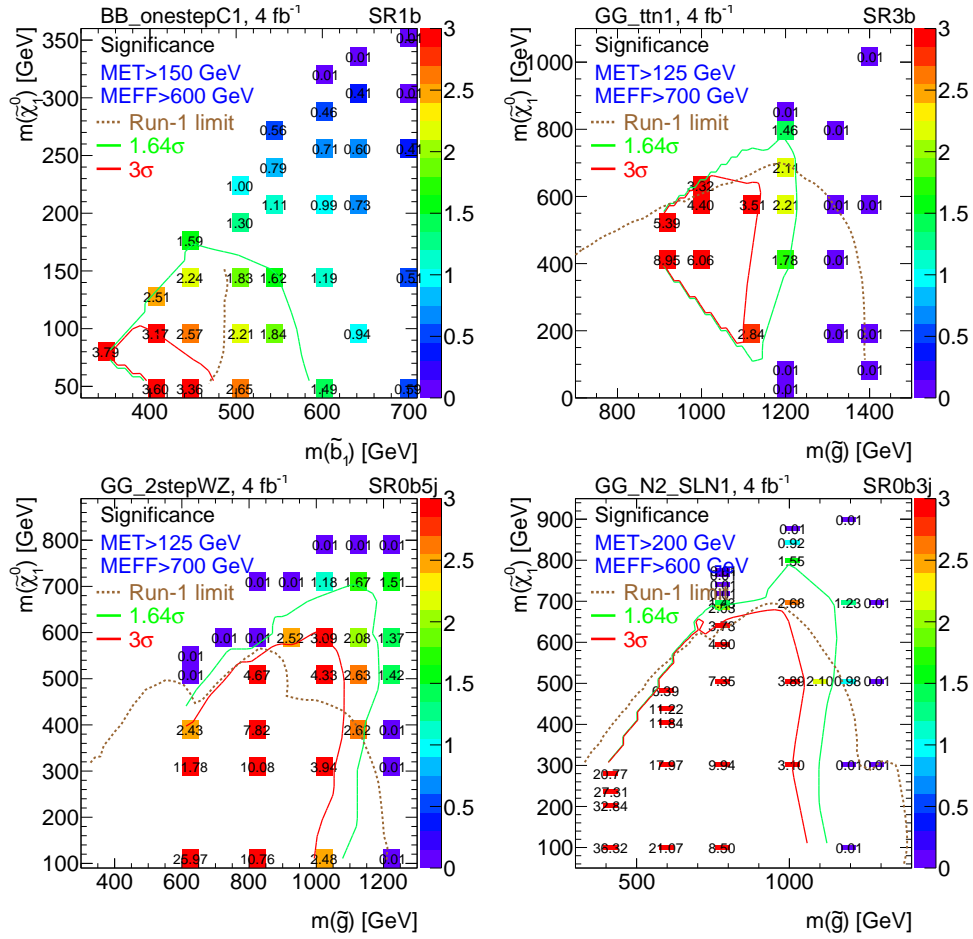


Figure 23: Discovery significance for the SRs defined in Table 13 (4 fb^{-1}) for SR1b in the $\tilde{b}_1 \tilde{b}_1^* \rightarrow t\bar{t} \tilde{\chi}_1^+ \tilde{\chi}_1^-$ grid (top left), SR3b in the $\tilde{g}\tilde{g} \rightarrow t\bar{t}t\bar{t} \tilde{\chi}_1^0 \tilde{\chi}_1^0$ grid (top right), SR0b5j in the $\tilde{g}\tilde{g}$ with $\tilde{g} \rightarrow q\bar{q}'WZ \tilde{\chi}_1^0$ grid (bottom left) and SR0b3j in the $\tilde{g}\tilde{g}$ with $\tilde{g} \rightarrow q\bar{q}(\ell\ell/\ell\nu) \tilde{\chi}_1^0$ grid (bottom right). The Run-1 limits in those models are shown with a brown line, and the 1.64σ and 3σ discovery contours from the proposed signal regions are shown in green and red, respectively.

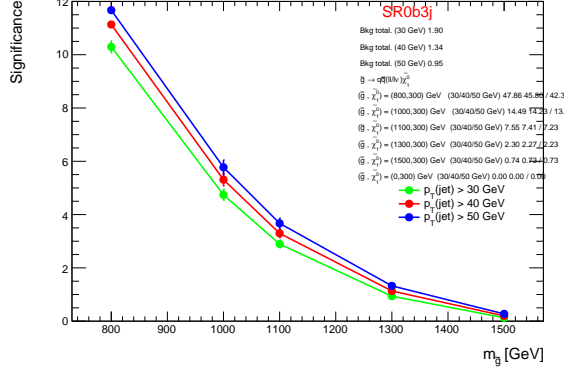


Figure 24: Significances of the signal region SR0b3j for $\tilde{g} \rightarrow q\bar{q}(l l/\bar{l}v)\chi_1^0$ models with variable $m_{\tilde{g}}$ and fixed m_{χ} of 300 GeV. The significance is computed for different p_T cuts on the jets. The significances are also shown for $p_T = 30/40/50$ GeV. The number of background and signal events are reported for the two different cuts for each signal point.

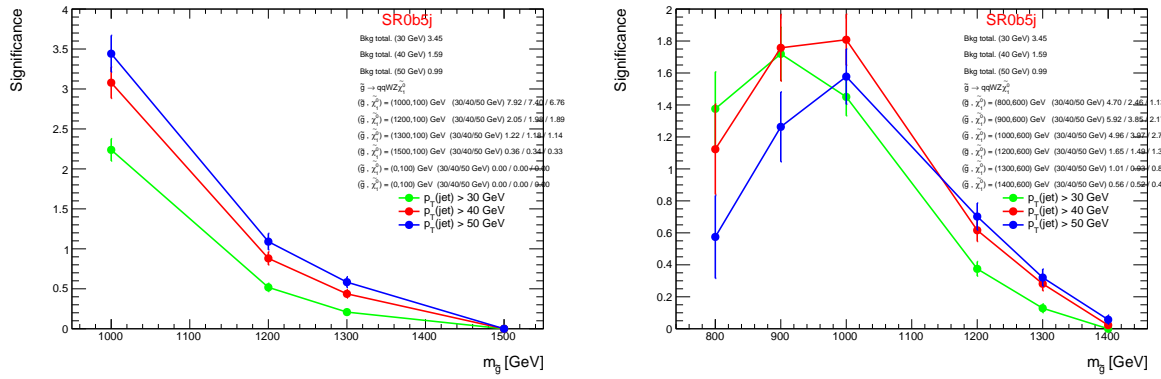


Figure 25: Significances of the signal region SR0b5j for $\tilde{g} \rightarrow q\bar{q}WZ\chi_1^0$ models with variable $m_{\tilde{g}}$ and fixed m_{χ} of 100 and 600 GeV. The significance is computed for different p_T cuts on the jets. The significances are also shown for $p_T = 30/40/50$ GeV. The number of background and signal events are reported for the two different cuts for each signal point.

7 Background estimation

The main challenge, in this analysis, is to achieve reliable predictions of the low Standard Model background leading to the same-sign leptons + jets final state. This background is composed partly of rare processes such as the associate production of a top quark pair with a massive boson, or the production of multiple bosons. The other contribution consists in experimental backgrounds originating from the imperfect discrimination between prompt leptons and other objects, or the occasional misreconstruction of the electron charge. The following sections provide more details about the nature of these different categories of background, and the foreseen methods that will be used to estimate their contributions to the signal regions.

7.1 Backgrounds with prompt SS dilepton or three leptons

There are two main sources of Standard Model background leading to pairs of same-sign prompt leptons:

- The associate production of top quark(s) and massive bosons, where the same-sign leptons pair originates from leptonic decays of one of the top quarks and of the boson. These processes are characterized by a large jet multiplicity, the presence of b -jet(s), and always have intrinsic missing momentum. Therefore they generally represent the largest contribution to the signal regions. The dominant processes are $pp \rightarrow t\bar{t}W(j)$, $pp \rightarrow t\bar{t}Z(j)$ and $pp \rightarrow t\bar{t}H$, while there are also minor contributions from $pp \rightarrow tZbj$, $t\bar{t}WW$, and $pp \rightarrow t\bar{t}t\bar{t}$.
- The production of multiple massive bosons. These processes have generally low jet multiplicities. However, due to their larger cross-sections, they contribute in a significant way to the background entering signal regions without b -jets requirements. The dominant processes include $pp \rightarrow W^\pm W^\pm jj$, WZ , ZZ , with minor contributions from $pp \rightarrow WH$, ZH , VVV and $H \rightarrow ZZ \rightarrow \ell\ell\ell\ell$ or $H \rightarrow WW \rightarrow \ell\nu + X$.

We estimate the contributions of these various processes to the signal regions by relying on the Monte-Carlo predictions, normalized with the best known theoretical cross-sections: these processes are too rare to allow use of control regions until a significant integrated luminosity will be collected. For example, in [46] which establishes projections of the sensitivity to the $t\bar{t}H$ signal strength in a final state very similar to this analysis, the impact of adding control regions for $t\bar{t} + V$ processes was found to be favorable only after collecting $\sim 100 \text{ fb}^{-1}$ of data.

Processes containing top quarks ($t\bar{t} + X$) have cross-sections below 1 pb, which have consequently not yet been much constrained experimentally. On the theoretical side, uncertainties on the cross sections are typically large: 30% for $t\bar{t}W$ and 50% for $t\bar{t}Z$ for the same-sign $\sqrt{s} = 7 \text{ TeV}$ analysis [47], 22% for both $t\bar{t}W$ and $t\bar{t}Z$ for the $\sqrt{s} = 8 \text{ TeV}$ analysis [16].

Cross-sections for diboson processes are known with a rather good accuracy, but only for the inclusive processes, while we are mostly interested in processes where several additional partons are produced, which carry subsequent additional uncertainties.

The validation regions described in section 9.2 help us to ensure that our understanding of these processes is sufficiently reliable, and that the systematic uncertainties assigned to the estimated rates are reasonable.

768 **7.2 Charge flip leptons**

769 The lepton charge mis-measurement commonly referred to as “charge flip” background, is an experimental
770 background strongly associated to analyses relying on same-sign leptons final states. In those events, the
771 electric charge of one of the two leptons forming an opposite-sign (OS) pair, coming from an abundant
772 SM process ($pp \rightarrow Z, t\bar{t}, W^+W^- \dots$), is mis-identified leading to a much rarer SS pair event. The most
773 frequent origin of this mis-identification is the following: when an electron goes through a medium (in
774 this case, the ATLAS inner detector), it can produce a hard photon by Bremsstrahlung radiation which
775 can then convert in an e^+e^- pair. If the converted electron with the largest p_T has an opposite charge
776 compared to the original electron (the one that emits the hard photon), wrong sign will be assigned to the
777 initial electron track, leading to a charge-flip event. Errors on the track charge assignment itself may occur
778 as well, but they are much rarer.

779 We rely on a purely data-driven method to estimate yields of events with charge flipped electrons.
780 Assuming one knows the electron charge flip rates $\xi(\eta, p_T)$, a simple way to predict these yields is to
781 select events with pairs of opposite-sign leptons in data and assign them a weight:

$$w = \xi(\eta^1, p_T^1) [1 - \xi(\eta^2, p_T^2)] + \xi(\eta^2, p_T^2) [1 - \xi(\eta^1, p_T^1)] \quad (1)$$

782 where $\xi = 0$ for muons.

783 The advantages of this method are a good statistical precision since the charge flip rate is quite small,
784 and the lack of dependency on the simulation and related uncertainties. Obviously, it requires a precise
785 measurement of the rates, which is described in the next paragraph. A slight inconvenient is that the
786 reconstructed electron energy, for charge flipped electrons, tends to be negatively biased (too low by a
787 few GeV), because of the hard Bremsstrahlung at the origin of the charge flip. Simply reweighting electrons
788 from opposite-sign lepton pairs therefore does not predict correctly the charge-flip background shape for
789 variables strongly depending on the electron momentum. But we do not rely on such discriminant
790 variables, therefore we simply neglect this effect for the moment.

791 In order to correctly define this background and to estimate the number of charge flip events in our signal
792 regions, one has to measure the rate (probability) of electron charge mis-measurement. The probability
793 of mis-identifying a muon was found to be negligible, at least for the p_T range considered in this analysis.
794 This section is organized as follows: first the procedure to extract the charge flip rate is explained and
795 then, the charge flip rates measured with the 2015 dataset are presented. A dedicated study of the charge
796 flip rates in different MC productions (MC12, DC14, MC15) can be found in Appendix 15.

797 **Measurement of the charge flip rates**

798 The charge flip rate is extracted with a data-driven technique using a likelihood fit, within a Z boson control
799 sample defined by requiring a pair of SS or OS electrons with invariant mass between 75 and 100 GeV.
800 Since the amount of material the electrons pass through is related to η , the probability of mis-measuring
801 the charge will depend on η . Moreover, since the inner detector track curvature is used to measured the
802 charge, the charge flip rate will also be dependent on the electron p_T . The extraction of charge flip rates
803 will then be performed for a specific (η, p_T) binning in order to take into account those effects. In the
804 following, the total number of bins is defined as the product of number of η bins and number of p_T bins:
805 # (total bins) = # (η bins) \times # (p_T bins). The notation “bin A ”, where A can take any values between 0 and
806 # (total bins), refer to one specific combination of (η, p_T) bins.

807 The likelihood fit used to measure the charge flip rate maximizes the function

$$L = \prod_{I,J} L_{\epsilon(I),\epsilon(J)}, \quad (2)$$

808 where $L_{\epsilon(I),\epsilon(J)}$ is the following Poisson distribution:

$$L_{\epsilon(I),\epsilon(J)} = P(N_{SS}^{obs} | \epsilon(I), \epsilon(J)) = \frac{(N_{SS}^{exp})^{N_{SS}^{obs}} e^{-N_{SS}^{exp}}}{N_{SS}^{obs}!}. \quad (3)$$

809 At this point, we set that the leading electron coming from Z boson falls into bin I while the subleading
 810 electron falls into bin J . In eq. 2 and 3, $\epsilon(I)$ ($\epsilon(J)$) is then the probability of mis-measuring the charge of
 811 an electron that falls into bin I (J). The variable N_{SS}^{obs} stands for the observed number of SS events while
 812 N_{SS}^{exp} is the expected number of SS events and is defined as:

$$N_{SS}^{exp} = N((1 - \epsilon(I))\epsilon(J) + (1 - \epsilon(J))\epsilon(I)), \quad (4)$$

813 with N the total number of events. This likelihood fit method is performed with a `TMinuit` routine and
 814 returns a charge flip rate values for each different (η, p_T) bin as well as the associate statistical errors.

815 Charge flip rate results

816 The comparison of charge flip rates extracted from Monte Carlo simulation and data is important in order
 817 to validate our choice of control region. In this section, the first results of charge flip rates measured in data
 818 are compared to the rates from an MC15 $Z \rightarrow e^+e^-$ sample. To extract the *nominal* charge flip rates, both
 819 electrons forming the SS or OS pair must pass the signal selections. As explained further in section 7.4,
 820 the method used to predict the yields of fake leptons requires estimates of the charge flip background
 821 also for baseline electrons failing the signal requirements. A similar methodology is used to extract the
 822 charge flip rates for pre-selected (non-signal) electrons albeit modified according to the specificities of the
 823 measurement (larger background, asymmetry between the definitions of the two selected electrons). For
 824 this last measurement, the definition of the binning in eq. 2 to 4 is different. Instead of referring to the
 825 leading and sub-leading electron, I will refer to the bin where the signal electron falls, while J refer to the
 826 bin where the non-signal electron falls. Then, $\epsilon(I)$ ($\epsilon(J)$) becomes the probability of mis-measuring the
 827 charge of a signal (non-signal) electron that falls into bin I (J). In other words, there is no requirement
 828 for the leading electron to be neither the signal nor the non-signal electron of the pair.

829 Figure 26 shows kinematic p_T distributions, before the background subtraction, for nominal measurement
 830 on left and loose measurement on right while the η distributions are shown on Figure 27. In those plots, the
 831 electrons forming an OS (black filled dots for data, blue area for MC) and a SS pair (black circle for data,
 832 green area for MC) are shown separately and the MC areas are normalized (scaled) to the data luminosity.
 833 The small discrepancies at low p_T may be due to some Drell-Yan processes that are not considered here
 834 and to the presence of fake electrons in the loose distributions. The discrepancies in the central region
 835 for the loose SS distribution on the right plot of Figure 27 can also be attributed to the presence of fake
 836 electrons in the sample.

837 The invariant mass of electrons forming the pair is also an important quantity to look at and it is shown
 838 on Figure 28, where the left plot is the nominal measurement while the right plot correspond to the loose

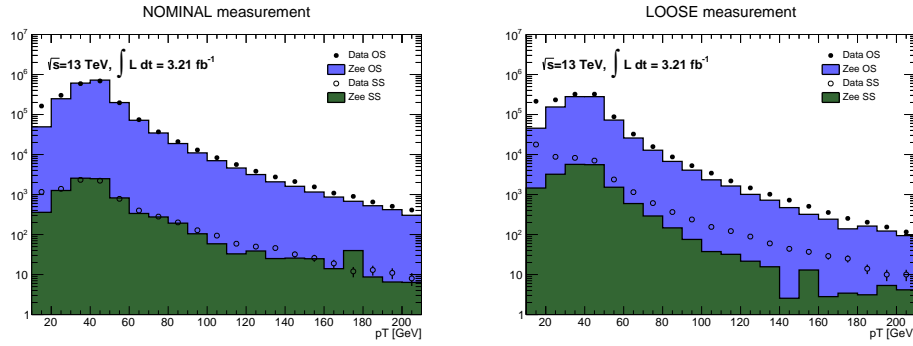


Figure 26: p_T distributions for nominal (left) and loose (right) measurements for signal electrons forming an OS pair (filled dots for data, blue area for MC) and a SS pair (empty circles for data, green area for MC). Only statistical uncertainties are shown.

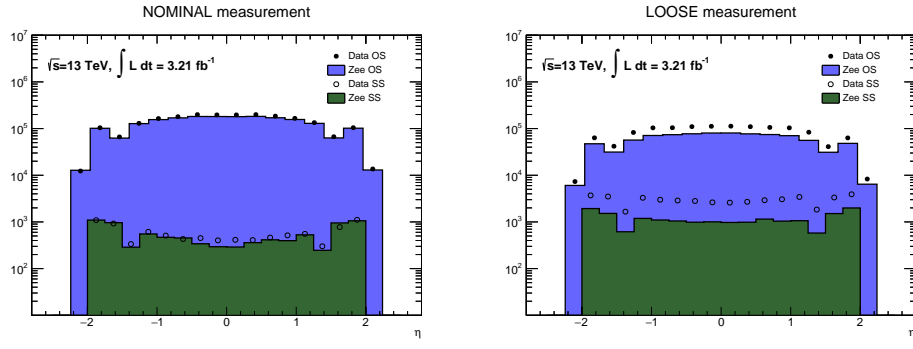


Figure 27: η distributions for nominal (left) and loose (right) measurements for signal electrons forming an OS pair (filled dots for data, blue area for MC) and a SS pair (empty circles for data, green area for MC). Only statistical uncertainties are shown.

839 measurement. Again, the electrons forming an OS (black filled dots for data, blue area for MC) and a SS
840 pair (black circle for data, green area for MC) are shown separately and the MC areas are normalized to
841 data luminosity. The background is not subtracted in these plots.

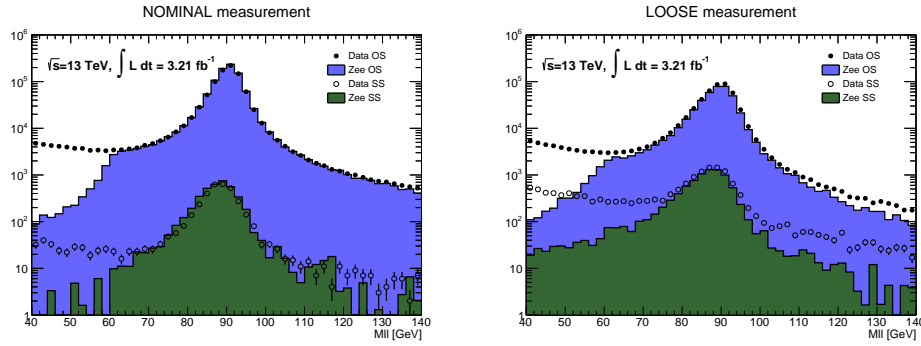


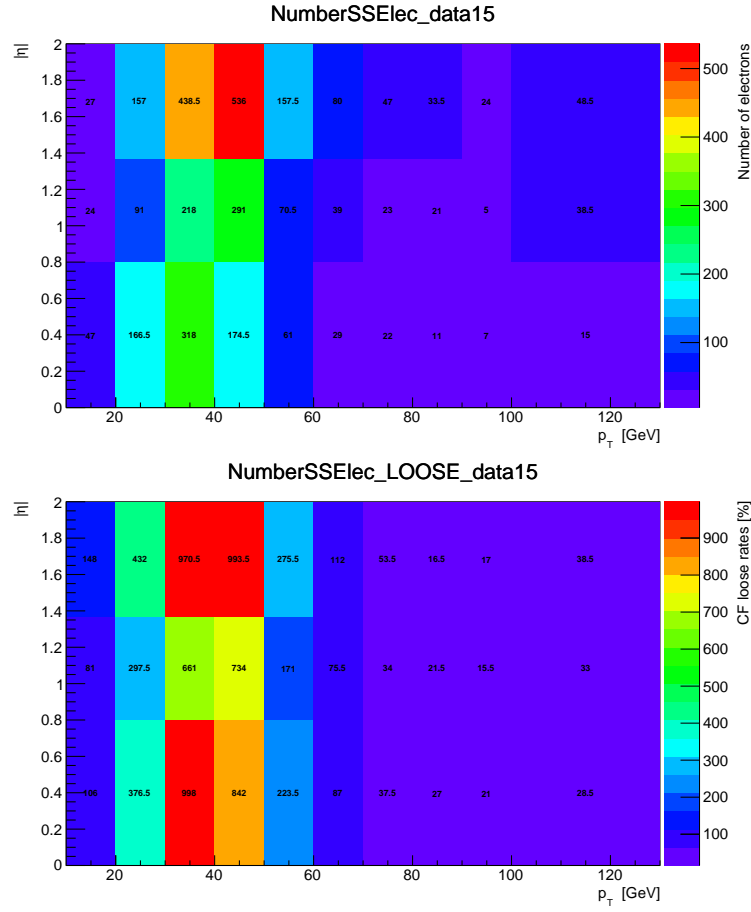
Figure 28: Invariant mass distributions for nominal (left) and loose (right) measurements for signal electrons forming an OS pair (filled dots for data, blue area for MC) and a SS pair (empty circles for data, green area for MC). Only statistical uncertainties are shown.

Despite the small shift toward lower energies in the SS distribution, which is due to the loss of energy during the radiation process, one can see that there is a nice agreement between OS and SS pairs within the Z peak. Outside the peak, especially at low energy, one can see a large discrepancy in all distributions which comes from the fact that $Z \rightarrow e^+e^-$ was the only background considered. Again Drell-Yan processes and fake electrons (in the loose measurement cases) are the main causes of those differences. One can also see on Figure 28 that the amount of SS events (empty circles) for loose measurements is greater than the number of SS events in the nominal measurement while it is the opposite for the OS distributions (filled dots). This is expected since the cuts required to pass the signal requirements were designed to reject as much as possible detector backgrounds such as charge-flip electrons, so by requiring that one electron in the pair fails one of these requirements, the effect is clearly to raise the number of SS events and in the same time, lower the number of OS events. A background subtraction procedure using a side-band method is used to estimate the amount of background events in the measurement region. This method uses the number of observed events that fall in the side-band regions, $50 < M_{ee} < 75$ GeV and $100 < M_{ee} < 125$ GeV, to correct the number of events inside the central-band defined as $75 < M_{ee} < 100$ GeV. The systematic uncertainties related to those chosen values of central and side bands width are further discussed in the next section.

Finally, the nominal charge flip rates were computed following the procedures explained above for the following set of bins: p_T bins = {10, 20, 30, 40, 50, 60, 70, 80, 90, 100, 7000} GeV, $|\eta|$ bins {0.0, 0.8, 1.37, 2.0}. In order to reduce the charge mis-identification background, events with an electron within the crack region ($1.37 < |\eta| < 1.52$) are vetoed as well as events where an electron from the pair has $|\eta| > 2.0$. To be sure we got enough statistics in each bin, the number of electrons forming a SS events for the nominal and loose measurements are shown respectively on the top and bottom of Figure 29, where the higher p_T bin contains the overflow. On those plots, one can see that most of the bins contain more than 20 electrons (except some bins at high p_T values), which is enough to produce trustable charge flip rate results. By comparing those two figures, one can also see that the number of SS electrons (N_{SS}) is greater in the loose measurement case, but the distribution of N_{SS} over the bins is similar between both measurements.

The nominal and loose rates extracted with data samples are presented respectively on Figure 30 extracted in data, where the higher p_T bins contain the overflow. On Figure 30, one can see that the expected trend, charge flip rate values are greater for higher p_T and η bins, is confirmed. On the top plot, the nominal measurement goes up to 0.75% in the barrel region ($0.0 < |\eta| < 1.37$) while it goes up to 3.7% in region $1.52 < |\eta| < 2.0$. On the bottom plot, the loose measurements are in general greater than the nominal ones in every bins and the rates goes up to 7.4% in the barrel region ($0.0 < |\eta| < 1.37$) while it goes up to 10.8% in region $1.52 < |\eta| < 2.0$. Another way to observe the charge flip dependency on p_T and η is to plot all the rates on the same figures in function of p_T as shown on Figure 31 where the $0.0 < |\eta| < 0.8$ range are shown in blue, the $0.8 < |\eta| < 1.37$ range in green and the $1.37 < |\eta| < 2.0$ range in orange. Despite some variations for the loose measurement in high p_T bins, one can see that charge flip rates become greater when the p_T value, as well as the η value, increases.

The comparison of charge flip rates from data and from MC for nominal measurement is plotted for different p_T range on Figure 32. The same comparison was done for the loose measurement, it is shown on Figure 33 and are notably used in section 9.1. Again, one can see that the charge flip rates for the loose measurement are much larger than for the nominal measurement (typically by a factor 10), illustrating the necessity of this auxiliary measurement. From those plots, one can see a fairly good agreement between data and MC results. In low p_T bins (below 40 GeV) in the nominal measurement, MC predictions seem to overestimate the charge flip rates at high $|\eta|$ ($1.52 < |\eta| < 2.0$). For the loose measurement, the same



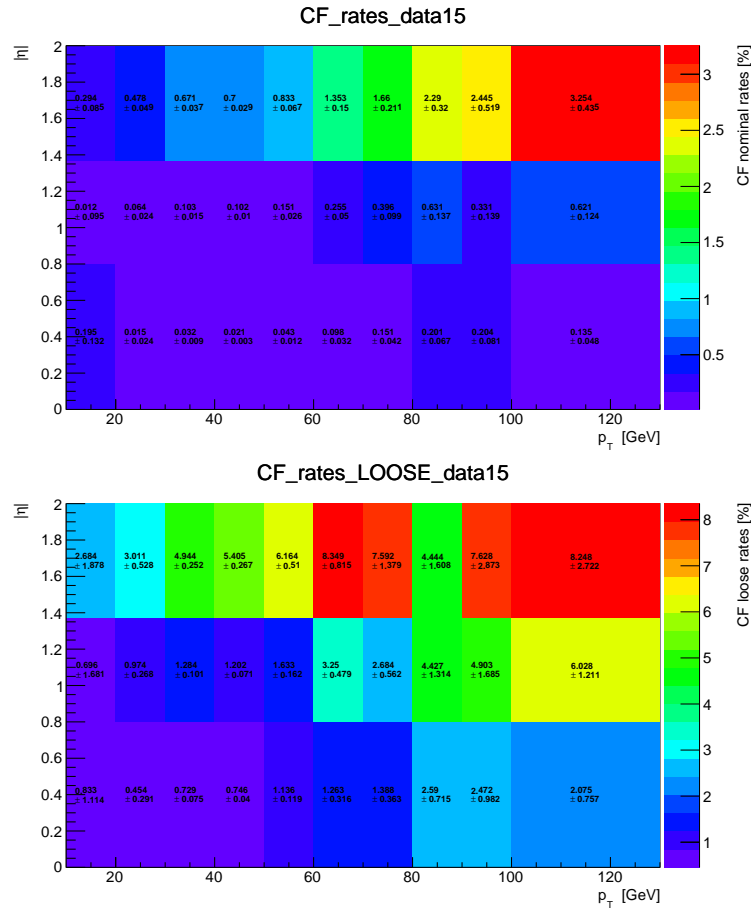


Figure 30: Mis-identification rates in 40 ($p_T, |\eta|$) bins with their respective statistical+systematic uncertainties for the NOMINAL (top) and LOOSE (bottom) measurement extracted in data, where the higher p_T bins contain the overflow.

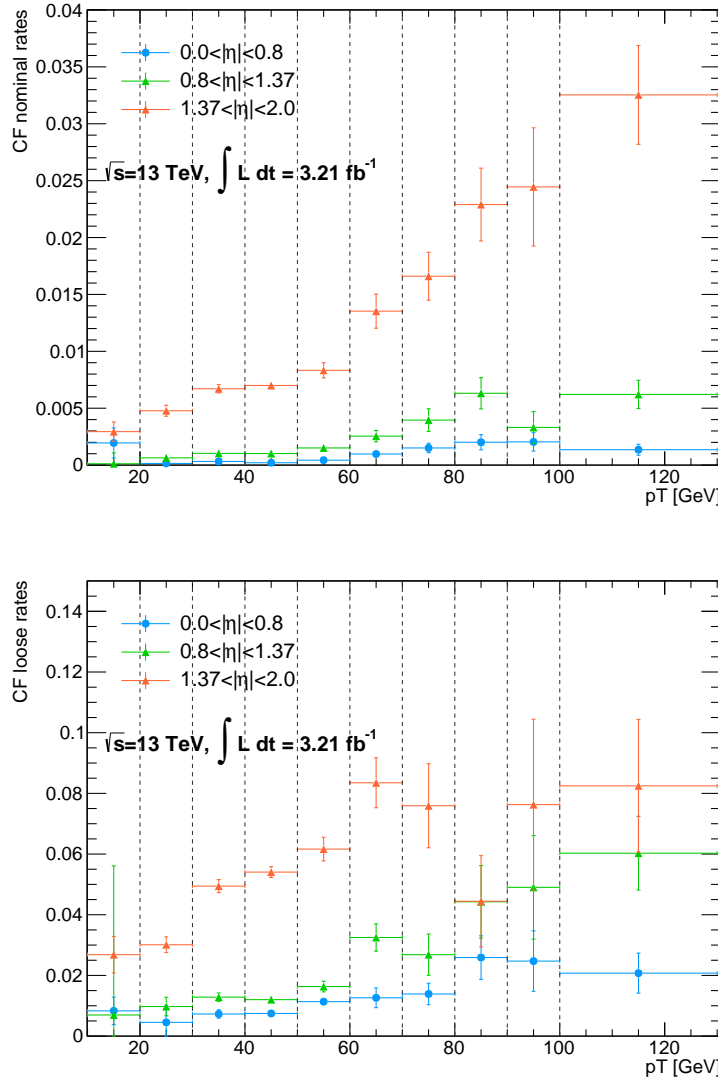


Figure 31: Mis-identification rates in function of the p_T distribution for three different η ranges: $0.0 < |\eta| < 0.8$ in blue, $0.8 < |\eta| < 1.37$ in green and $1.37 < |\eta| < 2.0$ in orange. Statistical and systematic uncertainties are included. The top (bottom) plot show nominal (loose) measurement extracted in data, where the higher p_T bin contains the overflow.

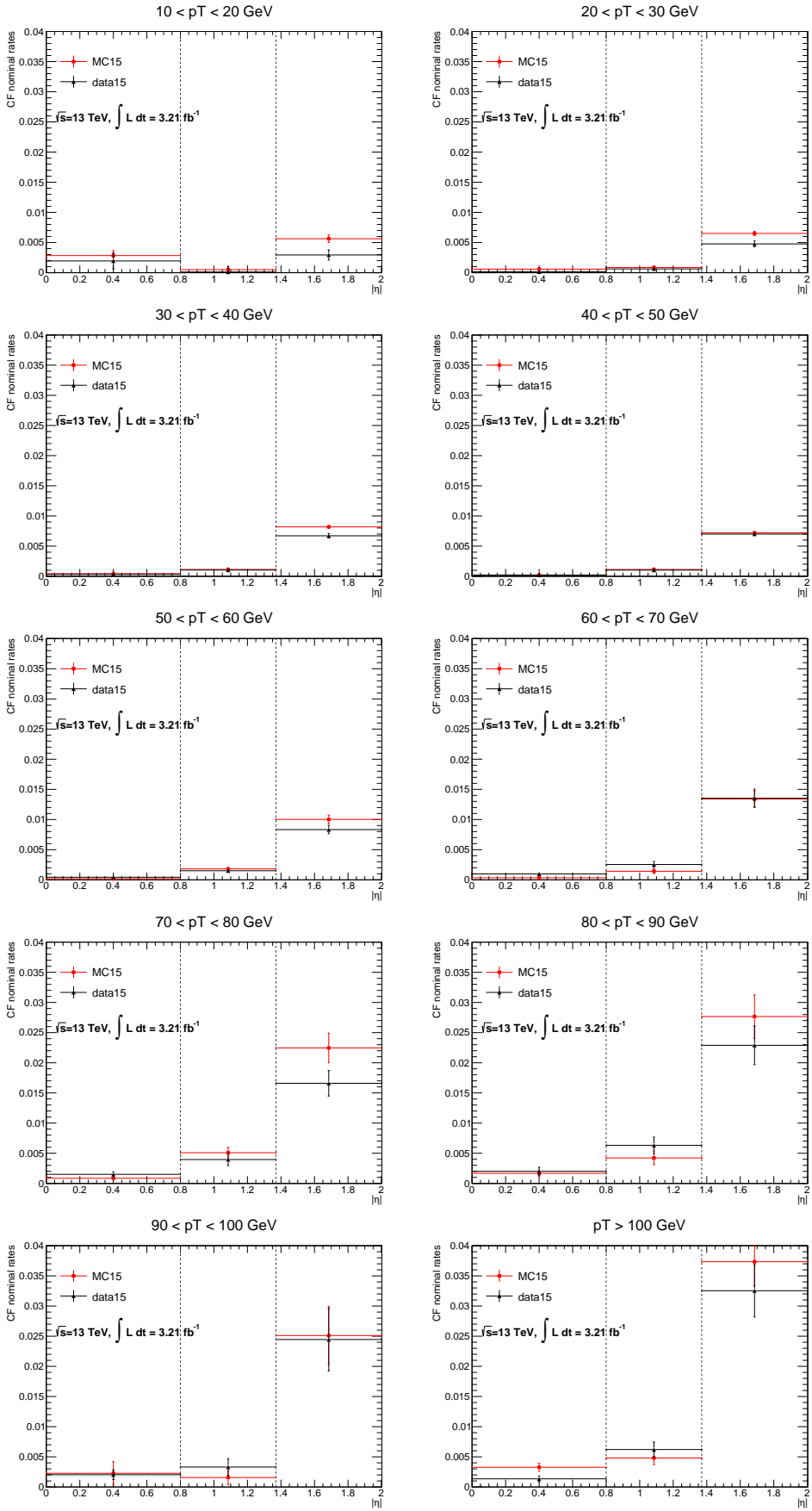
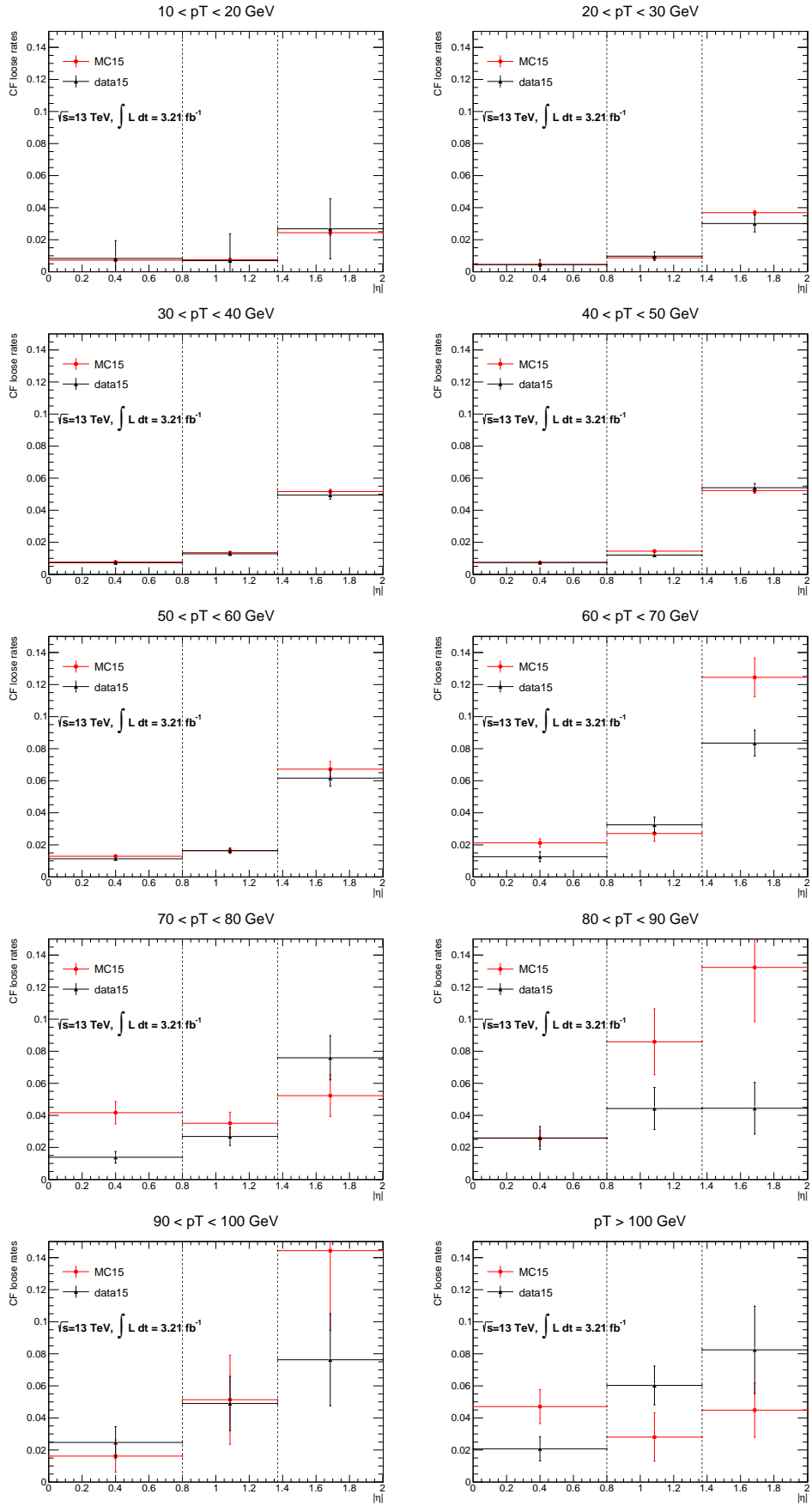


Figure 10: Charge flip 14110 extracted from data (black dots) and from MC $Z \rightarrow e^+e^-$ (red dots) for electrons satisfying the signal requirements, as a function of η and in various p_T bins. Statistical and systematic uncertainties are shown.



8th February 2016 ip 14:10 extracted from data (black dots) and from MC $Z \rightarrow e^+e^-$ (red dots) for electrons failing the signal requirements, as a function of η and in various p_T bins. Statistical and systematic uncertainties are shown.

890 **7.2.1 Systematics**

891 The uncertainties on the charge mis-identification rates coming from the background subtraction procedure
 892 are computed and assigned as systematics. As mentioned in the previous section, the standard measurement
 893 is computed using a central-band width of $75 < m_{ee} < 100$ GeV and side-band regions of 25 GeV for the
 894 background subtraction. To evaluate the systematics, the charge flip rates were extracted for five different
 895 configurations:

- 896 1. $75 < m_{ee} < 100$ GeV, no background subtraction;
- 897 2. $75 < m_{ee} < 100$ GeV, side-band of 20 GeV;
- 898 3. $75 < m_{ee} < 100$ GeV, side-band of 25 GeV (standard measurement);
- 899 4. $75 < m_{ee} < 100$ GeV, side-band of 30 GeV;
- 900 5. $80 < m_{ee} < 110$ GeV, side-band of 25 GeV

901 We then extract four different variations by comparing those five configurations. The effect of applying the
 902 background subtraction itself (called background ON and OFF) is computed by comparing configurations
 903 1 vs. 3. The Z mass window width effects are computed by comparing configurations 3 vs. 5, while the
 904 side-band width effects are calculated by comparing configuration 3 vs. 2 and 3 vs. 4. Then the largest
 905 deviation in each bins is taken as the systematic uncertainty on the charge flip rates.

906 Those variations are shown on Figure 34 for a p_T range of 20-30 GeV for both type of events where
 907 electrons satisfied the signal requirements on left and where electrons don't satisfied the signal requirements
 908 (auxiliary measurement) on right. The black dots represent the standard measurement and coloured dots
 909 represent the different configurations used to compute the systematics. Figure 35 shows the total systematic
 910 uncertainties in each $[p_T, \eta]$ bin after combining the different contributions associated to the background
 911 subtraction method. The upper plot stand for the electron passing the signal requirements while lower plot
 912 is for electrons failing the signal requirements.

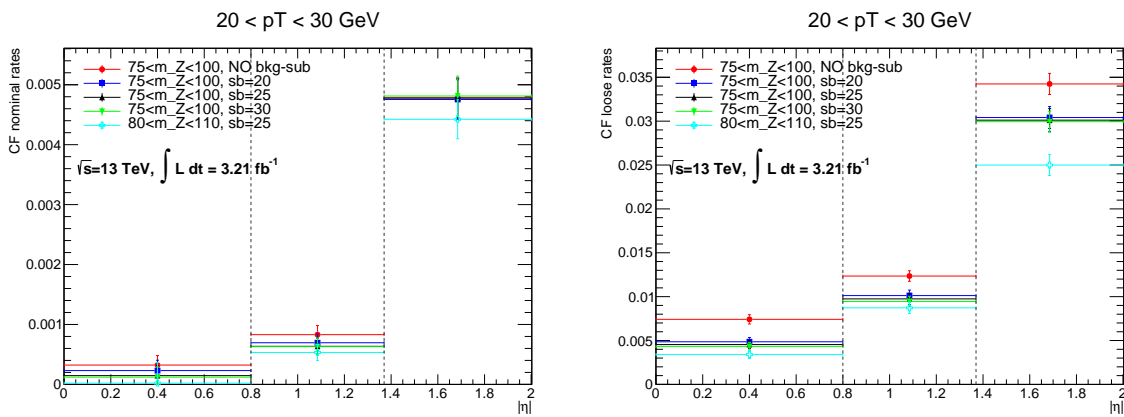


Figure 34: Charge flip rates in data for $20 < p_T < 30$ GeV bin using five different configurations of background subtraction for electrons satisfying the signal requirements on left handed plot and for electrons failing the signal requirements on the right handed plot. In each bin the largest deviation from the standard measurement (black dots) is taken to be the systematic uncertainty.

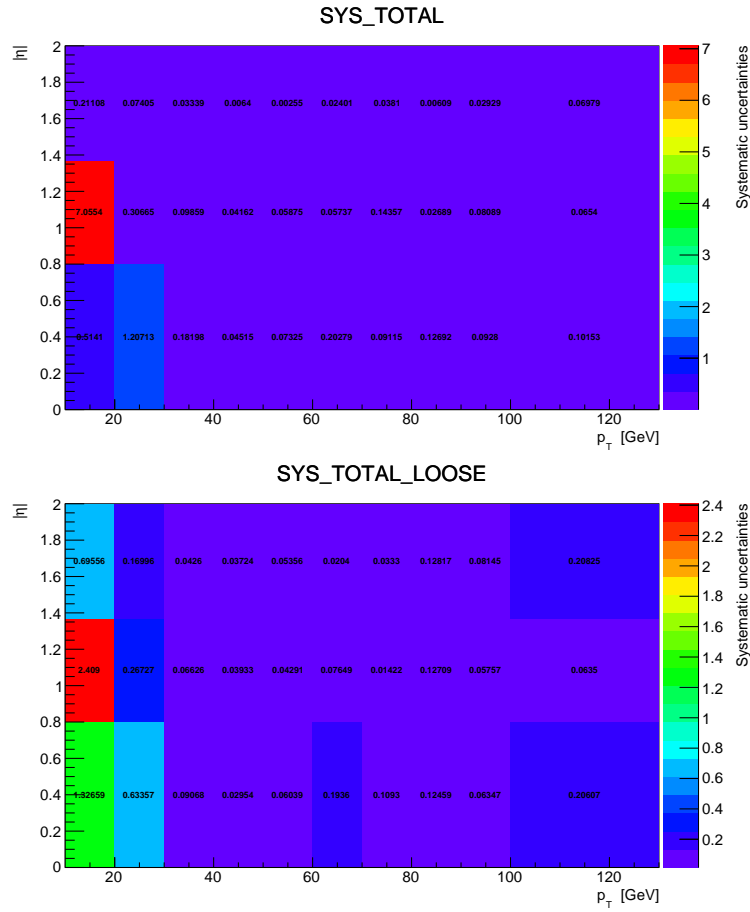


Figure 35: Total systematic uncertainties evaluated in each bins by taking the largest deviation coming from the comparison of different configurations in background subtraction method (in data) for electrons satisfying the signal requirements on the upper plot and for electrons failing the signal requirements on the lower plot.

913 7.3 Backgrounds with fake leptons: general information

914 The term “fake lepton” denotes here generically non-prompt leptons produced in heavy flavor meson
 915 decays, converted photons, light hadrons faking the electron shower, in-flight decays of kaons or pions
 916 to muons, etc. Common properties shared by these objects are a bad response to the electron/muon
 917 identification cuts, non-zero impact parameters, and the reconstructed leptons are often not well isolated.
 918 These properties can be used to discriminate the fake leptons against the prompt and isolated leptons we
 919 are interested in (and which we call “real leptons”).

920 We rely on two different and complementary methods to estimate the fake leptons yields in the signal
 921 regions, either purely data-driven or relying on the MC simulations, which are described respectively in
 922 Sections 7.4 and 8.1; we also cross-check the fake background estimate for the special case of the SR3b
 923 signal region with a third method described in section 8.2. First two methods have already been employed
 924 successfully in the Run-1 analysis [16]. The rest of this section provides some details about the dominant
 925 sources of fake leptons close to the signal regions according to the simulations predictions.

926 **7.3.1 Fake lepton sources close to the signal regions**

927 We studied in the MC simulations the sources of fake leptons close to the signal regions, which we briefly
928 summarize here. This information is important notably for the setup of the related background estimate
929 (the matrix method) and the assignment of systematic uncertainties. It is also genuinely interesting as
930 it may help further rejecting fake leptons by focusing on the relevant source and devising appropriate
931 discriminants.

932 Ideally we would study directly the composition of the signal regions; however, the limited MC statistics
933 does not really allow to do so with a high level of confidence on the results. Therefore, to have more reliable
934 conclusions, we performed these studies in a set of regions with relaxed selection criteria compared to
935 the signal regions (i.e. no m_{eff} cut, looser cuts on (b -) jet multiplicity and $E_{\text{T}}^{\text{miss}}$, etc.). Such criteria are
936 detailed in Table 15. However, the conclusions obtained in this section can be extrapolated to the signal
937 regions, notably since the source of fake leptons due to $t\bar{t}$ processes dominates over other sources both in
938 the relaxed and in the “nominal” signal regions.

939 The sources of fake leptons are identified through the classification performed by the `MCTruthClassifier`
940 tool, following the approach defined in section 4.5. In this present section, only $t\bar{t}$ and V+jets Monte Carlo
941 samples (as presented in Section 3.3) are analysed, since we expected the other potential sources (QCD
942 processes such as $pp \rightarrow b\bar{b}$, diboson...) to be very minor in the signal regions. To increase the available
943 statistics, we did not apply the requirements on the charges of the leptons here.

Table 15: The relaxed signal regions used to study the origin of fake leptons in simulation.

Signal region	N_{lept}	$N_{b-\text{jets}}^{>0}$	Other variables
SR0b	≥ 2	$=0$	$N_{\text{jets}}^{>5} \geq 3, E_{\text{T}}^{\text{miss}} > 70 \text{ GeV}$
SR1b	≥ 2	≥ 1	$N_{\text{jets}}^{>5} \geq 3, E_{\text{T}}^{\text{miss}} > 70 \text{ GeV}$
SR2b	≥ 2	≥ 2	-

944 **Fake electron sources**

945 The fake electrons are classified in a few general categories depending on the origin of the electron
946 (conversion from prompt photons, light hadron fakes including $\pi^0 \rightarrow \gamma\gamma$, non-prompt taus, bottom and
947 charm meson semileptonic decays). The relative abundances of these sources are shown in Fig 36 for
948 different p_{T} cuts on the electrons, in the relaxed signal regions defined in Table 15. They are presented
949 for both baseline and signal electrons definitions – the former being useful to understand the events input
950 to the matrix method in the signal regions. For completeness, the number of events in each category and
951 the associated statistical uncertainties are shown in Appendix 17 (Fig 119). The dependency on other
952 kinematic variables like $E_{\text{T}}^{\text{miss}}$, m_{eff} , etc. is shown in the same appendix.

953 Generally a strong dependency is observed on the fake electron p_{T} . At the baseline level, in the relaxed
954 SR0b and SR1b regions the dominant sources of fake electrons arise from both light hadron fakes and
955 bottom hadrons decays; however, at the signal level the dominant source is the bottom hadrons decays,
956 beside at high p_{T} (>30 GeV) where the light flavor sources are higher than 30%. In a selection with ≥ 2
957 b -jets, most of the fakes arise from light hadrons decays.

958 Fig 37 presents the p_{T} spectrum of the fake electrons in the relaxed signal regions, distinguishing the $t\bar{t}$
959 and V+ jets processes. In all signal regions the background will be dominated by fake electrons from

960 $t\bar{t}$ processes. The first p_T bin ($p_T < 20$ GeV) is depleted since due to the p_T requirements in the lepton
 961 selection, only events with three leptons may fill this bin, which are less frequent in $t\bar{t}$.

962 **Fake muon sources**

963 We classified fake muons into four categories, according to the decision of the `MCTruthClassifier` tool,
 964 and depending on the heavy flavor content of the hadron at the origin of the muon (light, tau, bottom and
 965 charm). We show the relative abundances of these sources in Fig 38 for different p_T cuts on the muons,
 966 in the relaxed signal regions defined in Table 15. They are presented for both baseline and signal muons
 967 definitions. The number of events in each category and the associated statistical uncertainties are shown
 968 in Appendix 17 (Fig 123). The dependency of other kinematic variables like E_T^{miss} , m_{eff} , etc. is shown in
 969 the same appendix.

970 One can see that the dominant source are always non-prompt muons arising from charmed or bottom
 971 hadron decays, in all p_T regions. In general, the non-prompt muons come mainly from b -sources (the
 972 fraction of such events is around 70% or more), except in the SR2b selection: this is interpreted as the fact
 973 that in $t\bar{t}$ events, tagging the 2 b -jets (as is required in this region) strongly reduces the rate of non-prompt
 974 muons originating from these, as the small impact parameter required for that muon to satisfy signal cuts
 975 contradicts the b -jet tagging which relies on the presence of displaced tracks and a secondary vertex.
 976 Fig 39 presents the p_T spectrum of these fake muons in the relaxed signal regions, distinguishing the
 977 $t\bar{t}$ and $V + \text{jets}$ processes. For all selections, the background will be dominated by low p_T fake muons
 978 originating from $t\bar{t}$.

979 **7.4 Backgrounds with fake leptons: the matrix method**

980 The matrix method is a purely data-driven approach used to estimate the amount of fake leptons in the
 981 regions of interest (i.e. validation regions, signal regions, etc). It relies on the different response of the
 982 prompt and fake leptons to identification, isolation and impact parameters requirements: the fake leptons
 983 have low probabilities to satisfy these requirements, unlike the prompt leptons. No attempt is made to
 984 consider the different categories of fake leptons separately for the extraction of fake rates, but systematic
 985 uncertainties are assigned to cover possible differences.

Methodology

A combination of tight requirements on discriminant variables such as the electron identification, the lepton isolation and impact parameters is defined (see Tab 9). The reconstructed leptons are then classified in two categories ("tight" and "loose"), depending on their success satisfying the tight requirements or not. If ϵ and ζ are respectively the probabilities for a prompt/fake lepton to satisfy the requirements, linear relationships can be established between the mean values of the rates of prompt/fakes and tight/loose leptons, which for the 1-lepton case are:

$$\begin{aligned} < N_{\text{tight}} > &= \epsilon < N_{\text{prompt}} > + \zeta < N_{\text{fake}} > \\ < N_{\text{loose}} > &= (1 - \epsilon) < N_{\text{prompt}} > + (1 - \zeta) < N_{\text{fake}} > \end{aligned} \quad (5)$$

986 This system of equations can be used to evaluate the number of prompt and fake leptons given the observed
 987 number of tight and loose leptons. In this analysis we are using a generalization of this method, able to
 988 handle events with arbitrary number of leptons – the well known dynamic matrix method. It was already
 989 used in the Run-1 analysis and is described in detail in [16, 48].

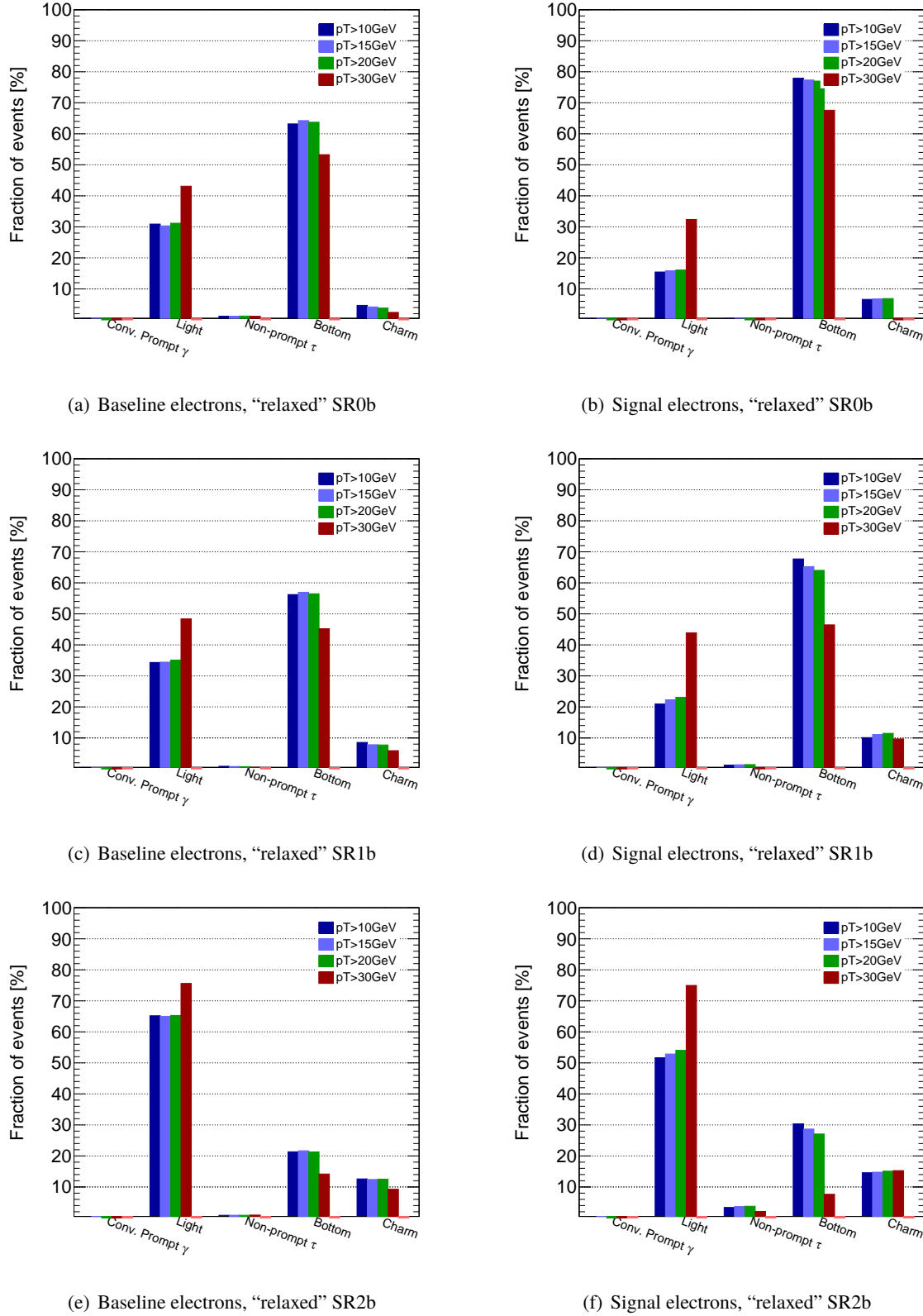


Figure 36: Sources of fake electron as a function of the electron p_T , as predicted by MC simulations (combined $t\bar{t}$ and $V + \text{jets}$) in the relaxed signal regions defined in Table 15. The results are shown for baseline (left) or signal electrons (right).

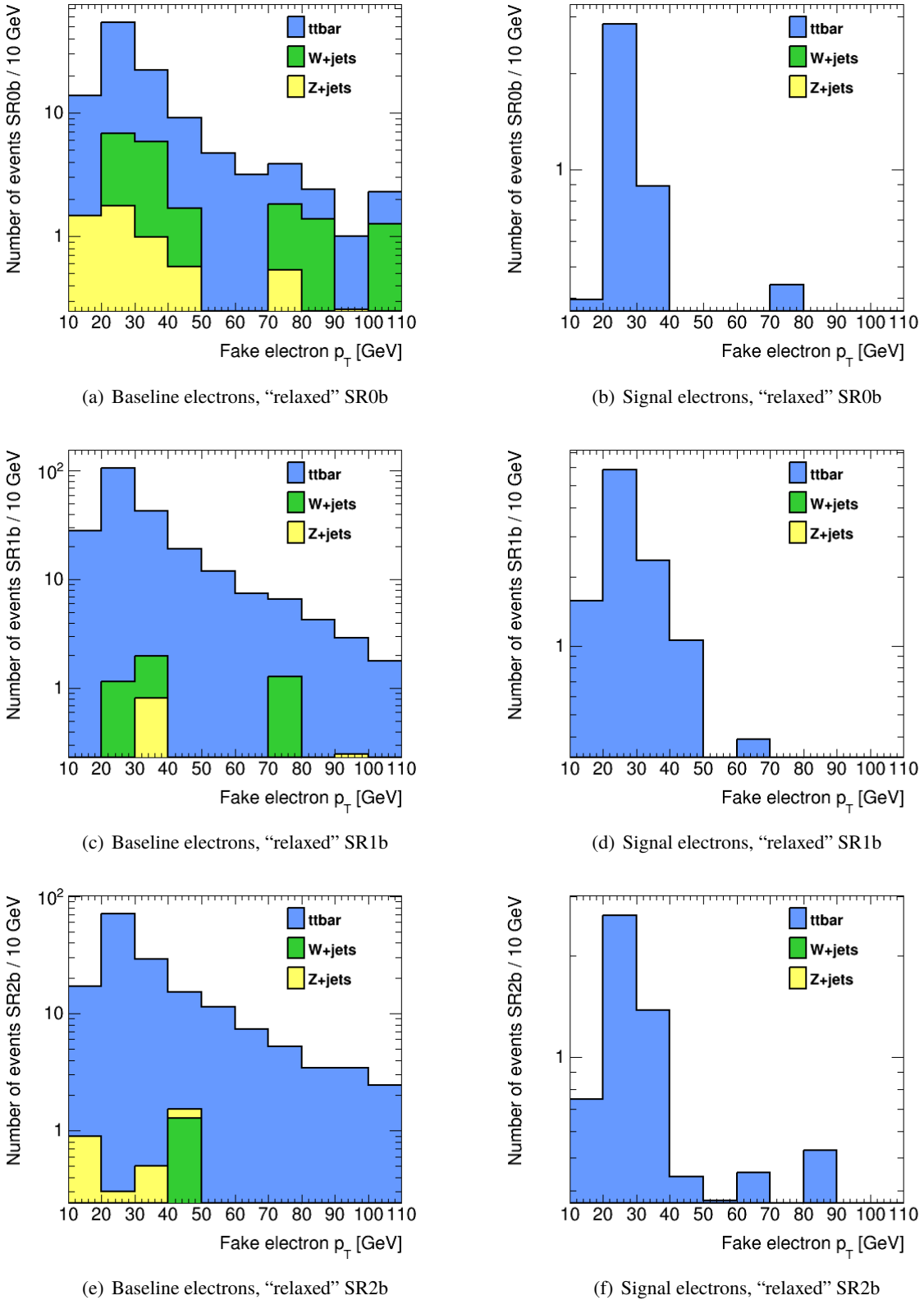


Figure 37: Transverse momentum distribution of the fake electrons as predicted by MC simulations in the relaxed signal regions defined in Table 15. Electrons originating from $t\bar{t}$ or $V+$ jets events are distinguished.

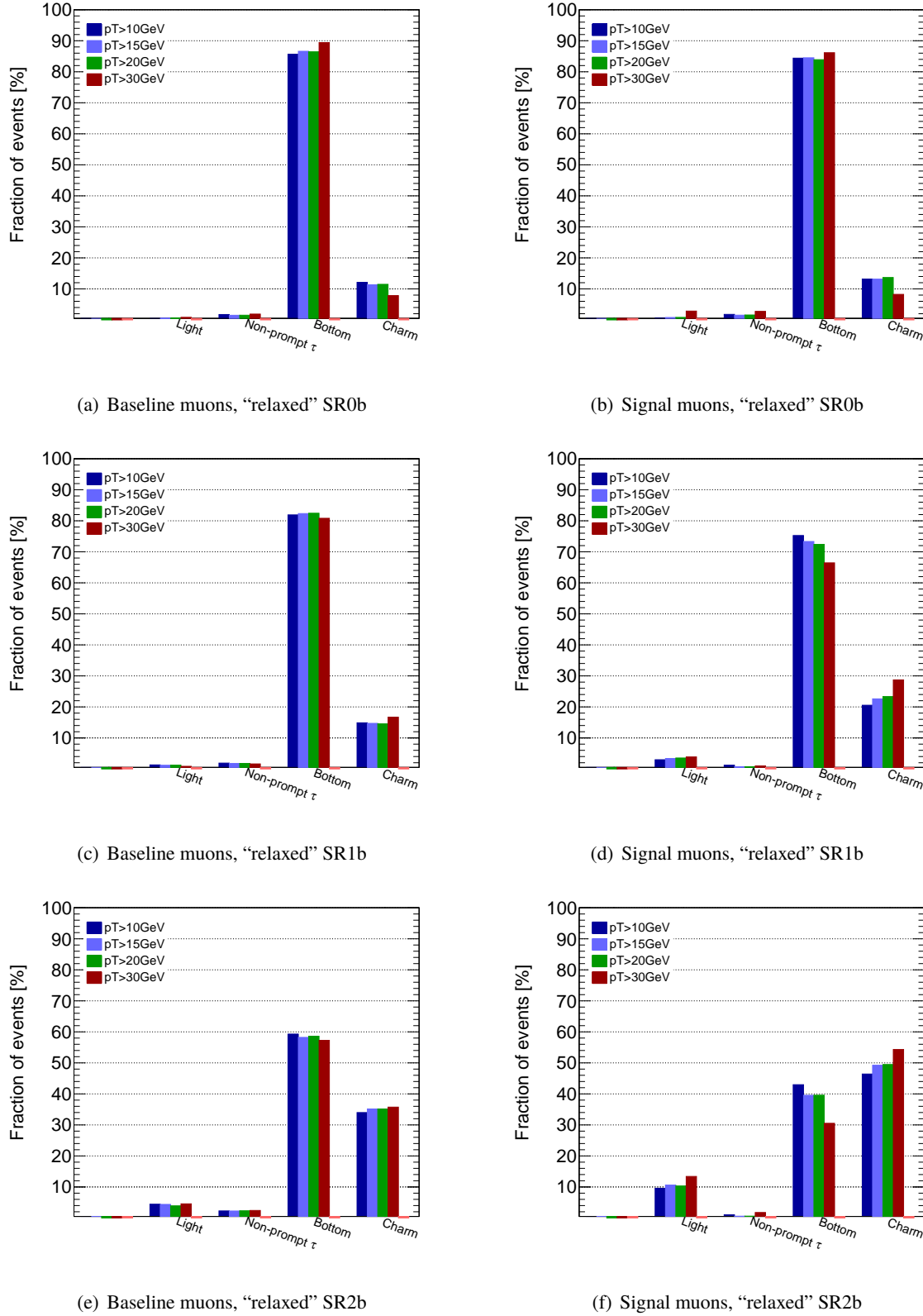


Figure 38: Sources of fake muons as a function of the muon p_T , as predicted by MC simulations (combined $t\bar{t}$ and $V + \text{jets}$) in the relaxed signal regions defined in Table 15. The results are shown for baseline (left) or signal muons (right).

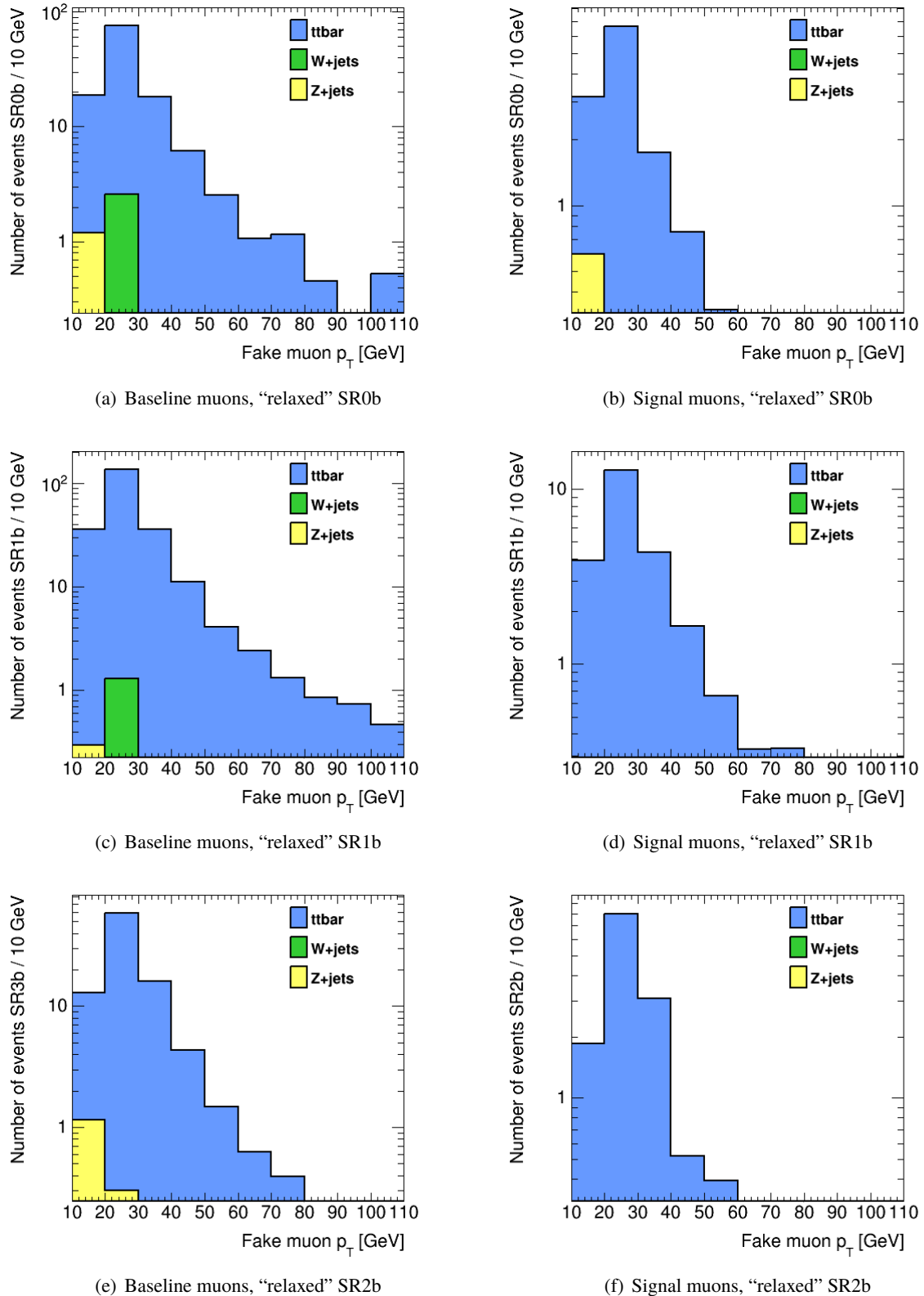


Figure 39: Transverse momentum distribution of the fake muons as predicted by MC simulations in the relaxed signal regions defined in Table 15. Muons originating from $t\bar{t}$ or $V+$ jets events are distinguished.

990 The method relies of the prior knowledge of the probabilities ϵ and ζ , which need to be measured
 991 in dedicated samples enriched in prompt and fake leptons, as presented in Sections 7.4.1 and 7.4.2.
 992 The uncertainties on the probabilities for fake leptons constitute the main source of uncertainties in the
 993 asymptotic regime. In the low statistics regime, one has to cope with the fact that the loose and tight
 994 leptons categories are not enough populated to provide reliable estimates: for example predictions of
 995 negative yields are a possible outcome. In general these estimates are accompanied by large statistical
 996 uncertainties.

997 Finally, one should note that the charge flip electron background interferes with the matrix method as
 998 the charged flipped electrons are notably more prone to fail impact parameter or tight identification
 999 requirements, and the related efficiencies are distinct from both those of prompt and fake electrons. They
 1000 correspond so to speak to a third category of objects, while the matrix method is based on the assumption
 1001 that only two categories are present. One way to solve the issue is to rely on the linearity of the matrix
 1002 method estimate with respect to its input number of events : therefore one can simply subtract the estimated
 1003 charge flip background in the tight and loose leptons categories, from the observed data. This requires a
 1004 dedicated measurement of the charge flip rate for electrons failing the tight requirement (Section 7.2).

1005 7.4.1 Measurement of the ϵ probabilities (prompt leptons)

1006 The real efficiency is measured in a high purity data sample with the standard Z tag-and-probe method.
 1007 The HLT_e24_lhmedium_iloose_L1EM20VH and HLT_mu20_iloose_L1MU15 single lepton triggers
 1008 triggers are used to select the events. A tag lepton, used to identify the $Z \rightarrow \ell\ell$ process, should fulfil
 1009 the signal leptons requirements (Table 9), have a p_T larger than 25 GeV and be matched with the relevant
 1010 single lepton trigger. An additional probe lepton, used for the efficiency measurement, should satisfy the
 1011 baseline selection (Table 9). For each tag-and-probe lepton pair both leptons are alternatively considered
 1012 as the possible tag, as it allows to increase the statistics and to remove any bias in the choice of the tag. To
 1013 enrich the selection in $Z \rightarrow \ell\ell$ events, the invariant mass of the tag-and-probe pairs is required to be in
 1014 the $80 < m_{ee} < 100$ GeV interval. The efficiency is measured as a function of p_T and η^2 . For illustration,
 1015 Figure 40 shows the invariant mass of the tag-and-probe pair distribution in data for events which pass or
 1016 fail the signal cuts.

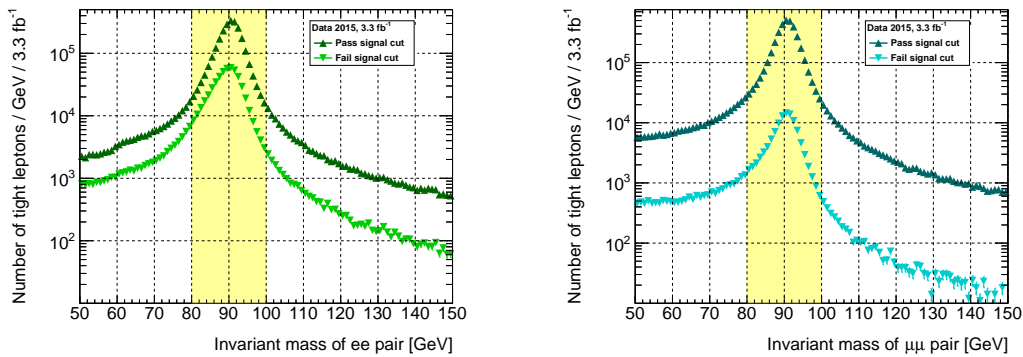


Figure 40: Invariant mass of the tag-and-probe electron (left) and muon (right) opposite-sign pair, for probes passing/failing the signal requirements.

² The electron efficiency η binning is driven by the calorimeter geometry removing the calorimeter crack region.

1017 A sizable background contamination is observed for the $p_T < 20$ GeV electrons. This contamination
 1018 is estimated using a background template method inspired by the one used by the e/γ CP group to
 1019 measure reconstruction and identification efficiencies measurements [41]. Related systematic uncertainties
 1020 are set by varying the m_{ee} measurement window and the background template method. Besides, the
 1021 HLT_2e12_lhloose_L12EM10VH trigger used in the analysis induces a sizable bias to the measurement.
 1022 As both electrons with and without di-electron trigger match can enter in the signal regions³, a systematic
 1023 uncertainty is set to cover this effect. As the real muon efficiency is fully dominated by the track isolation
 1024 cut, the measurement of the track isolation efficiencies performed by the muon CP group using the same
 1025 Z tag-and-probe technique is very similar. Therefore the systematic uncertainties associated to track
 1026 isolation efficiency measurement provided by the Muon CP group can be used to assess the systematic
 1027 uncertainties associated to the muon tag-and-probe measurement method.

1028 A last source of systematic uncertainty is considered to account for the extrapolation from events with
 1029 well isolated leptons, where the real lepton efficiencies are extracted, to the signal regions characterized
 1030 by a more busy environment, with several (b)-jets. Possible dependencies of the efficiencies to other
 1031 variables (i.e. $\Delta R(\ell, \text{jet})$, number of jets, etc) have been checked, and the difference with respect to the
 1032 nominal parametrization is ensured to be within the assigned systematic uncertainty. The opportunity of
 1033 measuring the efficiencies with a tag-and-probe method based on $t\bar{t}$ events has been studied in order to
 1034 measure the real lepton efficiencies with events with topology closer to the Signal Regions with leptons
 1035 close to (b)-jets. However, preliminary conclusions shown that the statistics uncertainties associated to
 1036 this method are too large to perform a measurement with a fine p_T and η binning. Therefore we chose
 1037 to consider this method only when more statistics will be available. More details are given in Appendix 16.
 1038

1039 Results

1040 The resulting real efficiencies, measured with the 2015 data at 13 TeV (3.2 fb^{-1}), are shown in Figure 41.
 1041 The electrons efficiencies are dominated by the calorimeter isolation cut at $p_T < 25$ GeV and by the loose
 1042 to tight likelihood identification cut at $p_T > 25$ GeV. The associated efficiencies increase from 44 – 70% at
 1043 low p_T up to 92 – 94% above 80 GeV. The real muon efficiencies, largely dominated by the track isolation
 1044 cut, vary from 85% at low p_T to > 95% above 35 GeV.
 1045

1046 Systematic uncertainties

1047 Three different sources are considered to assign the systematics uncertainty on the real lepton efficiency:

- 1048 • Real efficiency measurement : 27 variations of the tag-and-probe method are considered to assess
 1049 the electron measurement systematics. As done in the e/γ CP group [41] alternative m_{ee} windows
 1050 and 9 variations of the background subtraction methods are considered. The largest contribution
 1051 to the systematics arises from the m_{ee} window variation. This is expected as the proportion of
 1052 electrons affected by bremsstrahlung depends on m_{ee} . The resulting relative systematics vary from
 1053 5 – 7% in the low p_T range to $\sim 0.5\%$ for $p_T > 40$ GeV. The systematic uncertainties associated to
 1054 the muon efficiencies measurement vary from 1% in the low p_T range to $O(0.5\%)$ for $p_T > 20$ GeV.
 1055
- Di-lepton trigger inefficiency : The bias induced in the real electron efficiency is computed by
 1056 comparing the efficiency computed with and without trigger match. The resulting relative systematic
 1057 uncertainty is found to be at most 4% in the $20 < p_T < 35$ GeV range, 2% in the $35 < p_T < 60$ GeV
 1058 range and $O(0.5\%)$ for electrons in the $p_T > 60$ GeV range.

³ If the event is trigger by the di-electron trigger, the two leading electrons are match to the trigger whereas the third one is not.
 Also, if the event is triggered by the E_T^{miss} trigger the electrons are not match to any triggers.

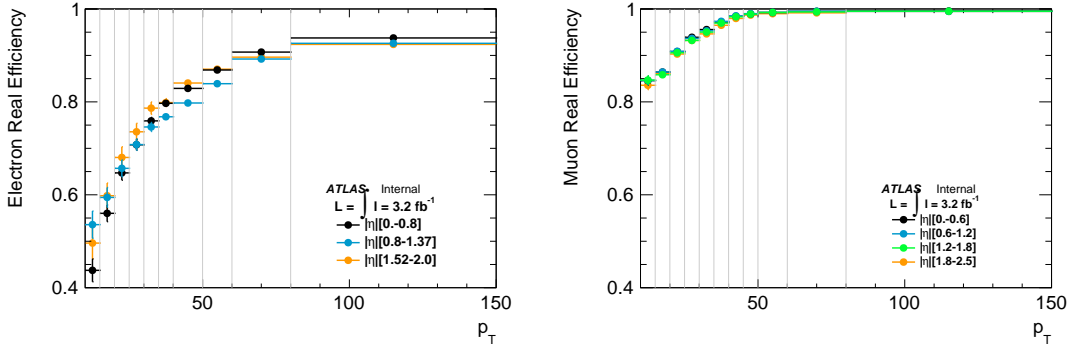


Figure 41: Electron (left) and muon (right) real efficiencies as a function of p_T and η , in data. The η binning used in the electron case corresponds to the geometry of the electromagnetic calorimeter. For muons a homogeneous η binning is considered. The error bars corresponds to the quadratic sum of the statistical and tag-and-probe measurement systematic uncertainties.

- Extrapolation to signal regions : This systematic is evaluated comparing the real efficiency measured in MC samples for processes such as $Z \rightarrow \ell\ell$, $t\bar{t}$ and a SUSY benchmark model $\tilde{g}\tilde{g} \rightarrow t\bar{t}t\bar{t}\tilde{\chi}_1^0\tilde{\chi}_1^0$ with $m_{\tilde{g}} - m_{\tilde{\chi}_1^0} > 1000$ GeV. The latter provides an extreme case of boosted tops leading to less well isolated leptons, ensuring that the considered uncertainties are conservative. The corresponding systematics uncertainties, parametrized as a function of the lepton p_T and $\Delta R(\ell, \text{jet})$, are shown in Table 16.

For both electrons and muons, the statistical uncertainties are found to be negligible with respect to the systematic ones. The signal region extrapolation systematic uncertainties are dominant for muons and electrons close to a jet ($\Delta R(e, \text{jet}) < 0.6$). For electrons with $\Delta R(e, \text{Jet}) > 0.6$, all the systematic uncertainties are at the same order magnitude at low p_T ($p_T < 30$ GeV), while the signal region extrapolation uncertainty dominates in the $p_T > 30$ GeV range. All the systematic are considered as correlated between p_T and η bins and more details can be found in Appendix 16. Despite the large signal region extrapolation systematic uncertainties, the impact of the real lepton efficiencies uncertainties on the estimation of the fake background is marginal with respect to ones from the fake leptons efficiencies.

electrons		
	$0.4 < \Delta R(l, \text{jet}) < 0.6$	$\Delta R(l, \text{jet}) > 0.6$
$p_T < 60$ GeV	8%	4%
$p_T > 60$ GeV	5%	5%
muons		
	$0.4 < \Delta R(l, \text{jet}) < 0.6$	$\Delta R(l, \text{jet}) > 0.6$
$p_T < 15$ GeV	28%	10%
$15 < p_T < 35$ GeV	18%	7%
$35 < p_T < 50$ GeV	10%	5%
$50 < p_T < 80$ GeV	5%	3%
$p_T > 80$ GeV	1%	1%

Table 16: SUSY signal extrapolation systematic uncertainty on the real lepton efficiency measurements.

1073 7.4.2 Measurement of the ζ probabilities (fake leptons)

1074 This parameter is measured in dedicated control regions enriched in fake leptons, using a Tag&Probe
 1075 method. Compared to the lepton identification efficiency, the fake lepton efficiency is much harder to
 1076 determine due to the difficulty to identify an event selection that would provide both a high purity and
 1077 enough statistics, especially for leptons with $p_T > 40$ GeV. In the Run-1 (8 TeV) analysis, the selection
 1078 was requiring at least two same-sign leptons together with a jet, and the fake electron probabilities were
 1079 determined separately for events with or without b -jets. Other analyses have been using inclusive selections
 1080 with a single lepton (dominated by QCD), which have the advantage to be much more populated, but
 1081 on the other hand are less representative of the properties of fake leptons that can be found in the signal
 1082 regions.

1083 A similar approach to Run-1 is used to perform the measurement with the Run-2 data. We select events
 1084 with two same-sign leptons ($p_T > 10$ GeV, satisfying the baseline requirements), one of which (referred to
 1085 as “tag”) should satisfy the signal requirements and be rather energetic (e.g. $p_T > 40$ GeV). For the electron
 1086 fake rate measurement, the tag should fire (and be matched) to HLT_mu26_imedium primary single muon
 1087 trigger. For the muon fake rate measurement, the events are selected with HLT_mu18_mu8noL1 di-lepton
 1088 trigger. The requirements imposed on the tag allow to enrich the selection in semileptonic $V +$ jets or
 1089 $t\bar{t}$ processes with one fake lepton, similar to the signal regions contents, while rejecting QCD events in
 1090 which the sources of fakes might differ. Selected events should also contain at least one b -jet, to enrich
 1091 the sample in fake leptons from $t\bar{t}$ processes which were seen in MC to dominate the contributions to
 1092 all signal regions. To reduce the contamination in diboson and $t\bar{t} + V$ processes, any event with a third
 1093 baseline lepton with $p_T > 10$ GeV is rejected. The remaining prompt SS background is subtracted using
 1094 Monte Carlo samples, while the charge flip background is subtracted using OS data events re-weighted by
 1095 the charge flip rate obtained in data, as explained in Section 7.2. To minimize the signal contamination
 1096 and the overlap with the signal regions, an upper cut of 125 GeV on E_T^{miss} is considered. Finally, the fake
 1097 rate is measured as the ratio between the number of tight (N_T) and tight + loose ($N_T + N_L$) leptons ⁴:

$$\zeta = \frac{N_T - N_T^{\text{bkg}}}{N_T + N_L - N_T^{\text{bkg}} - N_L^{\text{bkg}}}, \quad (\Delta\zeta)_{\text{stat}} = \frac{1}{N_T + N_L} \sqrt{(1 - \zeta)^2 N_T + \zeta^2 N_L} \quad (6)$$

1098 the latter expression indicates the statistical uncertainty assigned to the measured rate, derived with a first
 1099 order approximation.

1100 In general the probabilities vary largely with p_T thus require binned measurements. Given the low
 1101 statistics in data, we chose the performed the measurement only in two p_T bins [10,20] GeV and ≥ 20 GeV
 1102 for electrons and three p_T bins for muons ([10,15] GeV, [15,20] GeV and ≥ 20 GeV). The dependency
 1103 on other kinematic variables is studied in $V +$ jets and $t\bar{t}$ MC samples, and the difference with respect to
 1104 nominal measurement is ensured to be within the assigned systematic uncertainty.

1105 Before showing the actual measurements in data, we present studies based on $t\bar{t}$ and $V +$ jets Monte Carlo
 1106 samples (yielding fake leptons). They provide essentially three important pieces of information:

- 1107 • the nature of the fake lepton sources in the regions used for the data measurements. This helped
 1108 devising regions that have a composition as close as possible to the signal regions (see Section 7.3.1)
 1109 while trying to keep enough statistics for the measurement.

⁴ Loose = baseline lepton not passing the signal requirements.

- whether, and to which extent, the fake rates differ between the different sources of fake leptons. This is a crucial input to define the systematic uncertainties assigned on the measured fake rates and their extrapolation to the signal regions.
- how the fake rates depend on various variables related to the topology and the kinematics of the event (lepton p_T , number of jets, E_T^{miss} , $m_{\text{eff}} \dots$)

The leptons can be easily identified through truth-matching information, therefore the event selections used in these studies are looser than the ones used for the data measurements.

Nature of the fake leptons

We use $V + \text{jets}$ and $t\bar{t}$ MC samples to design a control region enriched in fake leptons that will be further defined in data to measure the lepton fake rates. This control region should have a similar composition and sources of fake leptons as the defined signal regions. During the optimization studies, it is found that the W and $Z + \text{jets}$ processes (with a jet faking an electron) can be highly reduced by requiring at least one b -jet in the event (CR_{1bF}). This is illustrated in Figure 42 for electrons (top) and muons (bottom). The nature of the fake leptons in this control region is shown in Figures 43 - 44, top. For completeness, Figures 43 - 44 (bottom) show also the origin of fake leptons in a control region region with at least 2 b -jets (CR_{2bF}). The latter is used to examine the difference between the nominal fake rate (measured in CR_{1bF}) and the fake rate representative for regions with at least two b -jets in the event (and measured in CR_{2bF}). Generally, a similar origin of the fake leptons as in the signal regions is obtained.

Fake lepton rate in $V + \text{jets}$ and in $t\bar{t}$ MC

In this paragraph we present the fake rate measured separately for different sources of fake leptons in $V + \text{jets}$ and $t\bar{t}$ MC. The truth classification presented in 4.5 is employed to build the different categories. No cut on number of b -jets or light jets is applied.

Figure 45 presents the fake rate for electrons arising from hadron decays (light flavor), non-prompt electrons (heavy flavor) and converted prompt photons, in $V+\text{jets}$ MC sample. For completeness we also show separately the fake rate for electrons arising from b -mesons and c -mesons decays. Results in $t\bar{t}$ MC are shown in figure 46. Generally the fake rate is highly dependent on the origin of the fake lepton. Thus, it is very important to design at best a control region with a similar composition as the signal regions to perform the measurement of the fake rate. The fake rates measured in $V + \text{jets}$ and in $t\bar{t}$ MC samples differ by a factor greater than 2 in the low p_T range for non-prompt electrons, the dominant source in the (relaxed) signal regions.

Figure 47 presents the fake rate for muons arising from hadron decays (light flavor) and for non-prompt muons (heavy flavor), in $V+\text{jets}$ MC sample. For completeness we also show separately the fake rate for muons arising from b -mesons and c -mesons decays. Results in $t\bar{t}$ MC are shown in figure 48. The fake rate measured in a region dominated by muons arising from c -mesons decays from $V+\text{jets}$ (in particular from $W+\text{jets}$) is up to 50% higher than the fake rate measured in a region dominated by c -mesons sources from $t\bar{t}$. This is mainly because in $t\bar{t}$ the fake muon actually comes from processes like $B \rightarrow cX$, hence they are less isolated. The $W+\text{jets}$ processes are not contributing significantly in any of the signal regions, thus the fake rate is not additionally measured in a region dominated by such processes.

Fake lepton rate in $W\gamma$ MC

The $W\gamma$ yields close-to and in the SRs are studied by comparing the contribution between $W\gamma$ and other processes using Monte Carlo prediction. This study shows negligible contribution from $W\gamma$ processes in all SRs. Compared to other sources leading to fake leptons, $W\gamma$ contributes less than 1% in regions close-to SR1b and SR3b. As the electron fake rate is highly dependent on the fake lepton sources, we

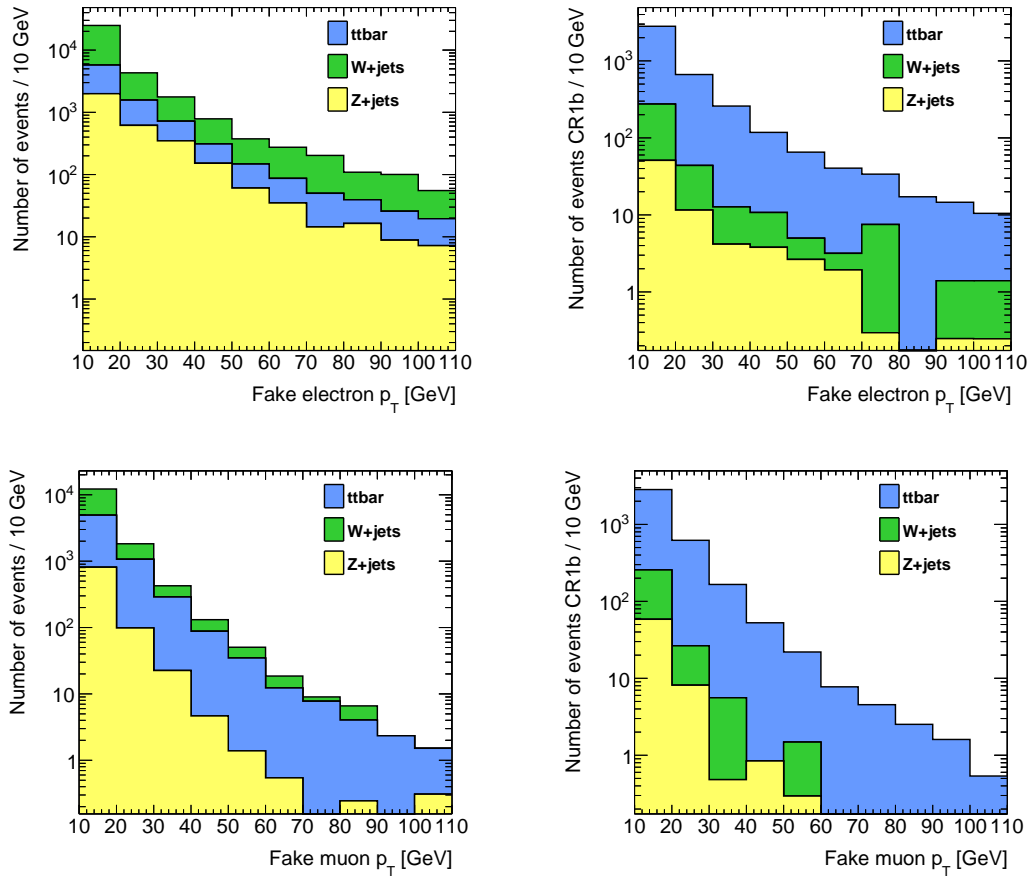


Figure 42: Transverse momentum distribution of the fake electrons as predicted by MC simulations after the baseline lepton selection (left) and after requiring at least one b -jet in the event (right). Fake electrons (top) and muons (bottom) originating from $t\bar{t}$ or $V + \text{jets}$ events are distinguished. $L = 3 \text{ fb}^{-1}$.

measure the fake rate also in $W\gamma$ MC samples. This allows us to quantify the difference between the nominal fake rate used in the analysis and the fake rate corresponding to photon conversion sources. A fake rate around 9% is obtained. Considering the small contribution and compatible fake efficiency, the $W\gamma$ process could be ignored in the fake rate measurement.

Fake electron efficiency measurement

As the ee channel is dominated by charge flip electrons, the measurement in data is performed using $e\mu$ pairs in which the muon is considered to be the tag lepton. The numbers of events with tight and loose probe electrons used for the measurement are shown in Table 17 for data and for Monte Carlo (which are used for the prompt SS subtraction). For illustration, Figure 49 shows the p_T distribution of numerator and denominator in data and MC. For completeness, we choose to show the detector background sources from $t\bar{t}$ and $V + \text{jets}$ (here the charge-flip is estimated from $t\bar{t}$). One can see that the MC prediction agrees rather well with data, and the selection is fully dominated by $t\bar{t}$ processes, as targeted. The measured electron fake rates (with their statistical uncertainties) in data, and in $V + \text{jets}$ and $t\bar{t}$ MC are shown in Table 18. The fake rate in data, in the second p_T bin is found to be larger than in MC. This difference is within the assigned systematic uncertainties.

Fake muon efficiency measurement

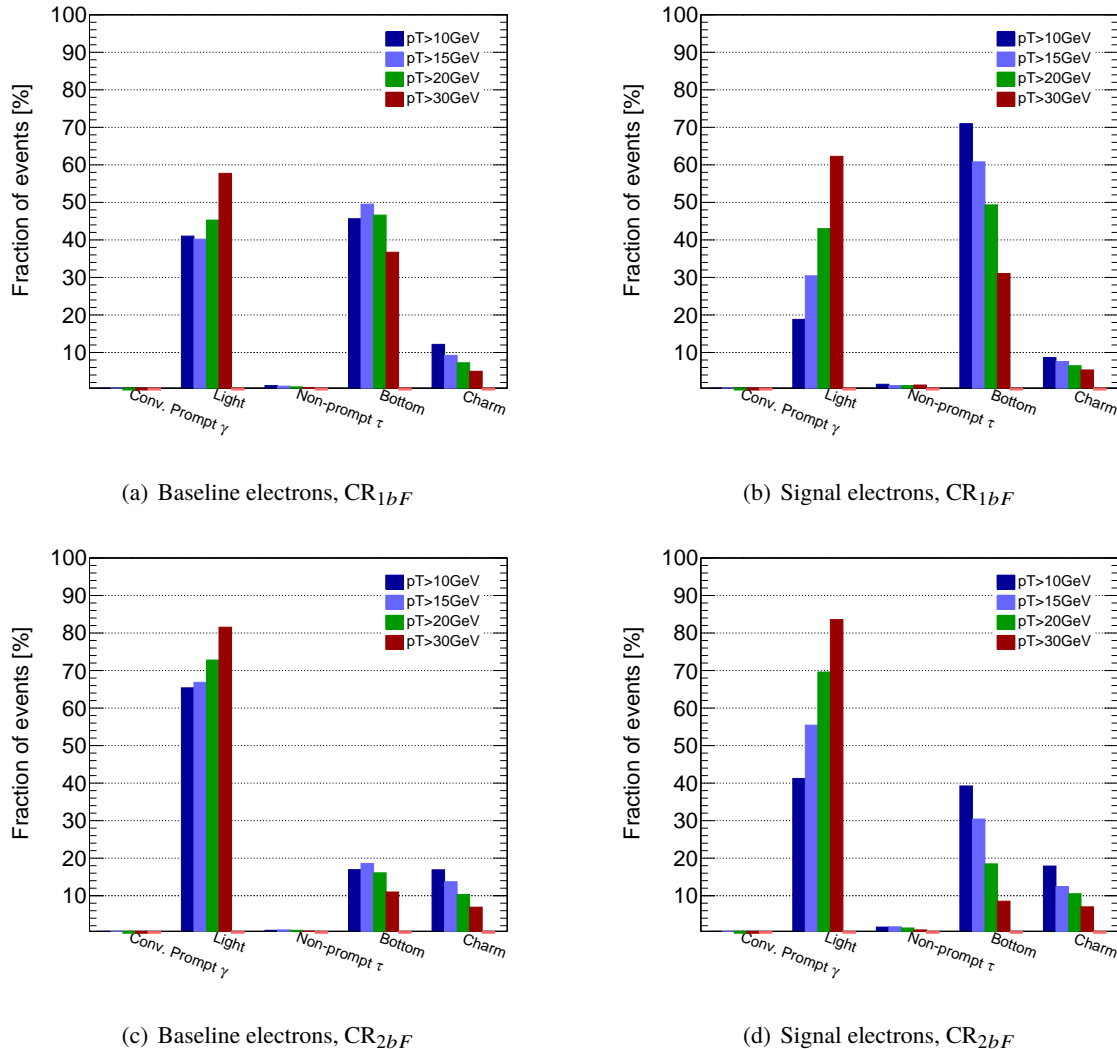


Figure 43: Sources of fake electron as a function of the electron p_T , as predicted by MC simulations (combined $t\bar{t}$ and $V+$ jets) in CR_{1bF} (top) and CR_{2bF} (bottom). The results are shown for baseline (left) or signal electrons (right).

1169 Same-sign dimuon pairs are used for the measurement in data, similarly to the electron case; the criteria
 1170 for the selection of the tag muon are identical, and it is in addition required to have a larger transverse
 1171 momentum than the probe muon. The measurement can be performed only up to 40 GeV, and above the
 1172 same value as in the [20, 40] GeV p_T bin is used.

1173 The numbers of events with tight and loose probe muons used for the measurement are shown in Table 19
 1174 for data and for Monte Carlo (which are used for the prompt SS subtraction). Figure 50 shows the
 1175 p_T distribution of numerator and denominator in data and MC. For completeness we choose to show
 1176 the detector background estimation from $t\bar{t}$ and $V+jets$ MC samples. Data and MC prediction are in fair
 1177 agreement and the selection is dominated by $t\bar{t}$ events. The measured muon fake rates (with their statistical
 1178 uncertainties) are shown in Table 20. Both the results in data and in $V+jets$ and $t\bar{t}$ MC are shown. A good
 1179 agreement between the two measurements is obtained.

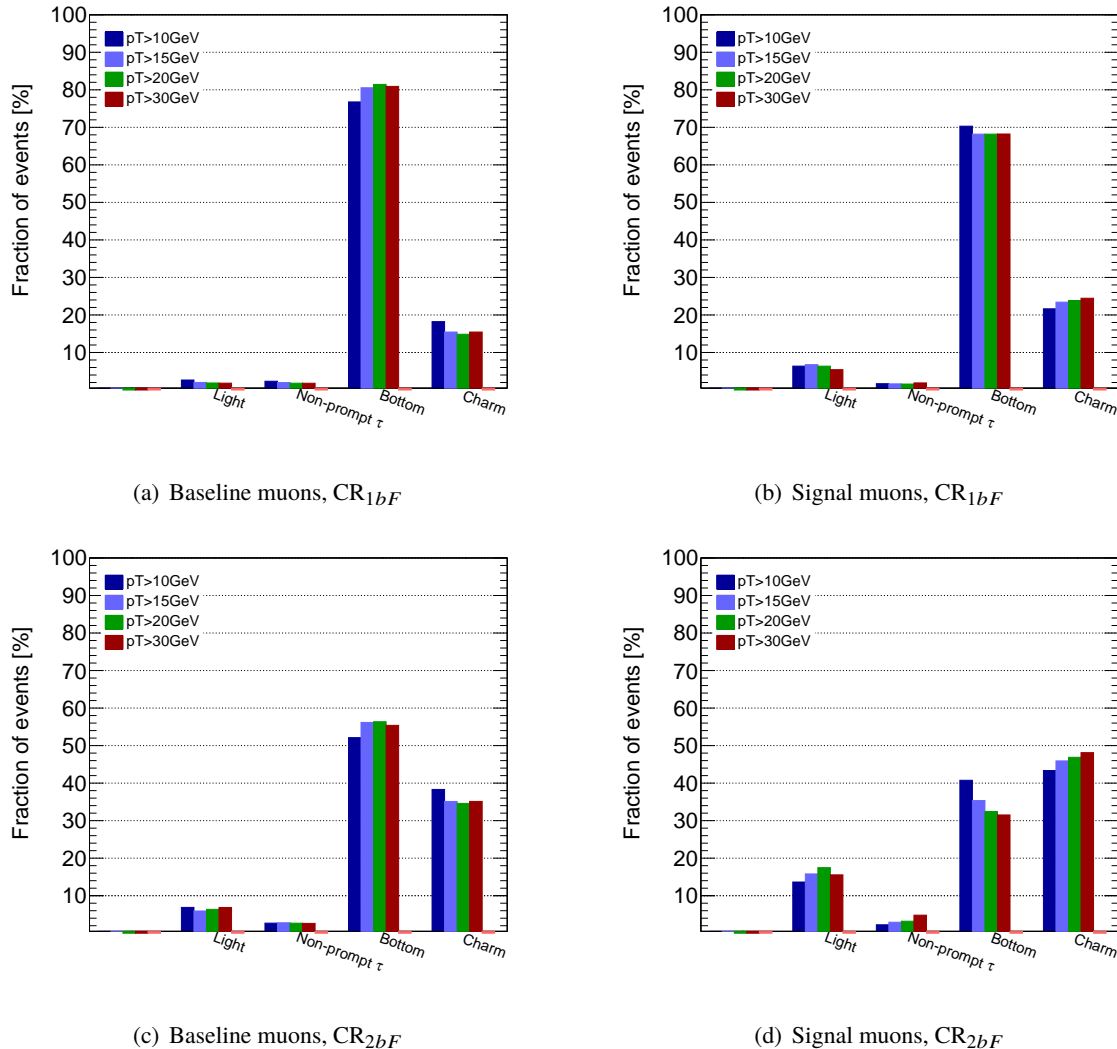


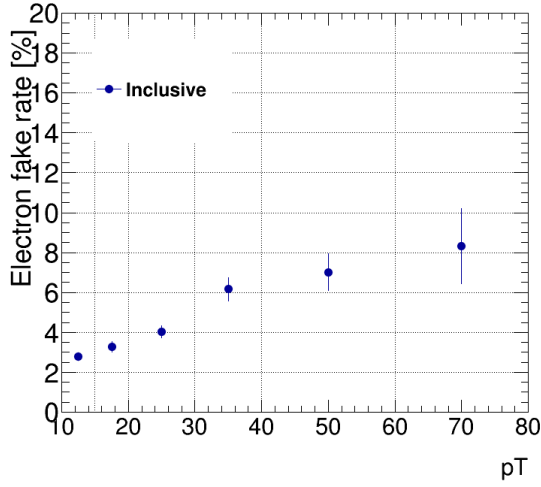
Figure 44: Sources of fake muons as a function of the muon p_T , as predicted by MC simulations (combined $t\bar{t}$ and $V + \text{jets}$) in CR_{1bF} (top) and CR_{2bF} (bottom). The results are shown for baseline (left) or signal muons (right).

1180 Corrections for regions with two or three b -jets

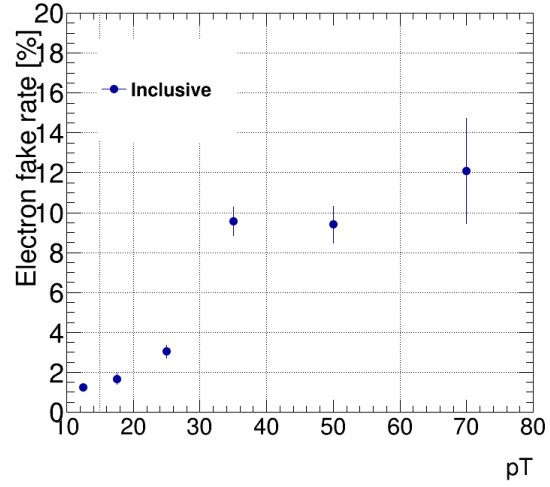
1181 In $t\bar{t}$ events, the fake lepton might have less chances to come from a B -meson decay if there are already
 1182 2 tagged jets (section 7.3.1). As the fake rate changes between a region with 1 b -jet or 2 b -jets, we chose
 1183 to study the fake rate separately in regions with at least 1, 2 and 3 b -jets in $V + \text{jets}$ and $t\bar{t}$ MC, and in data
 1184 when the statistic allows us. The results in MC are shown in Figure 51 for electrons (left) and for muons
 1185 (right). The fake rate is found to have a variation of $O(30\%)$. The fake rate measured in data in a region
 1186 with ≥ 2 b -jets is found to be consistent with the rate measured ≥ 1 b -jet – large statistical uncertainties are
 1187 obtained. All results are shown in Table 21 .

1188 Dependency to other kinematic variables

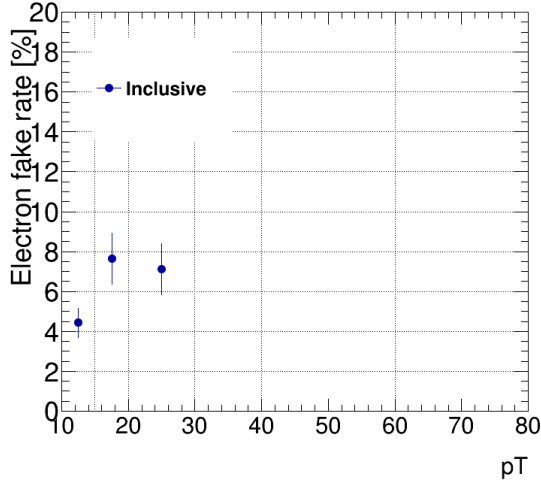
1189 In data we don't have enough statistics to performed a binned measurement in ΔR , number of jets in the
 1190 events, $E_{\text{T}}^{\text{miss}}$, η , etc. Therefore, we check the possible dependencies of the lepton fake efficiencies to other
 1191 variables in $V + \text{jets}$ and $t\bar{t}$ MC. The obtained results are shown in Figure 52 for electrons and in Figure 53



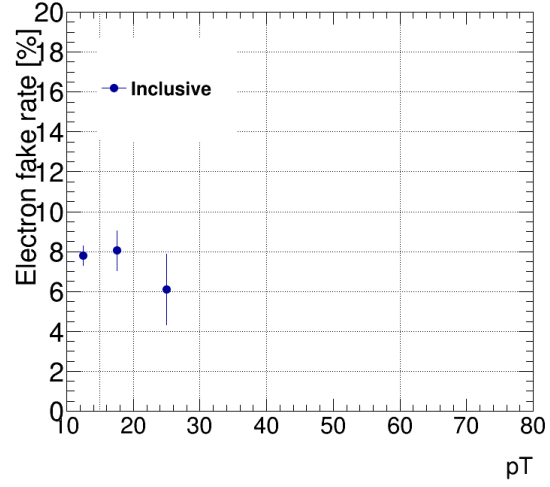
(a) Electrons, all sources



(b) Electrons, hadron decays



(c) Electrons, converted prompt photons



(d) Non-prompt electrons

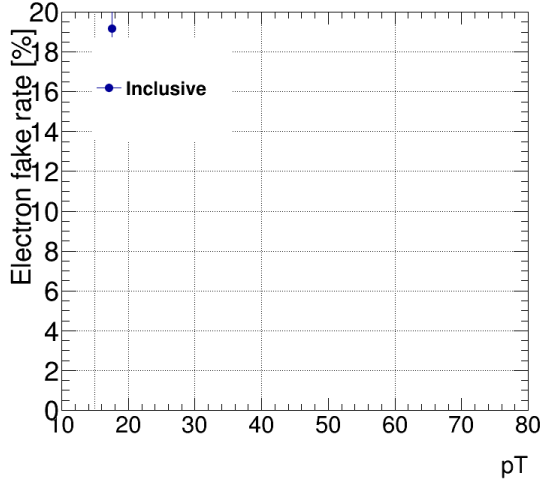
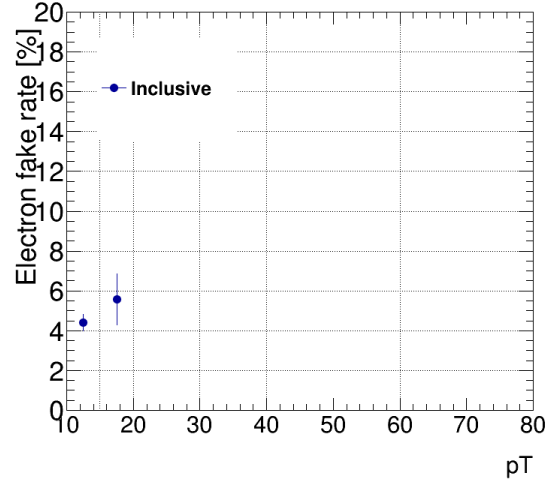
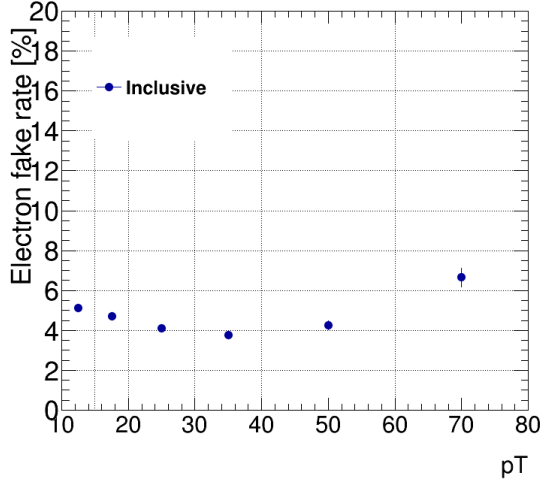
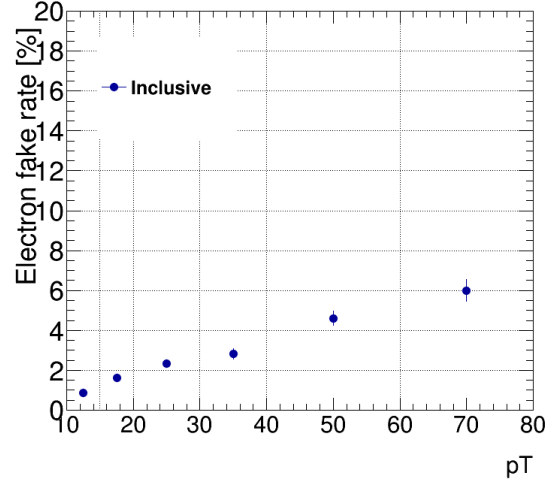
(e) Electrons, b -mesons decays(f) Electrons, c -mesons decays

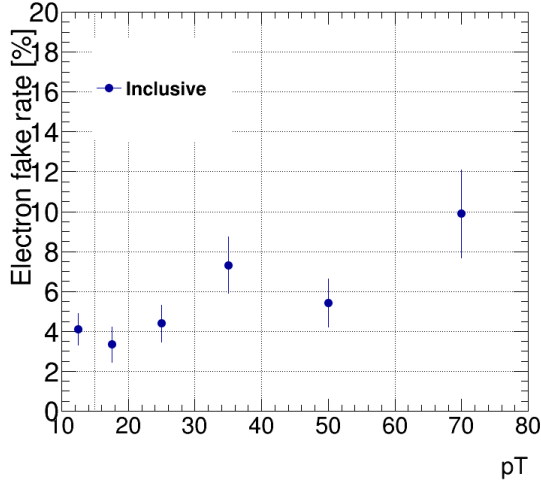
Figure 45: Electron fake rate in $V+jets$ MC sample. Results are shown separately for different sources of fake electrons.
8th February 2016 – 14:10



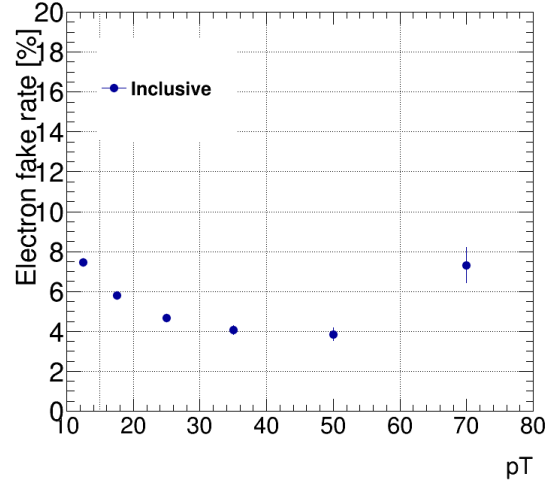
(a) Electrons, all sources



(b) Electrons, hadron decays



(c) Electrons, converted prompt photons



(d) Non-prompt electrons

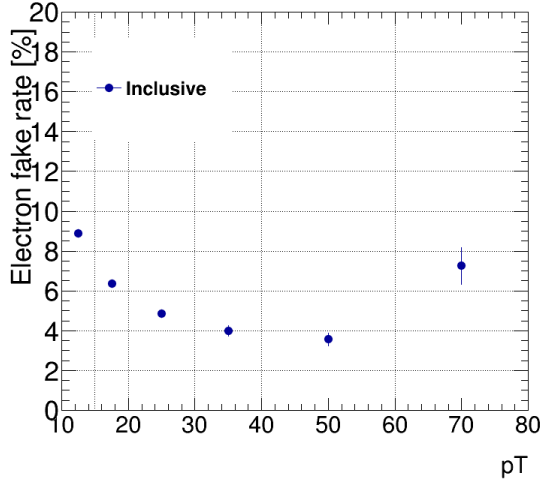
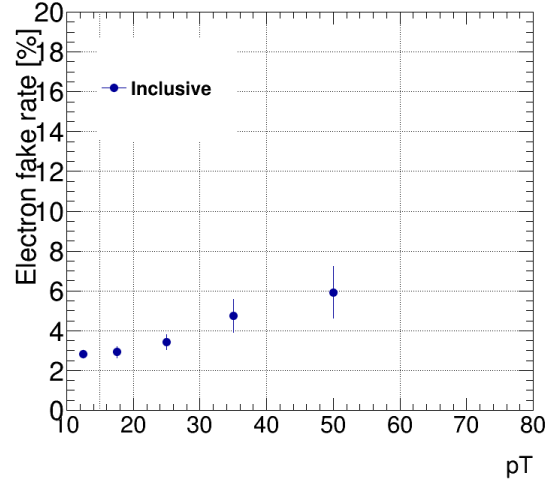
(e) Electrons, b -mesons decays(f) Electrons, c -mesons decays

Figure 46: Electron fake rate in $t\bar{t}$ MC sample. Results are shown separately for different sources of fake electrons.
8th February 2016 – 14:10

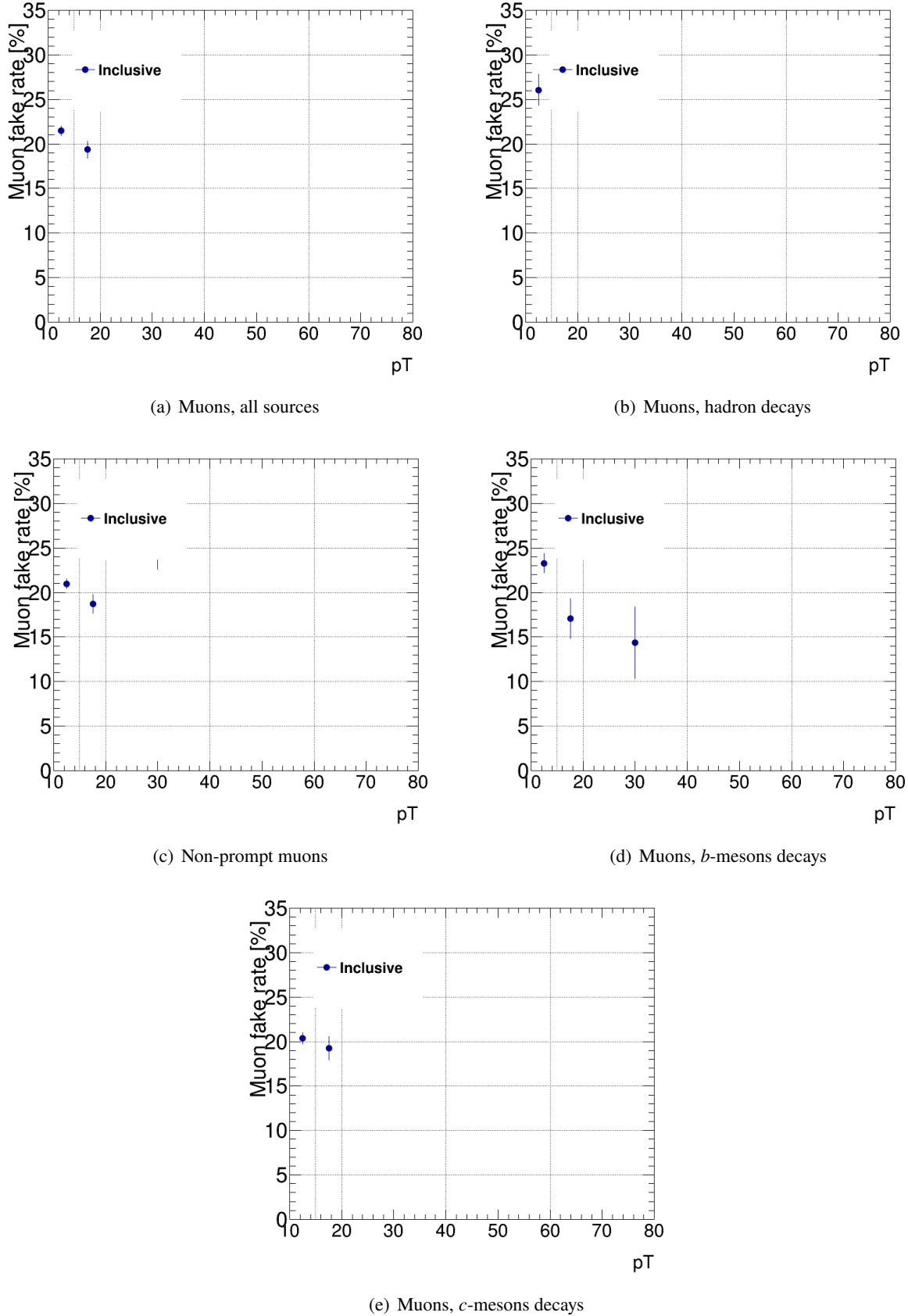


Figure 47: Muon fake rate in $V+jets$ MC sample. Results are shown separately for different sources of fake muons.
8th February 2016 – 14:10

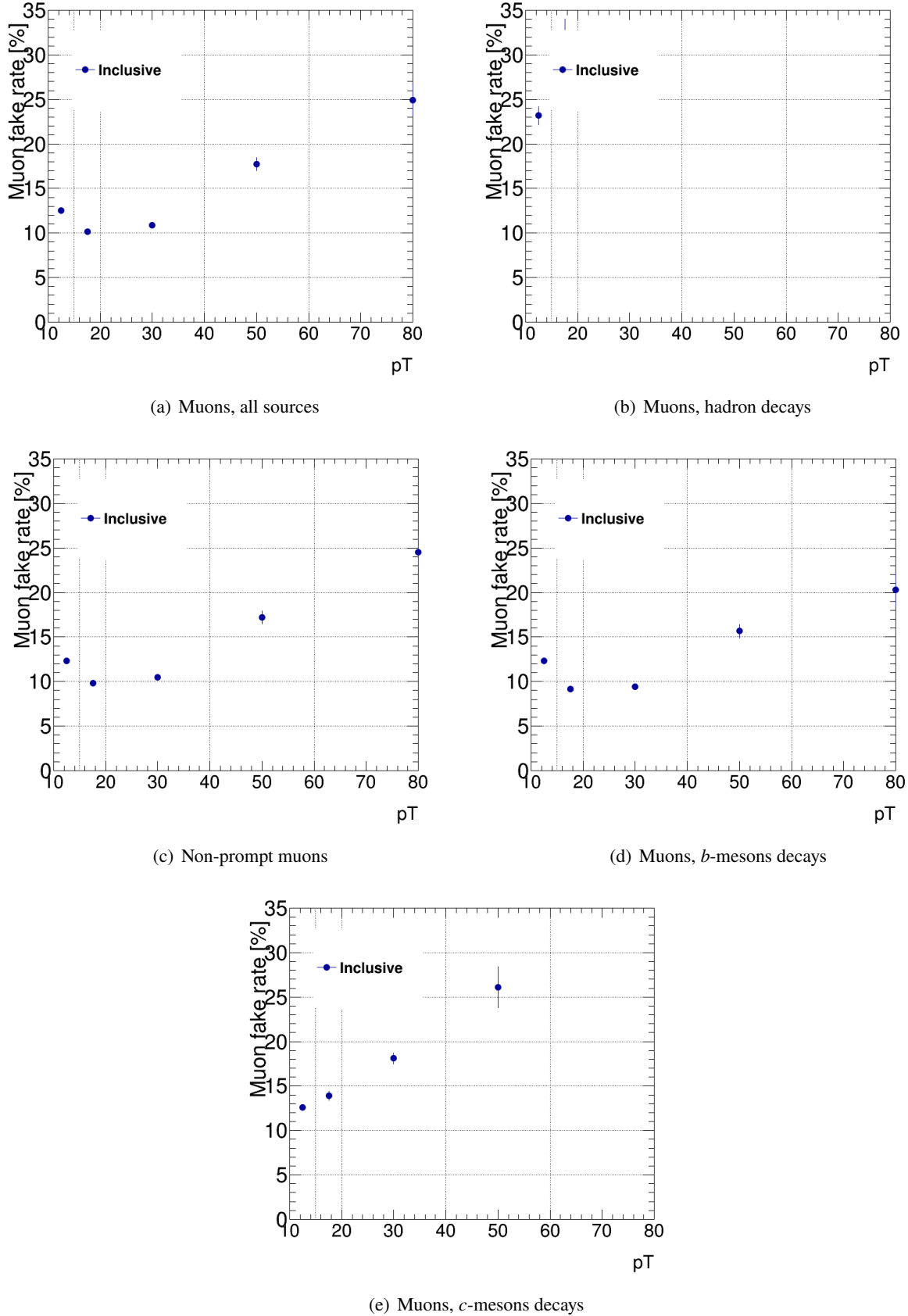
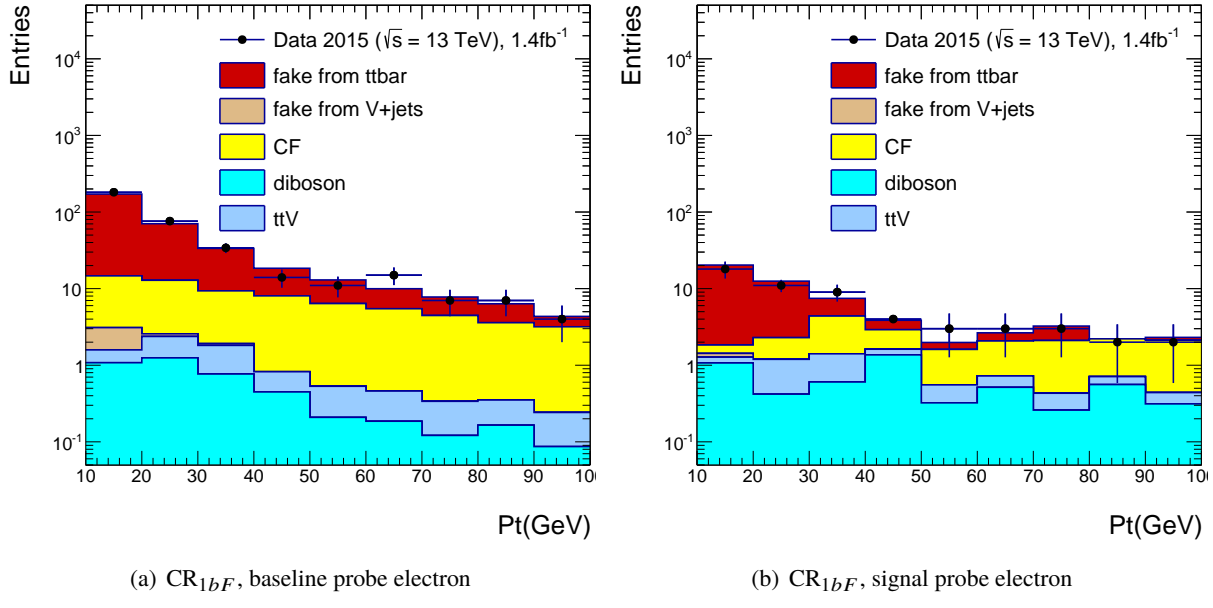
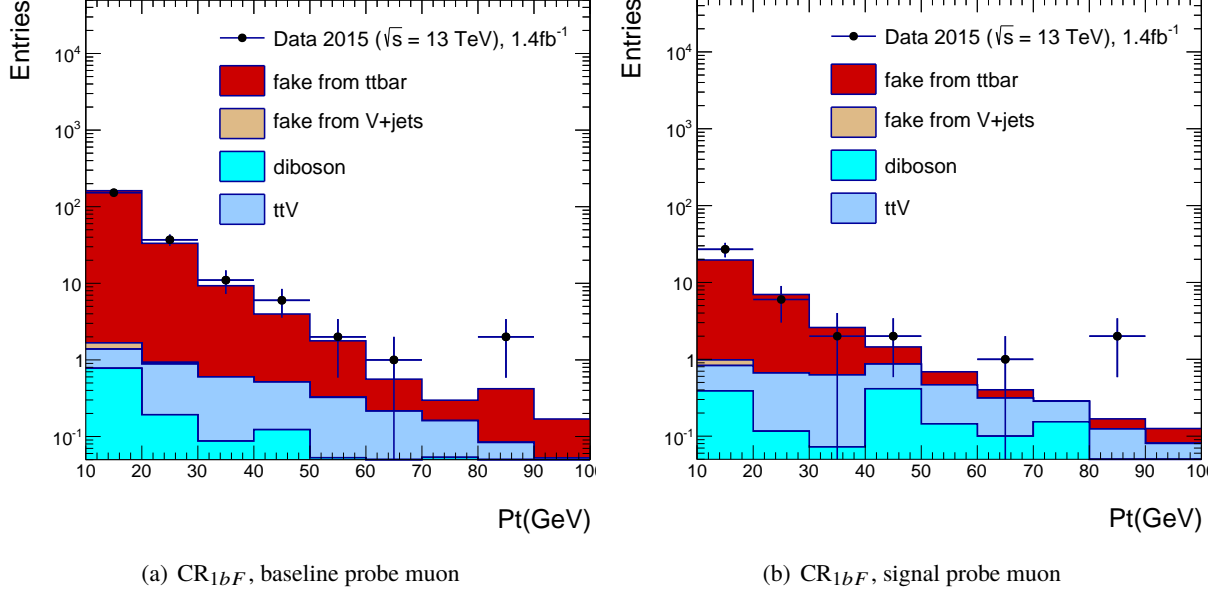


Figure 48: Muon fake rate in $t\bar{t}$ MC sample. Results are shown separately for different sources of fake muons.

Figure 49: Probe electron p_T distribution in data and MC.Figure 50: Probe muon p_T distribution in data and MC.

for muons. The strongest variations are seen for the muon fake rate, that increases steadily with p_T . The other variations are within the uncertainties assigned to the fake rate (see below).

1194 Systematic uncertainties

1195 The measurements of fake leptons efficiencies are associated to large uncertainties which cover the nature
 1196 of the fake leptons and the events that produce them being different between the measurement and signal
 1197 regions. In this analysis several sources of systematic uncertainties are considered :

Samples	$10 < p_T < 20 \text{ GeV}$	$p_T > 20 \text{ GeV}$
Events with a tight probe electron		
Data	33.00	39.00
Multi-boson	0.60 ± 0.14	1.73 ± 0.30
$t\bar{t} + W/Z$	0.42 ± 0.04	3.14 ± 0.10
Other	0.26 ± 0.06	1.30 ± 0.14
Charge flip	$1.26 \pm 0.05 \pm 0.88$	$11.02 \pm 0.31 \pm 1.73$
Events with a loose probe electron		
Data	387.00	186.00
Multi-boson	0.68 ± 0.16	0.99 ± 0.27
$t\bar{t} + W/Z$	0.66 ± 0.05	1.01 ± 0.06
Other	0.50 ± 0.10	0.51 ± 0.09
Charge flip	$12.89 \pm 0.46 \pm 16.16$	$28.07 \pm 0.93 \pm 4.44$
When tag muon fails signal cuts		
Data	30.00	9.00
Multi-boson	0.12 ± 0.05	0.06 ± 0.04
$t\bar{t} + W/Z$	0.02 ± 0.01	0.04 ± 0.01
Other	0.03 ± 0.02	0.01 ± 0.02

Table 17: Number of selected events with a tag muon and a tight/loose probe electron in data and MC, as used for the electron fake rate computation (first two tables), in the presence of at least one b-jet. Only statistical uncertainties are shown, including the uncertainties on the charge flip rates. The third table shows for reference the number of events in which the “tag” muon fails the signal requirements.

Sample	$10 < p_T < 2 \text{ GeV}$	$p_T > 20 \text{ GeV}$
Data	$0.076 \pm 0.014 \pm 0.038$	$0.123 \pm 0.024 \pm 0.065$
MC	0.047 ± 0.001	0.042 ± 0.001

Table 18: Measured electron (absolute) fake rate in data and in MC, including the presence of at least one b-jet. The statistical and the systematic uncertainties are displayed for the data measurements, and only the statistical uncertainty for the MC measurements. The results in MC correspond to a luminosity of 3 fb^{-1} .

- Uncertainty due to the subtraction of prompt leptons processes in the measurement region: it is assigned by varying the MC normalizations by 30%, to cover the uncertainty on the production cross section, MC statistics, etc.
- Fake rate evolution with p_T : while Fig. 53 shows a significant increase of the muon fake rate with p_T , the MC predictions suggest that the yield of high p_T fake leptons should be negligible in the signal regions (see e.g. Fig 42). By lack of time and statistics in data, we do not address this dependency, and observe that the uncertainty assigned below therefore reasonably covers the observed variations for fake leptons up to $p_T = 40 \text{ GeV}$ (Fig. 52 and 53) – and trusting the MC indications that higher p_T fakes are not a concern.
- Lepton fake rate in regions with 2-3 b jets: $O(30\%)$ the relative difference between the fake rate measured with ≥ 1 b-jet and with ≥ 2 -3 b-jets in MC.
- Dependency on other kinematic variables: $O(30\%)$ for both electrons and muons.

Samples	$10 < p_T < 15 \text{ GeV}$	$15 < p_T < 20 \text{ GeV}$	$p_T > 20 \text{ GeV}$
Events with a tight probe muon			
Data	45.00	15.00	18.00
Multi-boson	0.07 ± 0.17	0.31 ± 0.11	1.45 ± 0.23
$t\bar{t} + W/Z$	0.48 ± 0.04	0.52 ± 0.04	2.50 ± 0.09
Other	0.32 ± 0.07	0.24 ± 0.07	0.79 ± 0.12
Events with a loose probe muon			
Data	193.00	92.00	102.00
Multi-boson	0.69 ± 0.19	0.31 ± 0.10	0.70 ± 0.20
$t\bar{t} + W/Z$	0.27 ± 0.03	0.20 ± 0.03	0.42 ± 0.04
Other	0.32 ± 0.07	0.31 ± 0.06	0.30 ± 0.06
When tag muon fails signal cuts			
Data	6.00	2.00	5.00
Multi-boson	0.08 ± 0.06	0.03 ± 0.03	-0.05 ± 0.05
$t\bar{t} + W/Z$	0.01 ± 0.01	0.01 ± 0.01	0.04 ± 0.01
Other	0.01 ± 0.01	0.00 ± 0.00	0.07 ± 0.03

Table 19: Number of selected events with a tag muon and a tight/loose probe muon in data and MC, as used for the muon fake rate computation (first two tables), in the presence of at least one b-jet. Only statistical uncertainties are shown, including the uncertainties on the charge flip rates. The third table shows for reference the number of events in which the “tag” muon fails the signal requirements, but in that case numbers are biased since the tag muon is matched to a trigger requiring an isolated muon.

Sample	$10 < p_T < 15 \text{ GeV}$	$15 < p_T < 20 \text{ GeV}$	$p_T > 20 \text{ GeV}$
Data	$0.187 \pm 0.026 \pm 0.094$	$0.133 \pm 0.034 \pm 0.066$	$0.116 \pm 0.035 \pm 0.059$
MC	0.131 ± 0.002	0.103 ± 0.002	0.113 ± 0.002

Table 20: Measured muon fake rate in data and in MC, including the presence of at least one b-jet. The statistical and the systematic uncertainties are displayed for the data measurements, and only the statistical uncertainty for the MC measurements. The results in MC correspond to a luminosity of 3 fb^{-1} .

Sample	$\geq 1 \text{ b-jet}$	$\geq 2 \text{ b-jets}$	$\geq 3 \text{ b-jets}$
Electron fake rate			
Data	0.079 ± 0.014	0.09 ± 0.034	-
MC	0.051 ± 0.001	0.034 ± 0.001	0.040 ± 0.005
Muon fake rate			
Data	0.150 ± 0.018	0.194 ± 0.067	-
MC	0.121 ± 0.002	0.149 ± 0.003	0.155 ± 0.014

Table 21: Muon fake rate in data and in MC, as a function of number of b-jets in the event. Only the statistical uncertainty is displayed. The results in MC correspond to a luminosity of 3 fb^{-1} .

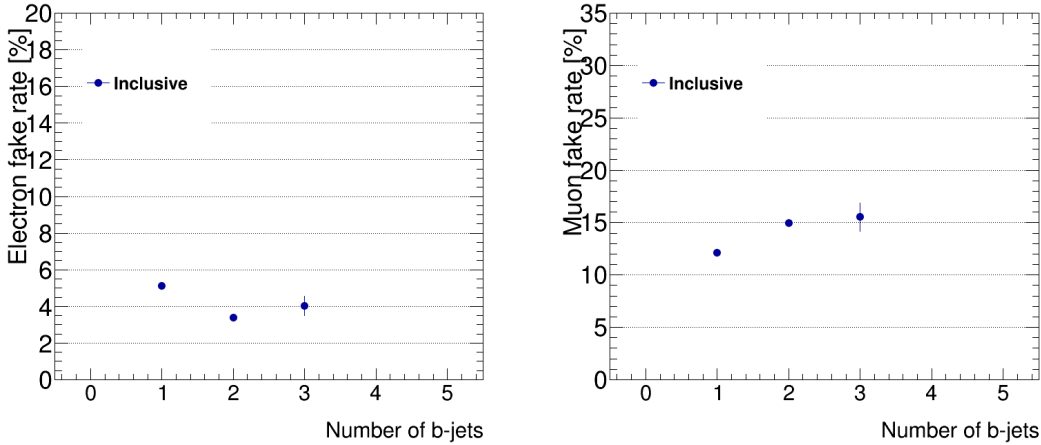


Figure 51: Electron (left) and muon (right) fake rate in Monte-Carlo as a function of number of b -jets in the event. Only the statistical uncertainties are shown. $L=3 \text{ fb}^{-1}$.

- 1210 To cover all these sources of systematic uncertainties, we choose to apply an overall systematic uncertainty
 1211 of 50% on the fake rates treated as uncorrelated between the different bins.
 1212 A Monte-Carlo closure test is performed to validate the measurement of the lepton fake rate and electron
 1213 charge-flip rate, as documented in Appendix 18.

1214 7.5 Neglected backgrounds

1215 Other sources of background such as cosmic rays or cavern background, as well as pile-up events where
 1216 two distinct proton-proton pairs may interact and produce leptons, have been evaluated in the past and
 1217 found to be negligible. Multiple scattering effects are partially included in the simulations but are also
 1218 not expected to contribute enough to require in-depth studies; the largest identified contribution is given
 1219 more attention in the following section.

1220 7.5.1 Double-parton scattering

- 1221 The contribution for $W^\pm + W^\pm$ arising from two different parton interactions in the same proton-proton
 1222 collision, in a double parton scattering process (DPS) could be relevant in the SR0b5j.
 1223 DPS effects are implemented in Sherpa diboson samples used in the analysis in the case of $V + jj$, but
 1224 not for $W^\pm + W^\pm$. To estimate a conservative upper bound on the number of events which might arise
 1225 from DPS, a standard ansatz is adopted: in this, for a collision in which a hard process (X) occurs, the
 1226 probability that an additional (distinguishable) process (Y) occurs is parametrized as:

$$\sigma_{XY}^{DPS} = \sigma_X \sigma_Y / \sigma_{eff} \quad (7)$$

1227 where σ_X is the production cross section of the hard process X and σ_{eff} (effective area parameter)
 1228 parameterizes the double-parton interaction part of the production cross section for the composite system
 1229 (X+Y). A value of σ_{eff} is 10-20 mb is assumed in this study (as obtained from 7 TeV measurements, and

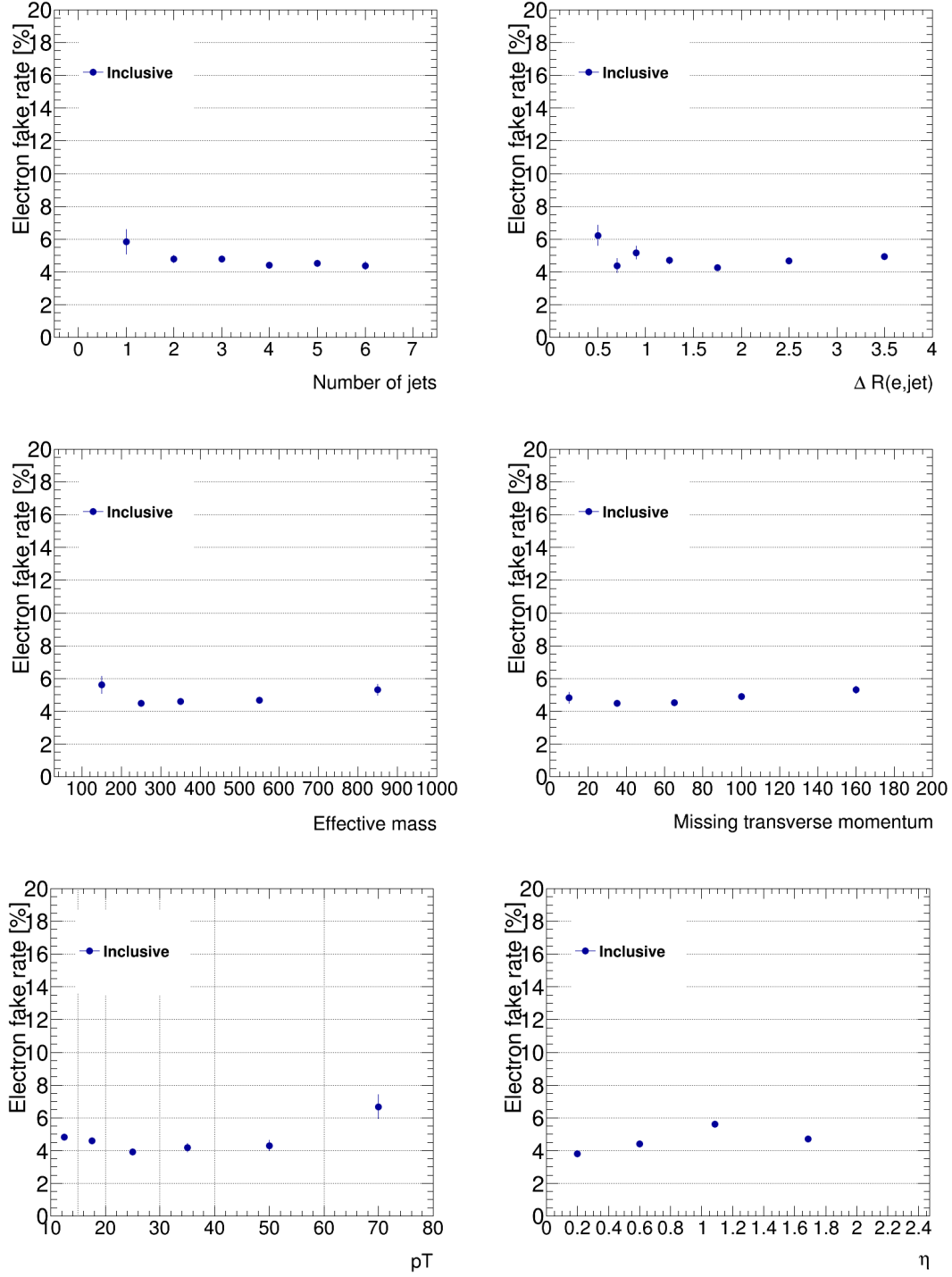


Figure 52: Electron fake rate in Monte-Carlo as a function of number of jets and $\Delta R(l, jet)$ (top), m_{eff} and E_T^{miss} (middle), and p_T and η (bottom) variables. Only the statistical uncertainties are shown. $L=3 \text{ fb}^{-1}$.

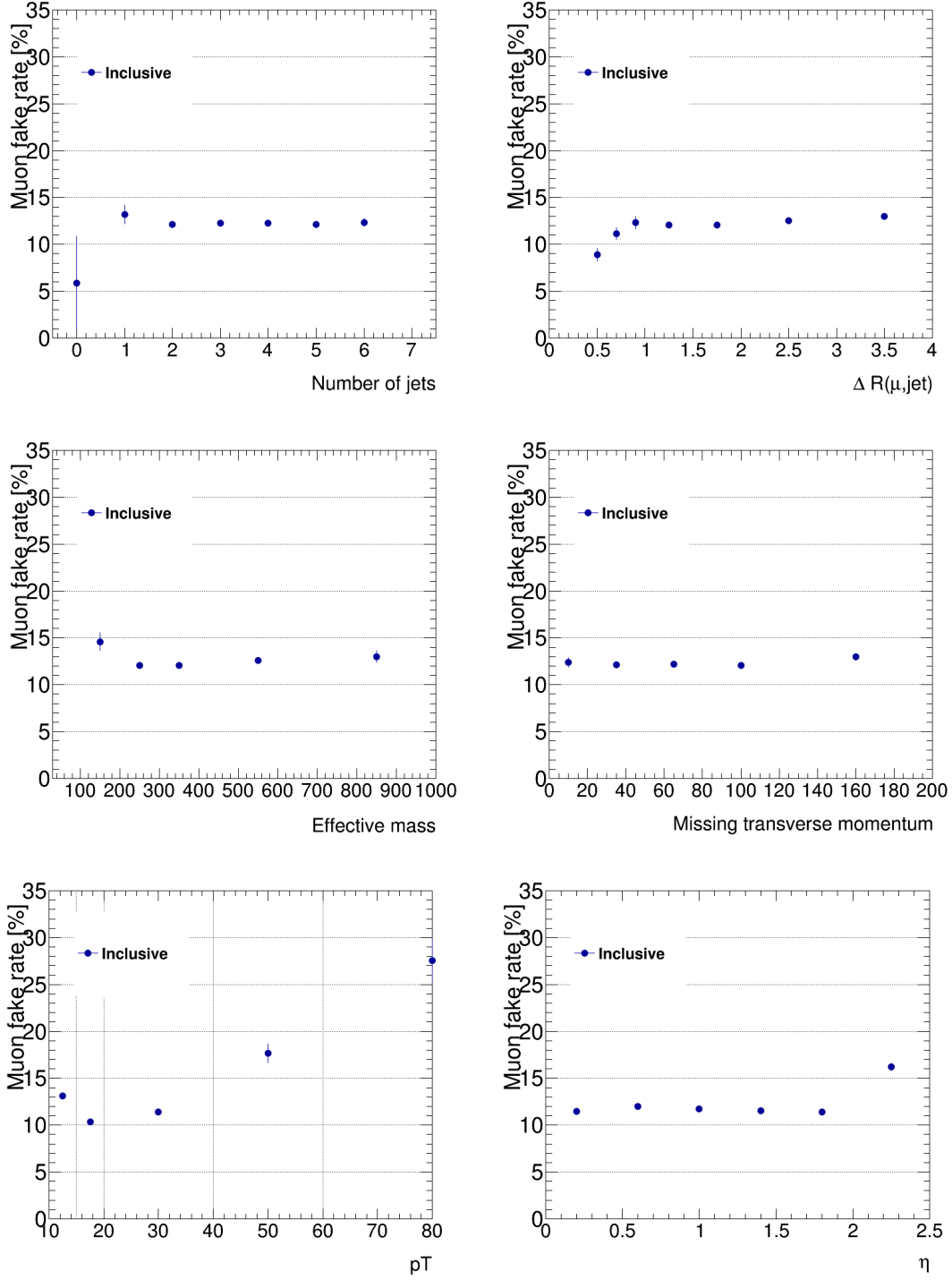


Figure 53: Muon fake rate in Monte-Carlo as a function of number of jets and $\Delta R(l, \text{jet})$ (top), m_{eff} and $E_{\text{T}}^{\text{miss}}$ (middle), and p_T and η (bottom) variables. Only the statistical uncertainties are shown. $L=3 \text{ fb}^{-1}$.

1230 with no observed dependence on \sqrt{s}), and it is independent on the processes involved. For the case of
 1231 $W^\pm + W^\pm$ production:

$$\sigma_{W^\pm W^\pm}^{DPS} = \frac{\sigma_{W^+} \sigma_{W^+} + \sigma_{W^-} \sigma_{W^-}}{\sigma_{eff}} \simeq 0.09 - 0.18 \text{ pb.} \quad (8)$$

1232 To evaluate a potential contribution to the signal region, the value of $\sigma_{W^\pm W^\pm}^{DPS}$ needs to be put in common
 1233 with the jet multiplicity and E_T^{miss} of that process. In absence of a suitable MC sample, and despite the
 1234 many caveats involved, we overlaid pairs of events from the standard W +jet samples at the ntuple level
 1235 (adding all the objects in the event and the E_T^{miss} x and y components, without further corrections to lepton
 1236 isolation or other variables). The jet multiplicity distributions obtained from that procedure are shown in
 1237 Figure 54. Normalizing those distributions to the expected $\sigma_{W^\pm W^\pm}^{DPS}$ cross section, one can roughly estimate
 1238 a contribution after the 5-jet cuts in SR0b5j of approximately 0.001-0.01 events for 4 fb^{-1} , and therefore
 1239 can be safely be neglected within this analysis.

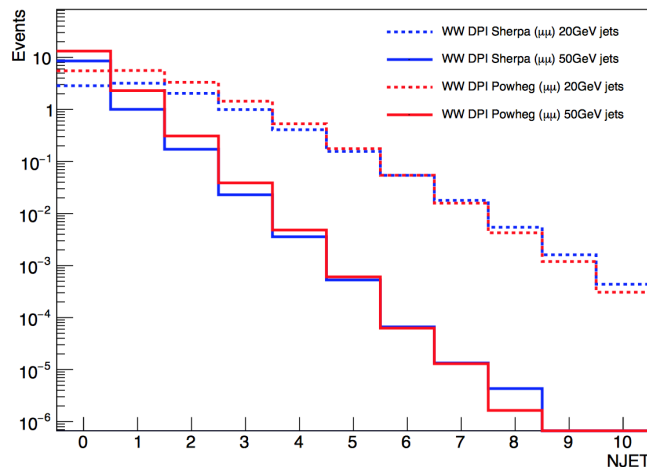


Figure 54: Jet multiplicity distribution for overlaid $W^\pm + W^\pm$ event samples obtained from Sherpa and Powheg to emulate the DPS production.

1240 8 Alternative methods for background estimates

1241 To further cross-check some of our background estimates, we compare their predictions to those obtained
 1242 through alternative methods, that rely on different assumptions. This section describes these alternative
 1243 methods: the first one (section 8.1) evaluates the fake lepton background with the help of the MC
 1244 simulations, while the second one (section 8.3) provides a data-driven estimate of the rate of mis-tagged
 1245 b -jets.

1246 8.1 Backgrounds with fake leptons: the MC template method

1247 We describe in this section a simulation-based method that provides an alternative estimate of the data-
 1248 driven backgrounds in the signal regions. The method is based on different assumptions than the matrix

method described in Section 7.4, and is intended primarily as a cross-check. We provide here a brief description of the MC method and present its background predictions for the signal regions. More details about the method can be found in Appendix 22.

The MC-based method relies on MC simulations to extrapolate background predictions from control regions with low E_T^{miss} , m_{eff} , and jet multiplicity to the signal regions (where E_T^{miss} , m_{eff} , or jet multiplicity are required to be high). The control regions are used to rescale MC samples with “fake” leptons so that they match the observed data. The main assumption of the method is that the MC simulations describe the kinematic distributions correctly (within the limited MC precision) and predict accurately the rate of fake leptons up to a global factor (for each type of fake lepton) independent of the event kinematics and the process type. This assumption makes the method a suitable cross-check of the matrix method, that assumes that the lepton fake rates are the same in control and signal regions regardless of the selection requirements. The other assumption is that the fake rates are uncorrelated in events with multiple fake leptons. Six non-overlapping control regions are defined by presence of b -jets and the flavors of the same sign leptons in the event:

- CR0b: events without b -jets where the leptons are ee , $e\mu$, and $\mu\mu$.
- CR1b: events with at least one b -jet where the leptons are ee , $e\mu$, and $\mu\mu$.

All the selected events contain two same-sign or more signal leptons and $E_T^{\text{miss}} > 25$ GeV. Events satisfying the signal regions requirements are excluded from the control regions. The purpose of the E_T^{miss} requirement is to remove multi-jet events that have two or more “fake” leptons and tend to have low E_T^{miss} .

The next step is to classify events into separate categories depending on the lepton source process. The three main categories are prompt isolated leptons, charge flip electrons, and “fake” leptons which consist of non-prompt leptons coming from hadron decays and hadrons misidentified as leptons. The fakes are further separated by lepton flavor and the jet flavor producing the fake lepton. The last separation is due to b -tagging where a b -tagged sample will be enhanced in b -quark induced fakes. To make the b -tagging requirement orthogonal to the fake rate correction, we separate the leptons that are coming from b -hadron decays, labelled as heavy-flavor (HF), from the rest of the fakes, labelled as light-flavor (LF), and derive a fake rate correction for each category. The classification is done based on the parent particle from the generator event record using the type and origin of the lepton provided by the MCTruthClassifier.

In total we have five categories (charge flip, EL HF, MU HF, EL LF, MU LF) that we derive correction factors for using a simultaneous fit to data in six control regions (CR0b and CR1b for ee , $e\mu$, and $\mu\mu$ channels). The fit uses a likelihood function defined as the product of the Poisson probabilities describing the observed events in the binned distributions from the expected number of events rescaled by the five correction factors which are left free in the fit. These correction factors are applied to the MC predictions in the signal regions to obtain an estimation of the fake and charge flip backgrounds.

The six distributions are chosen for variables that provide the best separation between processes with prompt leptons and processes with fake leptons and charge flip and are shown in Figure 56 and Figure 58.

The minimization of the negative log likelihood using the MINUIT package leads to the correction factors shown in Table 22. The large uncertainties in the correction factors are due to the limited amount of data. The uncertainties in the corrections correspond to how much the parameter needs to be varied for a one standard deviation change in the likelihood function. This uncertainty takes into account the

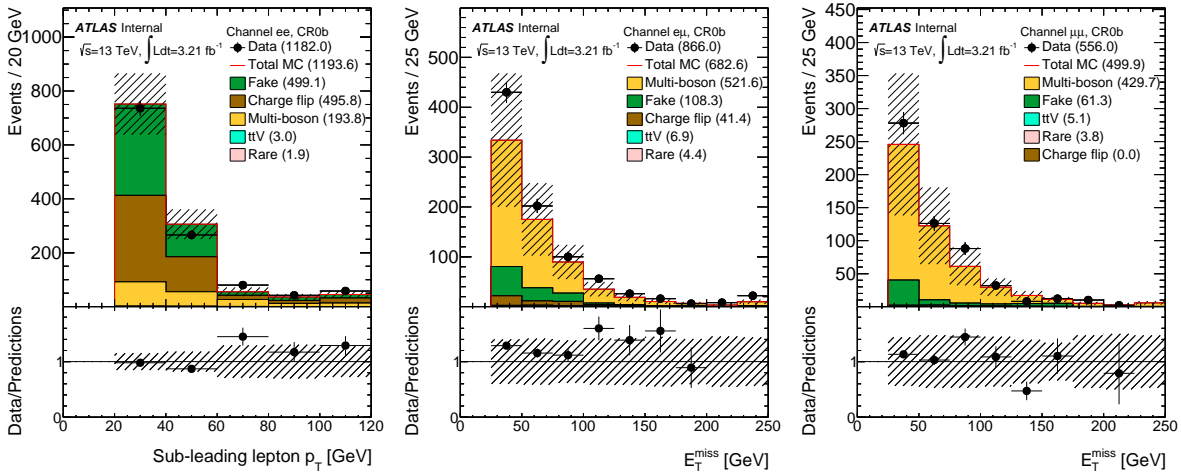


Figure 55: Pre-fit distributions for ee channel (left), for $e\mu$ channel (middle), and for $\mu\mu$ channel (right) from CR0b that were used in the fit to extract the fake rate and charge flip corrections. The hashed band represents the sum of systematic uncertainties on the predictions.

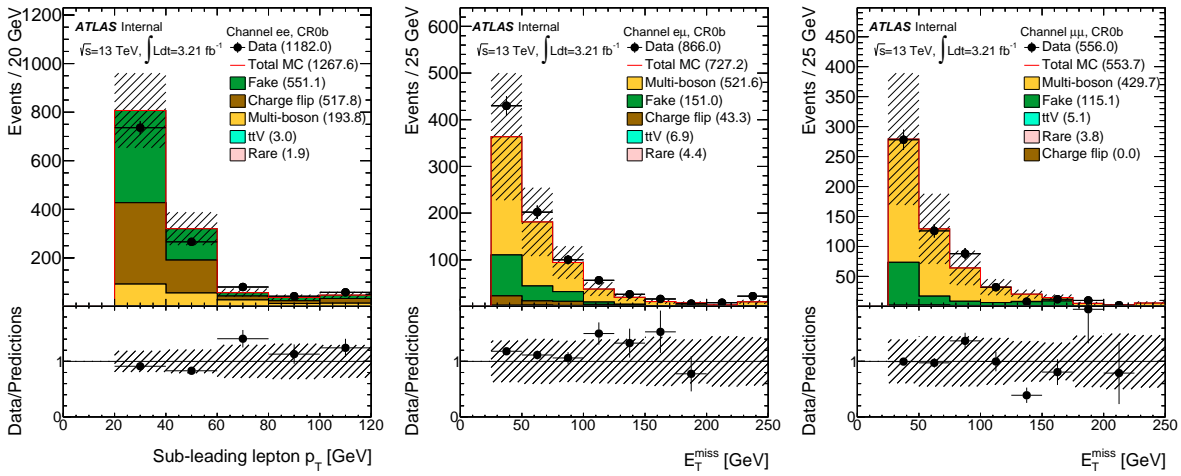


Figure 56: Post-fit distributions for ee channel (left), for $e\mu$ channel (middle), and for $\mu\mu$ channel (right) from CR0b that were used in the fit to extract the fake rate and charge flip corrections. The hashed band represents the sum of systematic uncertainties on the predictions.

1291 limited number of simulated events and is included as a systematic uncertainty on the expected number
1292 of background events.

1293 Distributions other than the six shown in Figures 56-58 were used to validate the accuracy of the simulations
1294 and are shown in Figures 63-64. The electron-electron channel in both control regions provides a good
1295 handle on the charge flip background due to the large number of events classified as charge flip. The
1296 fake electrons from heavy-flavor jets are constrained in the CR1b, while the fake electrons contributions
1297 from light-flavor jets are eliminated after the fit due to the lack of events in this category. Data and
1298 predictions in the control regions after correcting the rates of non-prompt leptons and charge flip agree
1299 within uncertainties.

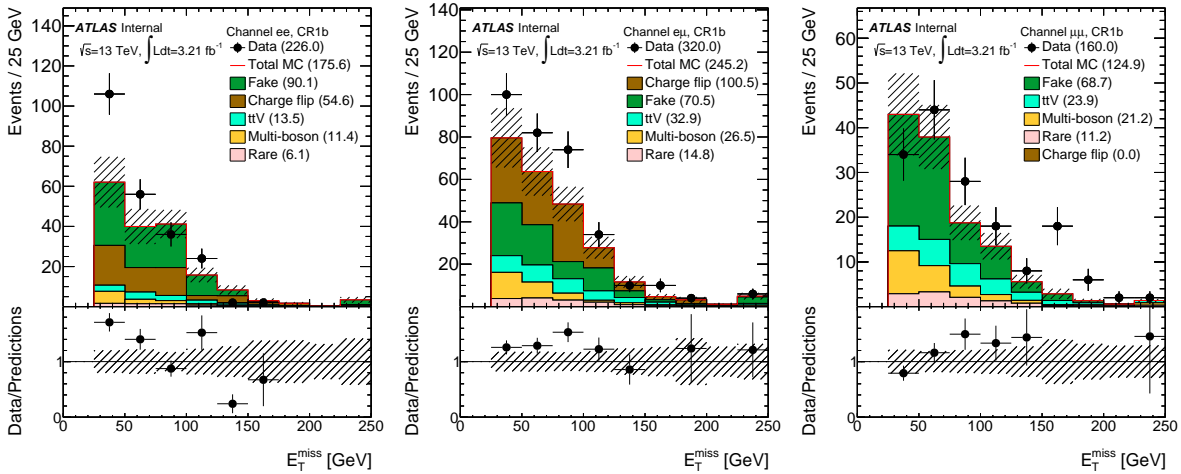


Figure 57: Pre-fit distributions for ee channel (left), for $e\mu$ channel (middle), and for $\mu\mu$ channel (right) from CR1b that were used in the fit to extract the fake rate and charge flip corrections. The hashed band represents the sum of systematic uncertainties on the predictions.

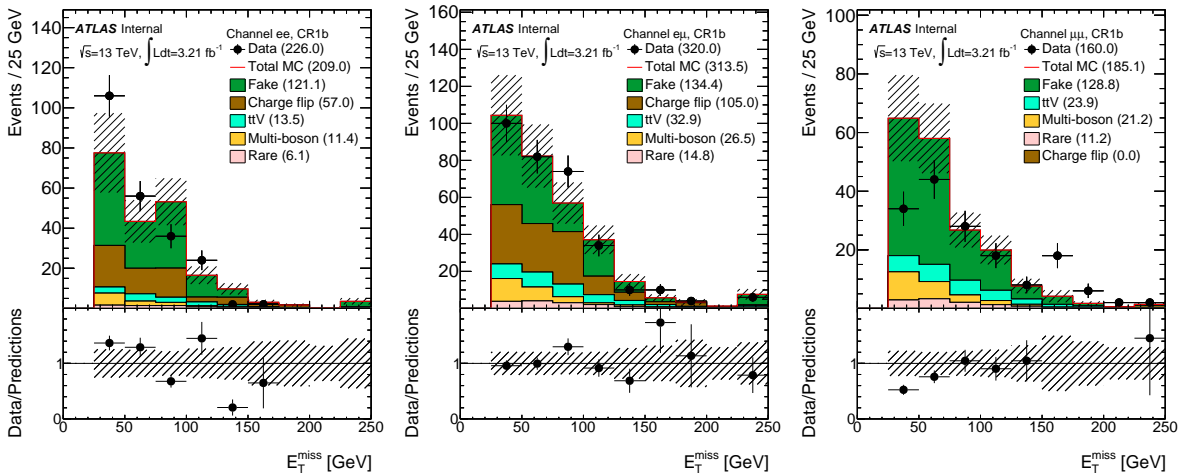


Figure 58: Post-fit distributions for ee channel (left), for $e\mu$ channel (middle), and for $\mu\mu$ channel (right) from CR1b that were used in the fit to extract the fake rate and charge flip corrections. The hashed band represents the sum of systematic uncertainties on the predictions.

Tables 23 and 24 show the expected number of events in the validation and signal regions using the MC template method and compares it to the expectation from the nominal data-driven method to estimate the fakes and charge flip composition. The two methods are consistent within uncertainties.

The main contributions to non-prompt leptons and charge flip events are from the high cross section processes: $t\bar{t}$, $Z+jets$, and $W+jets$. For our signal regions, the main contributor to fakes is $t\bar{t}$. The parton showering of all these processes is done with Pythia in order to be consistent. The systematic uncertainty in the method is evaluated by choosing a different generator, Sherpa. The difference in the expected number of background events due to the choice of parton shower used is taken into account in the systematic uncertainty shown in Tables 23-24.

Table 22: The fake-rate and charge flip corrections obtained after minimizing the likelihood function. The uncertainty in the corrections takes into account the limited statistics of simulated events.

Category	Correction	Uncertainty
Charge Flip	1.04	0.21
EL HF	2.26	0.68
EL LF	1.06	0.21
MU HF	1.88	0.22
MU LF	0.00	0.18

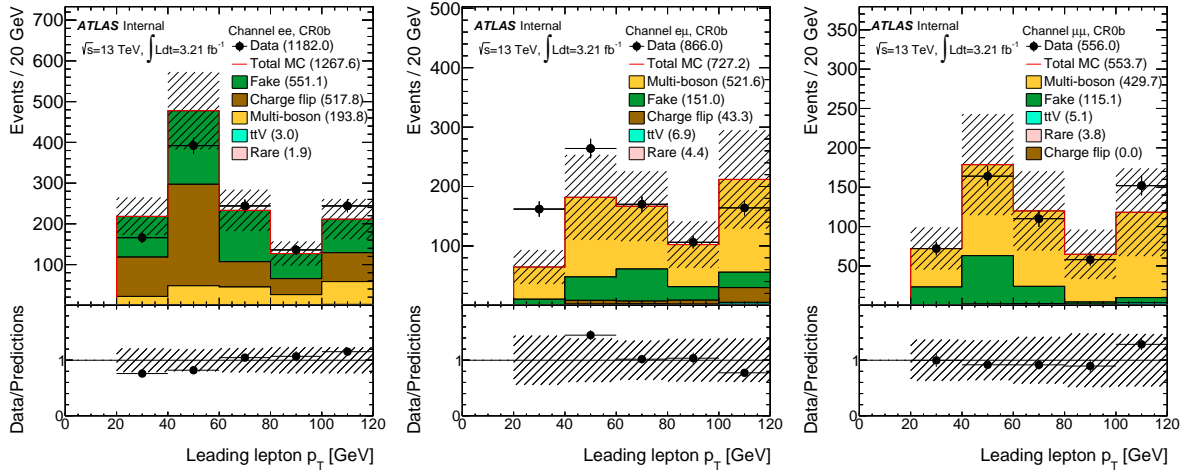


Figure 59: Post-fit distributions of the leading lepton p_T for CR0b for ee channel (left), $e\mu$ channel (middle), and $\mu\mu$ channel (right) used to validate the accuracy of the simulation. Fake-rate and charge flip corrections are applied to these distributions. The hashed band represents the sum of systematic uncertainties on the predictions.

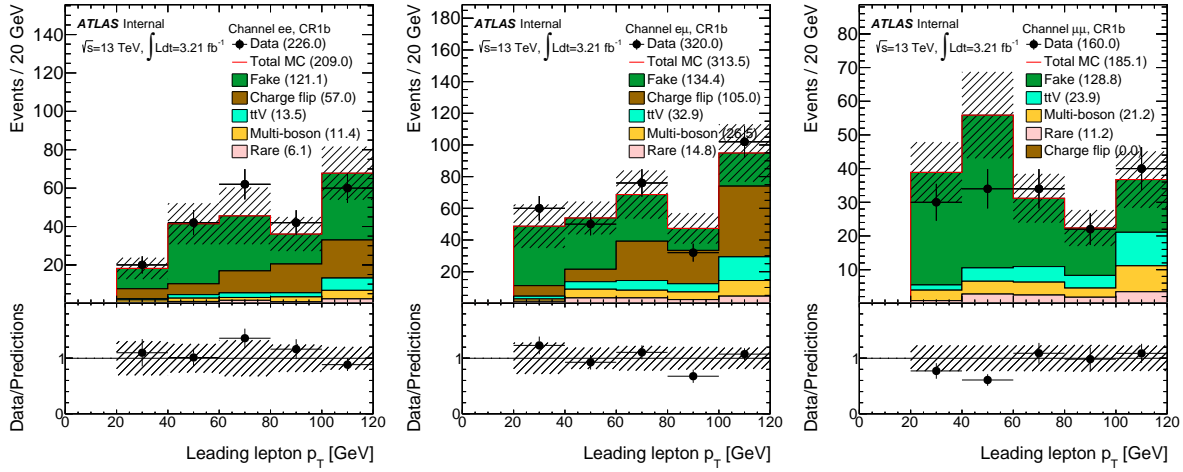


Figure 60: Post-fit distributions of the leading lepton p_T for CR1b for ee channel (left), $e\mu$ channel (middle), and $\mu\mu$ channel (right) used to validate the accuracy of the simulation. Fake-rate and charge flip corrections are applied to these distributions. The hashed band represents the sum of systematic uncertainties on the predictions.

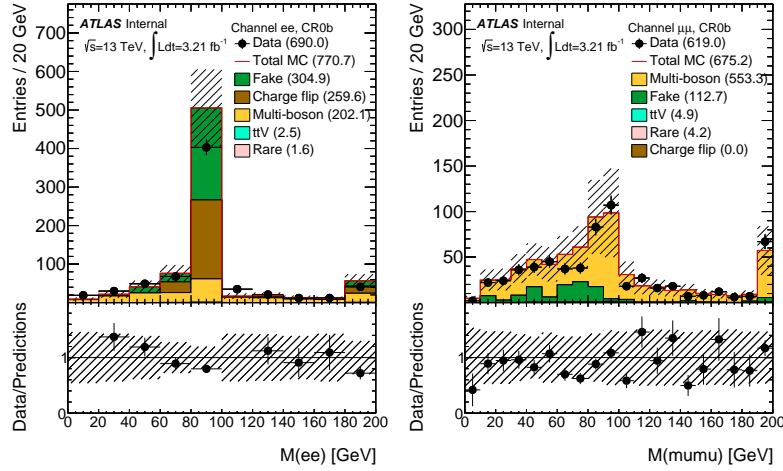


Figure 61: Post-fit distributions of the invariant mass of two leptons for CR0b for ee channel (left) and $\mu\mu$ channel (right) used to validate the accuracy of the simulation. Fake-rate and charge flip corrections are applied to these distributions. The hashed band represents the sum of systematic uncertainties on the predictions.

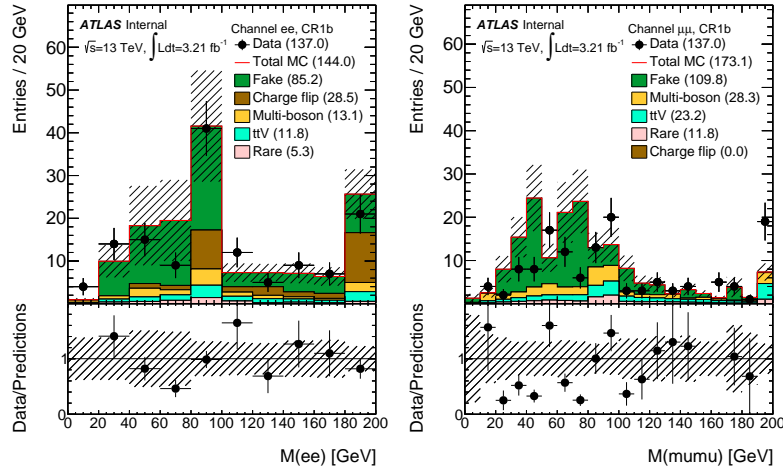


Figure 62: Post-fit distributions of the invariant mass of two leptons for CR1b for ee channel (left) and $\mu\mu$ channel (right) used to validate the accuracy of the simulation. Fake-rate and charge flip corrections are applied to these distributions. The hashed band represents the sum of systematic uncertainties on the predictions.

Table 23: The expected number of events in the validation regions with the fake and charge flip estimations compared between the MC template method and the nominal estimates described in previous sections.

Background	Method	VR-WW	VR-WZ	VR-ttV	VR-ttZ
Fake/non-prompt	Nominal	0.6 ± 0.5	8 ± 6	2.1 ± 1.4	0.6 ± 1.0
	MC based	0.01 ± 0.01	3.4 ± 1.8	1.8 ± 1.0	0.5 ± 0.4
Charge-flip	Nominal	0.26 ± 0.05	–	1.14 ± 0.15	–
	MC based	< 0.08	–	0.27 ± 0.23	–

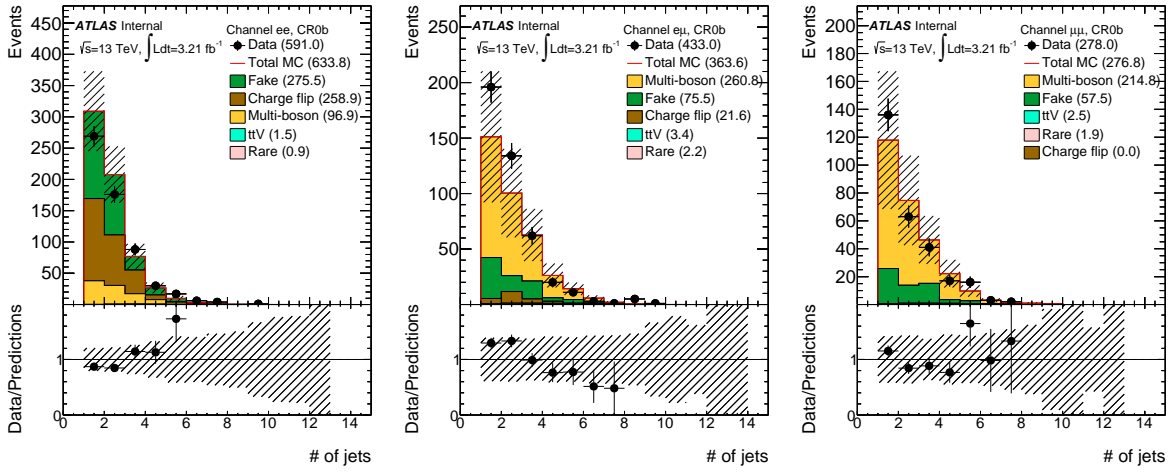


Figure 63: Post-fit distributions of the transverse mass for CR0b for ee channel (left), $e\mu$ channel (middle), and $\mu\mu$ channel (right) used to validate the accuracy of the simulation. Fake-rate and charge flip corrections are applied to these distributions. The hashed band represents the sum of systematic uncertainties on the predictions.

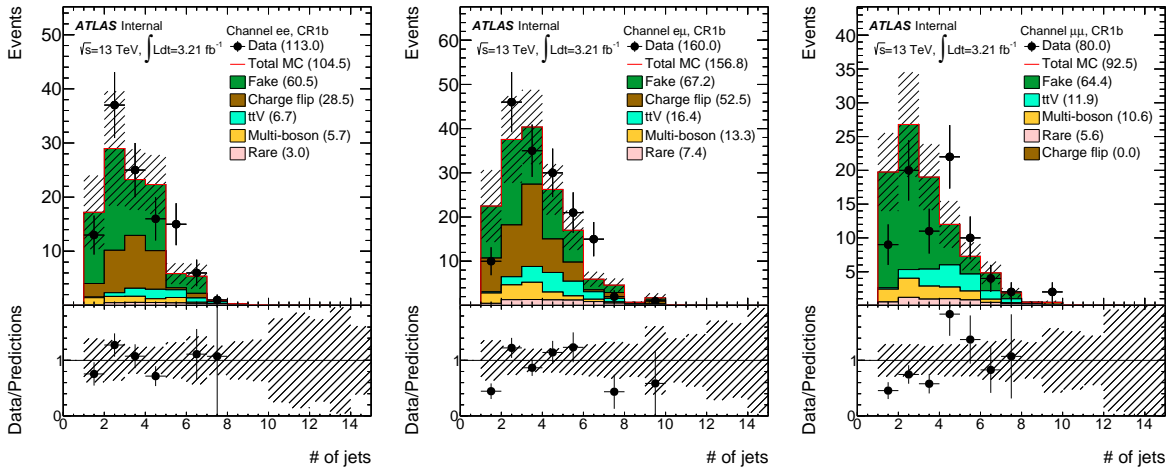


Figure 64: Post-fit distributions of the transverse mass for CR1b for ee channel (left), $e\mu$ channel (middle), and $\mu\mu$ channel (right) used to validate the accuracy of the simulation. Fake-rate and charge flip corrections are applied to these distributions. The hashed band represents the sum of systematic uncertainties on the predictions.

Table 24: The expected number of events in the signal regions with the fake and charge flip estimations compared between the MC template method and the nominal estimates described in previous sections.

Background	Method	SR0b3j	SR0b5j	SR1b	SR3b
Fake/non-prompt leptons	Nominal	< 0.2	0.05 ± 0.18	0.8 ± 0.8	0.13 ± 0.17
	MC based	< 0.15	< 0.15	2.7 ± 1.9	0.02 ± 0.01
Charge-flip	Nominal	–	0.02 ± 0.01	0.60 ± 0.12	0.19 ± 0.06
	MC based	–	< 0.08	1.0 ± 0.8	< 0.08

1309 8.2 Backgrounds with fake leptons and $\geq 3 b$ -jets: the ABCD method

1310 The lepton fake rate used in the matrix method (section 7.4) depends to some extent on the origin of the
 1311 fake lepton. All signal regions are dominated by fake leptons originating from $t\bar{t}$ processes; however the
 1312 region SR3b requires 3 tagged b -jets, which might reduce significantly the fraction of non-prompt leptons
 1313 produced in B meson decay.

1314 We provide here as a cross-check an independent data-driven estimate of the fake lepton background in
 1315 SR3b. For that we select events with ≥ 1 lepton and 2 b -jets, and measure the probability of the production
 1316 and reconstruction of a fake lepton, taken as the ratio between same-sign and one-lepton events. This ratio
 1317 is then assumed to be invariant by the adjunction of additional cuts, and we use it to rescale the number of
 1318 events with ≥ 1 lepton satisfying the SR3b cuts (except lepton requirements) in order to estimate the fake
 1319 lepton background yield in SR3b – so a typical “ABCD” estimate :

$$N_{\text{fakes}}^{\text{SR3b}} = \frac{N_{1 \text{ lepton}}^{\text{SR3b}} \times (N_{\text{SS leptons}}^{\text{SR2b}} - \text{prompt})}{N_{1 \text{ lepton}}^{\text{SR2b}}} \quad (9)$$

1320 where prompt represents the subtracted yields for processes with prompt same-sign leptons or charge flip
 1321 electrons in the sample with same-sign leptons and $\geq 2b$ -jets. To avoid signal contamination or spoiling
 1322 the SR3b blinding policy, the E_T^{miss} requirement used to select events in the $\geq 2b$ -jets sample was loosened
 1323 to $40E_T^{\text{miss}} < 125 \text{ GeV}$.

1324 Events were selected in the one-lepton sample from SUSY7 derivations, using the same framework as for
 1325 the rest of the analysis, and relying on the lowest unprescaled isolated single lepton triggers (e24_lhmed-
 1326 dium_iloose_L1EM20VH and mu24_iloose_L1MU15). Strictly speaking, this is not fully consistent with
 1327 our analysis phase space, as the trigger thresholds are higher than the offline $p_T > 20 \text{ GeV}$ required on the
 1328 leading lepton – and to a lesser extent, the isolation criteria differ. But this affects only a small fraction
 1329 of events, and is furthermore not a problem at first order thanks to the nature of the ABCD method (same
 1330 SS/1L ratio used for 2 b or 3 b selections).

1331 Assessment of possible biases

1332 As defined above, the different regions do not select the same number of objects , which might impact
 1333 e.g. on the effective mass, used in the selection. More important is the correlation between non-prompt
 1334 leptons and tagged b -jets : the presence of a non-prompt lepton arising from a B meson decay, and
 1335 satisfying signal requirements, generally coincides with a failed tagging of the underlying jet (notably
 1336 because of the lepton-jet overlap removal, isolation and impact parameter requirements). Therefore events
 1337 with same-sign leptons (out of which one non-prompt lepton) and $N b$ -jets might be considered as events
 1338 with $N + 1 b$ -jets.

1339 In order to assess the impact of these possible sources of bias on the results, we varied the definitions of
 1340 the background-enriched regions (one lepton or == 2 b -jets) by adding additional (b -) jets requirements
 1341 in some of them, as can be seen in Table 25.

1342 A closure test was also performed on a $t\bar{t}$ MC sample, checking the predicted rate of events with same-sign
 1343 leptons and $\geq 3b$ -jets (without further cuts). A good agreement was found ($\sim 15\%$), well within statistical
 1344 fluctuations (only ~ 20 raw MC events with SS+3 b).

	SS+2b	1L+2b	1L+3b	Fake lepton estimate in SR3b
1	$40 < E_T^{\text{miss}} < 125, == 2b$	—	0.60 ± 0.35 [= 0.30 (stat SS) ± 0.02 (stat 1L) ± 0.17 (bkg)]	
2	$E_T^{\text{miss}} > 40, == 2b$	—	0.37 ± 0.29 [= 0.22 (stat SS) ± 0.01 (stat 1L) ± 0.19 (bkg)]	
3	(1) + $\geq 3j$	—	0.54 ± 0.34 [= 0.29 (stat SS) ± 0.02 (stat 1L) ± 0.17 (bkg)]	
4	(1)	(1) + $\geq 3j$	$\geq 4j$	0.59 ± 0.34 [= 0.30 (stat SS) ± 0.02 (stat 1L) ± 0.17 (bkg)]
5	(1)	(1) + $== 3b$	$\geq 4b$	0.48 ± 0.28 [= 0.24 (stat SS) ± 0.05 (stat 1L) ± 0.14 (bkg)]

Table 25: Estimates of the fake lepton background in the SR3b signal region obtained with the ABCD method for $\mathcal{L} = 3.2 \text{ fb}^{-1}$, with different definitions of the background-enriched regions. The cuts mentioned are added to (or replace) the cuts defining SR3b (E_T^{miss} , m_{eff} , jets). The uncertainties include statistical and systematic (prompt bkg subtraction) sources.

1345 Results

1346

1347 The predicted yields of the fake lepton background in SR3b are detailed in Table 25 for 3.2 fb^{-1} , and
 1348 for the different variations mentioned above. For reference, the number of events observed in data in the
 1349 different categories for the nominal case are respectively 15 (SS+2b), 10578 (1L+2b) and 827 (1L+3b),
 1350 with a prompt+charge flip background of 7.3 events to be subtracted from the first number. An overall
 1351 30% uncertainty is assigned on the subtraction of the prompt same-sign and charge flip backgrounds. One
 1352 can see that the main limitation to the precision of the method is the very low number of events in the
 1353 same-sign leptons + 2 b -jets selection. The variations of the selection have some impact on the results, but
 1354 the large uncertainties prevent from identifying a systematic effect. Taking the largest difference (0.23)
 1355 as an additional systematic uncertainty does not substantially increase the total uncertainty (from 0.35 to
 1356 0.42).

1357 In conclusion, the expected rate of fake leptons in the SR3b signal region for $\mathcal{L} = 3.2 \text{ fb}^{-1}$ is 0.6 ± 0.4 (all
 1358 sources of uncertainties included). It is larger than the one obtained with the matrix method prediction
 1359 (cf Table 34), that is 0.13 ± 0.17 , but the two estimates are consistent within uncertainties. The statistical
 1360 uncertainties of the two methods are comparable in size, as by coincidence the lepton fake rate (10 – 20%)
 1361 is similar to the probability of b -tagging a third jet in $t\bar{t}$ -like events (ratio 1L+3b/1L+2b $\sim 10\%$). As a final
 1362 remark, one could also use the same method to cross-check the background prediction for a selection with
 1363 three leptons and three b -jets – which raised some interest during run-1 [45] – using this time opposite-sign
 1364 dilepton events instead of one-lepton events.

1365 8.3 Backgrounds with fake b -jets

1366 In the signal regions requiring at least three b -jets, an important part of the background originates
 1367 from processes with two real b -jets, and a third jet not originating from a b -quark but satisfying the b -
 1368 tagging requirements. Unlike the case of fake leptons, the b -tagging performance group usually provides
 1369 corrections (and associated uncertainties) to correct the simulation for mismodelling both of real and fake
 1370 b -jets. The fake leptons and charge flip background, being predicted from data, obviously do not need any
 1371 correction.

1372 9 Validation of the background estimates

1373 The data-driven background estimates described previously are based on control regions that are kinematically different than the signal regions, as they contain less stringent requirements on the jet multiplicity,
 1374 E_T^{miss} or m_{eff} . It is therefore very important to validate them in busier and more energetic events. To do so
 1375 we compare the background estimates to the data in regions where several kinematic variables are probed,
 1376 after applying a certain selection :

- 1378 • Loose: requiring at least two same-sign signal leptons in the event.
- 1379 • Intermediate: adding soft cuts i.e. at least one or two signal jets or b jets.
- 1380 • Hard: increase the number of jets in the event.

1381 These distributions are shown in section 9.1.

1382 Beside these “data-to-MC” plots, several validation regions are also designed, and their definition is
 1383 a balance between high purity, large statistics and low signal contamination. Their definition and the
 1384 obtained results are presented in section 9.2.

1385 Finally, section 9.3 presents the results in the auxiliary signal regions.

1386 9.1 Validation of the data-driven estimates

1387 Several distributions are shown for $L = 3.2 \text{ fb}^{-1}$ in combined or separate lepton channels, for a complete
 1388 validation of the background estimates. The statistical uncertainties on the background prediction are
 1389 included in the uncertainty band, as well as the theory uncertainties for the backgrounds with prompt
 1390 SS/3L, and the full systematic uncertainties for data-driven backgrounds. The lepton selection implies
 1391 that the signal definitions presented in Table 9 are satisfied. At least two light jets with $p_T > 25 \text{ GeV}$ and
 1392 $E_T^{\text{miss}} > 60 \text{ GeV}$ are required to reduce the contributions from Z and W plus jets processes which are not
 1393 present in the signal regions.

1394 Distributions in the $ee + e\mu + \mu\mu$ channel

1395 Figure 65 show several kinematic distributions after lepton selection, without any requirement on the
 1396 number of b -jets. It shows the number of (b -) jets with $p_T > 50 \text{ GeV}$ (20 GeV), the transverse mass
 1397 computed with the leading lepton, the H_T computed with all signal leptons and signal jets with $p_T > 20 \text{ GeV}$
 1398 in the event and the leading (subleading) lepton p_T .

1399 Distributions in the ee channel

1400 Several distributions are shown in the ee channel after the lepton selection with at least one b -jet (Figures 67-
 1401 68) and with a b -jet veto (Figures 70-71). Additional cuts on the number of jets are added for some
 1402 distributions to vary the fake lepton composition, and be closer to the signal regions.

1403 For the selections enriched in b -jets, the effective mass distribution is shown in Figure 66 and the missing
 1404 transverse energy distribution in Figure 67. The distributions of the number of (b -) jets with $p_T > 25 \text{ GeV}$,
 1405 the transverse mass computed with the leading lepton, the selected leptons p_T and the leading (subleading)
 1406 lepton p_T are illustrated in Figure 68. Same distributions (following the same order) are shown also for
 1407 the case with a b -jet veto.

1408 Distributions in the $e\mu$ channel

1409 The kinematic distributions in the $e\mu$ channel are shown in Figures 73-77 after the lepton selection with
1410 at least one b -jet and with a b -jet veto. As in the previous case, additional cuts on the number of jets are
1411 added for the m_{eff} and E_T^{miss} distributions. Same plots as in the ee channel (retaining the same order) are
1412 shown.

1413 Distributions in the $\mu\mu$ channel

1414 Figures 79-83 present the distributions of the key kinematic variables in the $\mu\mu$ channel, similarly to the
1415 other channels.

1416 Discussion

1417 One can observe (mostly from the ee channel) that the charge flip estimate agrees well with observed data.
1418 The fake lepton estimate agrees reasonably well with data in event selections requiring at least one b -jet;
1419 however the selections with a b -jet veto show a poor agreement (mostly the $e\mu$ channel), as the estimated
1420 yields of fake leptons clearly overshoot observed data.

1421 For a better validation of the background estimation in events with three leptons, the agreement between
1422 the observed number of data events and SM background is checked in regions with at least three leptons, at
1423 least two light jets with $p_T > 25$ GeV and $E_T^{\text{miss}} > 60$ GeV. Figures 84-85 show the distribution of number
1424 of leptons, and the p_T of the third lepton in a region with at least one b -jet and at least 0 b -jets. Overall,
1425 the agreement is good.

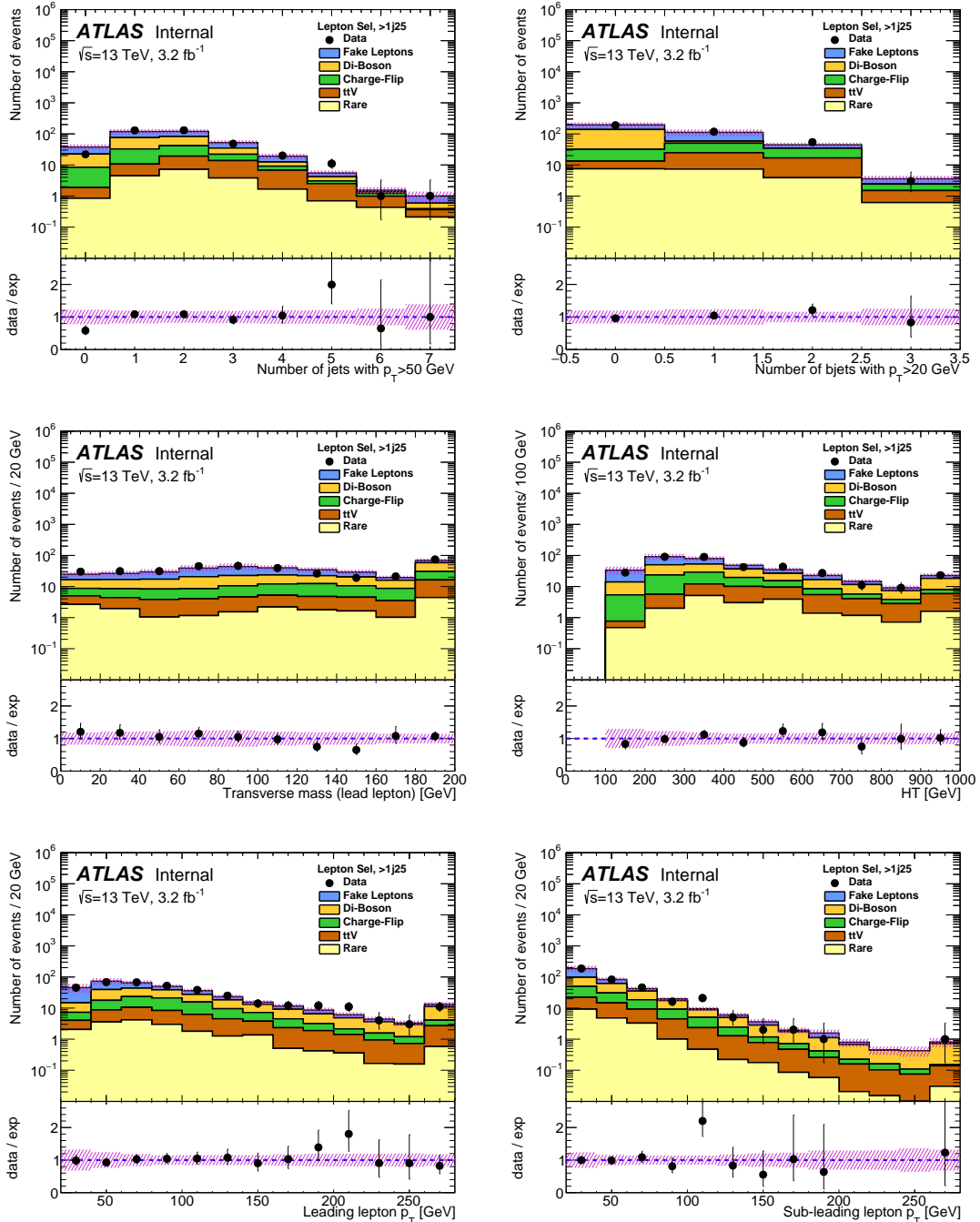


Figure 65: $ee + e\mu + \mu^+\mu^-$ channel, $E_T^{\text{miss}} > 60\text{GeV}$ and $N_{\text{jets}}^{25} \geq 2$: Distributions of jet multiplicity ($p_T > 50$ GeV) (top-left), b -jet multiplicity ($p_T > 20$ GeV) (top-right), m_T (middle-left), H_T (middle-right), leading lepton p_T (bottom-left) and subleading lepton p_T (bottom-right) after lepton selections.

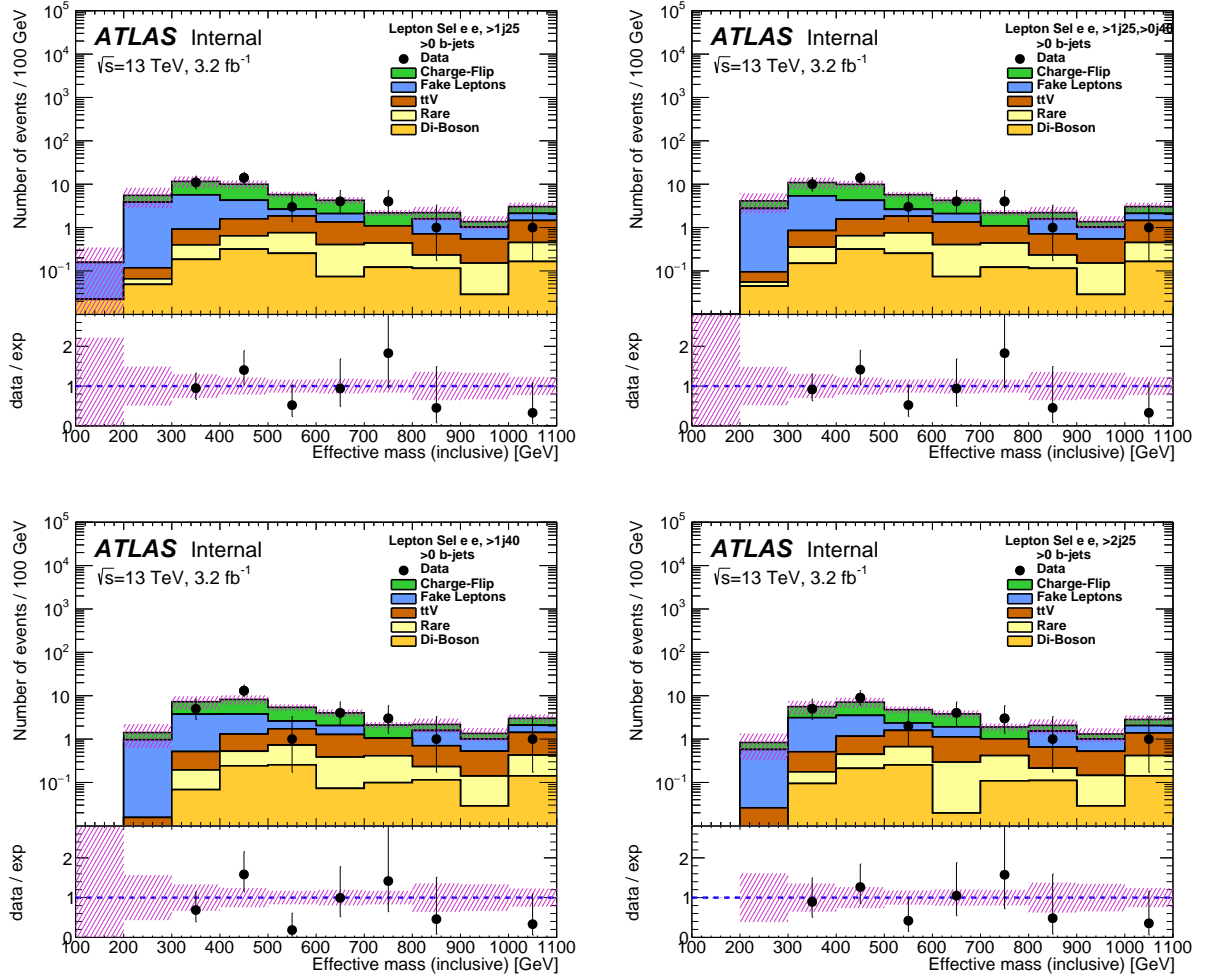


Figure 66: ee channel, $E_T^{\text{miss}} > 60\text{GeV}$ and $N_{\text{jets}}^{25} \geq 2$: Effective mass distribution after lepton selections with at least one b -jet ($p_T > 20$ GeV) and with at least 0, 1, 2 and 3 jets with $p_T > 40$ GeV (from top-left to bottom-right).

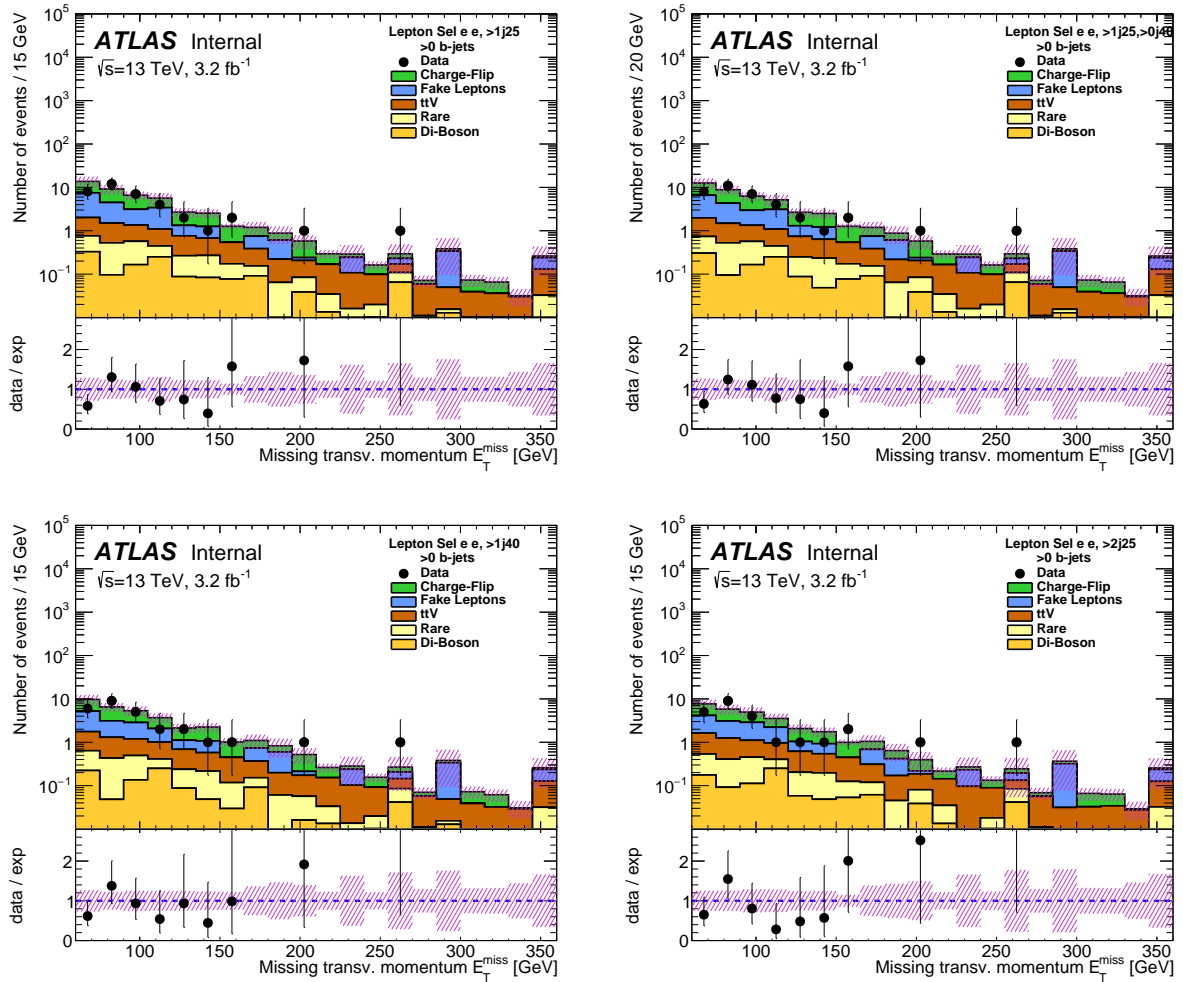


Figure 67: ee channel, $E_T^{\text{miss}} > 60\text{GeV}$ and $N_{\text{jets}}^{25} \geq 2$: Missing transverse energy distribution after lepton selections with at least one b -jet ($p_T > 20$ GeV) and with at least 0, 1, 2 and 3 jets with $p_T > 40$ GeV (from top-left to bottom-right).

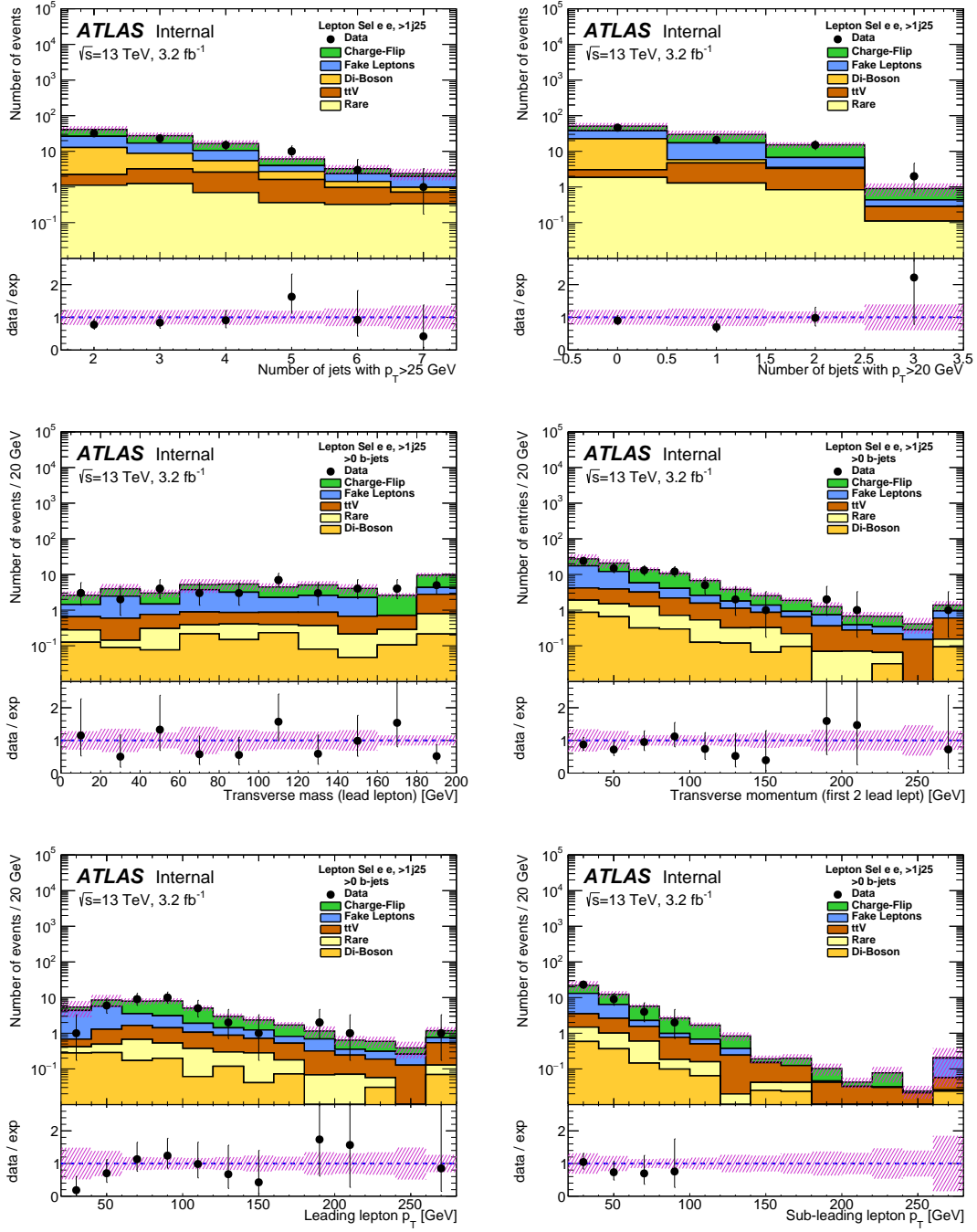


Figure 68: ee channel, $E_T^{\text{miss}} > 60 \text{ GeV}$ and $N_{\text{jets}}^{25} \geq 2$: Distributions of jet multiplicity ($p_T > 25 \text{ GeV}$) (top-left) and b -jet multiplicity ($p_T > 20 \text{ GeV}$) (top-right) after lepton selection, and of m_T (middle-left), selected leptons p_T (middle-right), leading lepton p_T (bottom-left) and subleading lepton p_T (bottom-right) after lepton selections with at least one b -jet ($p_T > 20 \text{ GeV}$).

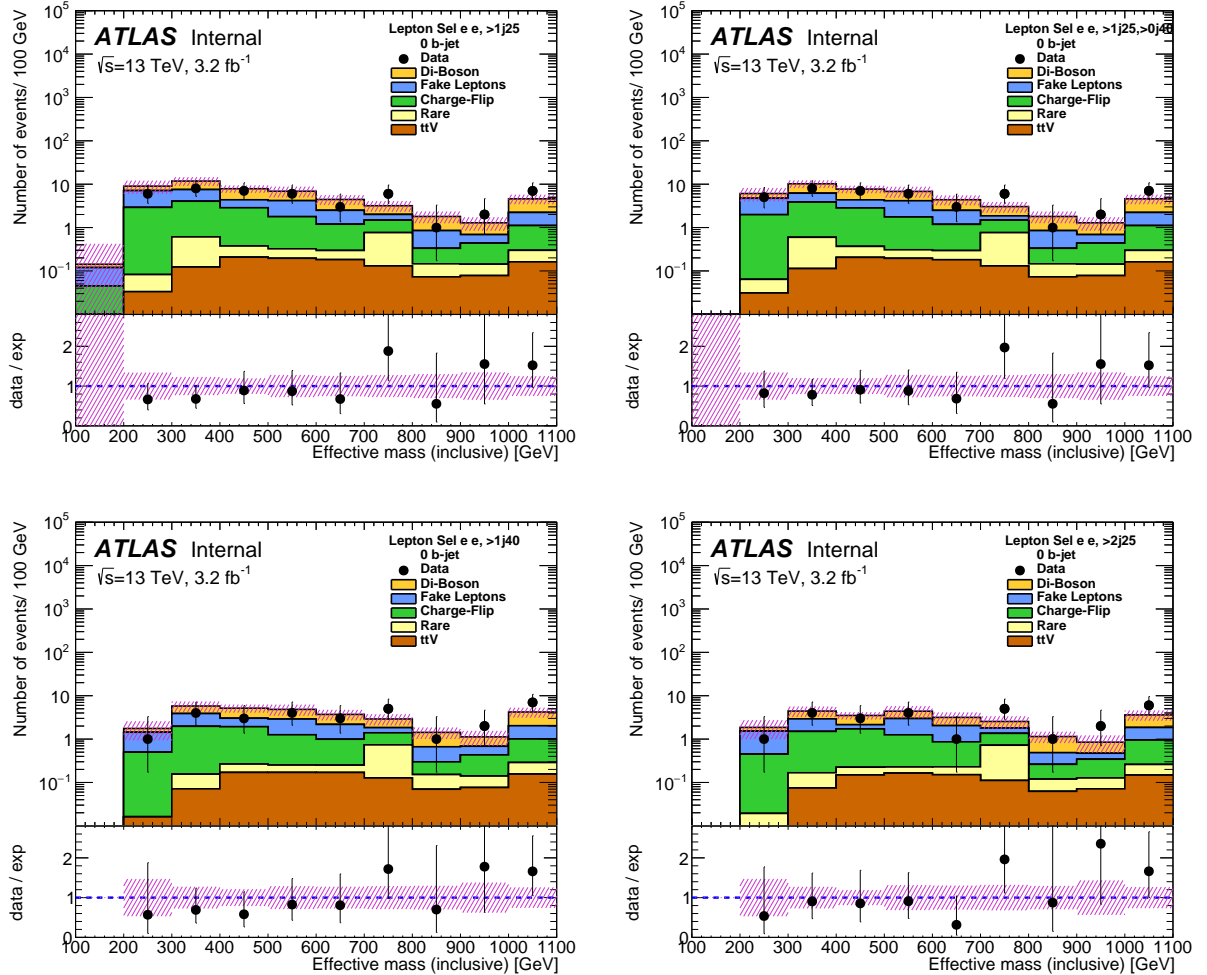


Figure 69: ee channel, $E_T^{\text{miss}} > 60\text{GeV}$ and $N_{\text{jets}}^{25} \geq 2$: Effective mass distribution after lepton selections with a b -jet veto ($p_T > 20$ GeV) and with at least 0, 1, 2 and 3 jets with $p_T > 40$ GeV (from top-left to bottom-right).

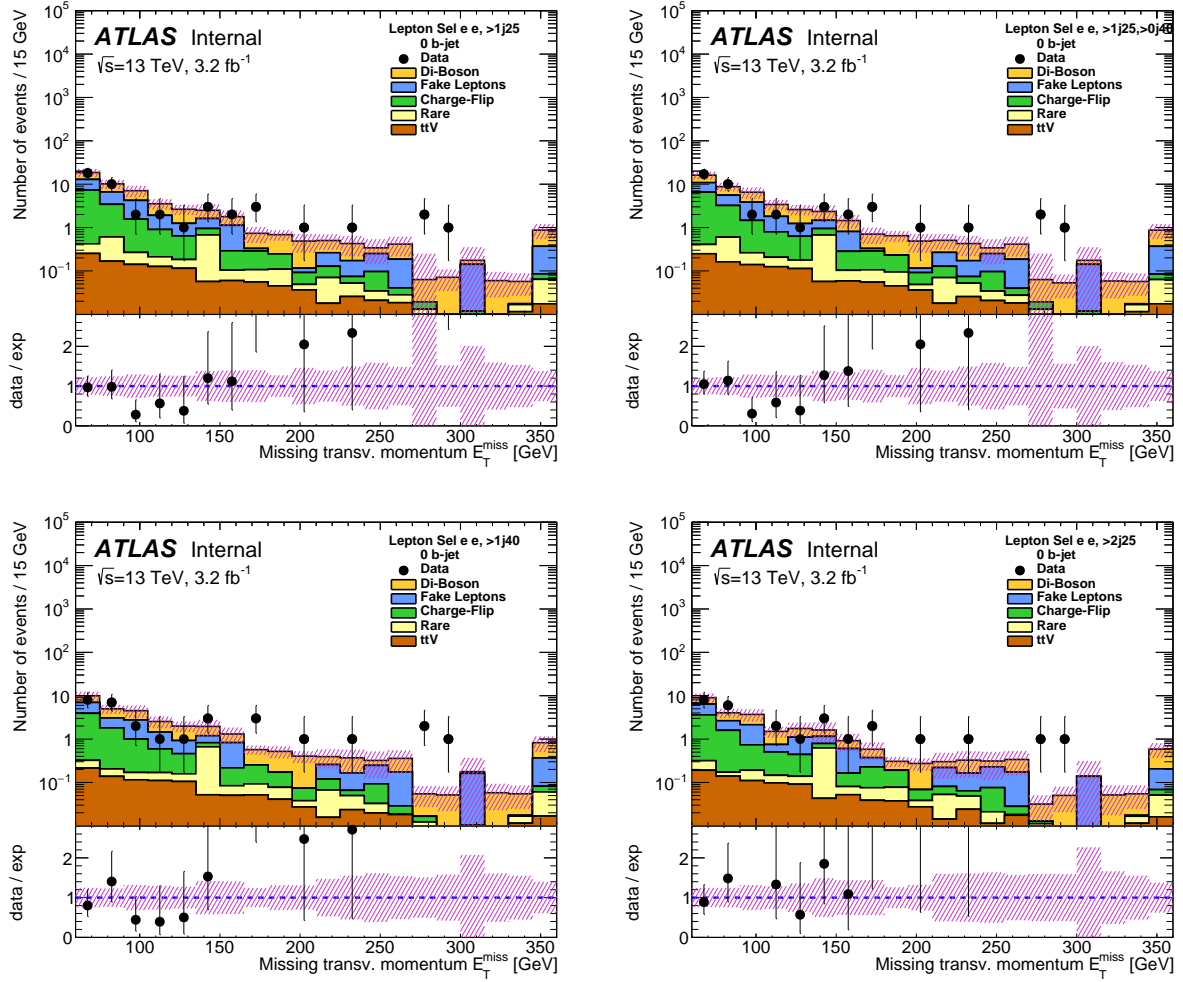


Figure 70: ee channel, $E_T^{\text{miss}} > 60\text{GeV}$ and $N_{\text{jets}}^{25} \geq 2$: Missing transverse energy distribution after lepton selections with a b -jet veto ($p_T > 20\text{ GeV}$) and with at least 0, 1, 2 and 3 jets with $p_T > 40\text{ GeV}$ (from top-left to bottom-right).

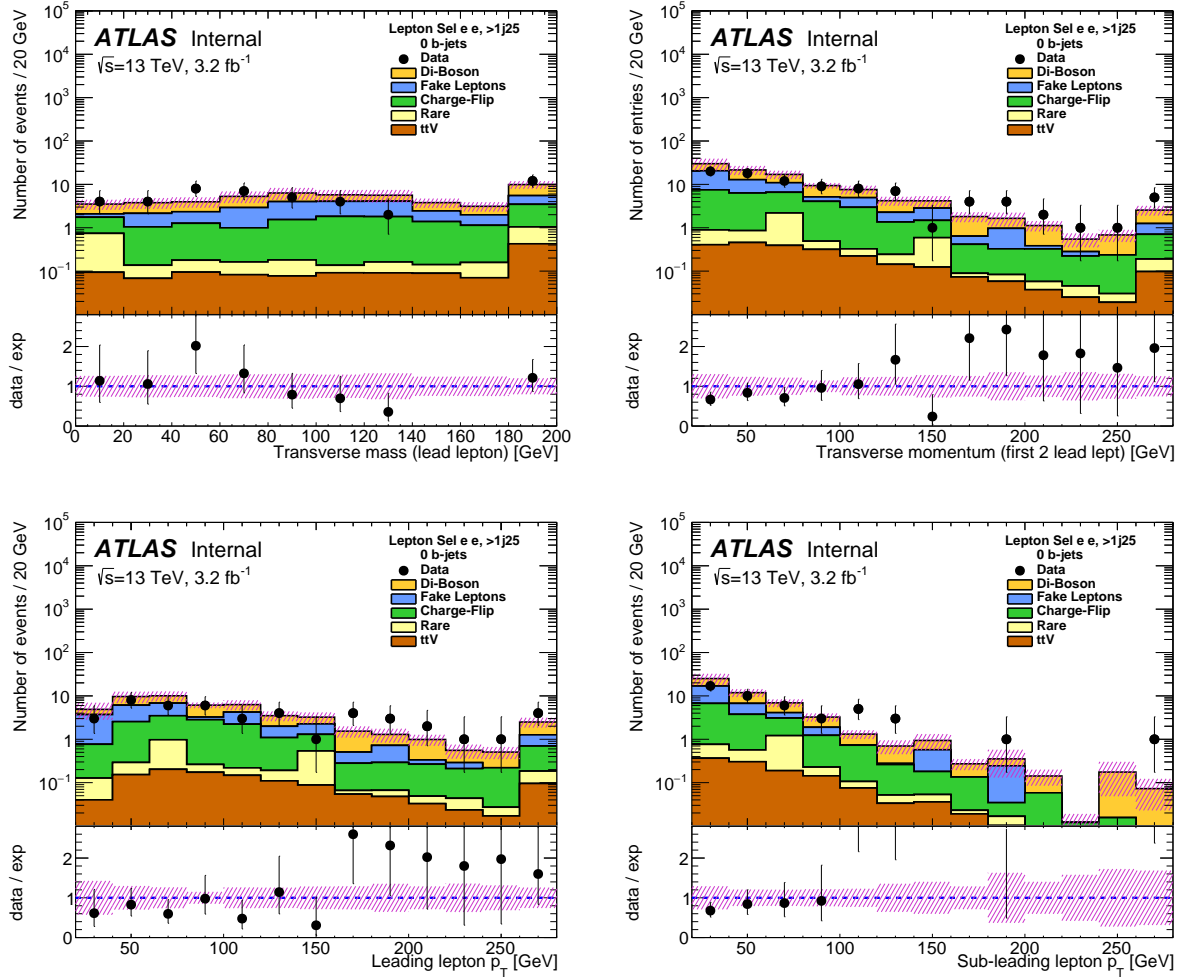


Figure 71: ee channel, $E_T^{\text{miss}} > 60 \text{ GeV}$ and $N_{\text{jets}}^{25} \geq 2$: Distributions of m_T (top-left), selected leptons p_T (top-right), leading lepton p_T (bottom-left) and subleading lepton p_T (bottom-right) after lepton selections with a b -jet veto ($p_T > 20 \text{ GeV}$).

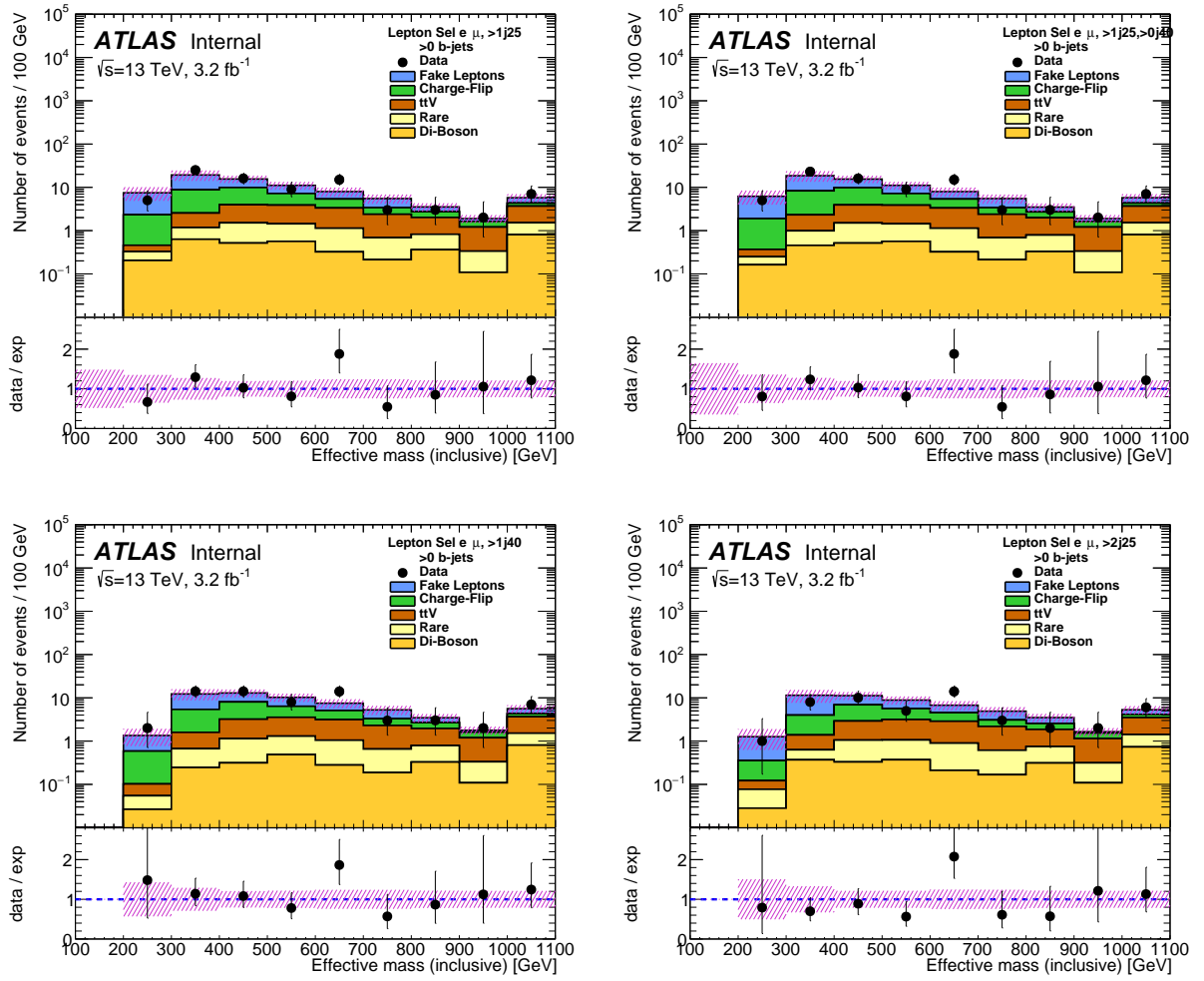


Figure 72: $e\mu$ channel, $E_T^{\text{miss}} > 60 \text{ GeV}$ and $N_{\text{jets}}^{25} \geq 2$: Effective mass distribution after lepton selections with at least one b -jet ($p_T > 20 \text{ GeV}$) and with at least 0, 1, 2 and 3 jets with $p_T > 40 \text{ GeV}$ (from top-left to bottom-right).

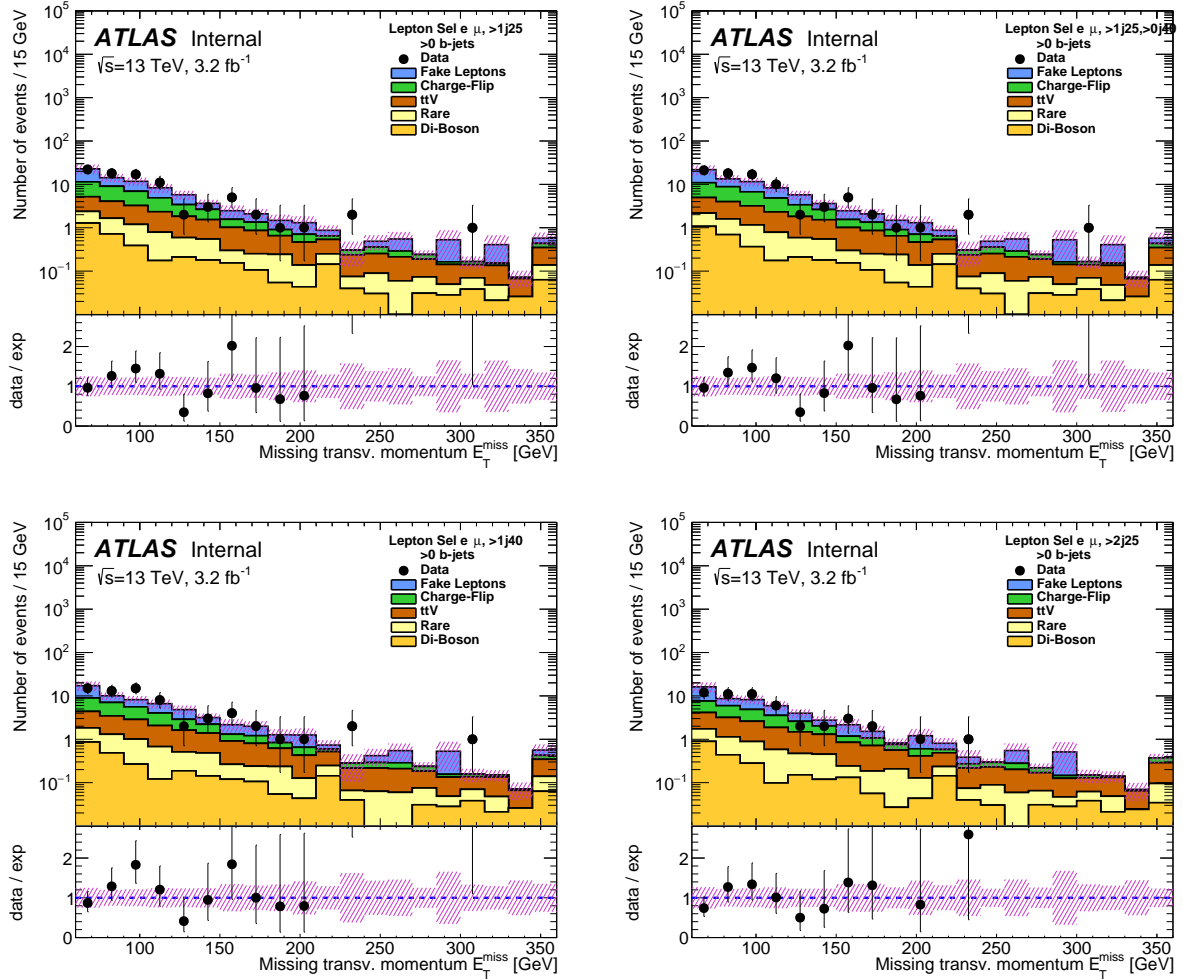


Figure 73: $e\mu$ channel, $E_T^{\text{miss}} > 60\text{GeV}$ and $N_{\text{jets}}^{25} \geq 2$: Missing transverse energy distribution after lepton selections with at least one b -jet ($p_T > 20\text{ GeV}$) and with at least 0, 1, 2 and 3 jets with $p_T > 40\text{ GeV}$ (from top-left to bottom-right).

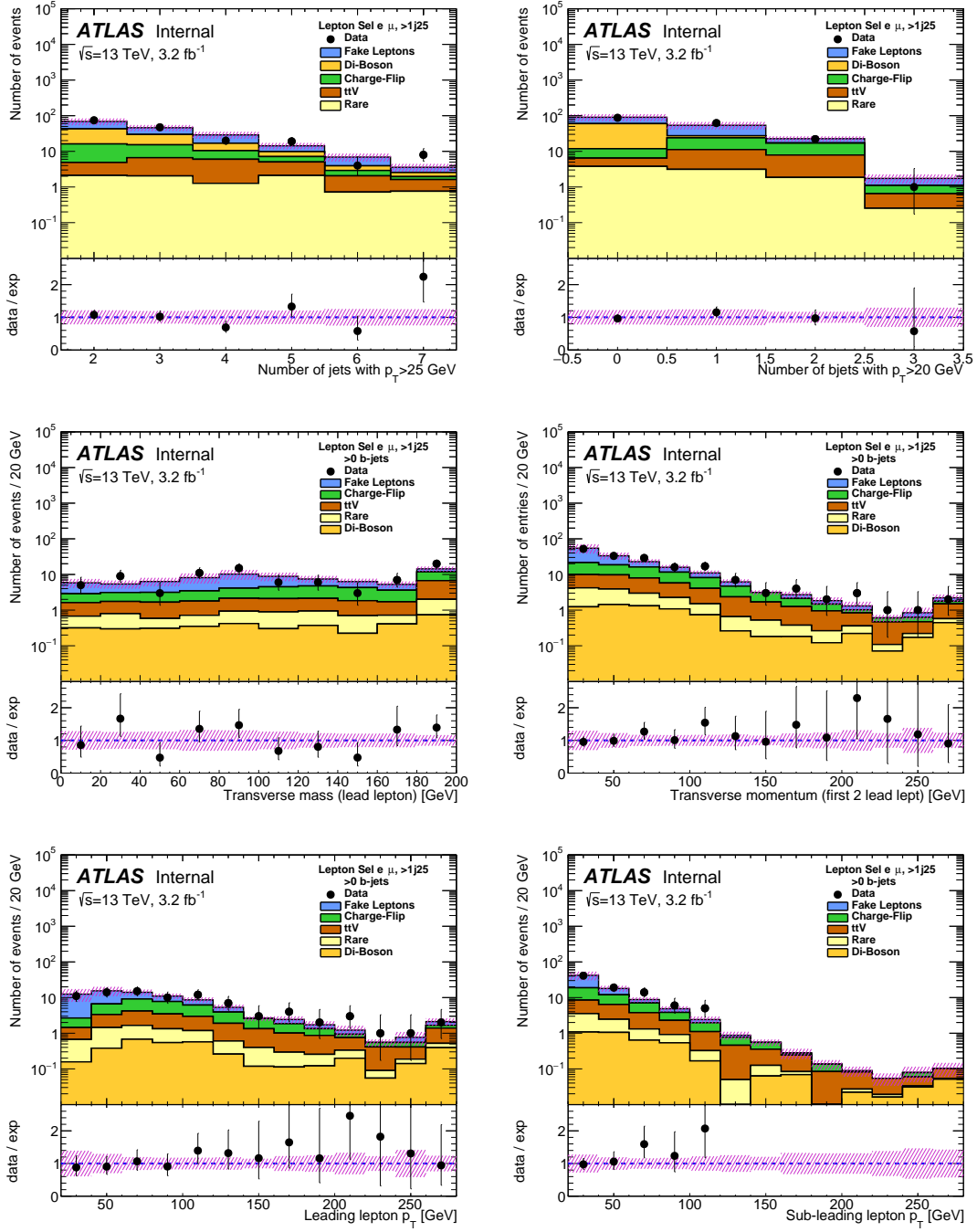


Figure 74: $e\mu$ channel, $E_T^{\text{miss}} > 60\text{GeV}$ and $N_{\text{jets}}^{25} \geq 2$: Distributions of jet multiplicity ($p_T > 25$ GeV) (top-left) and b -jet multiplicity ($p_T > 20$ GeV) (top-right) after lepton selection, and of m_T (middle-left), selected leptons p_T (middle-right), leading lepton p_T (bottom-left) and subleading lepton p_T (bottom-right) after lepton selections with at least one b -jet ($p_T > 20$ GeV).

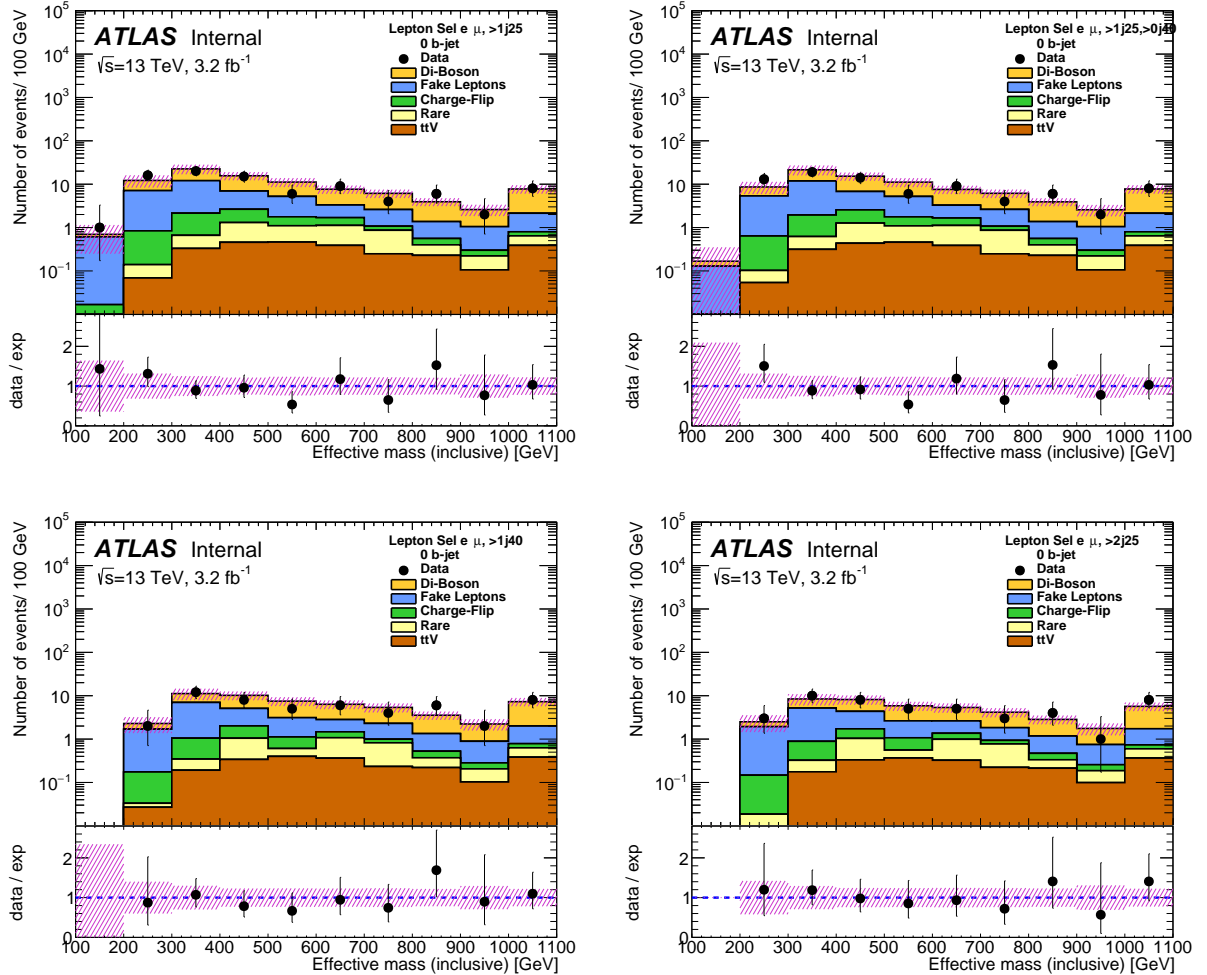


Figure 75: $e\mu$ channel, $E_T^{\text{miss}} > 60\text{GeV}$ and $N_{\text{jets}}^{25} \geq 2$: Effective mass distribution after lepton selections with a b -jet veto ($p_T > 20\text{ GeV}$) and with at least 0, 1, 2 and 3 jets with $p_T > 40\text{ GeV}$ (from top-left to bottom-right).

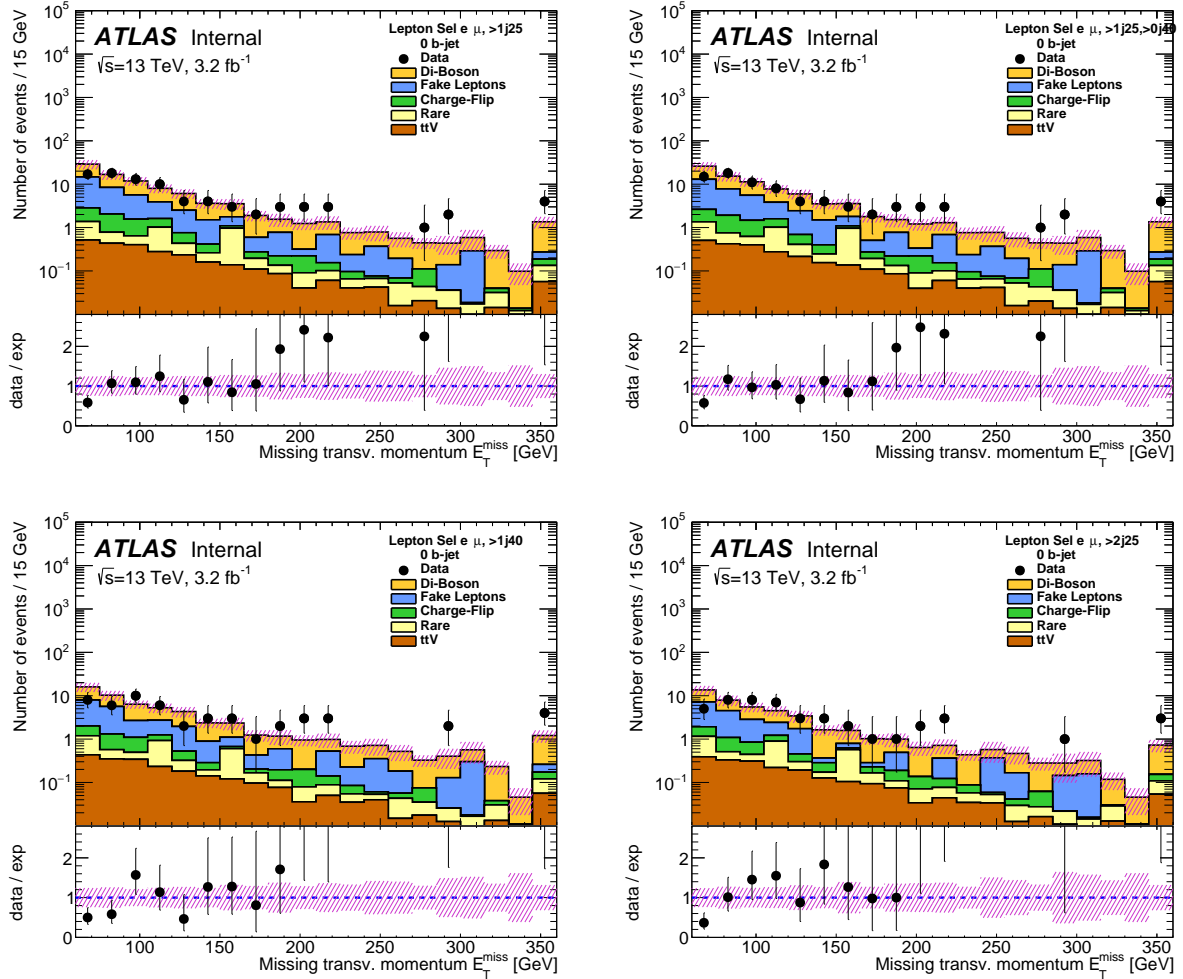


Figure 76: $e\mu$ channel, $E_T^{\text{miss}} > 60 \text{ GeV}$ and $N_{\text{jets}}^{25} \geq 2$: Missing transverse energy distribution after lepton selections with a b -jet veto ($p_T > 20 \text{ GeV}$) and with at least 0, 1, 2 and 3 jets with $p_T > 40 \text{ GeV}$ (from top-left to bottom-right).

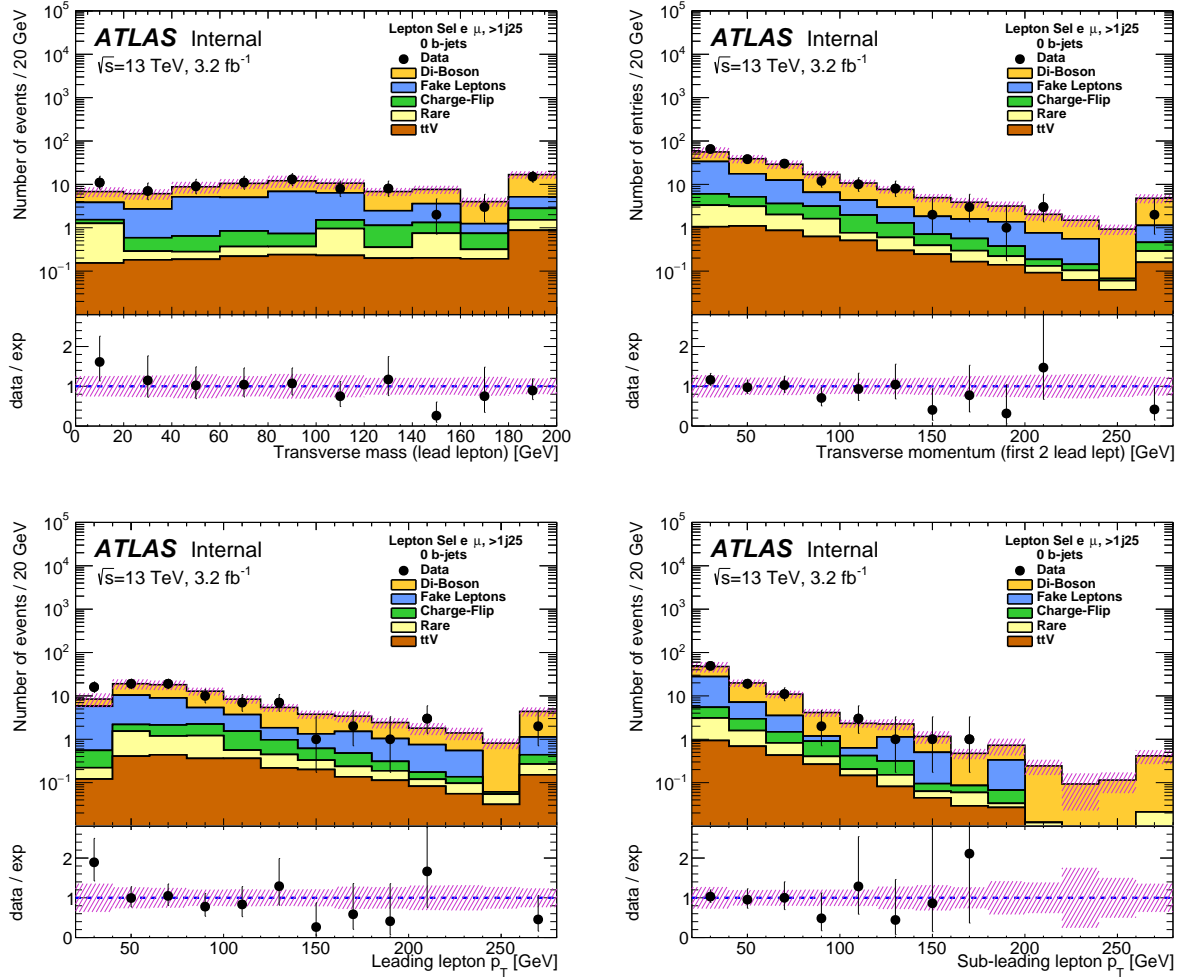


Figure 77: $e\mu$ channel, $E_T^{\text{miss}} > 60 \text{ GeV}$ and $N_{\text{jets}}^{25} \geq 2$: Distributions of m_T (top-left), selected leptons p_T (top-right), leading lepton p_T (bottom-left) and subleading lepton p_T (bottom-right) after lepton selections with a b -jet veto ($p_T > 20 \text{ GeV}$).

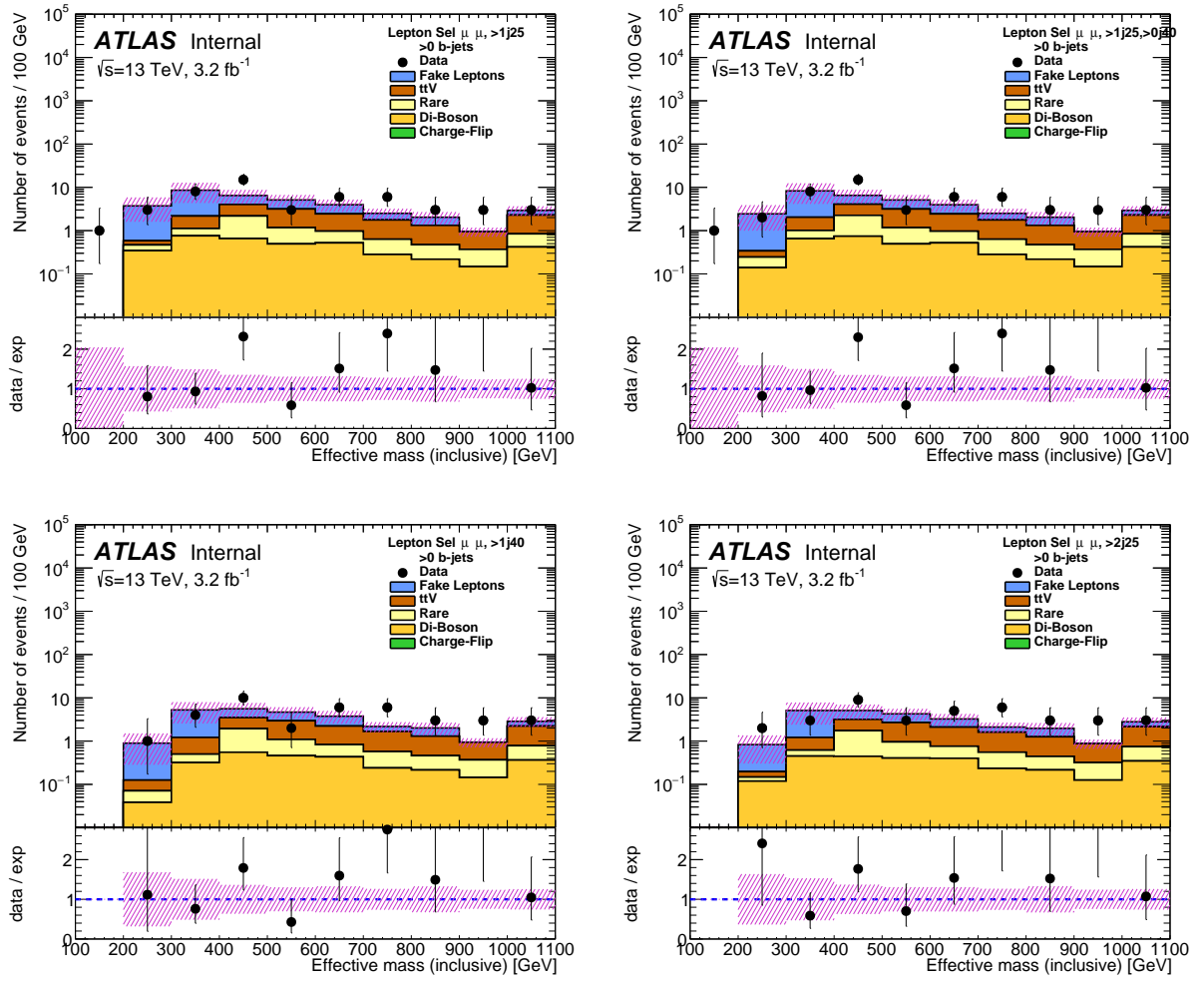


Figure 78: $\mu\mu$ channel, $E_T^{\text{miss}} > 60 \text{ GeV}$ and $N_{\text{jets}}^{25} \geq 2$: Effective mass distribution after lepton selections with a b -jet veto ($p_T > 20 \text{ GeV}$) and with at least 0, 1, 2 and 3 jets with $p_T > 40 \text{ GeV}$ (from top-left to bottom-right).

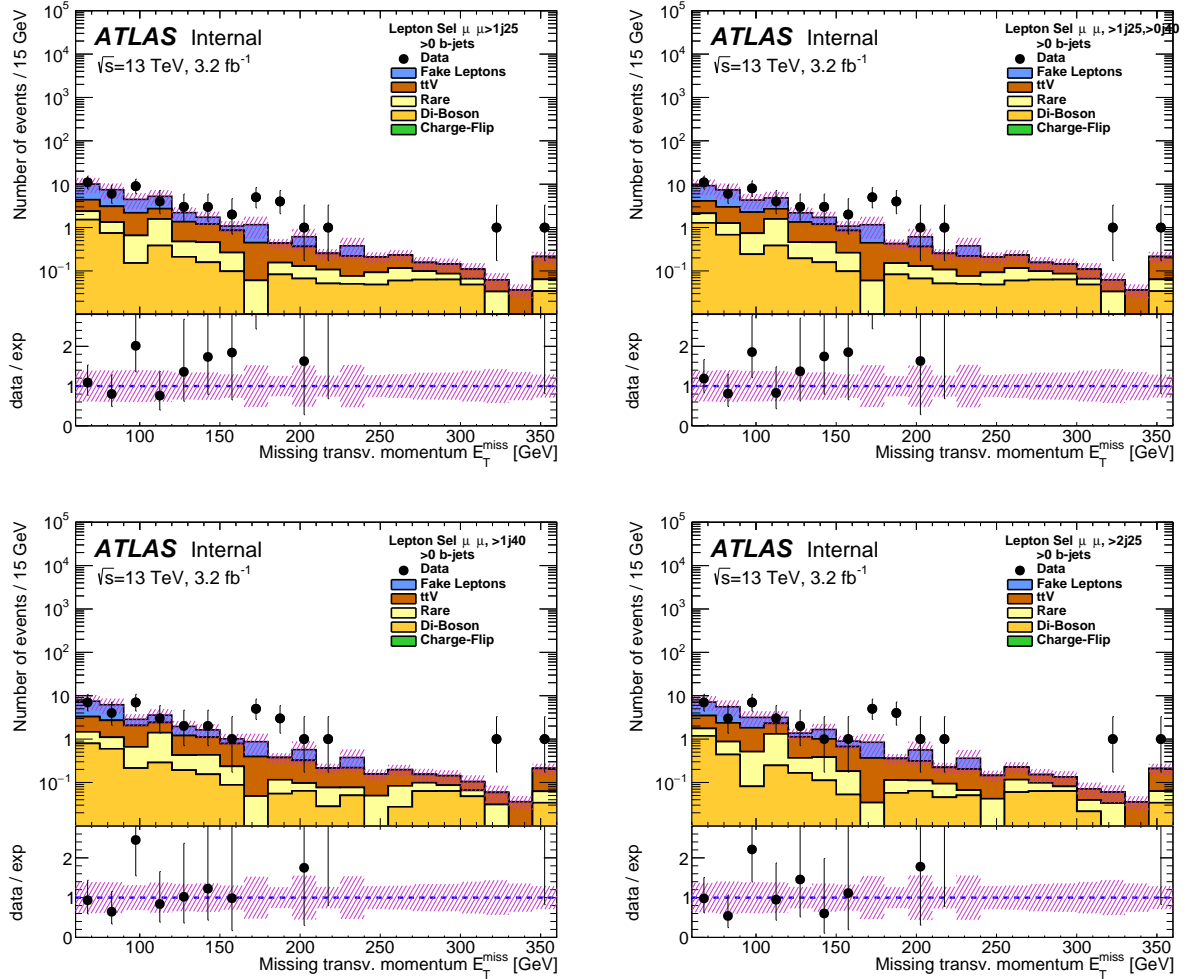


Figure 79: $\mu\mu$ channel, $E_T^{\text{miss}} > 60 \text{ GeV}$ and $N_{\text{jets}}^{25} \geq 2$: Missing transverse energy distribution after lepton selections with a b -jet veto ($p_T > 20 \text{ GeV}$) and with at least 0, 1, 2 and 3 jets with $p_T > 40 \text{ GeV}$ (from top-left to bottom-right).

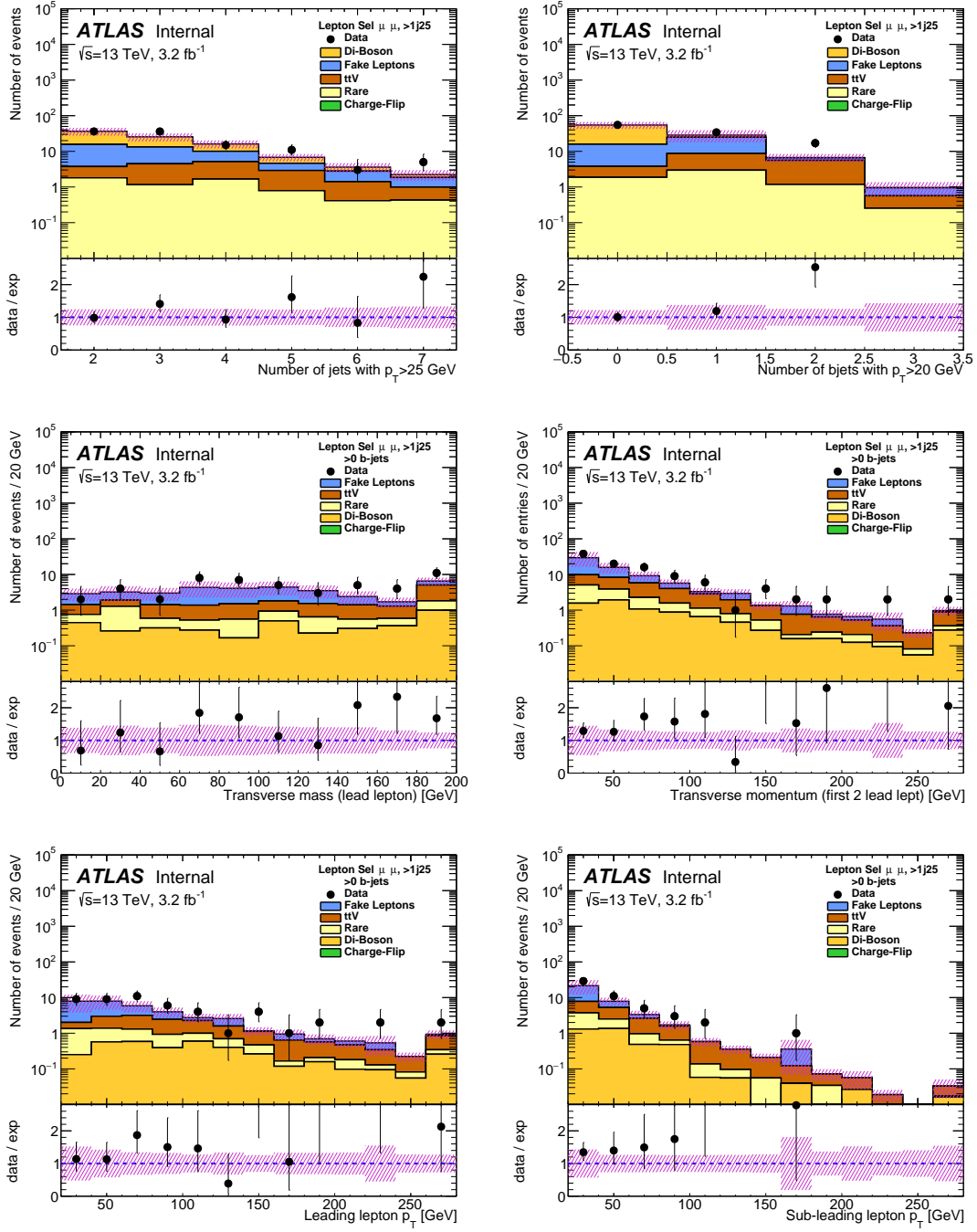


Figure 80: $\mu\mu$ channel, $E_T^{\text{miss}} > 60\text{GeV}$ and $N_{\text{jets}}^{25} \geq 2$: Distributions of jet multiplicity ($p_T > 25$ GeV) (top-left) and b -jet multiplicity ($p_T > 20$ GeV) (top-right) after lepton selection, and of m_T (middle-left), selected leptons p_T (middle-right), leading lepton p_T (bottom-left) and subleading lepton p_T (bottom-right) after lepton selections with at least one b -jet ($p_T > 20$ GeV).

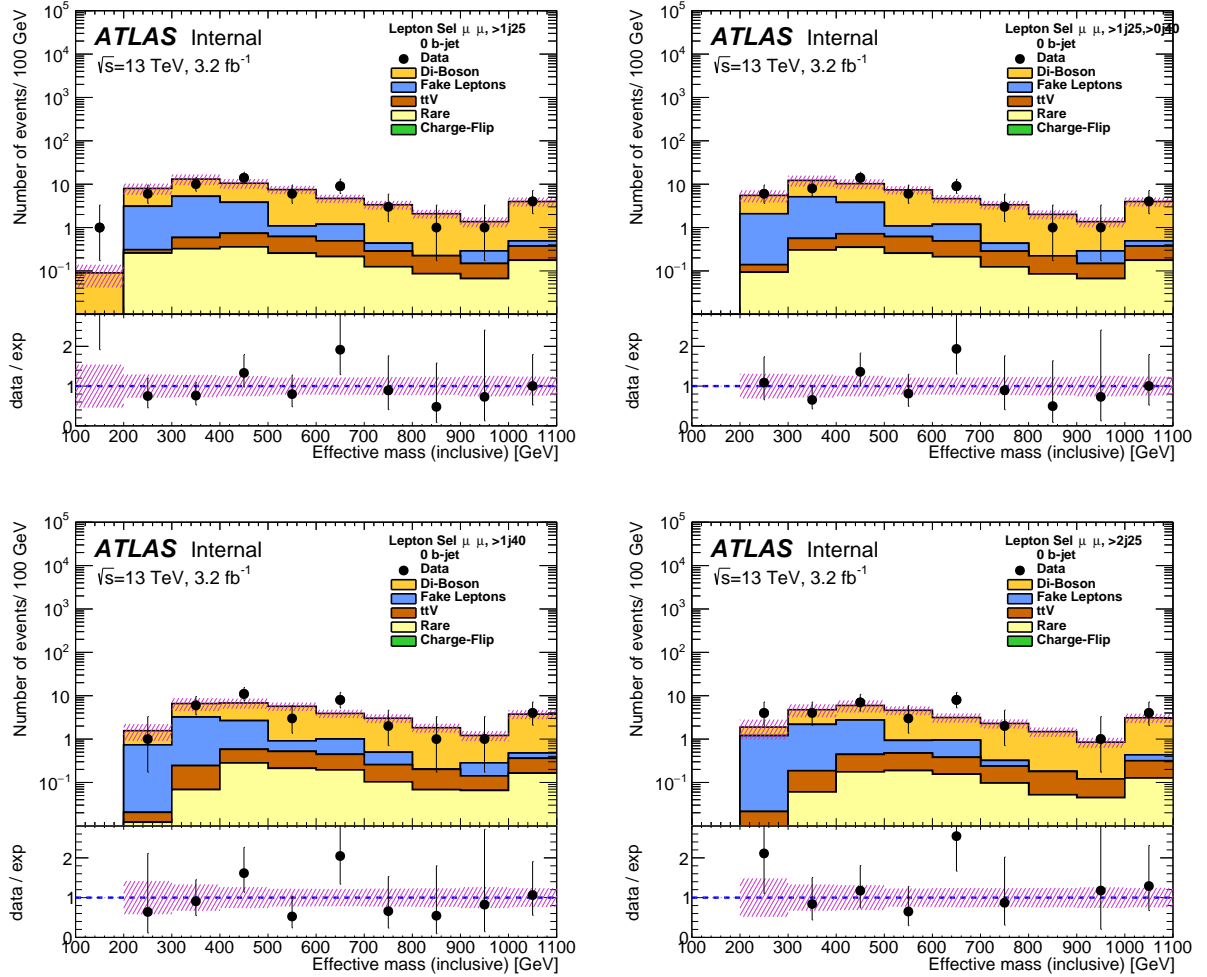


Figure 81: $\mu\mu$ channel, $E_T^{\text{miss}} > 60 \text{ GeV}$ and $N_{\text{jets}}^{25} \geq 2$: Effective mass distribution after lepton selections with a b -jet veto ($p_T > 20 \text{ GeV}$) and with at least 0, 1, 2 and 3 jets with $p_T > 40 \text{ GeV}$ (from top-left to bottom-right).

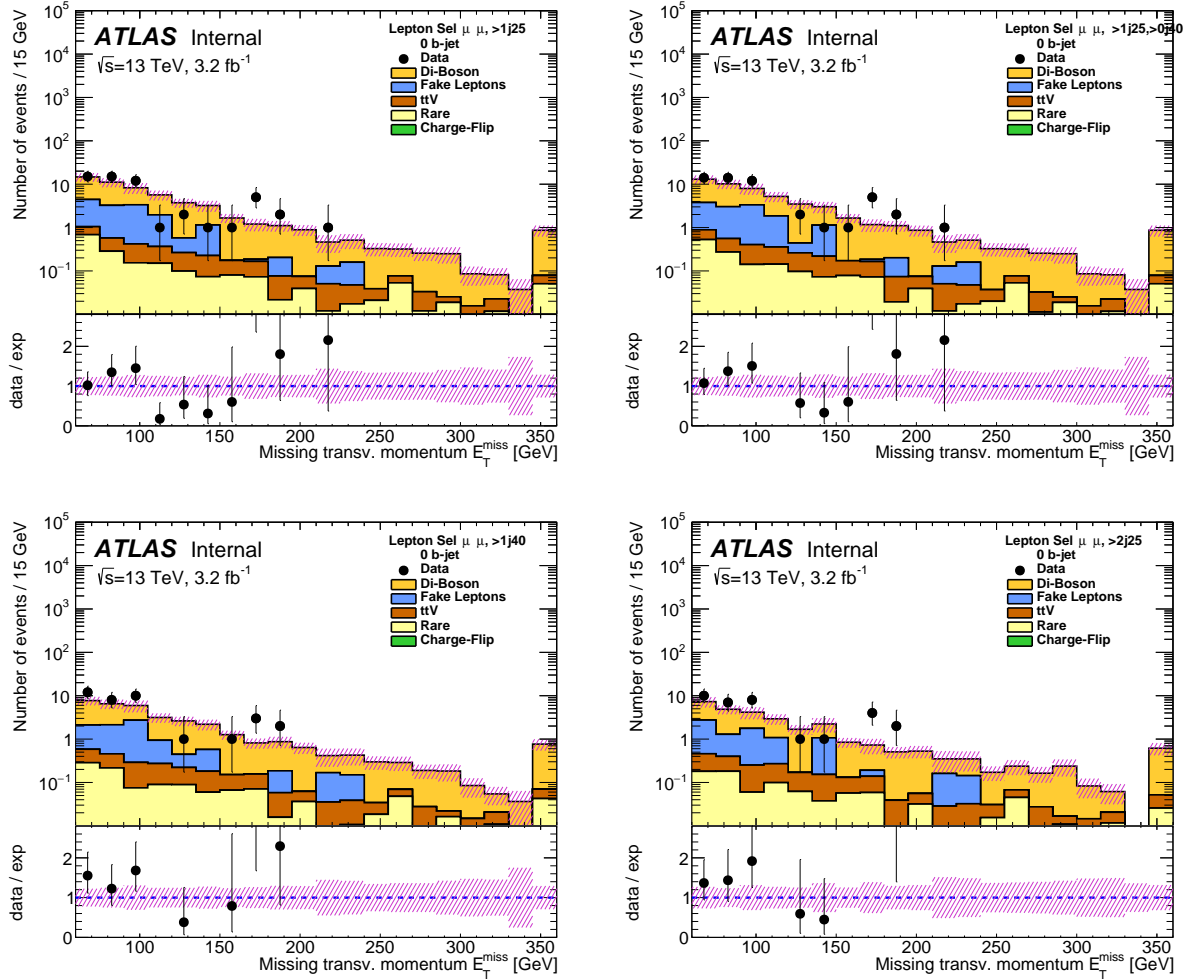


Figure 82: $\mu\mu$ channel, $E_T^{\text{miss}} > 60 \text{ GeV}$ and $N_{\text{jets}}^{25} \geq 2$: Missing transverse energy distribution after lepton selections with a b -jet veto ($p_T > 20 \text{ GeV}$) and with at least 0, 1, 2 and 3 jets with $p_T > 40 \text{ GeV}$ (from top-left to bottom-right).

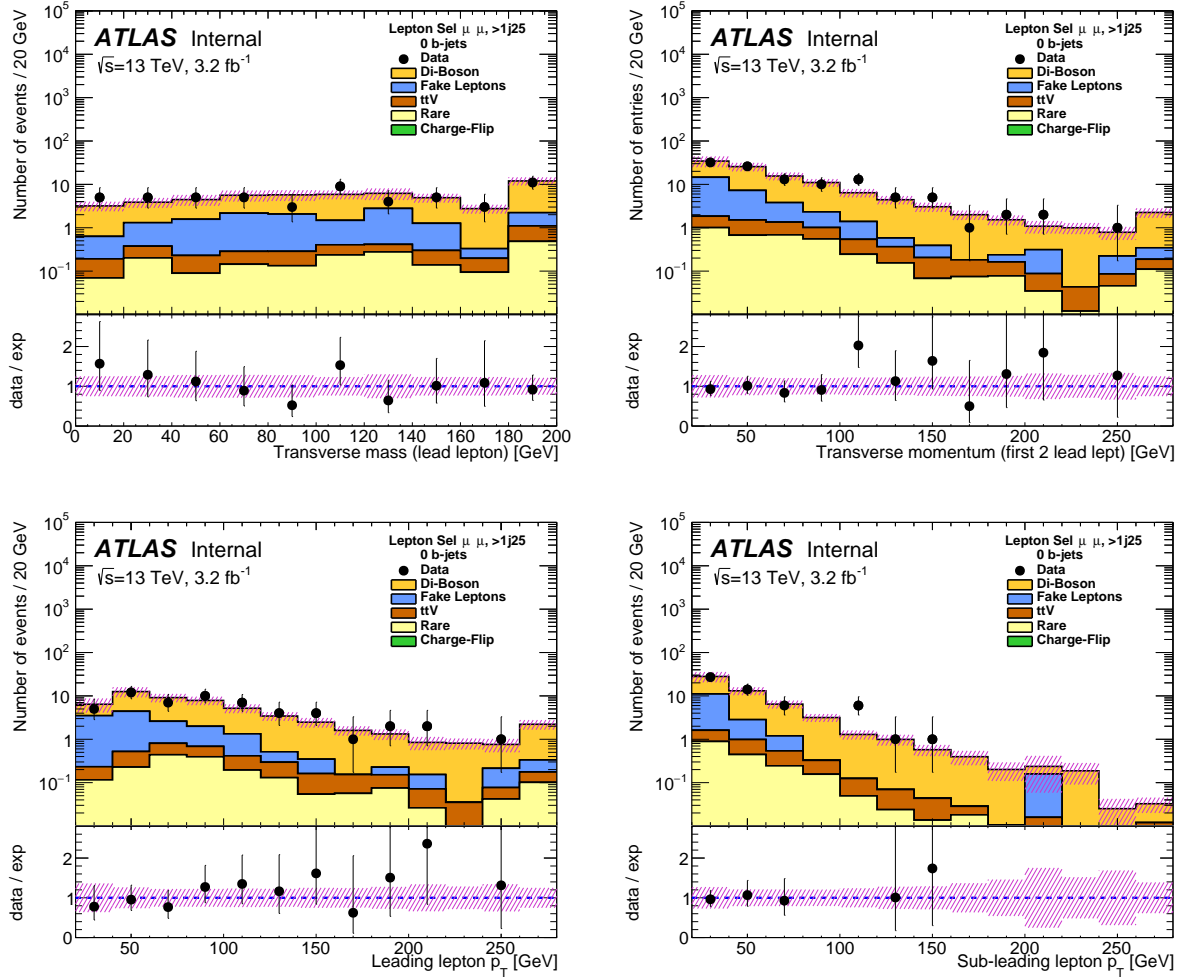


Figure 83: $\mu\mu$ channel, $E_T^{\text{miss}} > 60\text{GeV}$ and $N_{\text{jets}}^{25} \geq 2$: Distributions of m_T (top-left), selected leptons p_T (top-right), leading lepton p_T (bottom-left) and subleading lepton p_T (bottom-right) after lepton selections with a b -jet veto ($p_T > 20\text{ GeV}$).

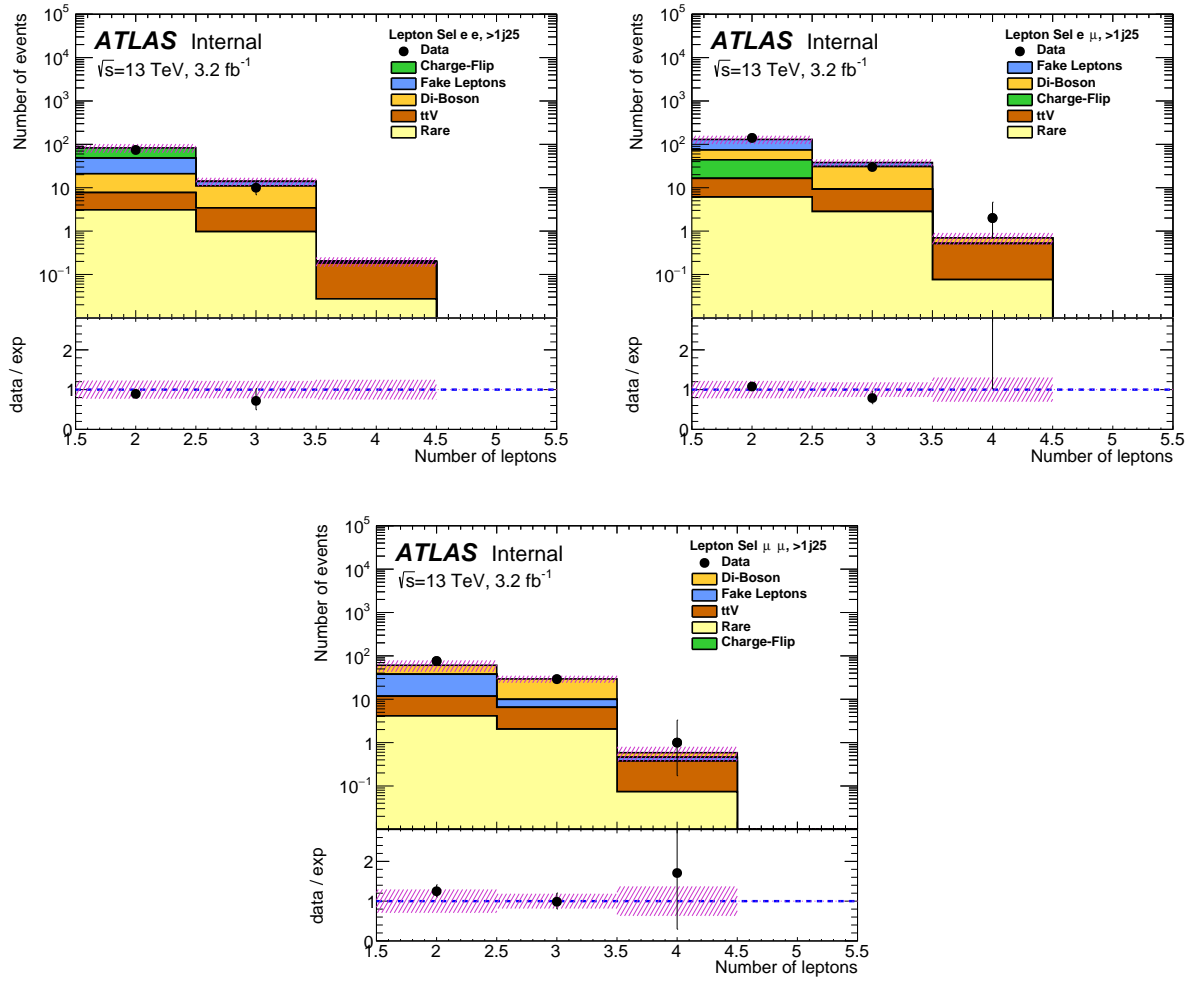


Figure 84: $E_T^{\text{miss}} > 60 \text{ GeV}$ and $N_{\text{jets}}^{25} \geq 2$: Number of leptons distribution after lepton selection in ee (left), $e\mu$ (middle) and $\mu\mu$ (right) channels.

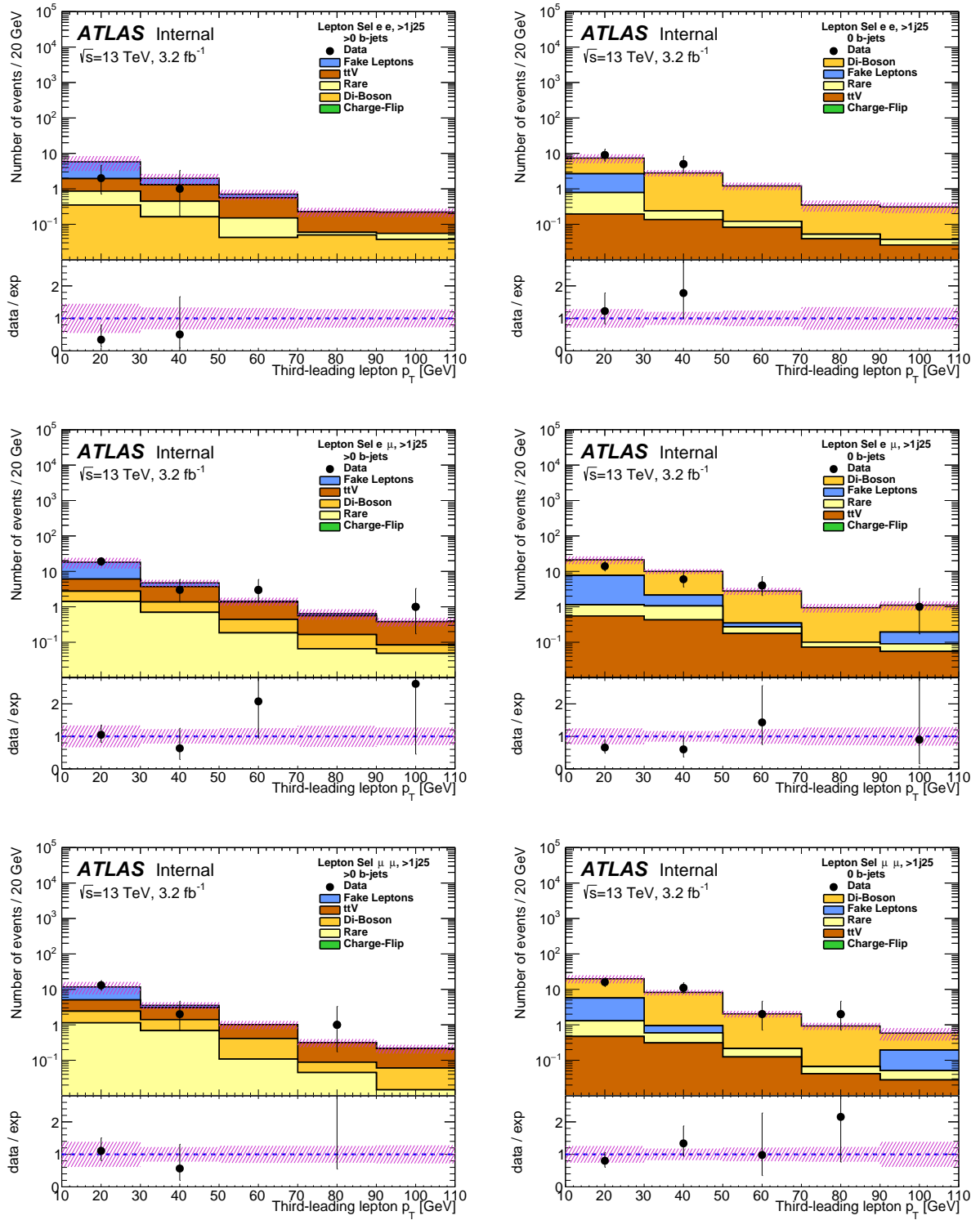


Figure 85: 3leptons, $E_T^{\text{miss}} > 60 \text{ GeV}$ and $N_{\text{jets}}^{25} \geq 2$: Third lepton p_T distribution after lepton selection with at least one b -jet (left) and 0 b -jets (right). Results are shown in ee (left), $e\mu$ (middle) and $\mu\mu$ (right) channels.

1426 9.2 Validation regions

1427 In this section the validation regions (VR) defined to check the prompt SS background are described.
 1428 The observed number of data events and the corresponding background estimation are also shown at the
 1429 end of the section. The definition of these validation regions is summarized in Table 26 and is detailed
 1430 below. In all validation regions the signal regions defined in Table 12 are vetoed to minimize the signal
 1431 contamination and any overlap between the regions. As a $t\bar{t} + V$ validation region is very sensitive to
 1432 models including third generation squarks (like direct sbottom pair production) we choose to veto any
 1433 event passing SR2b defined in Table 14. Given the excess observed in Run-1, we choose to veto also any
 1434 event passing the SR3L3b (Table 14) selection. The latter cut is applied in all validation regions. The
 1435 “signal removal” cuts are shown with “!SR” in the tables.

Table 26: Summary of the event selection in the validation regions. Requirements are placed on the number of signal leptons ($N_{\text{lept}}^{\text{signal}}$) and candidate leptons ($N_{\text{lept}}^{\text{cand}}$), the number of jets with $p_T > 25 \text{ GeV}$ (N_{jets}^{25}) or the number of b -jets with $p_T > 20 \text{ GeV}$ ($N_{b-\text{jets}}^{20}$). The three leading p_T leptons are referred to as $\ell_{1,2,3}$ with decreasing p_T and the two leading jets as $j_{1,2}$. Additional requirements are set on the invariant mass of the two leading electrons m_{ee} , the presence of SS leptons or a pair of same-flavour opposite-sign leptons (SFOS) and its invariant mass m_{SFOS} .

	$N_{\text{lept}}^{\text{signal}}$ ($N_{\text{lept}}^{\text{cand}}$)	$N_{b-\text{jets}}^{20}$	N_{jets}^{25}	$E_{\text{T}}^{\text{miss}}$ [GeV]	m_{eff} [GeV]	Other
VR-WW	=2 (=2) =1 SS pair	=0	≥ 2	35–200	300–900	$m(j_1 j_2) > 500 \text{ GeV}$ $p_{\text{T}}(j_2) > 40 \text{ GeV}$ $p_{\text{T}}(\ell_2) > 30 \text{ GeV}$ veto $80 < m_{ee} < 100 \text{ GeV}$
VR-WZ	=3 (=3)	=0	1–3	30–200	<900	$p_{\text{T}}(\ell_3) > 30 \text{ GeV}$
VR-ttV	≥ 2 (-) ≥1 SS pair	≥ 2	$\geq 5 (e^{\pm} e^{\pm}, e^{\pm} \mu^{\pm})$ $\geq 3 (\mu^{\pm} \mu^{\pm})$	20–200	200–900	$p_{\text{T}}(\ell_2) > 25 \text{ GeV}$ veto $\{E_{\text{T}}^{\text{miss}} > 125 \text{ and } m_{\text{eff}} > 650 \text{ GeV}\}$
VR-ttZ	≥ 3 (-) ≥1 SFOS pair	≥ 1	$\geq 4 (=1 b\text{-jet})$ $\geq 3 (\geq 2 b\text{-jets})$	20–150	100–900	$p_{\text{T}}(\ell_2) > 25 \text{ GeV}$ $p_{\text{T}}(\ell_3) > 20 \text{ GeV}$ (if e) $80 < m_{\text{SFOS}} < 100 \text{ GeV}$
All VRs	Veto events belonging to any SR, or if ℓ_1 or ℓ_2 is an electron with $ \eta > 1.37$ (except in VR-WZ)					

1436 $t\bar{t} + V$ background validation

1437 To validate the $t\bar{t} + Z$ and $t\bar{t} + W$ background estimation, several tentative regions defined with at least 1
 1438 or 2 b -jets in the event are optimized. Given the low statistics expected for 2.4fb^{-1} no $t\bar{t} + W$ validation
 1439 region could be proposed. A $t\bar{t} + Z$ enriched validation region ($ttZ 1\text{bIncl}$) is defined in Table 27 as a
 1440 combination of two orthogonal regions, “=1 b ” ($ttZ 1\text{bExcl}$) and “ ≥ 2 b -jets” ($ttZ 2\text{bIncl}$). Beside the
 1441 b -jet(s), at least three energetic signal leptons and at least 3 (4) soft jets ($p_T > 25 \text{ GeV}$) are required in the
 1442 event. A cut on the Z boson mass ($80 < m_{\ell\ell}^{\text{SFOS}} < 100 \text{ GeV}$) ensures a high purity, rejecting multi-boson
 1443 processes. The fake lepton background is reduced with minimum cuts on $E_{\text{T}}^{\text{miss}}$ and m_{eff} , and with tight
 1444 constraints on the electron acceptance ($|\eta|_{e1,2} < 1.37$). The reached purity is 70%.

1445 A second $t\bar{t} + V$ validation region ($ttV 2\text{bIncl}$) is defined in Table 28 with at least two b -jets and at least two
 1446 energetic signal leptons. The highest purity is found with at least five soft jets in the ee and $e\mu$ channels,
 1447 and at least three soft jets in the $\mu\mu$ channel. Cuts on m_{eff} and electron acceptance ($|\eta|_{e1,2} < 1.37$) are
 1448 applied to reduce the detector background. The obtained purity is 50%.

1449 In both validation regions the signal contamination is reduced by vetoing the signal regions (including
 1450 SR2b and SR3L3b) and by applying upper cuts on m_{eff} (900 GeV) and $E_{\text{T}}^{\text{miss}}$ (150–200 GeV). Note that
 1451 the m_{eff} cut can be tightened to further decrease the SUSY contamination from models like direct sbottom.

- 1452 Using DC14 MC samples, in $t\bar{t} + Z$ VR it was found to be up to 27% when the direct-sbottom model was
 1453 considered (sbottom mass of 550 GeV) and up to 20% for direct squark (2 step) via sleptons with W/Z
 1454 bosons in the cascade decay, otherwise smaller than 10%.

Table 27: $t\bar{t} + Z$ validation region definition ($ttZ\ 1bIncl = ttZ\ 1bExcl \parallel ttZ\ 2bIncl$).

VR	N_{lept}^{signal}	N_{b-jets}^{20}	Other variables
$ttZ\ 1bExcl$	$\geq 3, p_T: (l1, l2, e3 (\mu3)) = (25, 25, 20 (10))\text{ GeV}$	$==1$	$20 < E_T^{\text{miss}} < 150\text{ GeV}, 100 < m_{\text{eff}} < 900\text{ GeV}, N_{jets}^{25} \geq 4, \eta _{e1,2} < 1.37, 80 < m_{\ell\ell}^{\text{SFOS}} < 100\text{ GeV}, \text{!SR}$
$ttZ\ 2bIncl$	$\geq 3, p_T: (l1, l2, e3 (\mu3)) = (25, 25, 20 (10))\text{ GeV}$	≥ 2	$20 < E_T^{\text{miss}} < 150\text{ GeV}, 100 < m_{\text{eff}} < 900\text{ GeV}, N_{jets}^{25} \geq 3, \eta _{e1,2} < 1.37, 80 < m_{\ell\ell}^{\text{SFOS}} < 100\text{ GeV}, \text{!SR}$

Table 28: $t\bar{t} + V$ validation region definition ($ttV\ 2bIncl$).

VR	N_{lept}^{signal}	N_{b-jets}^{20}	Other variables
$ttV\ 2bIncl$	$\geq 2, p_T: (l1, l2, l3) = (25, 25, 10)\text{ GeV}$	≥ 2	$20 < E_T^{\text{miss}} < 200\text{ GeV}, 200 < m_{\text{eff}} < 900\text{ GeV}, \eta _{e1,2} < 1.37, N_{jets}^{25} \geq 5 \text{ in } ee \text{ and } e\mu, N_{jets}^{25} \geq 3 \text{ in } \mu\mu \text{ channels, !SR}$

1455 WZ + jets validation region

1456 Even if this type of background is minor in several of the defined signal regions, its contribution can be
 1457 significant in regions with no b jet requirement and three leptons. Therefore, a validation region ($WZ1j$
 1458 $0bExcl$) is defined as shown in Table 29. It requires exactly three leptons and a veto on the fourth-leading
 1459 baseline lepton in order to reduce the ZZ background contamination. The lower cut on E_T^{miss} (30 GeV) is
 1460 mainly reducing the charge flip. At least one and at most three jets with $p_T > 25$ GeV are required in the
 1461 event. The purity is around 81%. The signal contamination was studied with DC14 samples, and it was
 1462 found to be below 1%.

Table 29: $WZ + \text{jets}$ validation region definition ($WZ1j\ 0bExcl$).

VR	N_{lept}^{signal}	$N_{lept}^{baseline}$	N_{b-jets}^{20}	Other variables
$WZ1j\ 0bExcl$	$==3, p_T: (l1, l2, l3) = (30, 30, 30)\text{ GeV}$	< 4	$==0$	$30 < E_T^{\text{miss}} < 200\text{ GeV}, 100 < m_{\text{eff}} < 900\text{ GeV}, 1 \leq N_{jets}^{25} < 4, \text{!SR}$

1463 $W^\pm W^\pm + \text{jets}$ validation region

1464 Similarly to other diboson processes, the $W^\pm W^\pm + \text{jets}$ events contribute mainly in the signal regions with
 1465 no b jet requirement. The defined validation region ($W^\pm W^\pm mjj\ 0bExcl$) is presented in Table 30. A cut
 1466 on the invariant mass of the first two leading jets in the event is considered to remove most of the $WZ +$
 1467 jets processes. Even if it selects forward jets from VBS processes, which are not necessary populating the
 1468 signal regions defined in the analysis, it gives a confidence on this type of background. No other validation
 1469 region (i.e with two energetic jets) could be defined, because of the high background contamination. The
 1470 reached purity is around 44%. The signal contamination is reduced by applying an upper cut on E_T^{miss}
 1471 (200 GeV) – with the DC14 samples, it was found to be around 15%.

1472 Results in the validation regions with 3.2 fb^{-1} of data

Table 30: $W^\pm W^\pm$ validation region definition ($W^\pm W^\pm \text{mjj 0bExcl}$).

VR	N_{lept}^{signal}	$N_{lept}^{baseline}$	N_{b-jets}^{20}	Other variables
$W^\pm W^\pm \text{mjj 0bExcl}$	$==2, p_T: (11, 12) = (30, 30) \text{ GeV}$	$== 2$	$==0$	$35 < E_T^{\text{miss}} < 200 \text{ GeV}, 80 < m_{ee}^{\text{SS}} < 100 \text{ GeV}, m_{jj} > 500 \text{ GeV},$ $300 < m_{\text{eff}} < 900 \text{ GeV}, N_{jets}^{40} \geq 2, \eta _{e1,2} < 1.37, \text{ ISR}$

1473

1474 The event yields in the defined validation regions are shown in Table 31. The effective mass distribution in
 1475 the validation regions is shown in Figure 86. A comparison between the purely data driven estimation of
 1476 the detector background (DD-Total) and the estimation using the MC-based method (MC-Total) is shown
 1477 in Table 32. Generally a good agreement is observed, within the uncertainties, although the $t\bar{t}V$ and $t\bar{t}Z$
 1478 regions show some tension (data excess) at the level of 1.7σ . More about this excess in Appendix 19.

1479 In the plots, the prompt SS background uncertainties include the statistical component and the theoretical
 1480 systematic uncertainties as described in Section 10.2. For the detector background estimation the
 1481 uncertainties include all sources presented in section 7.

Table 31: The numbers of observed data and expected background events for the validation regions. The “Rare” category contains the contributions from $t\bar{t}\bar{t}$, $t\bar{t}t$, $t\bar{t}h$ and $t\bar{t}WW$ production. Background categories shown as “–” denote that they cannot contribute to a given region (charge flips or $W^\pm W^\pm jj$ in 3-lepton regions).

	$W^\pm W^\pm jj$	WZj	$t\bar{t}V$	$t\bar{t}Z$
Observed events	4	82	19	14
Total bkg events	3.4 ± 0.8	98 ± 15	12.1 ± 2.7	9.7 ± 2.5
Fake/non-prompt leptons	0.6 ± 0.5	8 ± 6	2.1 ± 1.4	0.6 ± 1.0
Charge-flip	0.26 ± 0.05	–	1.14 ± 0.15	–
$t\bar{t}W$	0.05 ± 0.03	0.25 ± 0.09	2.4 ± 0.8	0.10 ± 0.03
$t\bar{t}Z$	0.02 ± 0.01	0.72 ± 0.26	3.9 ± 1.3	6.3 ± 2.1
WZ	1.0 ± 0.4	78 ± 13	0.19 ± 0.10	1.2 ± 0.4
$W^\pm W^\pm jj$	1.3 ± 0.5	–	0.02 ± 0.03	–
ZZ	0.02 ± 0.01	8.2 ± 2.8	0.12 ± 0.15	0.30 ± 0.19
Rare	0.10 ± 0.05	2.8 ± 1.4	2.3 ± 1.2	1.1 ± 0.6

Table 32: Results in the defined validation regions using the data driven (DD-Total) and MC-based (MC-Total) methods to estimate the detector backgrounds. The quoted uncertainties are both statistical and systematical.

	$WZ1j \text{ 0bExcl}$	$W^\pm W^\pm \text{mjj 0bExcl}$	$ttV \text{ 2bIncl}$	$ttZ \text{ 1bIncl}$
DD-Total	98 ± 15	3.4 ± 0.8	12.1 ± 2.7	9.7 ± 2.5
MC-Total	100 ± 48	3.1 ± 1.5	10.0 ± 2.6	8.9 ± 2.3
Data	82	4	19	14

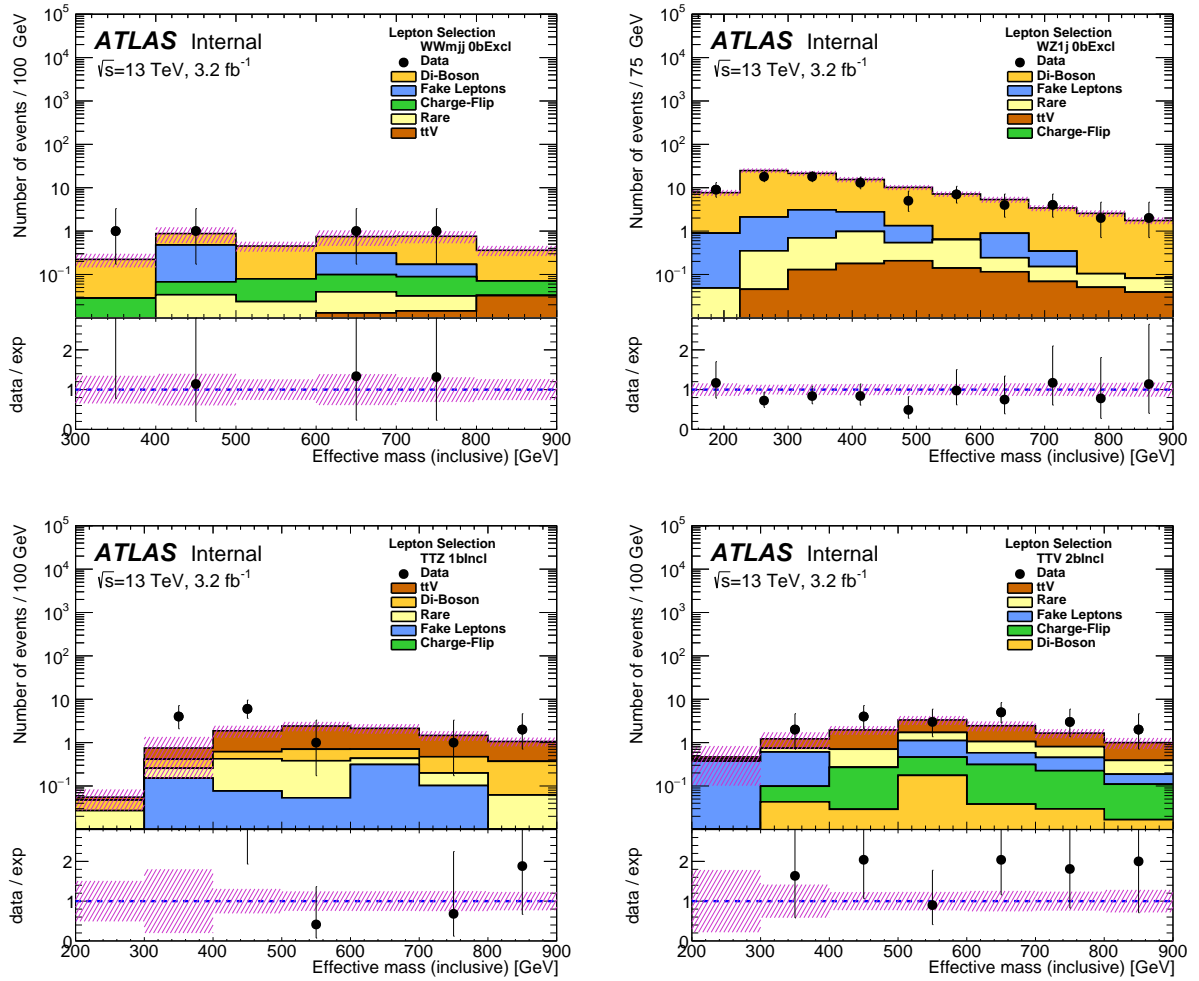


Figure 86: Effective mass distribution in $W^\pm W^\pm m_{jj}$ 0bExcl (top-left), $WZ1j$ 0bExcl (top-right), ttZ 1bIncl (bottom-left) and ttV 2bIncl (bottom-right) validation regions.

1482 9.3 Results in the auxiliary signal regions

1483 The event yields in the auxiliary signal regions defined in Table 14, section 6, are shown in Table 33.
 1484 The agreement between the observed number of events and the number of expected background events is
 1485 very good. For illustration, the missing transverse energy distribution close by and in the auxiliary signal
 1486 regions is shown in Figure 87; the results in the signal regions correspond to the last bin (inclusive) of
 1487 each plot.

Table 33: Results in the auxiliary signal regions. Only the total uncertainty is quoted.

	SR2b	SR3l3b
Fakes	1.30 ± 0.84	0.46 ± 0.49
Charge flip	1.66 ± 0.22	0.00 ± 0.00
ttZ, ttW	3.58 ± 1.08	0.11 ± 0.04
Di-Boson	0.10 ± 0.05	0.00 ± 0.00
Rare	1.04 ± 0.50	0.08 ± 0.05
Total	7.67 ± 1.82	0.66 ± 0.50
Data	6	1

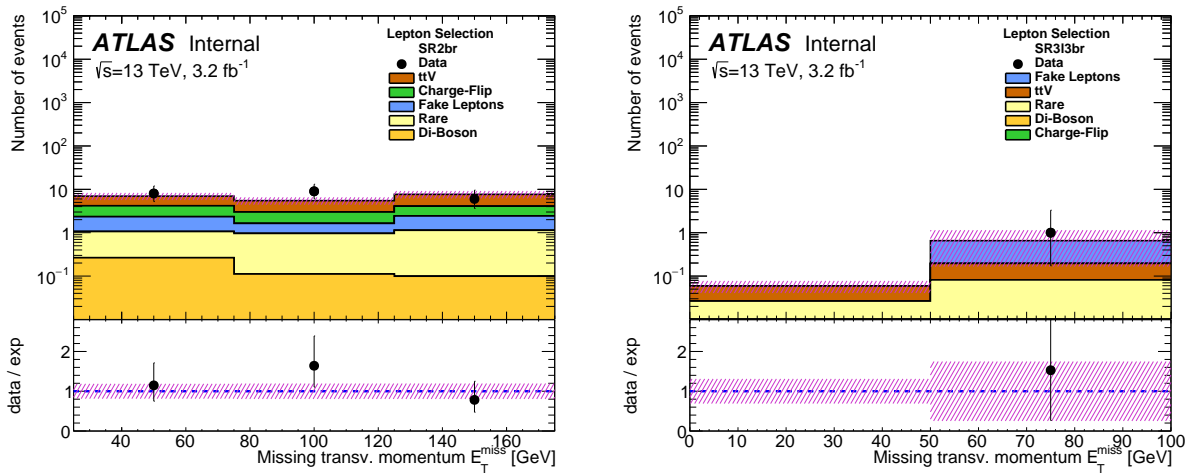


Figure 87: Missing transverse momentum distribution after SR2b (left) and SR3l3b (bottom-right) selection, beside the E_T^{miss} cut. The results in the auxiliary signal regions are shown in the last (inclusive) bin of each plot.

10 Systematic Uncertainties

10.1 Experimental systematics

All the experimental systematics provided by the SUSYTools `getSystInfoList()` method have been considered. The list of sources of uncertainty and the corresponding names of the variations are:

1492 Jet energy scale (`JET_GroupedNP_{1-3}__1{up,down}`)

One of the strongly reduced uncertainty sets provided by the JetEtMiss group for early Run-2 searches is used in this note. These sets are intended for use by analyses which are not sensitive to jet-by-jet correlations arising from changes to the jet energy scale (as expected for many early SUSY searches), and we use the scenario `InsituJES2012_3NP_Scenario1.config` (as included in the JetUncertainties package). We checked that the uncertainties obtained from one of the 3 other scenarios did not lead to significant changes. The jet energy is scaled up and down (in a fully correlated way) by the $\pm 1\sigma$ uncertainty of each nuisance parameter.

1500 **Jet energy resolution (JET_JER_SINGLE_NP__1up)**

1501 An extra p_T smearing is added to the jets based on their p_T and η to account for a possible underestimate of
 1502 the jet energy resolution in the MC simulation. This is done by the `JERSmearingTool` in the `JetResolution`
 1503 package.

1504 **Egamma resolution (EG_RESOLUTION_ALL__1{up,down})**

1505 A nuisance filtering scheme to reduce the ~8 NPs used to electron and photon resolution to only one as
 1506 implemented in SUSYTools is used.

1507 **Egamma scale (EG_SCALE_ALL__1{up,down})**

1508 A nuisance filtering scheme to reduce the ~16 NPs used to electron and photon resolution to only one as
 1509 implemented in SUSYTools is used.

1510 **Electron efficiency (EL_EFF_{ID,RECO,TRIGGER,Iso}_TotalCorrUncertainty__1{up,down})**

1511 These uncertainty sources are associated with the electron efficiency scale factors provided by the Egamma
 1512 CP group.

1513 **Muon efficiency (MUON_EFF_{STAT,SYS}__1{up,down},**

1514 **MUON_EFF_Trig{Stat,Syst}Uncertainty__1{up,down},**

1515 **MUON_ISO_{STAT,SYS}__1{up,down})**

1516 This uncertainty corresponds to the statiscal and systematic uncertainties in the muon efficiency scale
 1517 factors provided by the Muon CP group on the muon reconstruction, trigger and isolation.

1518 **Muon resolution uncertainty (MUONS_ID__1{up,down}, MUONS_MS__1{up,down})**

1519 This is evaluated as variations in the smearing of the inner detector and muon spectrometer tracks
 1520 associated to the muon objects by $\pm 1\sigma$ their uncertainty

1521 **Muon momentum scale (MUONS_SCALE__1{up,down})**

1522 This is evaluated as variations in the scale of the momentum of the muon objects

1523 **E_T^{miss} soft term uncertainties (MET_SoftTrk_Reso{Pare,Perp}, MET_SoftCalo_Scale{Up,Down})**

1524 Note that the effect of the hard object uncertainties (most notably JES and JER) are also propagated to the
 1525 E_T^{miss} .

1526 **Flavor tagging (FT_EFF_{B,C,Light}_systematics__1{up,down},**

1527 **FT_EFF_{B,C,Light}_extrapolation__1{up,down},**

1528 **FT_EFF_{B,C,Light}_extrapolation from charm__1{up,down})**

1529 Similarly to the case of the JES, a significant reduction in the number of nuisance parameters was provided
 1530 by the Flavour Tagging CP group at the beginning of Run-2.

1531

1532 **Pileup reweighting (PRW_DATASF__1{up,down})**

1533 This uncertainty is obtained by re-scaling the μ value in data by 1.00 and 1/1.23, covering the full differ-
 1534 ence between applying and not-applying the nominal μ correction of 1/1.16, as well as uncertainty on the
 1535 luminosity measurement which is expected to dominate.

1536

	SR0b3j	SR0b5j	SR1b	SR3b
Observed events	3	3	7	1
Total bkg events	1.5 ± 0.4	0.88 ± 0.29	4.5 ± 1.0	0.80 ± 0.25
$p(s = 0)$	0.13	0.04	0.15	0.36
Fake/non-prompt leptons	< 0.2	0.05 ± 0.18	0.8 ± 0.8	0.13 ± 0.17
Charge-flip	–	0.02 ± 0.01	0.60 ± 0.12	0.19 ± 0.06
$t\bar{t}W$	0.02 ± 0.01	0.08 ± 0.04	1.1 ± 0.4	0.10 ± 0.05
$t\bar{t}Z$	0.10 ± 0.04	0.05 ± 0.03	0.92 ± 0.31	0.14 ± 0.06
WZ	1.2 ± 0.4	0.48 ± 0.20	0.18 ± 0.11	< 0.02
$W^\pm W^\pm jj$	–	0.12 ± 0.07	0.03 ± 0.02	< 0.01
ZZ	< 0.03	< 0.04	< 0.03	< 0.03
Rare	0.14 ± 0.08	0.07 ± 0.05	0.8 ± 0.4	0.24 ± 0.14

Table 34: Observed and predicted number of events in the four signal regions for $\mathcal{L} = 3.2\text{fb}^{-1}$.

1537 10.2 Theoretical systematics

1538 The theoretical uncertainties on the $t\bar{t} + V$ production cross-sections are 22% for $t\bar{t}W$ [49] and $t\bar{t}Z$ [50]
 1539 In addition, uncertainties on the signal region fiducial acceptance for these processes were assessed by
 1540 using MC samples with varied factorization and renormalization scales. This led to overall uncertainties
 1541 of 30% on the $t\bar{t} + V$ contributions to the signal regions.

1542 For inclusive diboson production, cross-section uncertainties amount to 7% (computed with MCFM [51]).
 1543 Delays in production of samples with scale variations prevented us from checking scale impact on the
 1544 fiducial acceptance; however, after comparisons between SHERPA and POWHEG predictions, we established
 1545 an overall 30% uncertainty as well for these processes.

1546 Normalisation uncertainties between 35% and 100% were applied to processes with smaller contributions
 1547 (triboson production, $t\bar{t}h$, $t + Z$, etc.).

1548 11 Simultaneous fit method and results

1549 Tables 34 - 35 provides the observed and expected number of events in the signal regions, for the data
 1550 sample corresponding to an integrated luminosity of $\mathcal{L} = 3.21\text{ fb}^{-1}$. The debug stream was checked with
 1551 1.7 fb^{-1} and no SS/3L events were found. No excess over Standard Model prediction is observed. More
 1552 details about the data events can be found in appendix, section 26.

1553 For illustration, the missing transverse energy distribution close by and in the signal regions is shown in
 1554 Figure 88; the results in the signal regions correspond to the last bin (inclusive) of each plot.

1555 The sensitivity of the signal regions proposed in Section 6 is evaluated with more refined statistical
 1556 tools in this section, by using the HistFitter framework [52] to perform hypothesis tests for the different
 1557 signal scenarios of interest. The event yields assumed in these test are the ones predicted by the set of
 1558 Monte-Carlo samples described in section 3, and the object selections detailed in Sections 4 and 5. In all

	SR0b3j	SR0b5j	SR1b	SR3b
<i>ee</i> channel				
Fakes	-0.07 ± 0.26	-0.02 ± 0.03	-0.07 ± 0.28	0.001 ± 0.004
Charge-flip	–	0.007 ± 0.007	0.29 ± 0.08	0.11 ± 0.06
Data	2	1	3	0
<i>eμ</i> channel				
Fakes	-0.03 ± 0.05	0.07 ± 0.17	0.5 ± 0.5	0.13 ± 0.17
Charge-flip	–	0.02 ± 0.01	0.31 ± 0.08	0.09 ± 0.02
Data	1	2	1	1
<i>μμ</i> channel				
Fakes	-0.02 ± 0.03	0 ± 0	0.35 ± 0.33	0 ± 0
Charge-flip	–	–	–	–
Data	0	0	3	0

Table 35: Observed and predicted number of events in the four signal regions for $\mathcal{L} = 3.2\text{fb}^{-1}$. Results are shown in *ee* (top), *eμ* (middle) and *μμ* channels.

1559 of the following, the fits use simple counting experiments, i.e. no binning in any kinematic variable is
 1560 considered. This choice was made in order to reduce the number of nuisance parameters in the fits.

1561 11.1 Non-combination of signal regions

1562 A set of dedicated studies has been performed to assess if, with an integrated luminosity between 2 and 3
 1563 fb^{-1} , a significant extension of the reach of the analysis could be achieved by combining different signal
 1564 regions. For each of the four signal grid unders study, a “golden” signal region is selected as the one with
 1565 the best expected performance. This is used as baseline result for each grid. In addition, an additional fit
 1566 is also performed, where all signal regions are combined together.

1567 The results of this study are reported in Figure 89, where the signal region definitions in Table 11 have
 1568 been used. The fits are performed on MC only (i.e. blinding the data). All experimental systematics are
 1569 considered, and the only theory systematic included are the PDF error and a 30% flat uncertainty on the
 1570 background cross sections. As shown in the plots, the gain from combining the signal regions is overall
 1571 modest, and the decision was taken to perform simpler fits, i.e. without SR combination.

1572 11.2 Background-only fits

1573 The following tables show the event yields for background-only fits with *blinded* data. The purpose of
 1574 these studies is to evaluate the overall consistency of the fit setup and to have an idea of the impact of the
 1575 systematic uncertainties on the fit results. Tables 36, 37, 38 and 39 show the event yields before and after
 1576 the fits. These numbers are identical to the (condensed) ones presented in table 34. The systematic errors
 1577 after the fits are reported in Tables 40, 41, 42 and 43

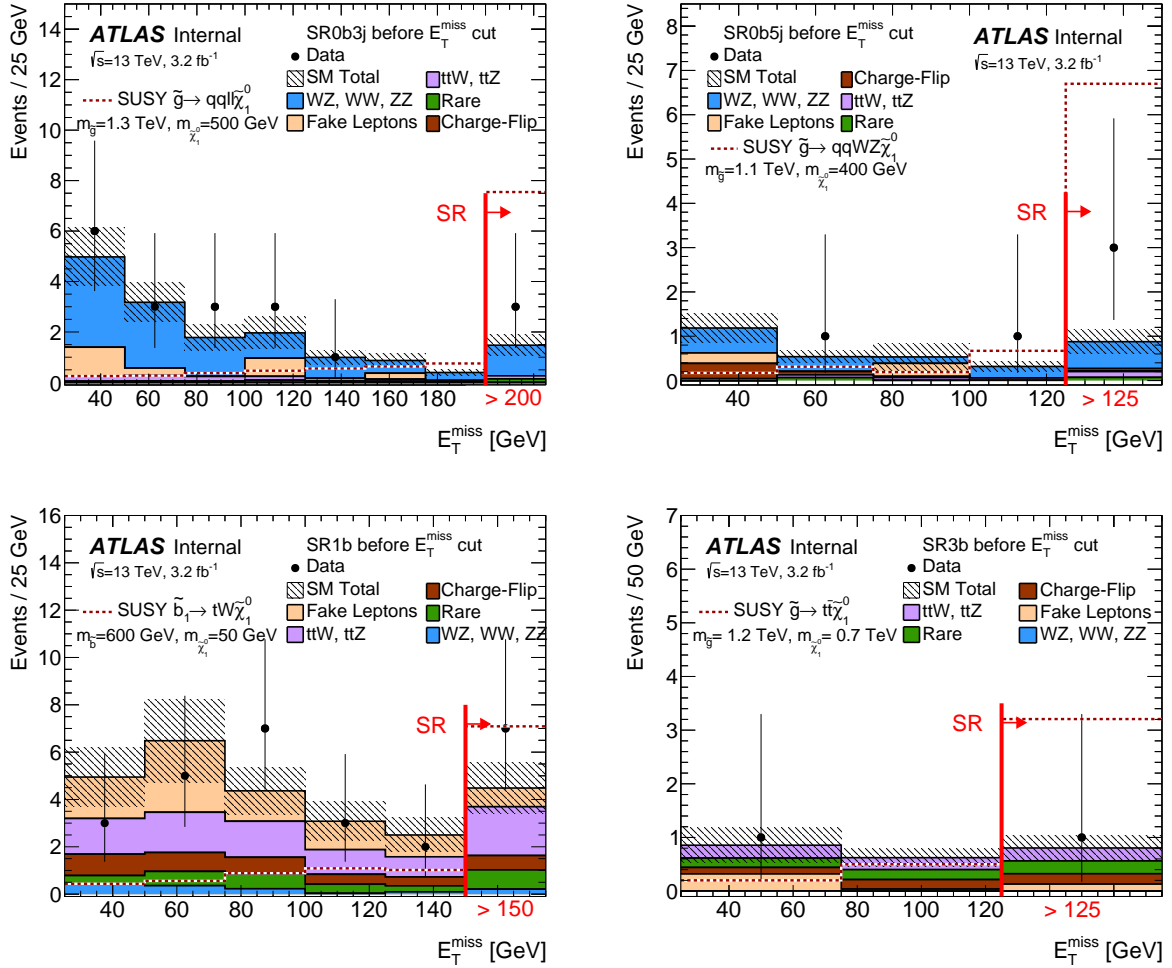


Figure 88: Missing transverse energy distribution close by and in the SR0b3j, SR0b5j, SR1b and SR3b signal regions (from top-left to bottom-right). The results in the signal regions correspond to the last bin (inclusive) of each plot.

1578 11.3 Discovery fits

1579 A first estimate of the level of agreement between data and MC can be obtained using *discovery* fits. These
 1580 are model-independent discovery fits in which an extra contribution is added to the SM backgrounds and a
 1581 fit to data in the signal regions is performed. The result of the fit is the “signal-strength” of the additional
 1582 contribution. The resulting event yields are shown in Tables 44, 45, 46 and 47.

1583 11.4 Model-independent upper limits

1584 Upper limits are set on possible BSM contributions to the signal region by fitting each of them independently
 1585 with a free toy signal, similarly to the previous section. To improve the stability of the test statistic,
 1586 we however use a simplified likelihood expressed as function of the total expected background together
 1587 with its total associated uncertainty, so that only one nuisance parameter and the arbitrary signal strength

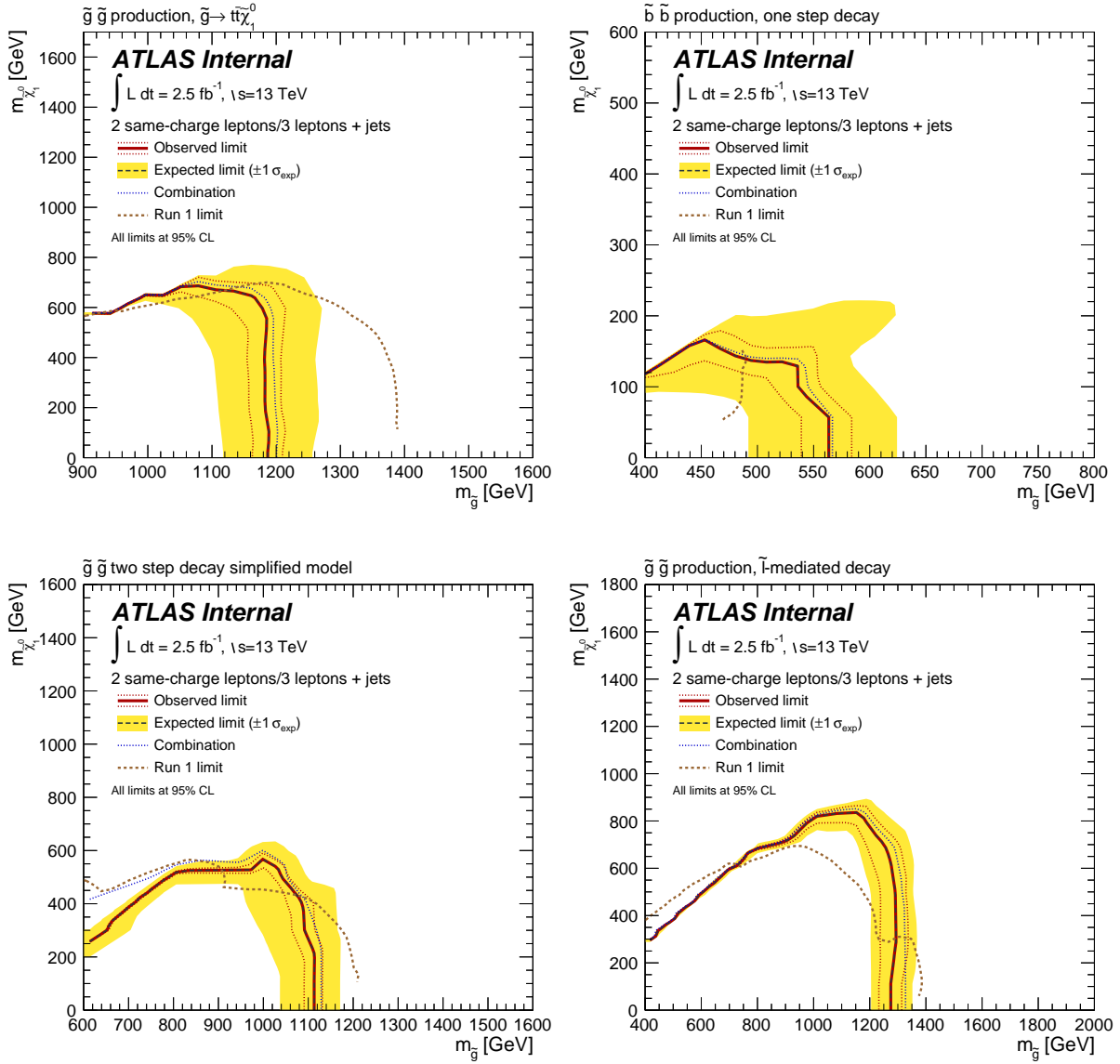


Figure 89: Comparison of the analysis sensitivities for different signal grids assuming 2.47 fb^{-1} . The exclusion curve obtained combining all the signal regions is only marginally better than the result obtained using only the best-performing signal region. Data is blinded in this plot.

remain free in the fit. We evaluate said upper limits with 10k toys and using a division of the scanned signal strength range into 75 intervals. The resulting upper limits are presented in Table 48.

	SR0b3j
Yields	
Observed events	1
Fitted bkg events	1.47 ± 0.44
Fitted WWjj events	0.00 ± 0.00
Fitted WZ events	1.20 ± 0.40
Fitted ttZ events	0.10 ± 0.04
Fitted ttW events	0.02 ± 0.01
Fitted Rare events	0.14 ± 0.08
Fitted OtherMultiBoson events	0.01 ± 0.01
Fitted Fakes events	0.00 ± 0.00
Fitted MisCharge events	0.00 ± 0.00
MC exp. SM events	1.47
MC exp. WWjj events	0.00
MC exp. WZ events	1.20
MC exp. ttZ events	0.10
MC exp. ttW events	0.02
MC exp. Rare events	0.14
MC exp. OtherMultiBoson events	0.01
MC exp. Fakes events	0.00
MC exp. MisCharge events	0.00

Table 36: Event yields for a background-only blind fit for SR0b3j, at an integrated luminosity of 3.21 fb^{-1} . Only systematic uncertainties are displayed for the individual processes, but the uncertainty on the total background also includes the statistical component.

Yields	SR0b5j
Observed events	0
Fitted bkg events	0.88 ± 0.29
Fitted WWjj events	0.12 ± 0.06
Fitted WZ events	0.49 ± 0.20
Fitted ttZ events	0.05 ± 0.03
Fitted ttW events	0.08 ± 0.04
Fitted Rare events	0.07 ± 0.05
Fitted OtherMultiBoson events	$0.00^{+0.04}_{-0.00}$
Fitted Fakes events	$0.05^{+0.06}_{-0.05}$
Fitted MisCharge events	0.02 ± 0.01
MC exp. SM events	0.88
MC exp. WWjj events	0.12
MC exp. WZ events	0.49
MC exp. ttZ events	0.05
MC exp. ttW events	0.08
MC exp. Rare events	0.07
MC exp. OtherMultiBoson events	0.00
MC exp. Fakes events	0.05
MC exp. MisCharge events	0.02

Table 37: Event yields for a background-only blind fit for SR0b5j, at an integrated luminosity of 3.21 fb^{-1} . Only systematic uncertainties are displayed for the individual processes, but the uncertainty on the total background also includes the statistical component.

Yields	SR1b
Observed events	4
Fitted bkg events	4.48 ± 1.02
Fitted WWjj events	0.03 ± 0.01
Fitted WZ events	0.18 ± 0.09
Fitted ttZ events	0.92 ± 0.31
Fitted ttW events	1.14 ± 0.38
Fitted Rare events	0.81 ± 0.42
Fitted OtherMultiBoson events	$0.00^{+0.00}_{-0.00}$
Fitted Fakes events	0.79 ± 0.57
Fitted MisCharge events	0.60 ± 0.09
MC exp. SM events	4.48
MC exp. WWjj events	0.03
MC exp. WZ events	0.18
MC exp. ttZ events	0.92
MC exp. ttW events	1.14
MC exp. Rare events	0.81
MC exp. OtherMultiBoson events	0.00
MC exp. Fakes events	0.79
MC exp. MisCharge events	0.60

Table 38: Event yields for a background-only blind fit for SR1b, at an integrated luminosity of 3.21 fb^{-1} . Only systematic uncertainties are displayed for the individual processes, but the uncertainty on the total background also includes the statistical component.

Yields	SR3b
Yields	SR3b
Observed events	0
Fitted bkg events	0.80 ± 0.25
Fitted WWjj events	0.00 ± 0.00
Fitted WZ events	0.00 ± 0.00
Fitted ttZ events	0.14 ± 0.06
Fitted ttW events	0.10 ± 0.05
Fitted Rare events	0.24 ± 0.14
Fitted OtherMultiBoson events	0.00 ± 0.00
Fitted Fakes events	0.13 ± 0.09
Fitted MisCharge events	0.19 ± 0.04
MC exp. SM events	0.80
MC exp. WWjj events	0.00
MC exp. WZ events	0.00
MC exp. ttZ events	0.14
MC exp. ttW events	0.10
MC exp. Rare events	0.24
MC exp. OtherMultiBoson events	0.00
MC exp. Fakes events	0.13
MC exp. MisCharge events	0.19

Table 39: Event yields for a background-only blind fit for SR3b, at an integrated luminosity of 3.21 fb^{-1} . Only systematic uncertainties are displayed for the individual processes, but the uncertainty on the total background also includes the statistical component.

Uncertainty of channel	SR0b3j
Total background expectation	1.47
Total statistical ($\sqrt{N_{\text{exp}}}$)	± 1.21
Total background systematic	$\pm 0.44 [29.65\%]$
alpha_theoryUncertWZ_SR0b3j	± 0.34
alpha_JET_scale_NP1	± 0.17
gamma_stat_SR0b3j_cuts_bin_0	± 0.16
alpha_PDF	± 0.09
Lumi	± 0.07
alpha_theoryUncertRare	± 0.07
alpha_pileupBKG	± 0.07
alpha_FT_B	± 0.06
alpha_JET_scale_NP2	± 0.05
alpha_JET_reso	± 0.04
alpha_JET_scale_NP3	± 0.04
alpha_theoryUncertTTbarV_SR0b3j	± 0.04
alpha_elID	± 0.02
alpha_MET_Soft_reso_Para	± 0.02
alpha_muSys	± 0.02
alpha_FT_Light	± 0.01
alpha_FT_C	± 0.01
alpha_muIsoSys	± 0.01
alpha_elReco	± 0.01
alpha_Mu_ID	± 0.01
alpha_MET_Soft_Scale	± 0.01
alpha_muStat	± 0.01
alpha_FT_Extra1	± 0.00
alpha_theoryUncertOtherMB	± 0.00
alpha_muIsoStat	± 0.00
alpha_EG_Resolution	± 0.00
alpha_MET_Soft_reso_Perp	± 0.00
alpha_Mu_MS	± 0.00
alpha_elTrig	± 0.00
alpha_FT_Extra2	± 0.00
alpha_Mu_Scale	± 0.00
alpha_EG_Scale	± 0.00
alpha_JET_AFII	± 0.00

Table 40: Systematics for a background-only blind fit in SR0b3j, at an integrated luminosity of 3.21 fb^{-1} .

Uncertainty of channel	SR0b5j
Total background expectation	0.88
Total statistical ($\sqrt{N_{\text{exp}}}$)	± 0.94
Total background systematic	$\pm 0.29 [33.52\%]$
gamma_stat_SR0b5j_cuts_bin_0	± 0.20
alpha_theoryUncertWZ_SR0b5j	± 0.14
alpha_JET_reso	± 0.08
alpha_pileupBKG	± 0.06
alpha_FT_B	± 0.06
alpha_PDF	± 0.06
alpha_JET_scale_NP1	± 0.06
alpha_JET_scale_NP3	± 0.06
alpha_syst_fake_SR0b5j	± 0.06
alpha_JET_scale_NP2	± 0.05
Lumi	± 0.04
alpha_theoryUncertTTbarV_SR0b5j	± 0.04
alpha_theoryUncertWWjj_SR0b5j	± 0.04
alpha_theoryUncertRare	± 0.03
alpha_Mu_MS	± 0.02
alpha_MET_Soft_reso_Perp	± 0.01
alpha_FT_C	± 0.01
alpha_elID	± 0.01
alpha_FT_Light	± 0.01
alpha_MET_Soft_Scale	± 0.01
alpha_muSys	± 0.01
alpha_muIsoSys	± 0.00
alpha_elReco	± 0.00
alpha_FT_Extra1	± 0.00
alpha_syst_misch_SR0b5j	± 0.00
alpha_elTrig	± 0.00
alpha_muStat	± 0.00
alpha_FT_Extra2	± 0.00
alpha_MET_Soft_reso_Para	± 0.00
alpha_muIsoStat	± 0.00
alpha_EG_Scale	± 0.00
alpha_Mu_ID	± 0.00
alpha_Mu_Scale	± 0.00
alpha_theoryUncertOtherMB	± 0.00
alpha_EG_Resolution	± 0.00
alpha_JET_AFII	± 0.00

Table 41: Systematics for a background-only blind fit in SR0b5j, at an integrated luminosity of 3.21 fb^{-1} .

Uncertainty of channel	SR1b
Total background expectation	4.48
Total statistical ($\sqrt{N_{\text{exp}}}$)	± 2.12
Total background systematic	± 1.02 [22.83%]
alpha_theoryUncertTTbarV_SR1b	± 0.59
alpha_syst_fake_SR1b	± 0.56
gamma_stat_SR1b_cuts_bin_0	± 0.52
alpha_theoryUncertRare	± 0.40
alpha_PDF	± 0.29
alpha_JET_scale_NP1	± 0.25
Lumi	± 0.15
alpha_FT_B	± 0.13
alpha_JET_scale_NP2	± 0.12
alpha_JET_reso	± 0.09
alpha_pileupBKG	± 0.07
alpha_JET_scale_NP3	± 0.06
alpha_theoryUncertWZ_SR1b	± 0.05
alpha_syst_misch_SR1b	± 0.05
alpha_FT_C	± 0.04
alpha_elID	± 0.04
alpha_MET_Soft_reso_Para	± 0.03
alpha_muSys	± 0.02
alpha_elReco	± 0.02
alpha_muIsoSys	± 0.01
alpha_MET_Soft_Scale	± 0.01
alpha_FT_Extra1	± 0.01
alpha_Mu_MS	± 0.01
alpha_theoryUncertWWjj_SR1b	± 0.01
alpha_elTrig	± 0.01
alpha_Mu_ID	± 0.01
alpha_muStat	± 0.01
alpha_MET_Soft_reso_Perp	± 0.01
alpha_Mu_Scale	± 0.00
alpha_EG_Resolution	± 0.00
alpha_muIsoStat	± 0.00
alpha_EG_Scale	± 0.00
alpha_JET_AFII	± 0.00
alpha_FT_Extra2	± 0.00
alpha_FT_Light	± 0.00
alpha_theoryUncertOtherMB	± 0.00

Table 42: Systematics for a background-only blind fit in SR1b, at an integrated luminosity of 3.21 fb^{-1} .

Uncertainty of channel	SR3b
Total background expectation	0.80
Total statistical ($\sqrt{N_{\text{exp}}}$)	± 0.90
Total background systematic	$\pm 0.25 [30.66\%]$
gamma_stat_SR3b_cuts_bin_0	± 0.16
alpha_theoryUncertRare	± 0.12
alpha_syst_fake_SR3b	± 0.09
alpha_theoryUncertTTbarV_SR3b	± 0.07
alpha_FT_B	± 0.07
alpha_PDF	± 0.06
alpha_FT_C	± 0.04
alpha_JET_scale_NP1	± 0.03
Lumi	± 0.02
alpha_FT_Light	± 0.02
alpha_syst_misch_SR3b	± 0.02
alpha_JET_reso	± 0.02
alpha_JET_scale_NP2	± 0.02
alpha_pileupBKG	± 0.01
alpha_elID	± 0.01
alpha_MET_Soft_reso_Perp	± 0.01
alpha_FT_Extra1	± 0.01
alpha_MET_Soft_reso_Para	± 0.00
alpha_Mu_MS	± 0.00
alpha_FT_Extra2	± 0.00
alpha_muSys	± 0.00
alpha_elReco	± 0.00
alpha_JET_scale_NP3	± 0.00
alpha_muIsoSys	± 0.00
alpha_MET_Soft_Scale	± 0.00
alpha_EG_Resolution	± 0.00
alpha_elTrig	± 0.00
alpha_muStat	± 0.00
alpha_EG_Scale	± 0.00
alpha_muIsoStat	± 0.00
alpha_JET_AFII	± 0.00
alpha_Mu_ID	± 0.00
alpha_Mu_Scale	± 0.00

Table 43: Systematics for a background-only blind fit in SR3b, at an integrated luminosity of 3.2 fb^{-1} .

Yields	SR0b3j
Observed events	3
Fitted bkg events	3.01 ± 1.61
Fitted WWjj events	0.00 ± 0.00
Fitted WZ events	1.20 ± 0.43
Fitted ttZ events	0.10 ± 0.04
Fitted ttW events	0.02 ± 0.01
Fitted Rare events	0.14 ± 0.08
Fitted OtherMultiBoson events	0.01 ± 0.01
Fitted DiscoveryMode_SR0b3j events	$1.54^{+1.66}_{-1.54}$
Fitted Fakes events	0.00 ± 0.00
Fitted MisCharge events	0.00 ± 0.00
MC exp. SM events	2.47
MC exp. WWjj events	0.00
MC exp. WZ events	1.20
MC exp. ttZ events	0.10
MC exp. ttW events	0.02
MC exp. Rare events	0.14
MC exp. OtherMultiBoson events	0.01
MC exp. DiscoveryMode_SR0b3j events	1.00
MC exp. Fakes events	0.00
MC exp. MisCharge events	0.00

Table 44: Event yields for a discovery fit SR0b3j, at an integrated luminosity of 3.21 fb^{-1} . Only systematic uncertainties are displayed for the individual processes, but the uncertainty on the total background also includes the statistical component.

Yields	SR0b5j
Observed events	3
Fitted bkg events	3.02 ± 1.73
Fitted WWjj events	0.12 ± 0.06
Fitted WZ events	0.49 ± 0.21
Fitted ttZ events	0.05 ± 0.03
Fitted ttW events	0.08 ± 0.04
Fitted Rare events	0.07 ± 0.05
Fitted OtherMultiBoson events	$0.00^{+0.04}_{-0.00}$
Fitted DiscoveryMode_SR0b5j events	2.14 ± 1.76
Fitted Fakes events	$0.05^{+0.06}_{-0.05}$
Fitted MisCharge events	0.02 ± 0.01
MC exp. SM events	1.88
MC exp. WWjj events	0.12
MC exp. WZ events	0.49
MC exp. ttZ events	0.05
MC exp. ttW events	0.08
MC exp. Rare events	0.07
MC exp. OtherMultiBoson events	0.00
MC exp. DiscoveryMode_SR0b5j events	1.00
MC exp. Fakes events	0.05
MC exp. MisCharge events	0.02

Table 45: Event yields for a discovery fit SR0b5j, at an integrated luminosity of 3.21 fb^{-1} . Only systematic uncertainties are displayed for the individual processes, but the uncertainty on the total background also includes the statistical component.

Yields	SR1b
Observed events	7
Fitted bkg events	7.03 ± 2.46
Fitted WWjj events	0.03 ± 0.01
Fitted WZ events	0.18 ± 0.09
Fitted ttZ events	0.93 ± 0.34
Fitted ttW events	1.15 ± 0.41
Fitted Rare events	0.82 ± 0.44
Fitted OtherMultiBoson events	$0.00^{+0.00}_{-0.00}$
Fitted DiscoveryMode_SR1b events	$2.51^{+2.70}_{-2.51}$
Fitted Fakes events	0.81 ± 0.60
Fitted MisCharge events	0.60 ± 0.09
MC exp. SM events	5.48
MC exp. WWjj events	0.03
MC exp. WZ events	0.18
MC exp. ttZ events	0.92
MC exp. ttW events	1.14
MC exp. Rare events	0.81
MC exp. OtherMultiBoson events	0.00
MC exp. DiscoveryMode_SR1b events	1.00
MC exp. Fakes events	0.79
MC exp. MisCharge events	0.60

Table 46: Event yields for a discovery fit SR1b, at an integrated luminosity of 3.21 fb^{-1} . Only systematic uncertainties are displayed for the individual processes, but the uncertainty on the total background also includes the statistical component.

Yields	SR3b
Observed events	1
Fitted bkg events	1.04 ± 0.67
Fitted WWjj events	0.00 ± 0.00
Fitted WZ events	0.00 ± 0.00
Fitted ttZ events	0.14 ± 0.06
Fitted ttW events	0.10 ± 0.05
Fitted Rare events	0.24 ± 0.14
Fitted OtherMultiBoson events	0.00 ± 0.00
Fitted DiscoveryMode_SR3b events	$0.23^{+0.68}_{-0.23}$
Fitted Fakes events	0.13 ± 0.09
Fitted MisCharge events	0.19 ± 0.04
MC exp. SM events	1.80
MC exp. WWjj events	0.00
MC exp. WZ events	0.00
MC exp. ttZ events	0.14
MC exp. ttW events	0.10
MC exp. Rare events	0.24
MC exp. OtherMultiBoson events	0.00
MC exp. DiscoveryMode_SR3b events	1.00
MC exp. Fakes events	0.13
MC exp. MisCharge events	0.19

Table 47: Event yields for a discovery fit SR3b, at an integrated luminosity of 3.21 fb^{-1} . Only systematic uncertainties are displayed for the individual processes, but the uncertainty on the total background also includes the statistical component.

Table 48: Signal model-independent upper limits on the visible signal cross-section ($\sigma_{\text{vis}} = \sigma_{\text{prod}} \times A \times \epsilon$) and on the number of BSM events (N_{BSM}) in the four SRs. The numbers (in parentheses) give the observed (expected under the SM hypothesis) 95% CL upper limits. Calculations are performed with pseudo-experiments. The $\pm 1\sigma$ variations on the expected limit due to the statistical and systematic uncertainties on the background prediction are also shown.

	SR0b3j	SR0b5j	SR1b	SR3b
$\sigma_{\text{vis}}^{\text{obs}} [\text{fb}]$	1.8	2.0	2.8	1.2
$N_{\text{BSM}}^{\text{obs}} (N_{\text{BSM}}^{\text{exp}})$	$5.9 (4.1^{+1.6}_{-0.8})$	$6.4 (3.6^{+1.2}_{-1.1})$	$8.8 (6.0^{+2.6}_{-1.6})$	$3.8 (3.7^{+1.1}_{-0.5})$

1590 11.5 Exclusion plots

1591 The exclusion limits for the models of interest are shown in Figure 90. The new limits set by this analysis
 1592 can be compared to the existing limits set by the combination of ATLAS SUSY searches with 8 TeV data.
 1593 The sensitivity reached with this first 13 TeV dataset is already at the level of the entire 8 TeV dataset, and
 1594 in all cases additional parameter space regions can be excluded, especially for large neutralino masses.

1595 Signal models featuring gluino pair production and light sleptons in their decay ($\tilde{g} \rightarrow q\bar{q}\tilde{\chi}_2^0 \rightarrow q\bar{q}\ell\tilde{\ell}^* \rightarrow$
 1596 $q\bar{q}\ell^+\ell^-\tilde{\chi}_1^0$) are probed using SR0b3j, excluding gluino masses of up to $m_{\tilde{g}} \approx 1.3$ TeV for a massless LSP
 1597 and excluding $\tilde{\chi}_1^0$ masses of up to $m_{\tilde{\chi}_1^0} \approx 850$ GeV for gluinos with $m_{\tilde{g}} \approx 1$ TeV. Similarly, models with
 1598 gluino production with a subsequent two-step gluino decay via $\tilde{\chi}_1^\pm$ and $\tilde{\chi}_2^0$ ($\tilde{g} \rightarrow q\bar{q}\tilde{\chi}_1^\pm \rightarrow q\bar{q}W\tilde{\chi}_2^0 \rightarrow$
 1599 $q\bar{q}WZ\tilde{\chi}_1^0$) are probed with SR0b5j with exclusion limits reaching $m_{\tilde{g}} \approx 1.1$ TeV (for massless $\tilde{\chi}_1^0$) and
 1600 $m_{\tilde{\chi}_1^0} \approx 500$ GeV (for $m_{\tilde{g}} \approx 0.9$ TeV).

1601 Exclusion limits in a simplified model of bottom squark production with chargino-mediated $\tilde{b}_1 \rightarrow tW^-\tilde{\chi}_1^0$
 1602 decays are obtained with SR1b and can reach mass values of $m_{\tilde{b}_1} \approx 550$ GeV for a massless $\tilde{\chi}_1^0$, while
 1603 $m_{\tilde{\chi}_1^0} \approx 130$ GeV are also excluded for $m_{\tilde{b}_1} \approx 450$ GeV. Finally, SR3b is used to set limits on the
 1604 $\tilde{g}\tilde{g}$ simplified model with $\tilde{g} \rightarrow t\bar{t}\tilde{\chi}_1^0$ decays via an off-shell top squark. In that case, gluino masses
 1605 of $m_{\tilde{g}} < 1.2$ TeV are excluded for $m_{\tilde{\chi}_1^0} \approx 500$ GeV, with $m_{\tilde{\chi}_1^0} < 700$ GeV also being excluded for
 1606 $m_{\tilde{g}} \approx 1.05$ TeV.

1607 The exclusion limits for the models of interest with their cross-section upper limits are shown in Figure 91.
 1608

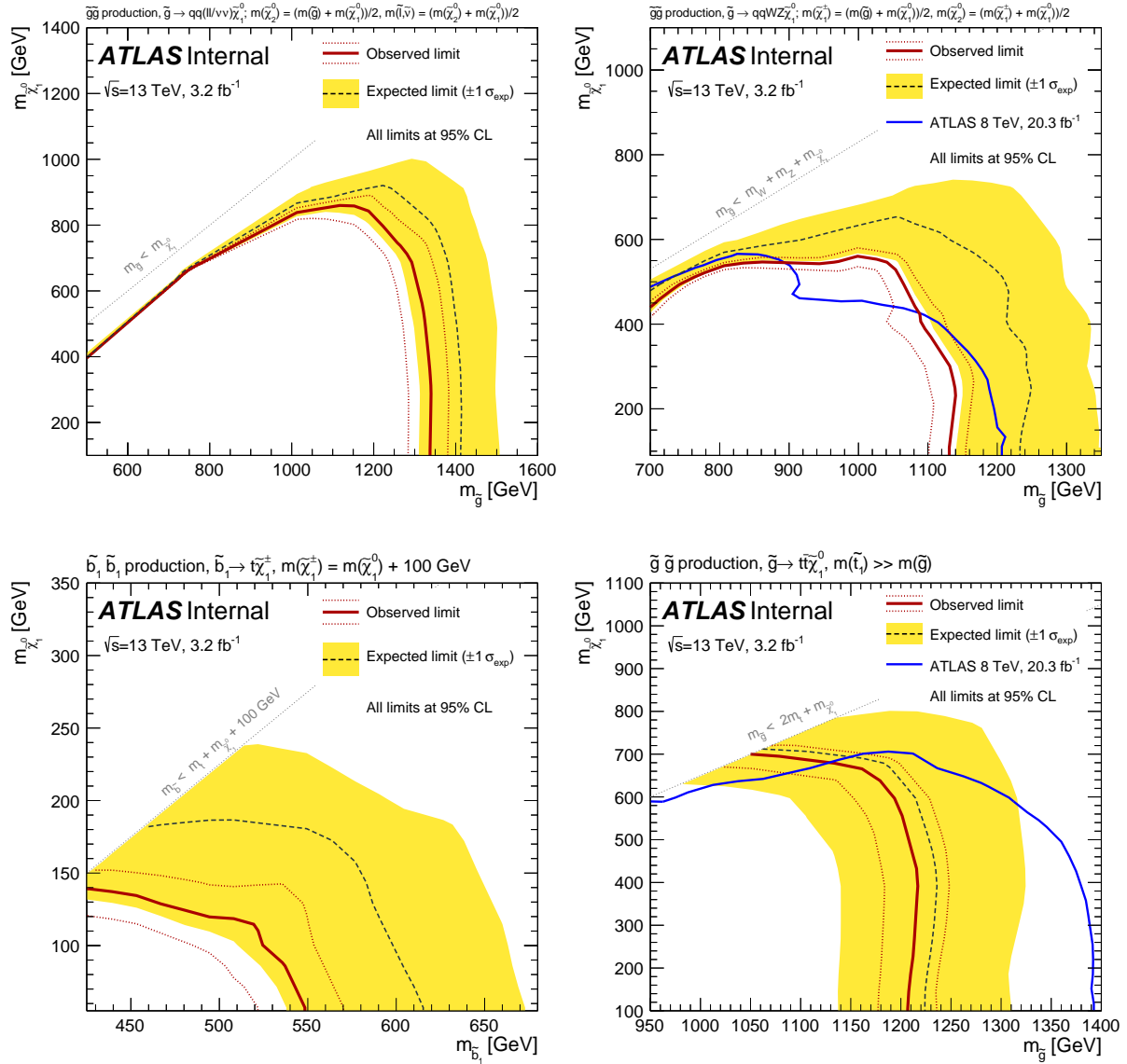


Figure 90: Observed and expected exclusion limits on the \tilde{g} , \tilde{b}_1 and $\tilde{\chi}_1^0$ masses in the context of SUSY scenarios with simplified mass spectra featuring $\tilde{g}\tilde{g}$ or $\tilde{b}_1\tilde{b}_1^*$ pair production with exclusive decay modes. The signal region used to obtain the limits is specified for each scenario. The contours of the band around the expected limit are the $\pm 1\sigma$ results, including all uncertainties except theoretical uncertainties on the signal cross-section. The dotted lines around the observed limit illustrate the change in the observed limit as the nominal signal cross-section is scaled up and down by the theoretical uncertainty. All limits are computed at 95% CL. Results are compared with the limits obtained by previous ATLAS searches

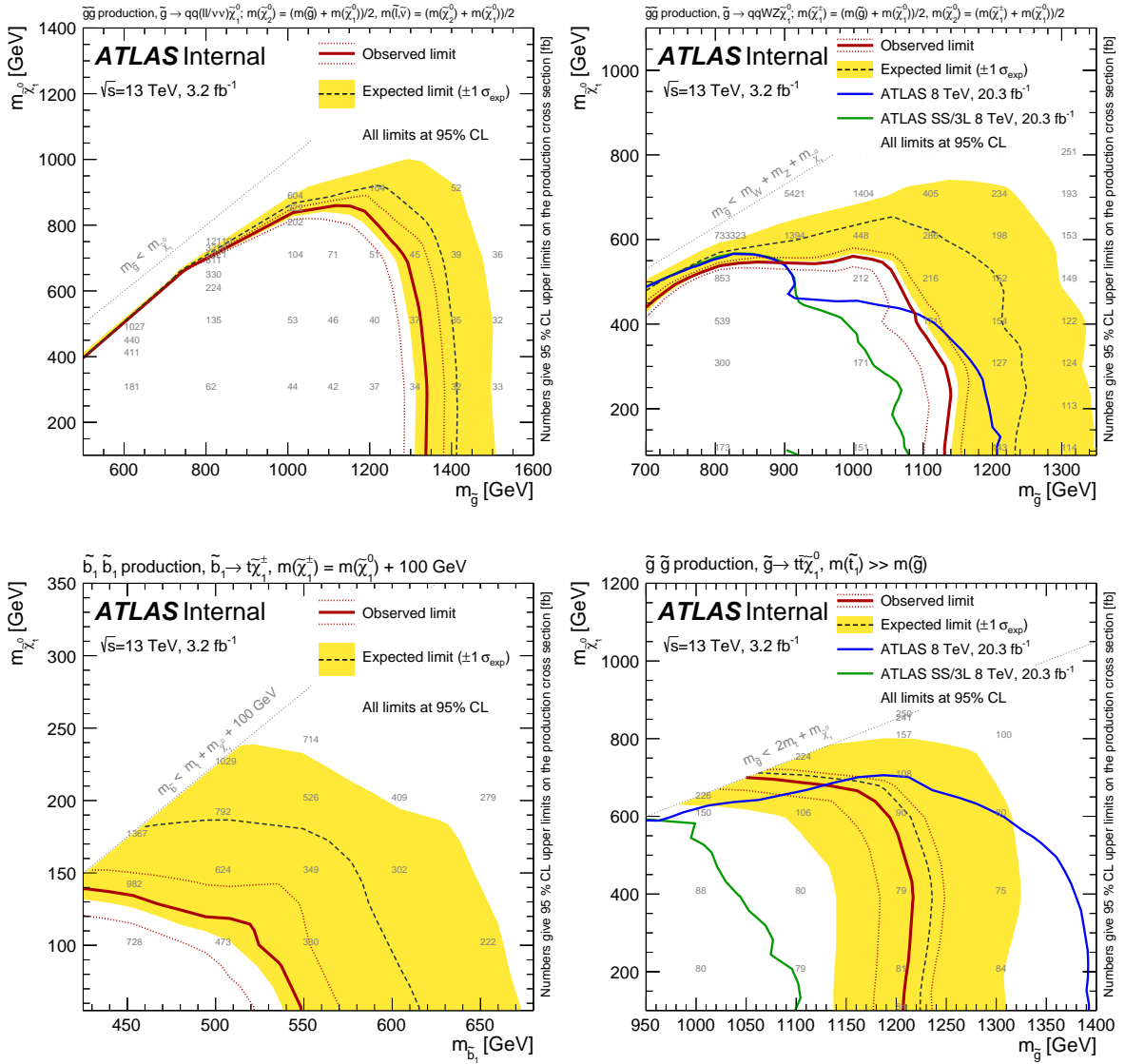


Figure 91: Observed and expected exclusion limits on the \tilde{g} , \tilde{b}_1 and $\tilde{\chi}_1^0$ masses in the context of SUSY scenarios with simplified mass spectra featuring $\tilde{g}\tilde{g}$ or $\tilde{b}_1\tilde{b}_1^*$ pair production with exclusive decay modes. The contours of the band around the expected limit are the $\pm 1\sigma$ results, including all uncertainties except theoretical uncertainties on the signal cross-section. The dotted lines around the observed limit illustrate the change in the observed limit as the nominal signal cross-section is scaled up and down by the theoretical uncertainty. All limits are computed at 95% CL. The grey numbers show 95% CL upper limits on cross-sections (in fb) obtained using the signal efficiency and acceptance specific to each model.

1609 12 Conclusion

1610 A search for supersymmetry in events with exactly two same-sign leptons or at least three leptons, multiple
1611 jets and E_T^{miss} is presented. The analysis is performed with proton-proton collision data at $\sqrt{s} = 13$ TeV
1612 collected with the ATLAS detector at the Large Hadron Collider corresponding to an integrated luminosity
1613 of 3.2 fb^{-1} . With no significant excess over the Standard Model background expectation, results are
1614 interpreted in the framework of simplified models featuring gluino and bottom squark production. In the
1615 $\tilde{g}\tilde{g}$ simplified models considered, $m_{\tilde{g}} < 1.1 - 1.3$ TeV and $m_{\tilde{\chi}_1^0} < 550 - 850$ GeV are excluded at 95%
1616 confidence level depending on the model parameters. Bottom squark masses of $m_{\tilde{b}_1} < 550$ GeV are also
1617 excluded for a light $\tilde{\chi}_1^0$ in a \tilde{b}_1 simplified model with $\tilde{b}_1 \rightarrow tW^-\tilde{\chi}_1^0$. These results are complementary to
1618 and extend the exclusion limits by previous searches.

1619 References

- 1620 [1] H. Miyazawa, *Baryon Number Changing Currents*, Prog. Theor. Phys. **36** (6) (1966) 1266.
- 1621 [2] P. Ramond, *Dual Theory for Free Fermions*, Phys. Rev. **D 3** (1971) 2415.
- 1622 [3] Y. A. Gol'fand and E. P. Likhtman,
1623 *Extension of the Algebra of Poincare Group Generators and Violation of p Invariance*,
1624 JETP Lett. **13** (1971) 323, [Pisma Zh.Eksp.Teor.Fiz.13:452-455,1971].
- 1625 [4] A. Neveu and J. H. Schwarz, *Factorizable dual model of pions*, Nucl. Phys. **B 31** (1971) 86.
- 1626 [5] A. Neveu and J. H. Schwarz, *Quark Model of Dual Pions*, Phys. Rev. **D 4** (1971) 1109.
- 1627 [6] J. Gervais and B. Sakita, *Field theory interpretation of supergauges in dual models*,
1628 Nucl. Phys. **B 34** (1971) 632.
- 1629 [7] D. V. Volkov and V. P. Akulov, *Is the Neutrino a Goldstone Particle?*, Phys. Lett. **B 46** (1973) 109.
- 1630 [8] J. Wess and B. Zumino, *A Lagrangian Model Invariant Under Supergauge Transformations*,
1631 Phys. Lett. **B 49** (1974) 52.
- 1632 [9] J. Wess and B. Zumino, *Supergauge Transformations in Four-Dimensions*,
1633 Nucl. Phys. **B 70** (1974) 39.
- 1634 [10] P. Fayet, *Supersymmetry and Weak, Electromagnetic and Strong Interactions*,
1635 Phys. Lett. **B 64** (1976) 159.
- 1636 [11] P. Fayet, *Spontaneously Broken Supersymmetric Theories of Weak, Electromagnetic and Strong
1637 Interactions*, Phys. Lett. **B 69** (1977) 489.
- 1638 [12] G. R. Farrar and P. Fayet, *Phenomenology of the Production, Decay, and Detection of New
1639 Hadronic States Associated with Supersymmetry*, Phys. Lett. **B 76** (1978) 575.
- 1640 [13] P. Fayet, *Relations Between the Masses of the Superpartners of Leptons and Quarks, the Goldstino
1641 Couplings and the Neutral Currents*, Phys. Lett. **B84** (1979) 416.
- 1642 [14] B Abbot et al., ‘Search for strongly produced superpartners in final states with same-sign leptons
1643 or three leptons and jets: preparing for 2015 analyses’, tech. rep. ATL-COM-PHYS-2015-329,
1644 CERN, 2013, URL: <http://cds.cern.ch/record/2012029/files/ATL-COM-PHYS-2015-329.pdf?version=4>.
- 1646 [15] *Search for supersymmetry at $\sqrt{s}=8$ TeV in final states with jets and two same-sign leptons or three
1647 leptons with the ATLAS detector*, JHEP **1406** (2014) 035, arXiv: [1404.2500](https://arxiv.org/abs/1404.2500) [hep-ex].
- 1648 [16] J.-F. Arguin et al., ‘Search for strongly-produced superpartners in final states with two same-sign
1649 leptons or three leptons at $\sqrt{s} = 8$ TeV’, tech. rep. ATL-COM-PHYS-2013-887, CERN, 2013,
1650 URL: <http://cds.cern.ch/record/1558979>.
- 1651 [17] G. Herten et al.,
1652 ‘Summary of the Searches for Inclusive Squarks and Gluinos with Run I LHC data at ATLAS’,
1653 tech. rep. ATL-COM-PHYS-2014-929, CERN, 2014,
1654 URL: <http://cds.cern.ch/record/1746381>.
- 1655 [18] C. Borschensky et al.,
1656 *Squark and gluino production cross sections in pp collisions at $\sqrt{s} = 13, 14, 33$ and 100 TeV,
1657 Eur.Phys.J. **C74**.12 (2014) 3174, arXiv: [1407.5066](https://arxiv.org/abs/1407.5066) [hep-ph].*

- [19] J. Alwall et al., *The automated computation of tree-level and next-to-leading order differential cross sections, and their matching to parton shower simulations*, *JHEP* **07** (2014) 079, arXiv: [1405.0301 \[hep-ph\]](#).
- [20] T. Sjostrand, S. Mrenna and P. Z. Skands, *A Brief Introduction to PYTHIA 8.1*, *Comput. Phys. Commun.* **178** (2008) 852–867, arXiv: [0710.3820 \[hep-ph\]](#).
- [21] ATLAS Collaboration, *ATLAS Pythia8 tunes to 7 TeV data*, ATL-PHYS-PUB-2014-021 (2014), eprint: <http://cds.cern.ch/record/1966419>.
- [22] S. Carrazza, S. Forte and J. Rojo, ‘Parton Distributions and Event Generators’, *Proceedings, 43rd International Symposium on Multiparticle Dynamics (ISMD 13)*, 2013 89–96, arXiv: [1311.5887 \[hep-ph\]](#), URL: <http://inspirehep.net/record/1266070/files/arXiv:1311.5887.pdf>.
- [23] L. Lonnblad and S. Prestel, *Matching Tree-Level Matrix Elements with Interleaved Showers*, *JHEP* **03** (2012) 019, arXiv: [1109.4829 \[hep-ph\]](#).
- [24] P. Nason, *A New method for combining NLO QCD with shower Monte Carlo algorithms*, *JHEP* **0411** (2004) 040, arXiv: [hep-ph/0409146 \[hep-ph\]](#).
- [25] S. Frixione, P. Nason and C. Oleari, *Matching NLO QCD computations with Parton Shower simulations: the POWHEG method*, *JHEP* **0711** (2007) 070, arXiv: [0709.2092 \[hep-ph\]](#).
- [26] S. Alioli et al., *A general framework for implementing NLO calculations in shower Monte Carlo programs: the POWHEG BOX*, *JHEP* **1006** (2010) 043, arXiv: [1002.2581 \[hep-ph\]](#).
- [27] T. Sjostrand, S. Mrenna and P. Z. Skands, *PYTHIA 6.4 Physics and Manual*, *JHEP* **0605** (2006) 026, arXiv: [hep-ph/0603175 \[hep-ph\]](#).
- [28] P. Z. Skands, *Tuning Monte Carlo Generators: The Perugia Tunes*, *Phys.Rev.* **D82** (2010) 074018, arXiv: [1005.3457 \[hep-ph\]](#).
- [29] M. Czakon and A. Mitov, *Top++: A Program for the Calculation of the Top-Pair Cross-Section at Hadron Colliders*, *Comput.Phys.Commun.* **185** (2014) 2930, arXiv: [1112.5675 \[hep-ph\]](#).
- [30] T. Gleisberg et al., *Event generation with SHERPA 1.1*, *JHEP* **02** (2009) 007, arXiv: [0811.4622](#).
- [31] S. Catani et al., *Vector boson production at hadron colliders: a fully exclusive QCD calculation at NNLO*, *Phys.Rev.Lett.* **103** (2009) 082001, arXiv: [0903.2120 \[hep-ph\]](#).
- [32] G. Aad et al., *The ATLAS Simulation Infrastructure*, *Eur.Phys.J.* **C70** (2010) 823–874, arXiv: [1005.4568 \[physics.ins-det\]](#).
- [33] S. Agostinelli et al., *GEANT4: A Simulation toolkit*, *Nucl.Instrum.Meth.* **A506** (2003) 250–303.
- [34] ATLAS Collaboration, *The simulation principle and performance of the ATLAS fast calorimeter simulation FastCaloSim*, ATL-PHYS-PUB-2010-013, 2010, URL: <http://cds.cern.ch/record/1300517>.
- [35] A. Sherstnev and R. Thorne, *Parton Distributions for LO Generators*, *Eur.Phys.J.* **C55** (2008) 553–575, arXiv: [0711.2473 \[hep-ph\]](#).
- [36] *AtlasProductionGroupMC15a twiki*, <http://twiki.cern.ch/twiki/bin/view/AtlasProtected/AtlasProductionGroupMC15a>.

- 1699 [37] *AtlasProductionGroupMC15b* twiki, <http://twiki.cern.ch/twiki/bin/view/AtlasProtected/AtlasProductionGroupMC15b>.
- 1700 [38] ATLAS Collaboration, *Improved luminosity determination in pp collisions at $\sqrt{s} = 7$ TeV using the ATLAS detector at the LHC*, *Eur. Phys. J. C* **73** (2013) 2518, arXiv: [1302.4393 \[hep-ex\]](#).
- 1701 [39] M. Cacciari, G. P. Salam and G. Soyez, *The Anti- $k(t)$ jet clustering algorithm*, *JHEP* **0804** (2008) 063, arXiv: [0802.1189 \[hep-ph\]](#).
- 1702 [40] ATLAS Collaboration, *Tagging and suppression of pileup jets with the ATLAS detector*, ATLAS-CONF-2014-018, 2014, URL: <http://cdsweb.cern.ch/record/1700870>.
- 1703 [41] ATLAS Collaboration, *Electron efficiency measurements with the ATLAS detector using the 2012 LHC proton–proton collision data*, ATLAS-CONF-2014-032 (), eprint: <http://cdsweb.cern.ch/record/1706245>.
- 1704 [42] D. Adams and others,
‘Recommendations of the Physics Objects and Analysis Harmonisation Study Groups 2014’, tech. rep. ATL-PHYS-INT-2014-018, CERN, 2014,
URL: <http://cds.cern.ch/record/1743654>.
- 1705 [43] *JetEtmiss Group*, *How to clean jets*, <http://twiki.cern.ch/twiki/bin/viewauth/AtlasProtected/HowToCleanJets2011>.
- 1706 [44] *InDetTrackingPerformanceGuidelines*, *Pre-recommendations for Run-2*, <http://twiki.cern.ch/twiki/bin/view/AtlasProtected/InDetTrackingPerformanceGuidelines>.
- 1707 [45] J Boyd et al., ‘Studies of events with three leptons and three b-tagged jets observed in the full 2012 ATLAS dataset’, tech. rep. ATL-PHYS-INT-2014-006, CERN, 2014,
URL: <http://cds.cern.ch/record/1698061>.
- 1708 [46] O. A. Ducu et al., ‘Run-2 prospects for top Yukawa coupling measurement in the ttH channel with two same-sign leptons’, tech. rep. ATL-COM-PHYS-2015-479, CERN, 2015,
URL: <https://cds.cern.ch/record/2021084>.
- 1709 [47] R Bruneliere et al., ‘Search for gluinos with two same sign leptons, jets and missing transverse momentum at $\sqrt{s}=7$ TeV (supporting INT note)’, tech. rep. ATL-PHYS-INT-2012-042, CERN, 2012, URL: <http://cds.cern.ch/record/1442562>.
- 1710 [48] T. Gillam, *PhD thesis chapter 4 on matrix method and beyond*, http://bytebucket.org/tpgillam/bayesmm/raw/7e941bec4067b092c24ac2e23815cd08090d6d2c/docs/theory_extract.pdf.
- 1711 [49] J. M. Campbell and R. K. Ellis, *$t\bar{t}W^{+-}$ production and decay at NLO*, *JHEP* **1207** (2012) 052, arXiv: [1204.5678 \[hep-ph\]](#).
- 1712 [50] M. Garzelli et al., *$t\bar{t}W^\pm$ and $t\bar{t}Z$ Hadroproduction at NLO accuracy in QCD with Parton Shower and Hadronization effects*, *JHEP* **11** (2012) 056, arXiv: [1208.2665 \[hep-ph\]](#).
- 1713 [51] J. M. Campbell, R. K. Ellis and C. Williams, *Vector boson pair production at the LHC*, *JHEP* **07** (2011) 018, arXiv: [1105.0020 \[hep-ph\]](#).
- 1714 [52] M. Baak et al., *HistFitter software framework for statistical data analysis*, *Eur.Phys.J.* **C75.4** (2015) 153, arXiv: [1410.1280 \[hep-ex\]](#).
- 1715 [53] *ElectronIsolationSelectionTool* twiki, <http://twiki.cern.ch/twiki/bin/view/AtlasProtected/ElectronIsolationSelectionTool>.

- 1740 [54] *Official Isolation Working Points twiki*,
1741 <http://twiki.cern.ch/twiki/bin/view/AtlasProtected/IsolationSelectionTool>.
- 1742 [55] ATLAS Collaboration, *Search for direct top-squark pair production in final states with two*
1743 *leptons in pp collisions at $\sqrt{s} = 8$ TeV with the ATLAS detector*, JHEP **1406** (2014) 124,
1744 arXiv: [1403.4853 \[hep-ex\]](https://arxiv.org/abs/1403.4853).

₁₇₄₅ **Appendix**

13 Details on the overlap removal comparisons of rel19 and rel20

This appendix contains yield and significance comparisons for the release 19 and release 20 definitions of the object overlap removal [42]. DC14 samples were used for this study. An integrated luminosity of 3 fb^{-1} was assumed, and the example signal sample used was Herwigpp_UEEE4_CTEQ6L1_Gtt_G1000_T5000_L100. Tables 49 and 50 show the expected event yields for the different processes at different stages of the cut-flow for the ee , $e\mu$ and $\mu\mu$ channels for the rel-19 (i.e previous) and rel-20 (new) overlap-removal definitions. Last column displays the signal significance calculated with a Poissonian estimator ($Z = \sqrt{2((S+B)\log(1+S/B)-S)}$) robust in the low statistical regime. Systematic uncertainties have been ignored for this comparison.

Table 49: Expected event yields for the object overlap-removal definition in rel-19 assuming 3 fb^{-1} of integrated luminosity.

Selection	Signal	Top	Top+V	Single-Top	WZ	WW	ZZ	W+jets	Z+jets	Total	Significance
<i>ee</i>											
Lep Flavour	71.10	5334	630084	148.5	53.44	891.5	102.7	1145	124.84	637885	0.09
m_{ee}	71.10	5312	630083	134.0	53.38	889.2	101.4	1138	124.29	637836	0.09
b-Jets	68.40	4512	11560	2.32	46.63	622.6	5.38	40.19	5.97	16796	0.53
4-Jets 50GeV	63.00	225.8	68.38	0.00	14.66	13.93	0.09	0.52	0.04	323.4	3.40
Same-Sign	21.75	2.95	0.98	0.00	1.79	0.43	0.01	0.00	0.00	6.16	6.39
Missing E_T	18.60	0.37	0.00	0.00	0.39	0.00	0.00	0.00	0.00	0.76	9.38
<i>eμ</i>											
Lep Flavour	115.35	11008	1909	249.3	61.12	1814	98.91	2497	41.82	17681	0.87
$m_{e\mu}$	115.35	10973	1909	190.5	60.99	1810	97.43	2483	41.59	17565	0.87
b-Jets	112.20	9346	28.20	5.47	53.31	1270	4.62	84.96	1.62	10794	1.08
4-Jets 50GeV	99.75	457.4	0.16	0.00	12.37	19.51	0.08	0.92	0.01	490.4	4.36
Same-Sign	33.45	3.91	0.00	0.00	3.21	0.00	0.04	0.02	0.01	7.20	8.59
Missing E_T	28.20	0.30	0.00	0.00	0.69	0.00	0.01	0.00	0.00	1.00	11.85
<i>μμ</i>											
Lep Flavour	46.65	5668	667954	58.50	50.33	963.8	133.0	1378	160.41	676368	0.06
$m_{\mu\mu}$	46.50	5654	667953	58.50	50.26	962.1	132.0	1371	159.96	676342	0.06
b-Jets	45.90	4843	8952	0.03	44.27	671.9	6.69	46.46	7.02	14572	0.38
4-Jets 50GeV	40.35	231.1	50.04	0.00	13.70	12.64	0.09	0.41	0.04	308.1	2.25
Same-Sign	13.95	0.22	0.00	0.00	1.65	0.00	0.02	0.00	0.00	1.89	6.28
Missing E_T	11.70	0.00	0.00	0.00	0.35	0.00	0.01	0.00	0.00	0.36	7.84

Table 50: Expected event yields for the object overlap-removal definition in rel-20 assuming 3 fb^{-1} of integrated luminosity.

Selection	Signal	Top	Top+V	Single-Top	WZ	WW	ZZ	$W+\text{jets}$	$Z+\text{jets}$	Total	Significance
<i>ee</i>											
Lep Flavour	66.30	5234	626767	147.4	51.70	876.3	100.2	1139	122.8	634439	0.08
$m_{\ell\ell}$	66.30	5213	626766	132.9	51.64	874.0	99.02	1132	122.2	634391	0.08
b-Jets	64.05	4455	11478	2.24	45.44	619.8	5.53	39.62	6.18	16652	0.50
4-Jets 50GeV	59.55	222.9	67.44	0.00	14.47	13.50	0.10	0.52	0.04	318.9	3.24
Same-Sign	21.00	2.81	0.98	0.00	1.77	0.21	0.01	0.00	0.00	5.79	6.33
Missing E_T	18.15	0.37	0.00	0.00	0.39	0.00	0.00	0.00	0.00	0.76	9.24
<i>eμ</i>											
Lep Flavour	120.15	11879	2036	312.0	65.48	1975	102.0	2708	41.61	19121	0.87
$m_{e\mu}$	120.15	11843	2035	252.4	65.35	1971	100.5	2694	41.39	19004	0.87
b-Jets	116.85	10140	32.78	5.43	57.35	1395	5.08	92.89	1.77	11731	1.08
4-Jets 50GeV	106.05	500.1	0.18	0.00	13.51	22.51	0.08	1.04	0.01	537.4	4.44
Same-Sign	36.00	4.28	0.00	0.00	3.44	0.00	0.05	0.02	0.01	7.80	8.90
Missing E_T	30.75	0.30	0.00	0.00	0.76	0.00	0.01	0.00	0.00	1.07	12.43
$\mu\mu$											
Lep Flavour	55.35	6750	792289	18.12	60.55	1151	149.6	1636	183.7	802239	0.06
$m_{\mu\mu}$	55.20	6735	792288	18.12	60.47	1149	148.6	1628	183.2	802211	0.06
b-Jets	54.90	5787	10788	0.10	53.44	813.0	7.75	55.16	8.40	17514	0.41
4-Jets 50GeV	49.05	279.5	60.96	0.00	16.76	14.78	0.10	0.54	0.05	372.7	2.49
Same-Sign	17.25	0.59	0.00	0.00	1.89	0.00	0.02	0.00	0.00	2.50	6.86
Missing E_T	14.85	0.00	0.00	0.00	0.42	0.00	0.00	0.00	0.00	0.42	8.95

14 Details about the isolation thresholds in IsolationSelectionTool

1755

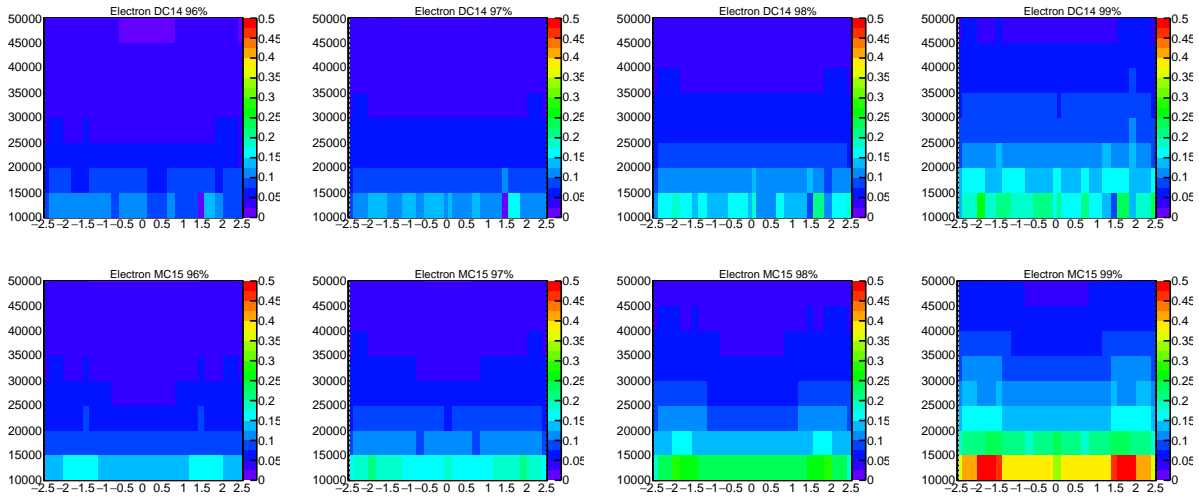


Figure 92: Thresholds on the $\text{ptvarcone20}/p_T$ used for the electron isolation working points in the DC14 pre-pre-recommendations (top) and in the MC15 pre-recommendations (bottom). These thresholds are shown as a function of the electron p_T and η for isolation efficiency of 96-99%.

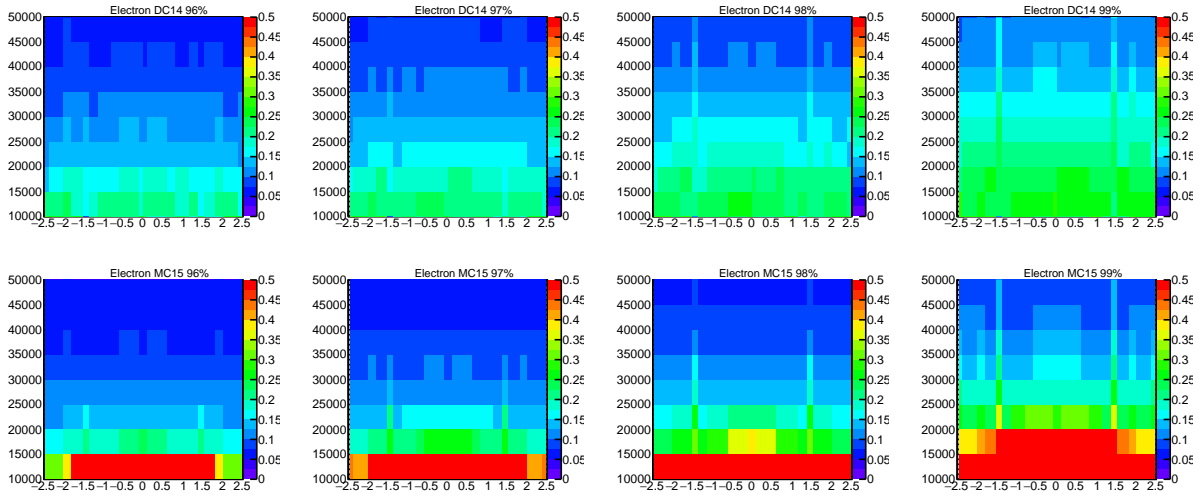


Figure 93: Thresholds on the $\text{topoetcone20}/p_T$ used for the electron isolation working points in the DC14 pre-pre-recommendations (top) and in the MC15 pre-recommendations (bottom). These thresholds are shown as a function of the electron p_T and η for isolation efficiency of 96-99%.

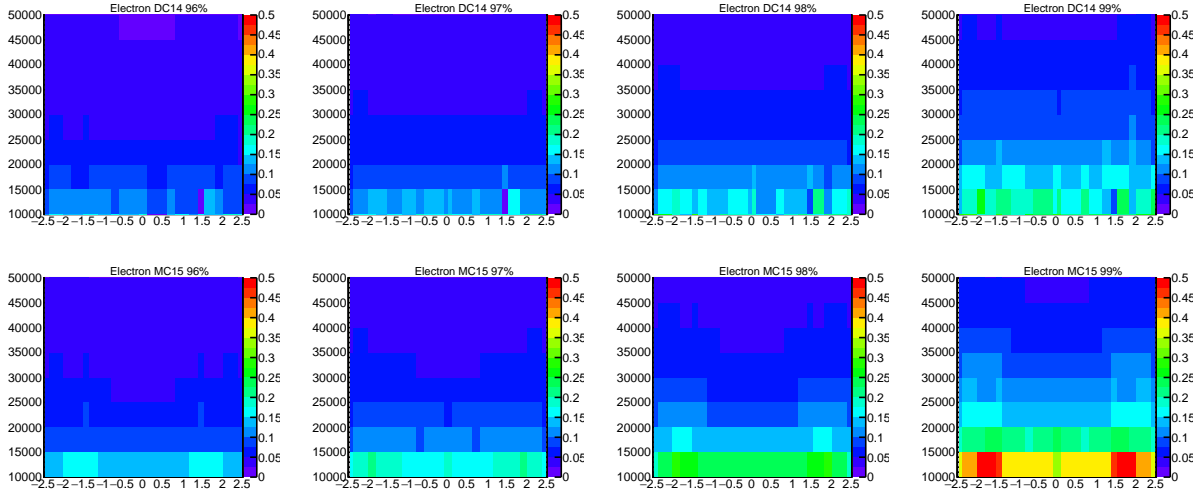


Figure 94: Thresholds on the $\text{ptvarcone30}/p_T$ used for the muon isolation working points in the DC14 pre-pre-recommendations (top) and in the MC15 pre-recommendations (bottom). These thresholds are shown as a function of the muon p_T and η for isolation efficiency of 96-99%.

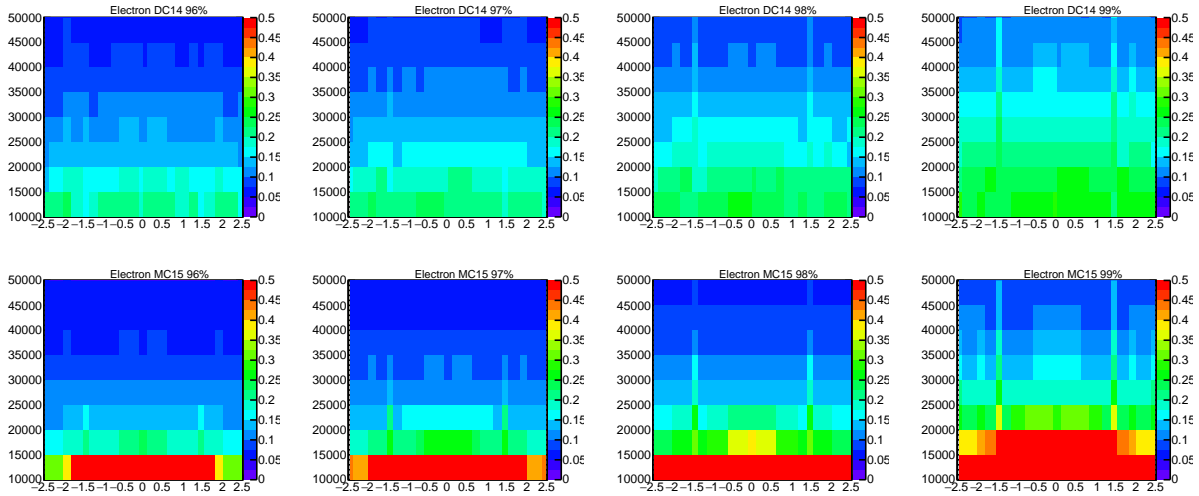


Figure 95: Thresholds on the $\text{topoetcone20}/p_T$ used for the muon isolation working points in the DC14 pre-pre-recommendations (top) and in the MC15 pre-recommendations (bottom). These thresholds are shown as a function of the muon p_T and η for isolation efficiency of 96-99%.

1756 15 Charge flip details

1757 15.1 Comparison of charge flip rates in different MC productions

1758 Monte Carlo comparison study

1759 To validate our choice of control region, we apply the likelihood fit method to a pure $Z \rightarrow e^+e^-$ MC
 1760 sample in order to compare the results with the ones obtain by running on data. This study compares
 1761 the charge flip rates extracted from different MC samples especially MC12 and MC15 ones, at $\sqrt{s} = 8$
 1762 TeV and $\sqrt{s} = 13$ TeV respectively. The goal of such study is to look if the amount of mis-identified
 1763 electrons increased in Run 2 with respect to Run 1. The reproduction of Run 1 results is also a good way
 1764 to cross-check our new likelihood fit method.

1765 A total of 4 different samples will be use in this study: MC12, DC14, MC15, MC12r20. The MC12 and
 1766 MC15 samples are the most important ones and they correspond official Monte Carlo simulated events,
 1767 respectively for Run 1 and Run 2 analyses. The DC14 sample is similar to MC15 one, but it was mainly
 1768 used to produce some Run 2 projection results. Finally, the MC12r20 sample (standing for *MC12 release*
 1769 20) is a sample using the Run 1 energy ($\sqrt{s} = 8$ TeV) and detector geometry (no IBL), but using a Run 2
 1770 reconstruction based on the latest recommendations included in release 20. The purpose of such a sample
 1771 is to disentangle the combined effects due to detector geometry and reconstruction by using the same
 1772 geometry as the MC12 sample but the same reconstruction as the MC15 sample. The motivations to study
 1773 a sample like that will be explained below.

	Electrons	Jets
Acceptance	$p_T > 10$ GeV $\eta < 2.47$	$p_T > 20$ GeV $\eta < 2.8$ (< 2.5 for b-jets)
PID	mediumPP (MC12) LooseLLH (DC14, MC15, MC12r20)	–
b-tagging	–	MV1 > 0.98, 70% (MC12, DC14) MV2c20 > -0.5911, 80% (MC15, MC12r20)

Table 51: Electrons, jets and b-jets baseline selection cuts for different MC samples.

1774 The baseline selection cuts for different objects (electrons, jets and *b*-jets) are described in Table 51. The
 1775 fact that PID requirements for electrons as well as *b*-tagging requirements for *b*-jets are not the same
 1776 between different MC samples is due to the improvement of some variables between the Run 1 and Run
 1777 2 configurations. In Table 51 the efficiency associated to the MV1 variable is 70% and 80% for MV2c20
 1778 variable.

1779 Using the pair formed by the two signal leading electrons, one can now count the number of SS and OS
 1780 pairs along all $Z \rightarrow e^+e^-$ events and used those numbers as inputs in the likelihood method defined above
 1781 in order to extract the nominal charge flip rates in different MC samples.

1782 The left plot on Fig. 96 compares the charge flip rates between three MC samples: MC12, DC14 and
 1783 MC15 for 6 different η bins and $30 < p_T < 40$ GeV, while the right plot shows the ratios between MC15
 1784 and MC12 charge flip rates with the same binning. Similar plots corresponding to 8 other p_T bins can be
 1785 found in Appendix 15.2. For both plots, only statistical errors are shown. For the majority of the 54 total

	MC12	DC14, MC15, MC12r20
PID	TightPP	TightLLH
Track isolation	$pTcone20/p_T < 0.06$	$pTvarcone20/p_T < 0.06$
Calorimeter isolation	$topoETcone20/p_T < 0.06$	
Impact parameter	$ z_0 \cdot \sin \theta < 0.4\text{mm}$ $ d_0/\sigma(d_0) < 3.0$	

Table 52: Signal selection cuts applied on $Z \rightarrow e^+ e^-$ events on top of overlap removal procedure for different MC samples.

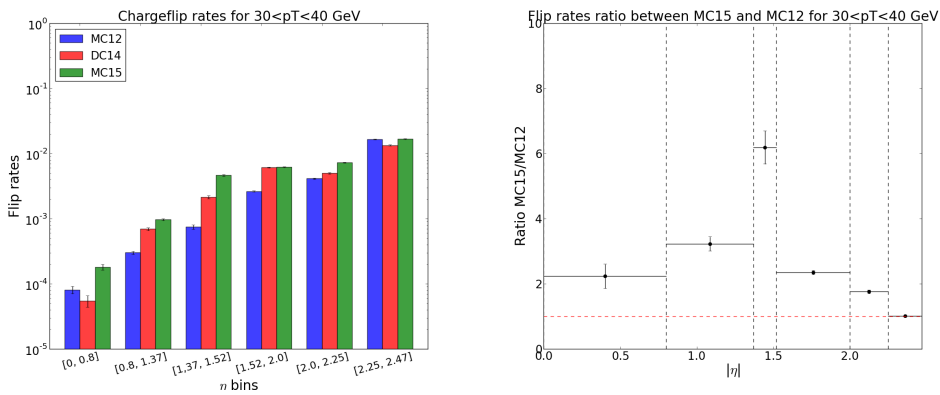


Figure 96: Left plot: Charge flip rates extracted from MC12 sample in blue, DC14 sample in red and MC15 in green. The rates are computed for 6 different η bins and one p_T bin ($30 < p_T < 40$ GeV), only statistical uncertainties are shown. Right plot: Ratios between MC15 and MC12 charge flip rates with the same binning of left plot, only statistical uncertainties are shown.

bins the ratio is positive and greater than 2.0 (vary between 0.5 and 8.0), meaning that the charge flip rates from MC15 are often twice as large as charge flip rates from MC12 sample.

The right plot on Fig. 96 clearly shows that the charge flip rates extracted from an MC15 sample are generally greater than the ones extracted from an MC12 sample. The two main effects that may have changes from MC12 to MC15 are the reconstruction of the event (object definition, variables, etc.) and the geometry of the ATLAS detector, which is different with the new IBL tracking system installed for Run 2. The amount of material added in Run 2 (IBL and services), but also the position of the IBL, may have increased the charge mis-measurement rate because if the track curvature change direction early (near to the collision point) the odds of mis-identified the charge are greater than in the case where the track curvature is modified later during its path. To be able to distinguish between those two possible effects, a new MC sample was used (MC12r20), a sample based on Run 1 geometry (no IBL) but with Run 2 reconstruction. By comparing this sample to the MC12 and/or MC15 ones, it was easier to distinguish whether geometry or reconstruction was the most influential on the charge flip rate measurement.

This comparison is shown in Fig. 97, again for 6 different η bins and one p_T bin ($30 < p_T < 40$ GeV), comparing the charge flip rates extracted from MC12, MC12r20 and MC15 samples on left plot and the charge flip rates ratio between MC15 and MC12r20 on right plot. Again, similar plots corresponding to 8 other p_T bins can be found in Appendix 15.3. On those plots, one can see that the computed ratio varies between 0.5 and 2.0 over the 54 total possible bins but in most cases the ratio is ≈ 1.0 . By comparing

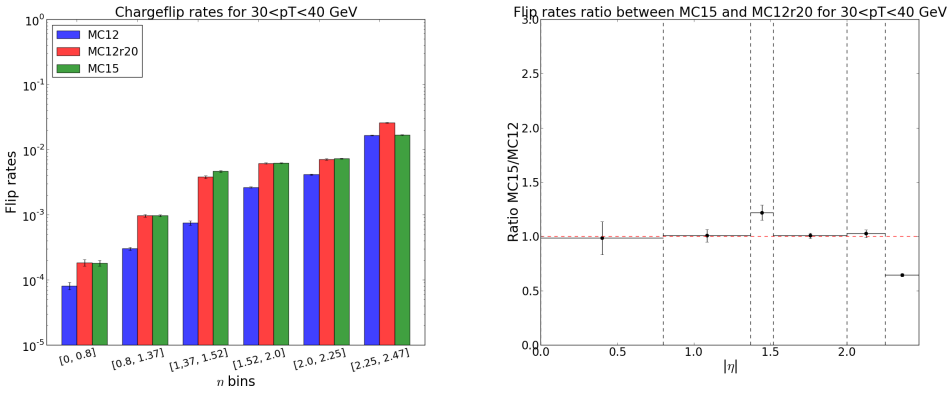


Figure 97: Left plot: Charge flip rates extracted from MC12 sample in blue, MC12r20 sample in red and MC15 in green. The rates are computed for 6 different η bins and one p_T bin ($30 < p_T < 40$ GeV), only statistical uncertainties are shown. Right plot: Ratios between MC15 and MC12r20 charge flip rates with the same binning of left plot, only statistical uncertainties are shown.

1804 those two samples which use the same reconstruction, we disentangled geometry and reconstruction and
 1805 with the results shown on the right plot of Fig. 97, it is possible to conclude that the new geometry is not
 1806 the main cause creating an increase in the charge flip rates as seen on left plot in Fig. 96. Nevertheless, we
 1807 cannot assume that difference in geometry has no effect at all on the charge mis-measurement rates since
 1808 the ratios between MC12r20 and MC15 samples are not in perfect agreement with 1.0, but it is clearly
 1809 less relevant compared to difference in reconstruction.

1810 The origin of a disagreement between MC12 and MC15 samples coming from the reconstruction can be
 1811 studied by looking at different variables used in the signal selection cuts in Table 52. In order to understand
 1812 which variables among PID, track and calorimeter isolation, longitudinal and transverse impact parameter
 1813 are associated to the disagreement, one can compute the charge flip rates by applying only one of the cuts
 1814 presented in Table 52, rather than applying all the signal selection cuts on both electrons forming the pair.
 1815 This was done for two specific binning, the first one composed of 9 p_T bins between the range [20, 150]
 1816 GeV and only one η bin ([0, 2.47]), while the second composed of 6 η bins between the range [0, 2.47]
 1817 and only one p_T bin ([20, 150] GeV).

1818 The top plots of Fig. 98 show the charge flip rates for those two sets of bins when all signal cuts are
 1819 applied. One can easily see that the rates computed with MC12 sample are lower in each bin than the one
 1820 computed with MC15 sample. The middle and bottom plots present the same results but only when the
 1821 PID or d_0 requirements are applied. It is clear that the d_0 significance variable strongly affect the charge
 1822 flip rate measures. This effect leads to an increase in the MC15 results with respect to MC12 ones of a
 1823 factor ~ 2 in the p_T binned bottom left plot. The middle plots show a different behavior while the MC12
 1824 charge flip rates are almost always greater than the one from other samples in each p_T or η bins. This
 1825 could be understood as the fact that the PID requirement used in MC15 sample (TightLLH) is tighter than
 1826 the one used in MC12 sample (TightPP), which reduces the rates. The increasing rates in MC12 sample
 1827 for p_T below 60 GeV in the middle left plot was not an expected feature and it is not clear yet why there
 1828 is such a pattern at low p_T . Other similar plots using whether only track isolation, calorimeter isolation or
 1829 longitudinal impact parameter as signal selection variables have been done and are presented in Appendix
 15.4. In those plots, one can still see an increase between MC15 and MC12 charge flip rates, but the

difference is rather small compared to the one due to d_0 significance cut (bottom left plot on Fig. 98).

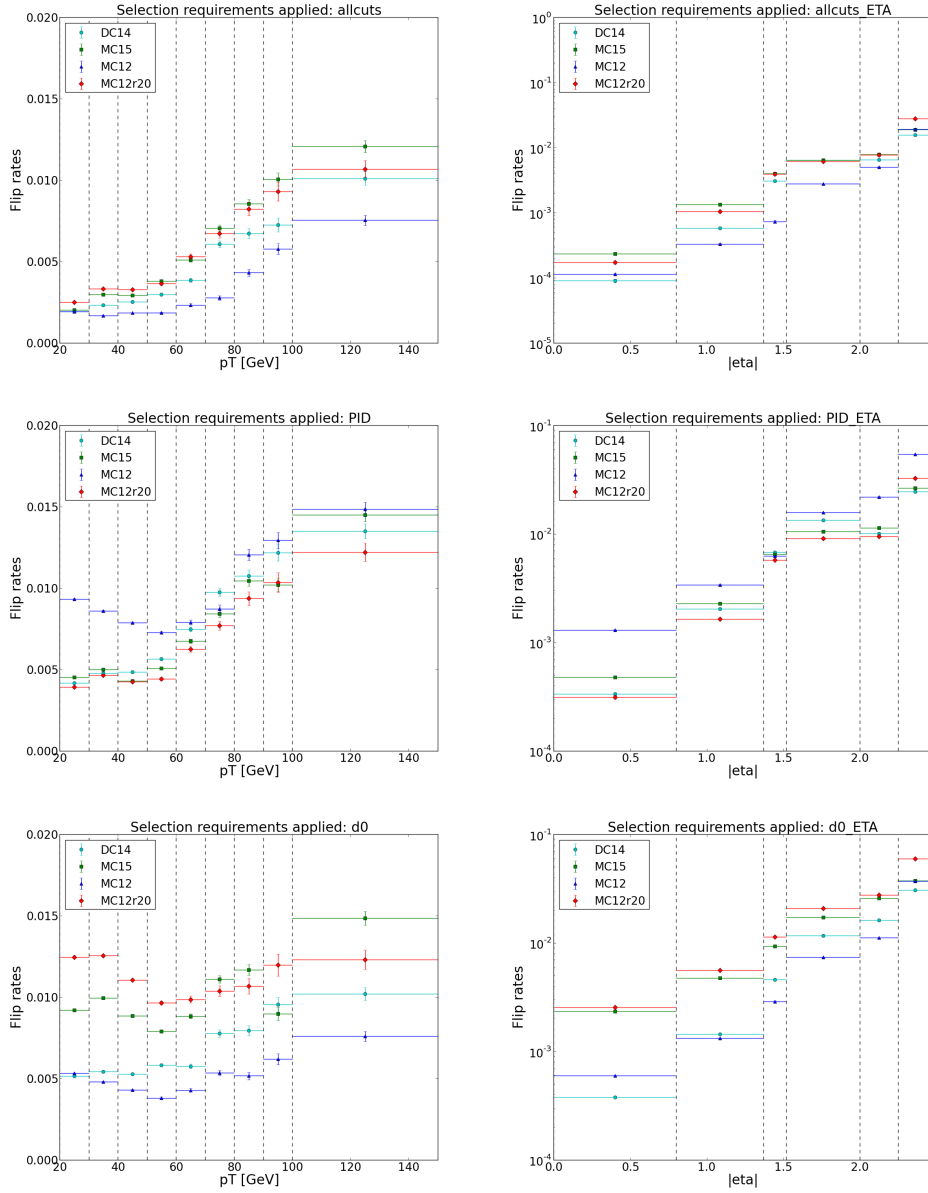


Figure 98: Charge flip rates extracted from different MC samples with a p_T binning for the left handed plots and with an η binning for the right handed plots (only statistical uncertainties are shown). On the top plots, all the cuts presented in Table 52 are considered as signal selection cuts, on the middle ones, only PID (TightPP or TightLLH) and transverse momentum ($p_T > 20$ GeV) cuts are considered as signal selection cuts and on the bottom plots only transverse impact parameter ($|d_0/\sigma(d_0)| < 3.0$) and transverse momentum ($p_T > 20$ GeV) cuts considered as signal selection cuts.

Figure 99 shows the charge flip rates extracted again for different MC samples and with all signal selection cuts applied except the d_0 significance in order to understand in a better way its influence on the rates. The feature at low p_T for MC12 sample is still present, meaning that the d_0 significance cut could be the

one that compensate the effect coming from the PID requirements (shown on the middle left plot of Fig. 98). Furthermore, the MC12 and MC15 charge flip rates are closer to each other in comparison of the distribution shown on the top left plot in Fig. 98. This comparison shows again that cutting or not on the d_0 significance have a large impact on the disagreement between charge flip rates coming from MC12 and MC15 results. This study is still ongoing and one of the main future hypothesis is that the d_0 definitions used in MC12 and MC15 samples are not the same: d_0 could be defined with respect to the primary vertex in MC12 sample and with respect to the beam spot in MC15. Nevertheless, this study has shown that the charge mis-measurement rates were increased between the old MC12 samples used in Run 1 and the new MC15 samples used during Run 2.

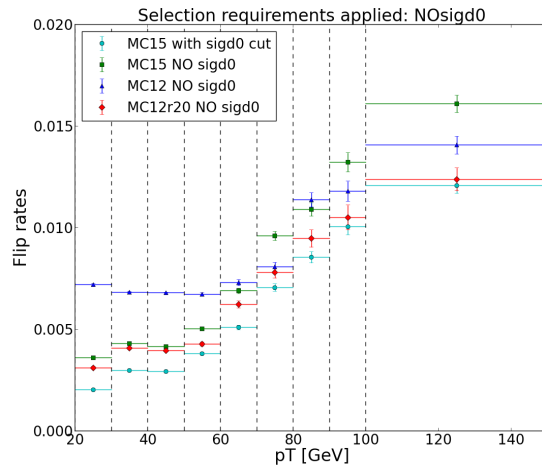


Figure 99: Charge flip rates extracted from different MC samples with a p_T binning and for the case where all signal selections cuts from Table 52 are applied except the d_0 significance cut (only statistical uncertainties are shown).

15.2 Charge flip rates plots: MC12 vs. DC14 vs. MC15

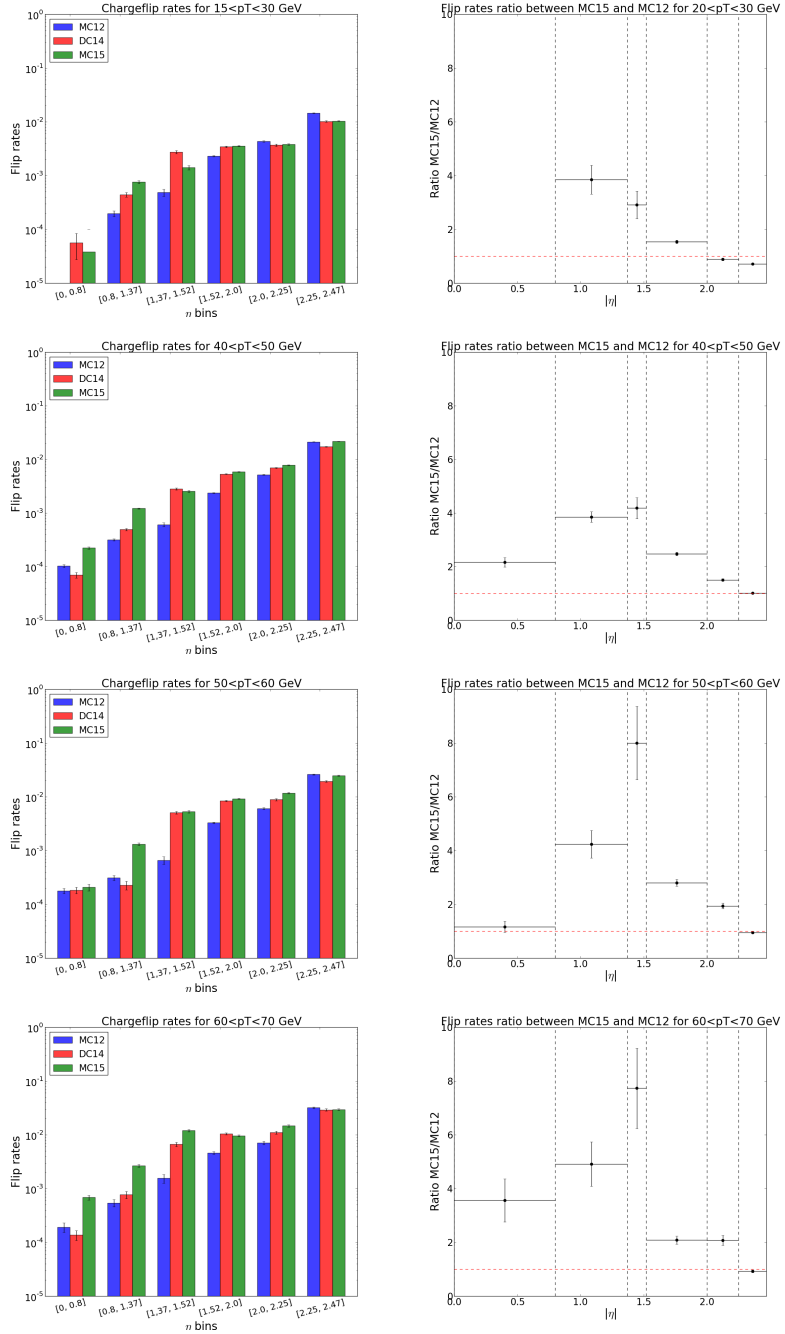


Figure 100: On the left, charge flip rates extracted from MC12 sample in blue, DC14 sample in red and MC15 in green. On the right, ratios between MC15 and MC12 charge flip rates. Only statistical uncertainties are shown. The rates and ratios are computed for 6 different η bins and one p_T bin (from top-to bottom): $20 < p_T < 30$ GeV, $40 < p_T < 50$ GeV, $50 < p_T < 60$ GeV, $60 < p_T < 70$ GeV.

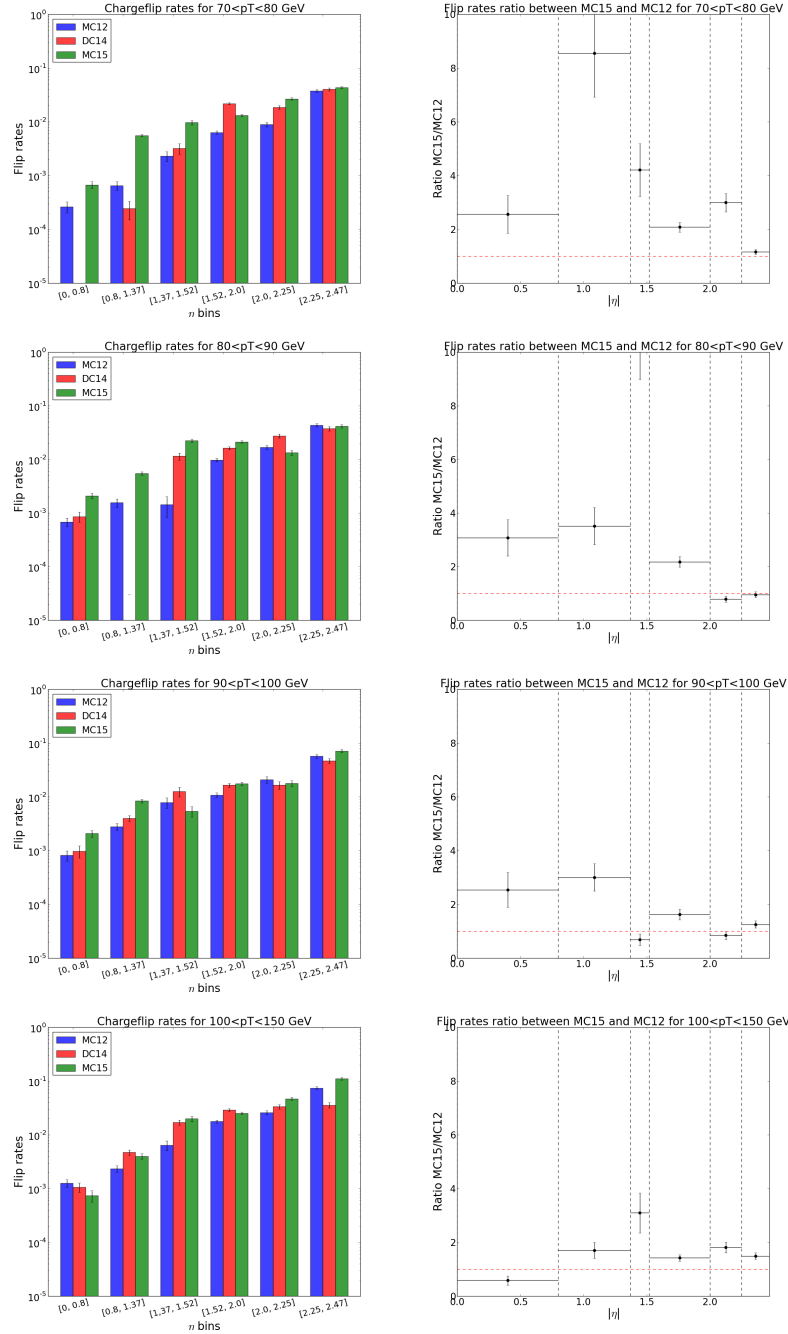


Figure 101: On the left, charge flip rates extracted from MC12 sample in blue, DC14 sample in red and MC15 in green. On the right, ratios between MC15 and MC12 charge flip rates. Only statistical uncertainties are shown. The rates and ratios are computed for 6 different η bins and one p_T bin (from top-to bottom): $70 < p_T < 80$ GeV, $80 < p_T < 90$ GeV, $90 < p_T < 100$ GeV, $100 < p_T < 150$ GeV.

1845 15.3 Charge flip rates plots: MC12 vs. MC15 vs. MC12r20

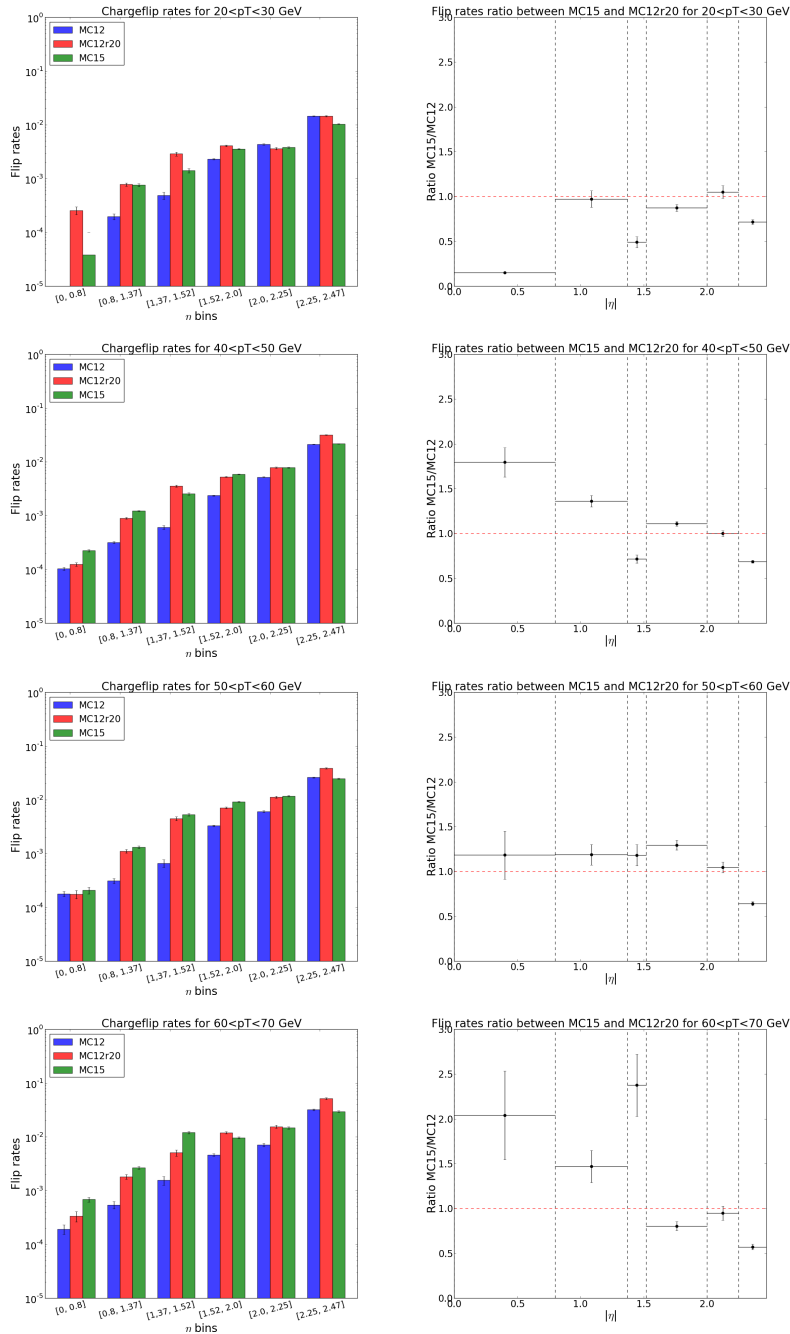


Figure 102: On the left, charge flip rates extracted from MC12 sample in blue, MC12r20 sample in red and MC15 in green. On the right, ratios between MC15 and MC12r20 charge flip rates. Only statistical uncertainties are shown. The rates and ratios are computed for 6 different η bins and one p_T bin (from top-to bottom): $20 < p_T < 30 \text{ GeV}$, $40 < p_T < 50 \text{ GeV}$, $50 < p_T < 60 \text{ GeV}$, $60 < p_T < 70 \text{ GeV}$.

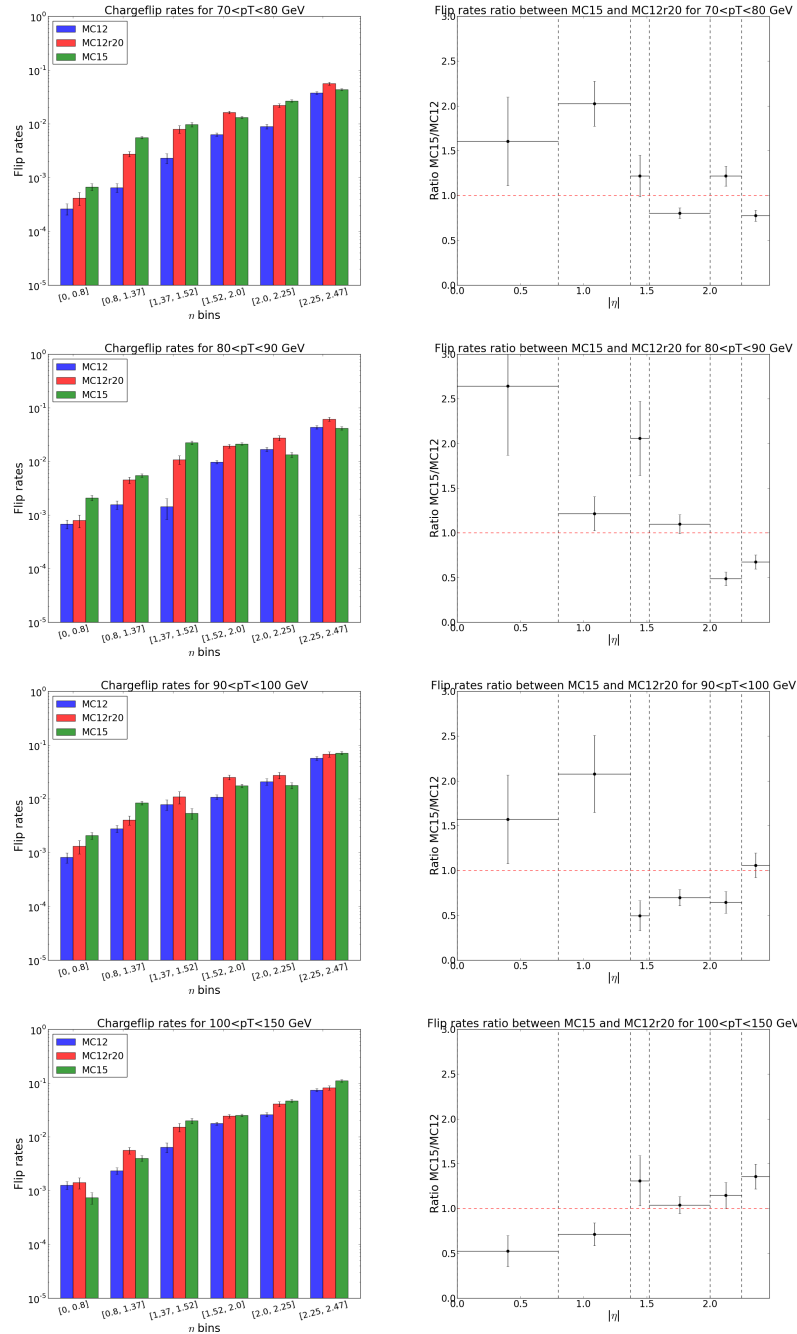


Figure 103: On the left, charge flip rates extracted from MC12 sample in blue, MC12r20 sample in red and MC15 in green. On the right, ratios between MC15 and MC12r20 charge flip rates. Only statistical uncertainties are shown. The rates and ratios are computed for 6 different η bins and one p_T bin (from top-to bottom): $70 < p_T < 80$ GeV, $80 < p_T < 90$ GeV, $90 < p_T < 100$ GeV, $100 < p_T < 150$ GeV.

1846 **15.4 Charge flip rates plots using variables z_0 , $ptvarcone20/pT$ or $topoETcone20/pT$ as signal selection cuts**

1847

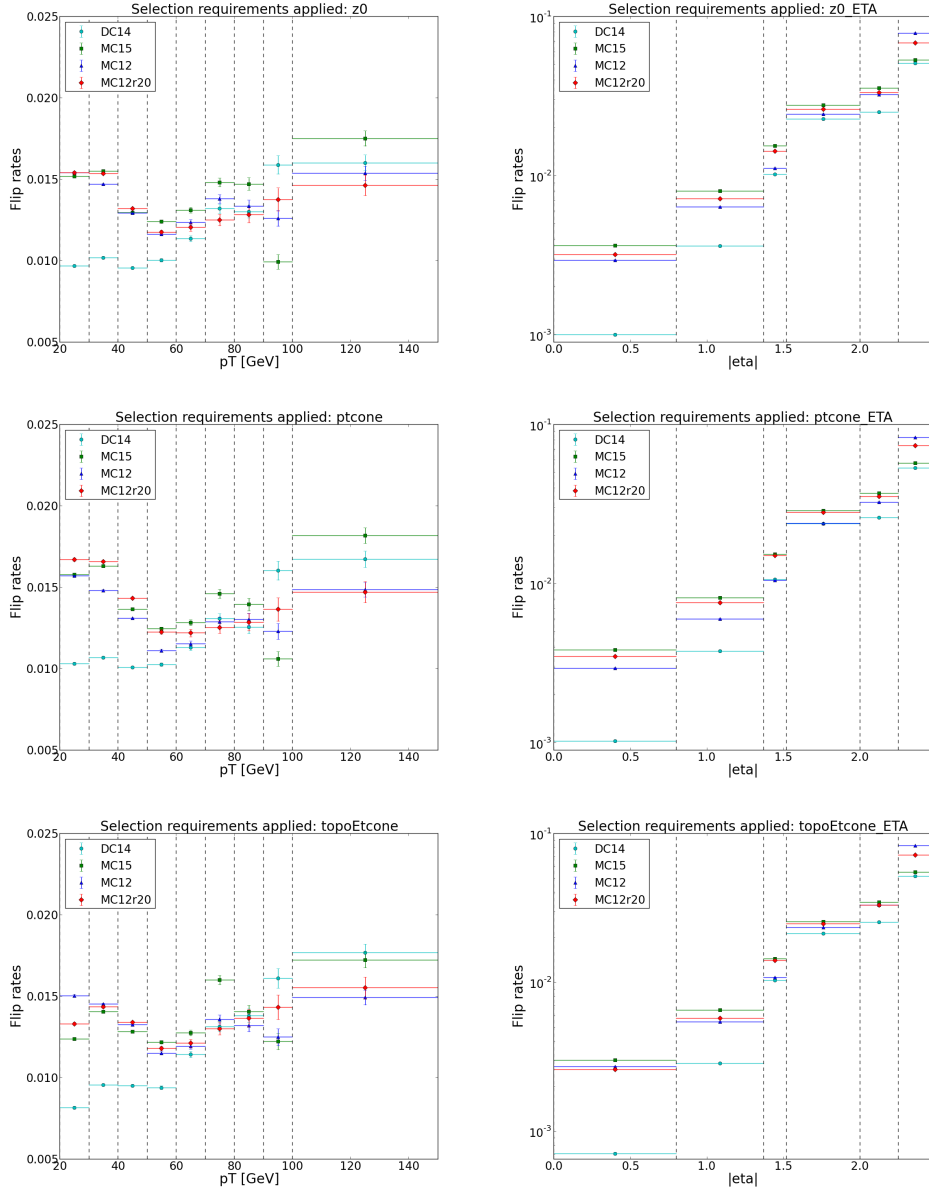


Figure 104: Charge flip rates extracted from different MC samples with a p_T binning (left) and η binning (right). Only statistical uncertainties are shown. On the top plots, only longitudinal impact parameter ($|z_0 \cdot \sin \theta| < 0.4\text{mm}$) and transverse momentum ($p_T > 20\text{ GeV}$) cuts considered as signal selection cuts. On the middle ones, only track isolation ($ptvarcone20/p_T < 0.06$) and transverse momentum ($p_T > 20\text{ GeV}$) cuts considered as signal selection cuts and on the bottom plots only calorimeter isolation ($topoETcone20/p_T < 0.06$) and transverse momentum ($p_T > 20\text{ GeV}$) cuts considered as signal selection cuts.

1848 16 Real leptons efficiencies

1849 This appendix presents more details on the measurement of the real lepton efficiency in data selecting
 1850 either Z or $t\bar{t}$ events. A general description is given in Section 16.1. The methods and the obtained results
 1851 are presented in Section 16.2 (Z -measurement) and 16.4 ($t\bar{t}$ -measurement). As shown in Section 7.4.1,
 1852 the efficiency measured in a sample enriched in Z events is used as input to the matrix method; more
 1853 details on the evaluation of the associated systematic uncertainties are presented in Section 16.3.

1854 **16.1 Description of the real lepton efficiencies**

1855 The real lepton efficiency is defined as the ratio between the number of (prompt) leptons passing the signal
 1856 lepton definition and the number of (prompt) leptons passing the baseline definition. Thus, it measures
 1857 the efficiency of the signal lepton definition cuts with respect to the baseline ones. Table 53 shows these
 1858 definitions. The efficiency associated to each signal cut (given the baseline definition) is shown in Figure
 1859 105, considering either $Z \rightarrow \ell\ell$ (top) or $t\bar{t}$ (bottom) simulated events.

	Baseline electron	Baseline muon
Acceptance	$p_T > 10 \text{ GeV} \eta^{\text{clust}} < 2.47$ except $1.37 < \eta^{\text{clust}} < 1.52$	$p_T > 10 \text{ GeV}, \eta < 2.5$
Quality	LooseLLH	xAOD::Muon::Medium
ℓ -jet Isolation	$\Delta R(e, \text{jet}) > 0.4$	$\Delta R(\mu, \text{jet}) > 0.4$
Impact parameter	$ d_0/\sigma(d_0) < 5.0$	
	Signal Electron	Signal Muon
Quality	TightLLH $ \eta < 2.0$	- -
Isolation	$E_{\text{T}}^{\text{topocone}20}/p_T < 0.06$ $p_{\text{T}}^{\text{varcone}20}/p_T < 0.06$	$p_{\text{T}}^{\text{varcone}30}/p_T < 0.06$
Impact parameter	$ z_0 \cdot \sin(\theta) < 0.4 \text{ mm}$	$ z_0 \cdot \sin(\theta) < 0.4 \text{ mm}$ $ d_0/\sigma(d_0) < 3.0$

Table 53: Summary of the electron and muon selection criteria. The signal selection requirements are applied on top of the baseline selection. The lepton-jet isolation requirement is applied after electron-jet overlap removal.

1860 **Discussion on real electron efficiency**

1861 The left plots from Figure 105 shows that the prompt electron efficiency increase from $\sim 45\%$ in the
 1862 $[10-25] \text{ GeV } p_T$ range to $\sim 95\%$ when $p_T > 80 \text{ GeV}$. The dominant contribution to the electron efficiency
 1863 losses is the tight likelihood (LH) identification cut in the $p_T > 25 \text{ GeV}$ range and the calorimeter isolation
 1864 requirement in the $p_T < 25 \text{ GeV}$ range. The loose LH to tight LH efficiency increase form $\sim 75\%$ to
 1865 $\sim 84\%$ in the $[10-25] \text{ GeV } p_T$ range to reach a plateau at $\sim 84\%$ in the $[25-50]$ range and increase again to
 1866 reach a $\sim 95\%$ efficiency plateau at 80 GeV . The calorimeter isolation cut efficiency increase form $\sim 58\%$
 1867 at low p_T to a $\sim 99\%$ plateau at $p_T > 80 \text{ GeV}$ for the $Z + jets (t\bar{t})$ processes. The efficiency associated to
 1868 the track isolation cut is $\sim 93\%$ in the $[10-15] \text{ GeV } p_T$ range and the increase up to a $\sim 100\%$ efficiency
 1869 plateau at $p_T > 60 \text{ GeV}$. The contribution of the longitudinal impact parameter cut to the real efficiency

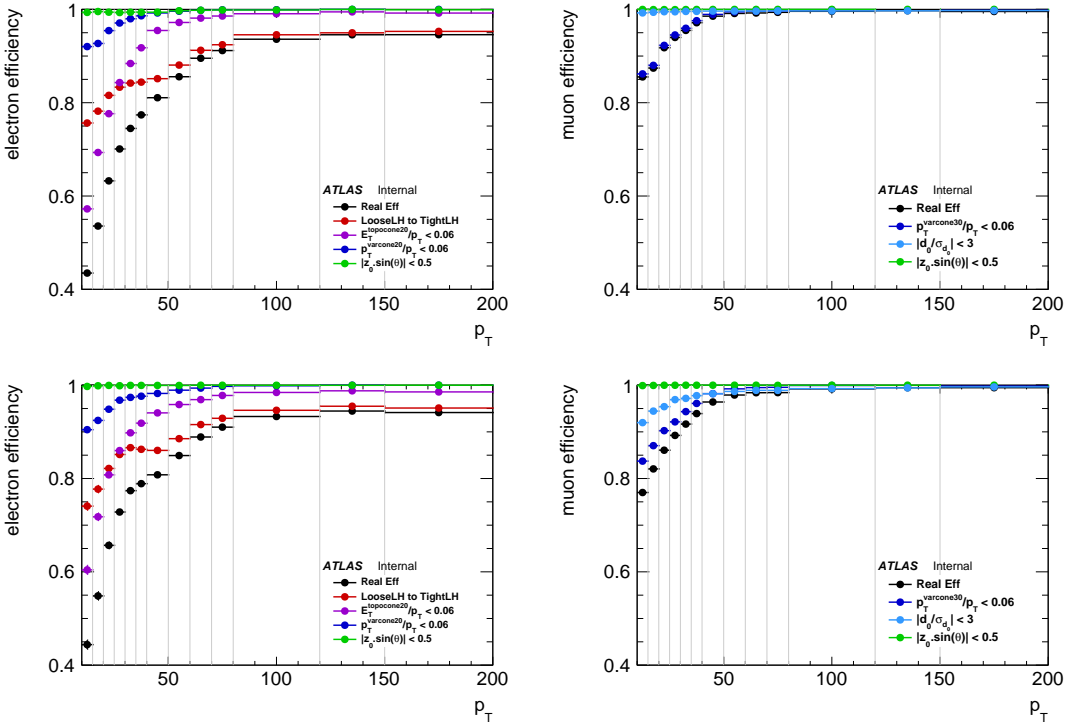


Figure 105: Efficiencies of the signal electrons (left) and muons (right) definition cuts as a function of p_T . The leptons are selected from $Z + jets$ (top) and $t\bar{t}$ (bottom) simulated events using a loose truth match. The black points correspond to the total real lepton efficiency, the purple (dark blue) to the calorimeter (track) isolation criteria, the light blue (green) to the cut on transverse (longitudinal) impact parameter and the red points to the tight likelihood electron identification efficiency with respect to the loose likelihood electron identification.

is negligible. Only few percent efficiencies differences are observed between $Z \rightarrow ee$ and $t\bar{t}$ electron efficiencies mostly driven by the calorimeter isolation at high p_T .

Discussion on real muon efficiency

As the same muon identification is used for the baseline and the signal definitions, the muon efficiencies are much higher than the electron ones. The associated efficiencies computed using $Z \rightarrow \mu\mu$ events increases from $\sim 85\%$ at low p_T to a $\sim 99\%$ efficiency plateau at $p_T > 60$. The dominant contribution to the muon efficiency is the track isolation cut. The associated efficiency increases from $\sim 85\%$ at low p_T up to a $\sim 99\%$ efficiency plateau at $p_T > 50$ GeV. An other difference with electrons is that a tight longitudinal impact parameter cut is used in the muons signal definition while this cut it is already used at baseline level in the electron case. The impact of this cut on muon efficiency is negligible for $Z \rightarrow \mu\mu$ events but is sizeable in $t\bar{t}$ as b -jets are present in the final state. The associated efficiencies for $t\bar{t}$ processes vary from $\sim 93\%$ at low p_T to $\sim 99\%$ at $p_T > 80$ GeV and become the dominant cut $p_T > 50$ GeV. As a result, the $t\bar{t}$ efficiencies are lower than the $Z \rightarrow \mu\mu$ ones by $\sim 5\%$ at low p_T and $\sim 1\%$ for $p_T > 80$ GeV.

1884 **16.2 Real leptons efficiency measured using Z events**

1885 **Presentation of the method**

1886 The leptons used for the efficiencies measurements are extracted from data using $Z \rightarrow ee/\mu\mu$ events with
 1887 a tag-and-probe method. The tag lepton is imposed to pass the signal lepton requirement, $p_T > 25$ GeV
 1888 and to be matched to the relevant primary single lepton trigger. In the case of the $Z \rightarrow ee$ events a
 1889 additional $|\eta| < 2$ requirement is used for the tag selection. The probe lepton, used for the real efficiencies
 1890 measurements, should pass the baseline lepton requirements. The invariant mass of the two leptons should
 1891 satisfy $80 < m_{\ell\ell} < 100$ GeV and the two leptons are requested to have opposite charge and same flavour.
 1892 For each tag-and-probe lepton pairs, both leptons are alternatively considered as the possible tag to avoid
 1893 any bias in the choice of the tag and to increase the statistics. Data to Monte Carlo comparison of the
 1894 tag-and-probe electron pair invariant mass distributions ($m_{\ell\ell}$) shown in Figure 106 shows that background
 1895 subtraction is only needed for electron with $p_T < 20$ GeV. Similar plots dedicated to muons shows that
 1896 the muon background contamination is marginal over the whole p_T range.

1897

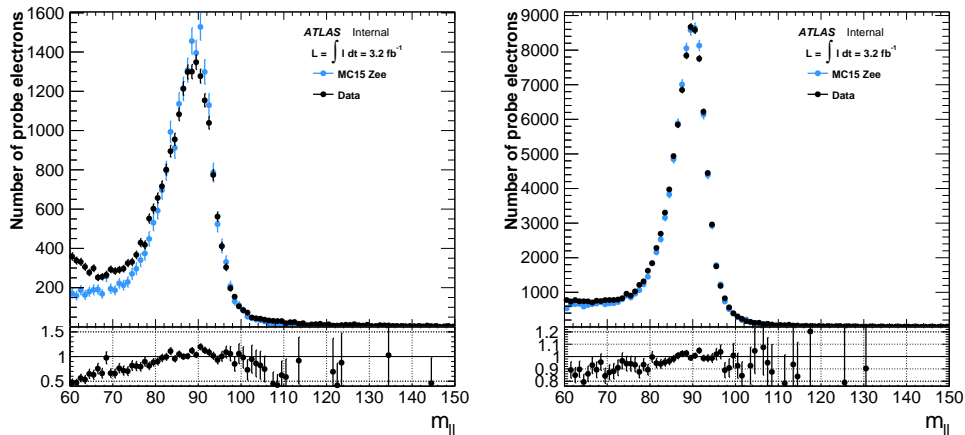


Figure 106: Distributions of the electron tag-and-probe pairs invariant mass ($m_{\ell\ell}$) computed using $Z+jets$ Monte Carlo simulations (light blue) and 2015 run 2 data (black points). The left (right) plot shows the $m_{\ell\ell}$ computed with probe electrons in the [10-15] ([20-25]) GeV p_T range. The Monte Carlo distributions are normalized to the data using a Gaussian fit of the Z mass peak ($85 < m_{\ell\ell} < 95$ GeV).

1898 The background contamination associated to these low p_T electrons is estimated using a background tem-
 1899 plate method similar to the one used by the e/γ performance group for their efficiency measurements [40].
 1900 The following formula summarize the real lepton efficiencies definition computed with the number of
 1901 probe electron passing the baseline (N_{Baseline}), signal (N_{Signal}) lepton definitions and the estimated baseline
 1902 probe lepton background contamination ($N_{\text{Baseline}}^{\text{Bkg}}$)⁵.

$$\epsilon = \frac{N_{\text{Signal}}}{N_{\text{Baseline}} - N_{\text{Baseline}}^{\text{Bkg}}}$$

⁵ As the background contamination is found to be negligible for signal electrons, no background subtraction is done for signal electrons.

1903 **Evaluation of the background contamination**

1904

1905 The background contamination has been evaluated on data using a background template method. A sample
1906 enriched in background is obtained by reverted loose calorimeter and track isolation cuts and requesting the
1907 electron object to fail the medium LH identification. Two variation of the background template definition
1908 has been also defined to asses a systematic on the template definition. Table 54 summarize the background
1909 template definitions. The $m_{\ell\ell}^{\text{Temp}}$ distribution associated to the template is then used to estimate the amount
1910 of background in the measurement region ($80 < m_{\ell\ell} < 100$ GeV).

1911

cuts \ template	Variation 1	baseline	Variation 2
Identification	-	fail mediumLH	fail mediumLH
Calorimeter Isolation	$E_T^{\text{topocone20}}/p_T > 20\%$	$E_T^{\text{topocone20}}/p_T > 15\%$	$E_T^{\text{topocone20}}/p_T > 20\%$
Track Isolation	$p_T^{\text{varcone20}}/p_T > 15\%$	$p_T^{\text{varcone20}}/p_T > 8\%$	$p_T^{\text{varcone20}}/p_T > 15\%$

Table 54: Definitions of the the background templates cuts used to estimate the background contamination associated to the Z tag-and-probe method.

1912 As the templates cuts also removes background objects, the templates has to be normalized to provide
1913 the correct background estimates. The $120 < m_{\ell\ell} < 150$ GeV region is used for this normalisation
1914 as less prompt electrons contribution is expected in the upper $m_{\ell\ell}$ tail. The background in the tail is
1915 estimated by integrating the baseline $m_{\ell\ell}$ distributions in this region after subtracting the prompt electron
1916 contribution. As the signal electron definitions allows to get a pure sample of prompt lepton, the prompt
1917 lepton contamination is estimated by integrating the signal $m_{\ell\ell}^{\text{Sig}}$ distribution divided by the real electron
1918 efficiency computed using Monte Carlo simulation.

1919 The baseline electron selection already provides a relatively pure sample of prompt electrons. Therefore
1920 the background template suffers from low statistics in the tails. To avoid any bias in the normalisation
1921 factor due to statistical fluctuations, the template is fitted using an exponential using the following $m_{\ell\ell}^{\text{Temp}}$
1922 range : $m_{\ell\ell}^{\text{Temp}}[60 - 80] \cup [100 - 120]$ GeV. The $80 < m_{\ell\ell} < 100$ range is removed from the fit to get
1923 rid of eventual prompt lepton contamination arising from $Z \rightarrow ee$ events. As the low $m_{\ell\ell}$ tail of the
1924 templates is statistically dominating, the fit is mostly driven by the $m_{\ell\ell}^{\text{Temp}}[60 - 80]$ range. The background
1925 contamination is then :

$$N_{\text{Baseline}}^{\text{Bkg}} = \int_{80}^{100} N_{\text{Temp}} dm_{\ell\ell} \cdot \frac{N_{\text{Baseline}}^{\text{Tail}} - N_{\text{Signal}}^{\text{Tail}}/\epsilon_{Z \rightarrow ee}^{\text{MC}}}{N_{\text{Temp}}^{\text{Tail}}}$$

1926 The background estimates are summarized in table 55. The estimated background contribution in the [10-
1927 15] GeV p_T range is relatively small as it represents less than 1% of the baseline statistics. Low background
1928 contamination is also observed in the central region ($|\eta| < 0.8$) with less than 1% of the baseline statistics.
1929 This is expected as the electron identification is better in central region of the calorimeter and the hadronic
1930 background contribution decreases with p_T .

1931 Figure 107 shows the baseline $m_{\ell\ell}$ distributions before and after background template subtraction. The
1932 data after background subtraction is compared to Monte Carlo simulations and the template distribution
1933 and their corresponding fit are also shown. The simulated $m_{\ell\ell}$ distributions are normalized to the data

$p_T \setminus \eta $	[0-0.8]	[0.8-1.37]	[1.52-2.0]
[10-15] GeV	0.9 ± 0.7	3.2 ± 0.7	4.6 ± 0.5
[15-20] GeV	0.1 ± 0.1	0.7 ± 0.2	0.9 ± 0.2

Table 55: Background contamination (in %) estimated using the template method. The p_T and η binning corresponds to the ones used for the final measurements.

1934 after background subtraction using a Gaussian fit in the $85 < m_{\ell\ell} < 95$ GeV range. The top and the
 1935 bottom plots corresponds to the $10 < p_T < 15$ GeV range and the $15 < p_T < 20$ GeV range respectively.
 1936 The left, middle and right plots correspond to the $|\eta| < 0.8$, $0.8 < |\eta| < 1.37$ and $1.52 < |\eta| < 2$. ranges
 1937 respectively. After background subtraction, the data agree well with the Monte Carlo simulation within
 1938 the statistical uncertainties and a flat data to MC ratio is observed for all the p_T and $|\eta|$ ranges. The
 1939 largest improvements are observed in the $p_T[10 - 15] \cup |\eta|[0.8 - 2.0]$ range where a sizeable background
 1940 contamination is subtracted.

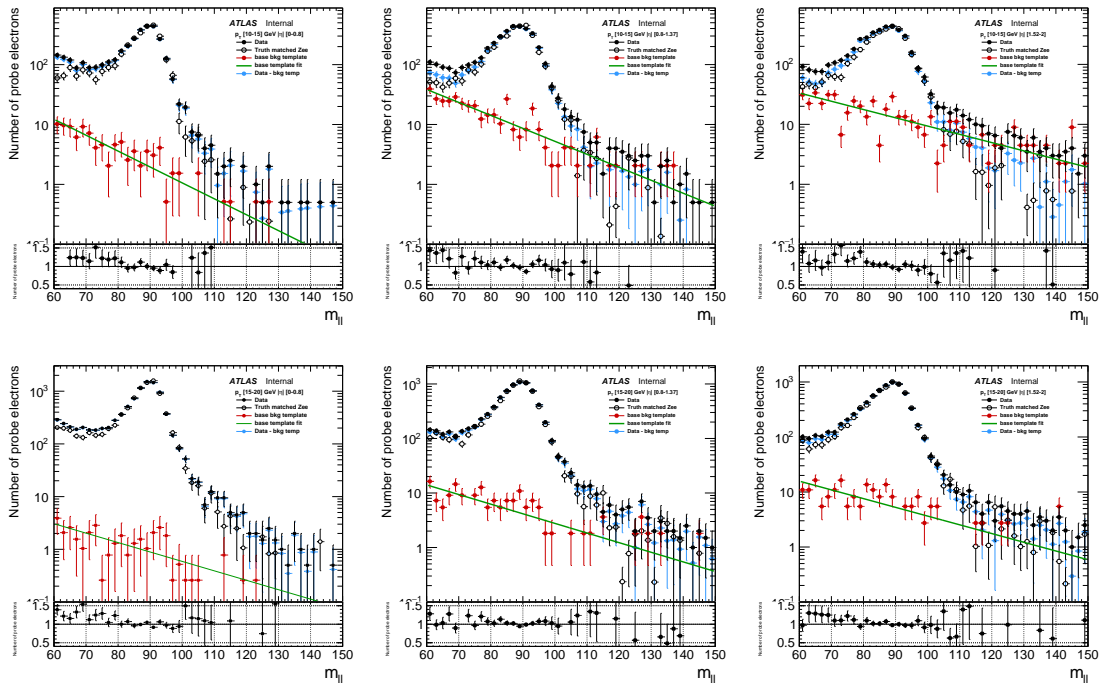


Figure 107: Plots illustrating the background subtraction procedure. The top (bottom) plots corresponds to the [10-15] ([15-20]) GeV p_T range and the left, medium and right ones to the [0-0.8], [0.8-1.37] and [1.52-2] $|\eta|$ range respectively. The $m_{\ell\ell}$ distributions from data (full points) before (black) and after (blue) background subtraction are shown along with the corresponding Monte Carlo distributions (open points). The Monte Carlo distribution is normalized to the data after background subtraction using a Gaussian fit of the Z peak region. The ratio corresponds to the comparisons of the data (after background subtraction) with the Monte Carlo. The corresponding background templates (red) and their respective fit (green lines) are also shown.

1941 Measurements systematics

1942 A systematic uncertainty associated to the electron tag-and-probe measurement method has been set

varying the background template definition, the template fit range and the $m_{\ell\ell}$ window used for the efficiency measurement. The variation of the templates definitions cuts are presented in table 55 and the additional template fit ranges are the following : [60 – 70] \cup [100 – 120] and [65 – 75] \cup [100 – 120]. The two other measurement $m_{\ell\ell}$ windows considered are the following : [75 – 105] and [85 – 95]. In total 27 variations of the measurement method are considered in the $p_T < 20$ GeV range and 3 in the $p_T > 20$ GeV range. The largest contribution to the systematic uncertainties arises from the $m_{\ell\ell}$ window variations. This result is expected as electrons extracted from the lower $m_{\ell\ell}$ tail are affected by bremsstrahlung effects. Thus, the efficiency computed with electrons extracted with a large $m_{\ell\ell}$ window will be lower than the ones computed using a tight window. In the $10 < p_T < 15$ GeV range, the order of magnitude of the $m_{\ell\ell}$ window variation is 6% whereas the background subtraction one is 1%. This result shows the robustness of the background subtraction method.
 The track isolation efficiency requirement used in the signal muons definitions has been measured by the muon CP group using a very similar method. As the real muon efficiency is fully dominated by the track isolation cut (see top right plot from Figure 105), the systematic uncertainties associated to the efficiency measurement of this cut is used to asses the measurement systematic of the muons.

1958 Data to Monte Carlo comparisons

In this section, for information only (only the data measurements are used for the fake estimates) real lepton efficiencies computed with the Z tag-and-probe method in data are compared to the ones using simulated $Z \rightarrow \ell\ell$ processes. All 2015 run 2 data is considered which corresponds to an integrated luminosity of $\sim 3.2 \text{ fb}^{-1}$ after good run list requirements. All the Monte Carlo lepton scale factors provided by the CP group are applied and the simulation is reweighed to the pile-up observed in data. Besides, an additional loose truth match is added for the Monte Carlo lepton selection.

The left plots from Figure 108 shows the electron (top) and the muon (bottom) real leptons efficiencies as a function of p_T measured on data and with simulated $Z \rightarrow ee$ and $Z \rightarrow \mu\mu$ processes. The associated uncertainties corresponds to the quadratic sum of the statistical and the measurement systematic uncertainties. The statistical uncertainties take both the background subtraction statistical uncertainties and the ones from the measurements into account⁶. A reasonable data to Monte Carlo agreement is observed with $\sim 2\%$ real efficiencies differences in the $p_T < 40$ GeV range and within the percent level in the $p_T > 40$ GeV range. These differences are covered by the measurement systematic uncertainties. The real muon efficiencies computed on Monte Carlo agree with the ones computed on data within 2% in the $p_T < 20$ GeV range, within the percent level in the $20 < p_T < 35$ GeV range and smaller than 0.5% in the $p_T > 35$ GeV range.

The middle plots from Figure 108 shows the electron (top) and the muon (bottom) real efficiencies as a function of $|\eta|$ measured using data and Monte Carlo. The shown errors corresponds to the statistics only. The efficiencies computed on Monte Carlo are 2% lower than the data ones, which corresponds to the efficiencies differences observed in the 40 GeV p_T range that dominates the statistics. The muon efficiencies agree within 0.5% and improves at high $|\eta|$. The right plots from Figure 108 shows the electron (top) and the muon (bottom) real efficiencies as a function of $\Delta R(l, jets)$ measured on data and Monte Carlo. The Data and Monte Carlo real electron efficiencies agree within 2%, whereas the muon real efficiencies agrees within the percent level.

1983 Results

Figure 109 shows the leptons real efficiencies (ϵ) computed as a function of p_T and η used by the the

⁶ The measurement statistic uncertainties are driven by the statistical fluctuations in the [80-100] $m_{\ell\ell}$ range and the background subtraction ones by the fluctuations in the [120-150] GeV range where the background template normalisation is estimated.

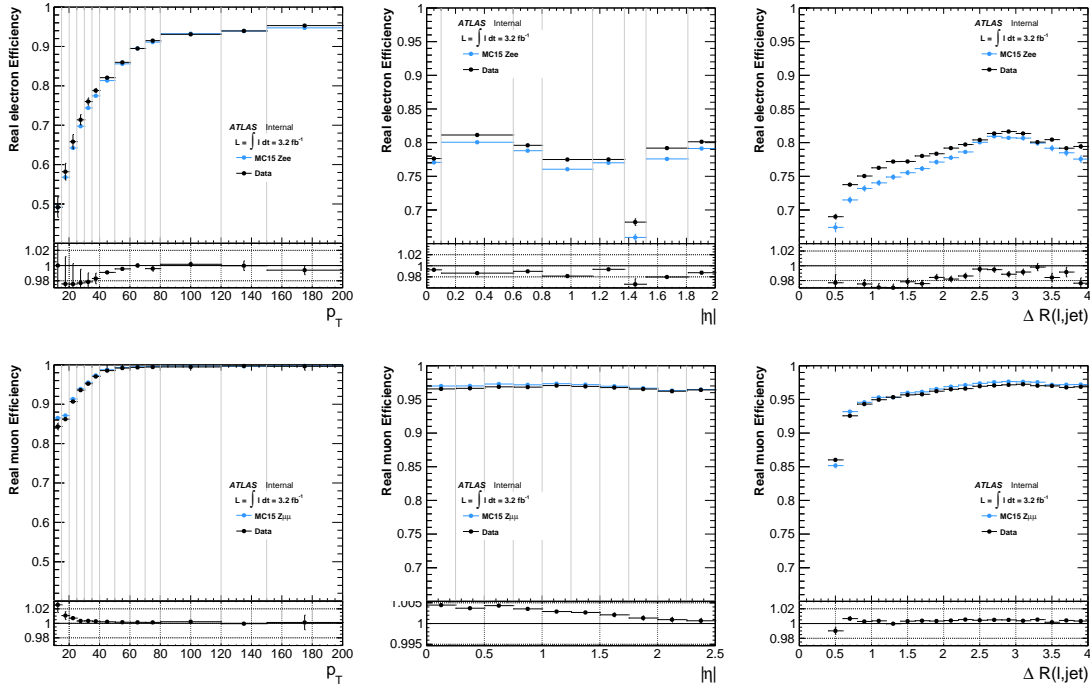


Figure 108: Real lepton efficiencies as a function of lepton p_T (left), η (middle) and $\Delta R(\ell, Jet)$ (right) measured using the Z tag-and-probe method described below. The top (bottom) plot corresponds to the electron (muon) real efficiencies. The black points corresponds to the efficiency computed using 2015 data. The blue points corresponds to the real leptons efficiency computed using $Z \rightarrow \ell\ell$ simulated events with lepton loose truth match reweighed to the data pile-up. The uncertainties shown in the left plots corresponds to the quadratic sum of the statistical and the measurement method uncertainties, whereas only statistical uncertainties are shown in the middle and the right plots. The binning used for the electron real efficiency measurement as a function of η corresponds to the geometry of the electromagnetic calorimeter.

matrix method. The electron η binning is driven by the electromagnetic calorimeter geometry removing the crack region ($|\eta| \in [1.37 - 1.52]$) not considered in the analysis. The error bars show the quadratic sum of the statistic and the tag-and-probe measurement systematic uncertainties.

16.3 Z tag-and-probe systematics uncertainties

Besides the systematics from the Z tag-and-probe measurement other sources of systematics have been considered.

Trigger systematics

Following the analysis trigger strategy, the electrons entering in the Signal Regions might be required to have fired one of the di-lepton triggers or not. For example if the event is fired with the E_T^{miss} trigger or if the considered lepton is the 3rd leading lepton, no trigger match should be applied for the efficiency computations. On the other hand, if the event is triggered by the di-lepton and the considered lepton is the leading or the sub-leading one, a trigger matching should be applied before the real lepton efficiency computation. Figure 110 shows the real lepton efficiencies computed with and without the relevant real

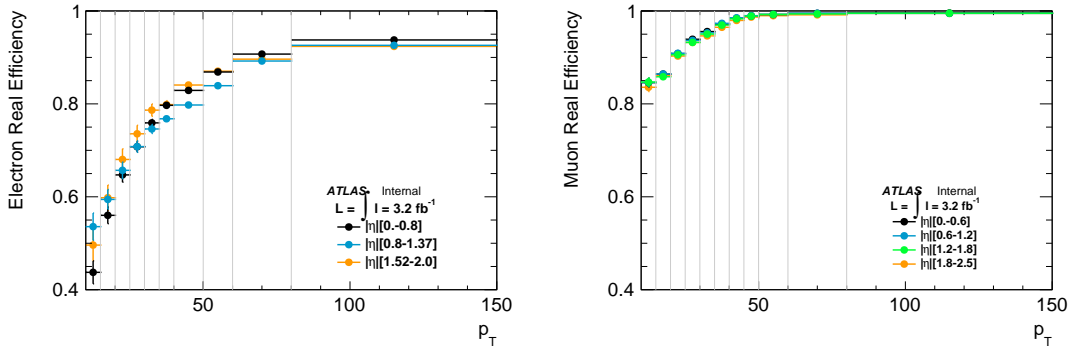


Figure 109: Real lepton efficiencies as a function of lepton p_T and η measured using the Z tag-and-probe method described below. The left (right) plot corresponds to the electron (muon) real efficiencies. The binning used for the electron real efficiency measurement corresponds to the geometry of the electromagnetic calorimeter removing the calorimeter crack region ($1.37 < |\eta| < 1.52$) and homogeneous η binning has been chosen for the muons.

lepton trigger as a function of p_T . The right plot dedicated to the muon efficiencies show that the trigger strategy does not affect the muon efficiency measurement, whereas the left plot, dedicated to electrons shows a sizeable bias is induced by the di-electron trigger. As the di-electron trigger is using a 12 GeV E_T threshold, this bias is expected in the $10 < p_T < 15$ GeV range. The unexpected bias seen in the $p_T > 15$ GeV range is understood to be due to the `e12_lhloose` trigger inefficiencies reported by the egamma trigger group. As the real lepton efficiencies are measured with events triggered by a single lepton trigger⁷, an additional systematic is assigned as the differences between the efficiencies measured with leptons matched with the `e12_lhloose` trigger and the lepton without trigger match. Moreover as a $p_T > 20$ GeV requirement is applied on the two leading leptons, the leptons with $p_T < 20$ will never be trigger matched to the di-lepton trigger. Therefore no systematics is assigned in the $10 < p_T < 20$ GeV range. A relative systematic uncertainty of 4% is assigned to electrons in the $20 < p_T < 30$ GeV range, 2% in the $30 < p_T < 50$ GeV range, 1% in the $50 < p_T < 60$ GeV range and 0.5% for electrons in the $p_T > 60$ GeV range.

SUSY signal topology extrapolation systematics

The real lepton efficiencies are measured with a sample enriched in $Z \rightarrow ll$ events characterized by well isolated leptons. The different processes entering in the signal region are accompanied by many (b)jets and with a different event topology⁸. Thus, the leptons present in the final state are not necessarily well isolated. As tight isolation cuts are used for the signal lepton definitions, their associated real efficiency can be smaller. These potential efficiencies differences are assigned as a systematic uncertainty by comparing the real lepton efficiencies computed with $Z \rightarrow ll$ processes and the ones computed considering several SUSY benchmark model : $\tilde{g}\tilde{g} \rightarrow t\bar{t}t\bar{t} \tilde{\chi}_1^0 \tilde{\chi}_1^0$. Boosted topologies are selected by applying the following requirement to select the models $m_{\tilde{g}} - m_{\tilde{\chi}_1^0} > 1000$ GeV. As the topology of one of the main irreducible backgrounds $t\bar{t}V$ is close to the $t\bar{t}$ one, the efficiencies measured with leptons from $t\bar{t}$ are also considered. The efficiencies comparisons are made for each measurements p_T bins considering two $\Delta R(\ell, \text{Jets})$ ranges : [0.4-0.6] and $\Delta R(\ell, \text{Jets}) > 0.6$. The obtained efficiencies ratios are then used to define the systematics.

⁷ The tag is matched to the single lepton trigger in order to provide unbiased probe leptons for the efficiency measurements.

⁸ Some SUSY processes can lead to events with very boosted top quarks reducing the angular distance between the physical objects.

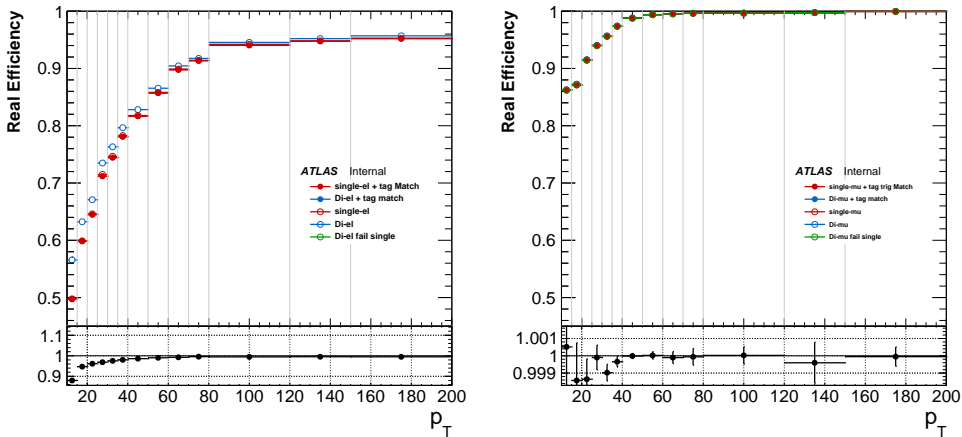


Figure 110: Real electron (left) and muon (right) efficiency computed with and without di-lepton trigger applied using $Z \rightarrow ll$ simulated events. The full dots shows the real lepton efficiencies computed with a trigger match on the tag lepton and the open ones correspond to the efficiencies computed with a Z tag-and-probe method with trigger match on the tag lepton. The blue points correspond to the efficiency measurements with the di-lepton trigger and the red ones with the single lepton trigger only. As only $Z \rightarrow ll$ events with two baseline leptons are used to compute these efficiencies, applying the di-lepton trigger is equivalent to match the probe lepton to the $e12_lhloose$ lepton trigger.

2023 Figure 111 shows kinematic distributions of the baseline truth matched leptons from the processes con-
 2024 sidered for the systematic study. The top and the bottom plots, dedicated to the lepton p_T and $|\eta|$
 2025 distributions, show that the leptons from the SUSY process are more boosted and more central than the
 2026 ones from Z and $t\bar{t}$ processes.
 2027

2028 Figure 112 shows the $\Delta R(\ell, \text{jet})$ (top) and n_{jets} (bottom) distribution of truth matched baseline lepton
 2029 extracted from $Z \rightarrow ll$, $t\bar{t}$ and the SUSY benchmark processes. The $\Delta R(\ell, \text{jet})$ distribution associated
 2030 to the SUSY signals peaks at 0.3 and most of the statistics is contained in the $\Delta R(\ell, \text{jet}) < 1$ range.
 2031 In comparison $\sim 60\%$ of the electrons from $Z \rightarrow ll$, $t\bar{t}$ are not accompanied with a signal jet and the
 2032 $\Delta R(\ell, \text{jet})$ distribution of remaining leptons peaks at π . The jet multiplicity of the $Z \rightarrow ll$ electrons peaks
 2033 at 0 jets whereas the benchmark SUSY signal ones at 8 jets. These plots confirm that the leptons produced
 2034 in the SUSY benchmarks are accompanied with much more jets and are therefore less isolated than the
 2035 ones from $Z \rightarrow \ell\ell$ processes. Considering this extreme topology enables to assess a conservative SUSY
 2036 signal topology extrapolation systematic that should cover all SUSY signal processes considered by the
 2037 analysis.

2038 Figure 113 shows the real lepton efficiencies as a function of p_T . These efficiencies are computed with
 2039 truth matched lepton from $Z \rightarrow ll$, $t\bar{t}$ and $\tilde{g}\tilde{g} \rightarrow t\bar{t}t\bar{t}\tilde{\chi}_1^0\tilde{\chi}_1^0$. The $Z \rightarrow ll$ and $t\bar{t}$ leptons are reweighted to
 2040 the signal p_T distributions as large difference were found in the p_T distributions. The ratio shown in the
 2041 efficiencies plots corresponds to the $\tilde{g}\tilde{g} \rightarrow t\bar{t}t\bar{t}\tilde{\chi}_1^0\tilde{\chi}_1^0$ efficiencies divided the $Z \rightarrow ll$ ones. The left plot,
 2042 dedicated to the electron efficiencies as a function of p_T , shows that the $Z \rightarrow ll$ to SUSY signal efficiency
 2043 ratio is p_T dependent in the $p_T < 40$ GeV range and stabilize in the $p_T > 40$ GeV range. The observed
 2044 differences are mostly due to the calorimeter isolation cut and the track isolation in a lesser extent at
 2045 low p_T . The right plot dedicated to muons efficiencies shows that the p_T dependency of ratio is more

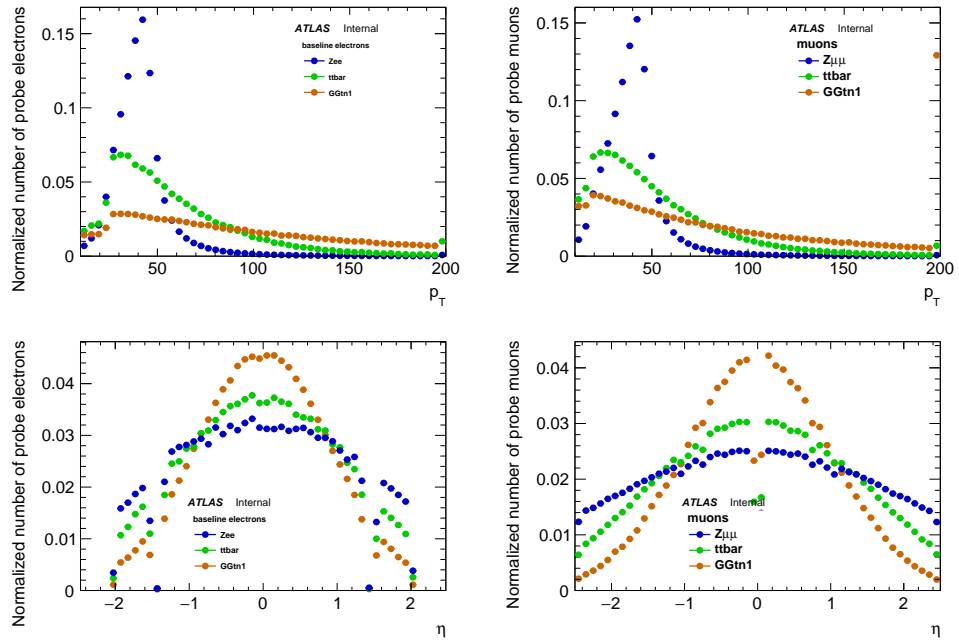


Figure 111: p_T (top) and η baseline electron (left) and muons (right) distributions. Three processes are considered, $Z \rightarrow ll$ (blue), $t\bar{t}$ (green) and $\tilde{g}\tilde{g} \rightarrow t\bar{t}t\bar{t} \tilde{\chi}_1^0 \tilde{\chi}_1^0$ with $m_{\tilde{g}} - m_{\tilde{\chi}_1^0} > 1000$ GeV (orange). A truth match on the leptons is applied.

2046 pronounced in the muon case because of the d_0/σ_{d_0} cut (which induces p_T dependent differences). The
 2047 associated relative efficiencies differences starts with 13% at low p_T and decrease down to $\sim 1\%$ in the
 2048 $p_T > 80$ GeV range. In a lesser extent, the track isolation cut also induces efficiency differences at low p_T .
 2049

2050 As tight isolation cuts are used to define signal electrons, the very different (b-)jet multiplicity of the process
 2051 is expected to induce $\Delta R(\ell, \text{jet})$ dependent efficiencies differences. Figure 114 shows the real electron
 2052 (top) and muon (bottom) efficiencies as a function of $\Delta R(l, \text{jets})$ considering three characteristic p_T ranges
 2053 : [15-20], [40-50] and [70-80] GeV. As expected a large SUSY signal efficiency decrease is observed in
 2054 the $\Delta R(\ell, \text{jet})[0.4 - 0.6]$ range for all the p_T range and for both electrons and muons. The efficiency losses
 2055 are smaller for $Z \rightarrow \ell\ell$ events in almost all the configurations, therefore larger efficiencies differences are
 2056 observed at low $\Delta R(\ell, \text{jet})$ range. Nevertheless, for electrons with $p_T > 60$ GeV, the ratio between Z and
 2057 $\tilde{g}\tilde{g} \rightarrow t\bar{t}t\bar{t} \tilde{\chi}_1^0 \tilde{\chi}_1^0$ efficiencies are flat as a function of $\Delta R(\ell, \text{jet})$. As already observed in Figure 113 the Z
 2058 to signal muon efficiencies differences decreases as a function of p_T .

2059 The efficiency differences as a function of $\Delta R(\ell, \text{jet})$ are then considered for each measurement p_T bin
 2060 without p_T reweighing to get as close as possible to the efficiency measurement configuration. A $Z \rightarrow \ell\ell$
 2061 to SUSY signal extrapolation systematic uncertainty depending on p_T and $\Delta R(\ell, \text{jet})$ is then proposed
 2062 and presented in Table 56. The systematic proposal has been validated by verifying that the systematic
 2063 uncertainties assigned as a function p_T and $\Delta R(\ell, \text{jet})$ covers the $Z \rightarrow ll$ to boosted SUSY signal efficiencies
 2064 differences seen as a function of $|\eta|$ and n_{jets} ⁹.

⁹ If it is not the case, the systematic uncertainties are enlarged.

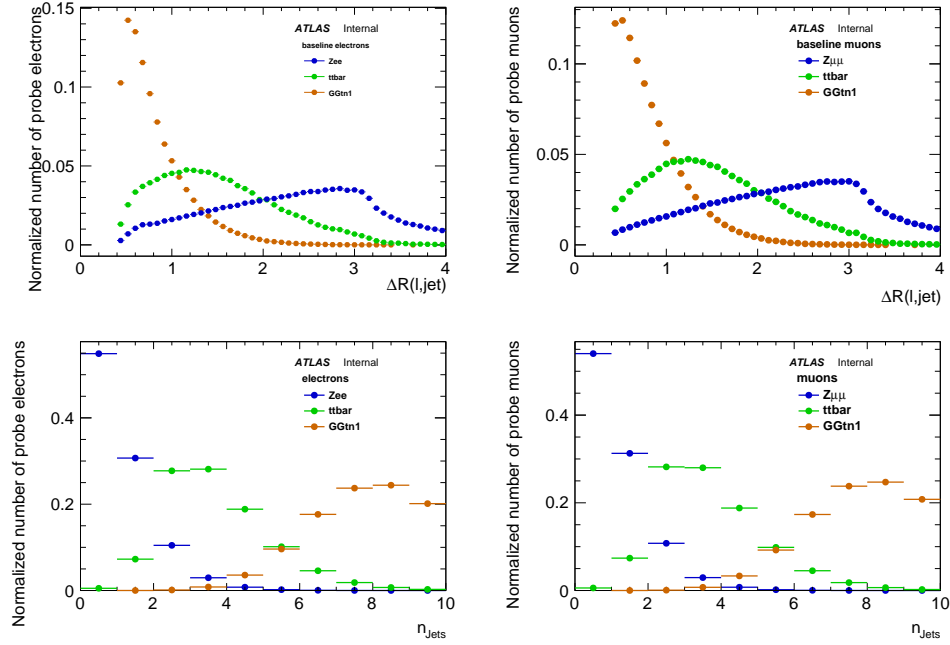


Figure 112: $\Delta R(\ell, \text{jet})$ (top) and n_{jets} (bottom) baseline electron (left) and muons (right) distributions. Three processes are considered, $Z \rightarrow ll$ (blue), $t\bar{t}$ (green) and $\tilde{g}\tilde{g} \rightarrow t\bar{t}t\bar{t} \tilde{\chi}_1^0 \tilde{\chi}_1^0$ with $m_{\tilde{g}} - m_{\tilde{\chi}_1^0} > 1000 \text{ GeV}$ (orange). A truth match on the leptons is applied.

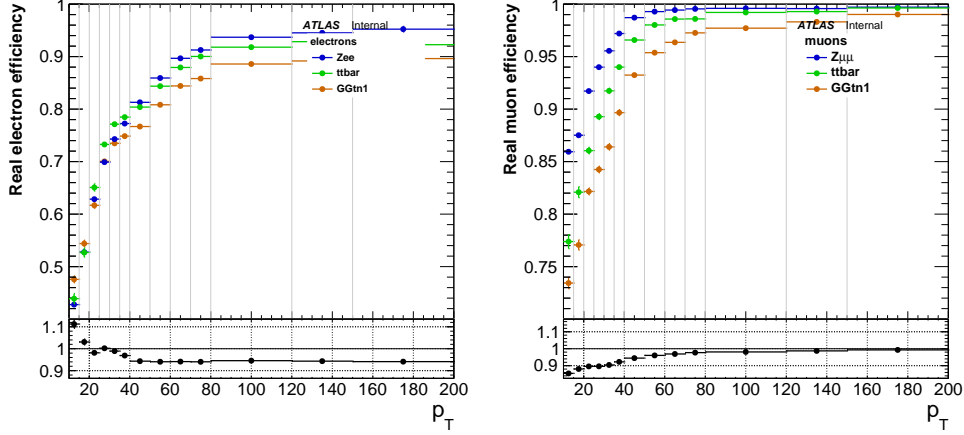


Figure 113: Real electron (left) and muon (right) efficiencies as a function p_T . Three processes are considered, $Z \rightarrow ll$ (blue), $t\bar{t}$ (green) and $\tilde{g}\tilde{g} \rightarrow t\bar{t}t\bar{t} \tilde{\chi}_1^0 \tilde{\chi}_1^0$ with $m_{\tilde{g}} - m_{\tilde{\chi}_1^0} > 1000 \text{ GeV}$ (orange). A truth match on the leptons is applied and a p_T reweighting to the SUSY signal electron p_T is used to compute the efficiencies.

2065 Summary of the real lepton efficiencies systematics

2066 Table 57 summarizes the relative contributions of the different systematic uncertainties for electron (right
2067 column) and muons (left column). The first systematic uncertainty corresponds to the measurement. In the

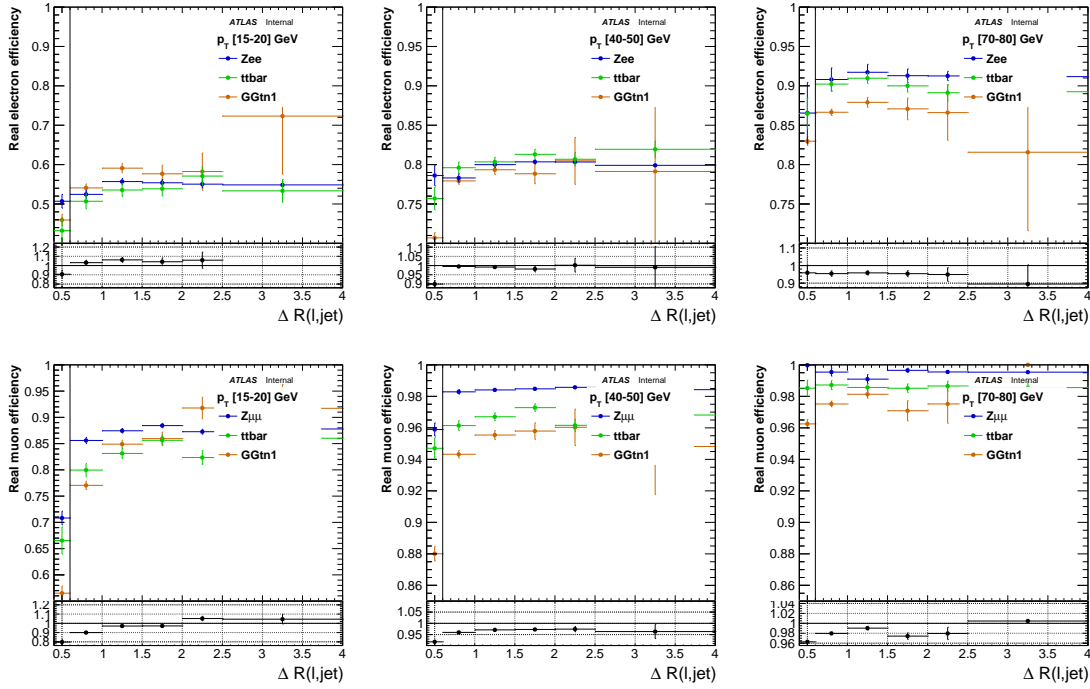


Figure 114: Real electron electrons (top) and muons (bottom) efficiencies as a function of $\Delta R(\ell, \text{jet})$ computed for three different p_T ranges. The left plots correspond to the [15-20] GeV range, the middle to the [40-50] GeV, and the right ones to the [70-80] GeV p_T range. Three processes are considered, $Z \rightarrow ll$ (blue), $t\bar{t}$ (green) and $\tilde{g}\tilde{g} \rightarrow t\bar{t}t\bar{t}\tilde{\chi}_1^0\tilde{\chi}_1^0$ with $m_g - m_{\tilde{\chi}_1^0} > 1000$ GeV (orange). Prompt leptons are selected using a loose truth match and no p_T reweighting is applied.

electrons		
	$0.4 < \Delta R(\ell, \text{jet}) < 0.6$	$\Delta R(\ell, \text{jet}) > 0.6$
$p_T < 60$ GeV	8%	4%
$p_T > 60$ GeV	5%	5%
muons		
	$0.4 < \Delta R(l, \text{Jet}) < 0.6$	$\Delta R(l, \text{jet}) > 0.6$
$p_T < 15$ GeV	28%	10%
$15 < p_T < 35$ GeV	18%	7%
$35 < p_T < 50$ GeV	10%	5%
$50 < p_T < 80$ GeV	5%	3%
$p_T > 80$ GeV	1%	1%

Table 56: Real lepton efficiencies $Z+\text{Jets}$ to SUSY signal extrapolation systematics. These numbers are computed comparing lepton efficiencies computed on $Z+\text{Jets}$ events with one computed on gtt signals with $m_g - m_{\tilde{\chi}_1^0} > 1000$ GeV (boosted topology).

2068 electron case, the three numbers corresponds to the measurements η ranges ([0-0.8]/[0.8-1.37]/[1.52-2]),

2069 shows that larger measurement uncertainties are observed at large pseudorapidity. As the impact of the
 2070 bremsstrahlung decreases with p_T , the measurement systematic decreases with p_T . The second electron
 2071 systematic uncertainty corresponds to the trigger one. As the e12_lhloose trigger efficiency increases
 2072 with p_T the trigger systematic decreases with p_T . The last systematic uncertainties corresponds to the
 2073 signal extrapolation ones, more detail is given in the previous paragraph.

	electrons	muons
$p_T < 15 \text{ GeV}$	5.3/5.2/6.7 (<i>meas</i>) ± 0 (<i>trig</i>) $\pm 8/4$ (<i>signal</i>) %	1 (<i>meas</i>) $\pm 28/10$ (<i>signal</i>) %
$15 < p_T < 20 \text{ GeV}$	3.0/3.5/4.5 (<i>meas</i>) ± 0 (<i>trig</i>) $\pm 8/4$ (<i>signal</i>) %	0.5 (<i>meas</i>) $\pm 18/7$ (<i>signal</i>) %
$20 < p_T < 25 \text{ GeV}$	2.5/2.7/3.4 (<i>meas</i>) ± 4 (<i>trig</i>) $\pm 8/4$ (<i>signal</i>) %	0.1 (<i>meas</i>) $\pm 18/7$ (<i>signal</i>) %
$25 < p_T < 30 \text{ GeV}$	1.6/1.7/2.4 (<i>meas</i>) ± 4 (<i>trig</i>) $\pm 8/4$ (<i>signal</i>) %	0.1 (<i>meas</i>) $\pm 18/7$ (<i>signal</i>) %
$30 < p_T < 35 \text{ GeV}$	0.9/1.3/1.7 (<i>meas</i>) ± 2 (<i>trig</i>) $\pm 8/4$ (<i>signal</i>) %	0.1 (<i>meas</i>) $\pm 18/7$ (<i>signal</i>) %
$35 < p_T < 40 \text{ GeV}$	0.5/0.8/1.0 (<i>meas</i>) ± 2 (<i>trig</i>) $\pm 8/4$ (<i>signal</i>) %	0.1 (<i>meas</i>) $\pm 10/5$ (<i>signal</i>) %
$40 < p_T < 50 \text{ GeV}$	0.2/0.3/0.4 (<i>meas</i>) ± 2 (<i>trig</i>) $\pm 8/4$ (<i>signal</i>) %	0.1 (<i>meas</i>) $\pm 10/5$ (<i>signal</i>) %
$50 < p_T < 60 \text{ GeV}$	0.2/0.1/0.2 (<i>meas</i>) ± 1 (<i>trig</i>) $\pm 8/4$ (<i>signal</i>) %	0.1 (<i>meas</i>) $\pm 5/3$ (<i>signal</i>) %
$60 < p_T < 80 \text{ GeV}$	0/0/0.4 (<i>meas</i>) ± 0.5 (<i>trig</i>) ± 5 (<i>signal</i>) %	0.1 (<i>meas</i>) $\pm 5/3$ (<i>signal</i>) %
$p_T > 80 \text{ GeV}$	0.1/0.20.3/ (<i>meas</i>) ± 0.5 (<i>trig</i>) ± 5 (<i>signal</i>) %	0.1 (<i>meas</i>) ± 1 (<i>signal</i>) %

Table 57: Summary of the systematic uncertainties. The first uncertainties corresponds to the tag-and-probe method measurement method (*meas*). Thee values are given for electrons as corresponding to the three $|\eta|$ measurements ranges ([0-0.8]/[0.8-1.37]/[1.52-2]). The second electron uncertainty correspond to the di-electron trigger bias (*trig*). And the last ones to the $Z \rightarrow \ell\ell$ to SUSY signal extrapolation uncertainty (*signal*). Two values are given corresponding to the following $\Delta R(\ell, \text{jet})$: [0.4-0.6] / $\Delta R(\ell, \text{jet}) > 0.6$

2074 Z tag-and-probe efficiencies tables

2075

2076 Tables 58, 59 shows the summary of the electron and muons efficiencies used for the matrix method fake
 2077 estimates. The first systematic uncertainties corresponds to the statistical ones and are negligible with
 2078 respect to the seconds ones that corresponds to the systematic ones.

2079 16.4 Real leptons efficiency measured using $t\bar{t}$ events

2080 Presentation of the method

2081 In order to have an efficiency measurement as close to the signal region as possible, a tag-and-probe
 2082 method has been put in place to select leptons from $t\bar{t}$ events.

2083 The selection of the $t\bar{t}$ events is based on the following criteria :

- 2084 • Exactly two baseline leptons with a p_T larger than 30 GeV are requested. This brings rejection
 2085 against $W + jets$, $t\bar{t}Z$, tri-bosons or other complex processes.
- 2086 • A least one b-jet (using the b-jet definitions from the analysis) is required. This brings rejection
 2087 against $Z/W + jets$ and VV events.
- 2088 • A $E_T^{miss} > 30 \text{ GeV}$ requirement is added if the two selected leptons are ee or $\mu\mu$. This brings further
 2089 rejection against $Z+jets$ events and other background events.

$\backslash \text{pt} (\text{GeV}) \setminus \eta $	[0-0.8]	[0.8-1.37]	[1.52-2]
[10-15]	$43.7 \pm 0.8 \pm 4.2/2.9\%$	$53.6 \pm 0.8 \pm 5.1/3.5\%$	$49.6 \pm 0.8 \pm 5.2/3.9\%$
[15-20]	$56.0 \pm 0.4 \pm 4.8/2.8\%$	$59.4 \pm 0.5 \pm 5.2/3.2\%$	$59.8 \pm 0.5 \pm 5.5/3.6\%$
[20-25]	$64.7 \pm 0.3 \pm 6.0/4.0\%$	$64.7 \pm 0.3 \pm 6.1/4.1\%$	$68.0 \pm 0.3 \pm 6.5/4.5\%$
[25-30]	$70.7 \pm 0.2 \pm 6.4/4.2\%$	$70.8 \pm 0.2 \pm 6.4/4.2\%$	$73.6 \pm 0.2 \pm 6.8/4.5\%$
[30-35]	$75.9 \pm 0.1 \pm 6.3/3.5\%$	$74.6 \pm 0.2 \pm 6.2/3.5\%$	$78.7 \pm 0.2 \pm 6.8/3.7\%$
[35-40]	$80.0 \pm 0.1 \pm 6.6/3.6\%$	$76.8 \pm 0.1 \pm 6.4/3.5\%$	$79.8 \pm 0.2 \pm 6.6/3.7\%$
[40-50]	$82.9 \pm 0.1 \pm 6.8/3.7\%$	$79.8 \pm 0.1 \pm 6.6/3.6\%$	$84.1 \pm 0.1 \pm 6.9/3.8\%$
[50-60]	$86.9 \pm 0.1 \pm 7.0/3.6\%$	$83.9 \pm 0.2 \pm 6.8/3.5\%$	$87.0 \pm 0.2 \pm 7.0/3.6\%$
[60-80]	$90.7 \pm 0.2 \pm 4.6/4.6\%$	$89.2 \pm 0.2 \pm 4.5/4.5\%$	$89.6 \pm 0.4 \pm 4.5/4.5\%$
$p_T > 80$	$93.8 \pm 0.2 \pm 4.7/4.7\%$	$90.3 \pm 0.5 \pm 4.7/4.7\%$	$92.4 \pm 0.5 \pm 4.6/4.6\%$

Table 58: Electron efficiencies tables. The first and the second uncertainties are the statistical and the systematic one respectively. The shown systematic uncertainties (*syst*) corresponds to the quadratic sum of the tag-and-probe, trigger and the signal extrapolation systematic uncertainties. Two values are given corresponding to the two signal extrapolation systematic $\Delta R(\ell, \text{jet})$ ranges : [0.4-0.6] (left) / $\Delta R(\ell, \text{jet}) > 0.6$ (right) range.

$\backslash \text{pt} (\text{GeV}) \setminus \eta $	[0-0.6]	[0.6-1.2]	[1.2-1.8]	[1.8-2.5]
[10-15]	$84.6 \pm 0.4 \pm 24/8.5\%$	$84.6 \pm 0.4 \pm 24/8.5\%$	$84.7 \pm 0.4 \pm 24/8.5\%$	$83.6 \pm 0.4 \pm 23/8.4\%$
[15-20]	$86.4 \pm 0.2 \pm 16/6.1\%$	$86.4 \pm 0.2 \pm 16/6.1\%$	$85.8 \pm 0.3 \pm 15/6.0\%$	$86.1 \pm 0.3 \pm 16/6.0\%$
[20-25]	$90.8 \pm 0.1 \pm 16/6.4\%$	$90.9 \pm 0.2 \pm 16/6.4\%$	$90.6 \pm 0.2 \pm 16/6.3\%$	$90.3 \pm 0.2 \pm 16/6.3\%$
[25-30]	$93.9 \pm 0.1 \pm 17/6.6\%$	$93.7 \pm 0.1 \pm 17/6.6\%$	$93.2 \pm 0.1 \pm 17/6.5\%$	$93.2 \pm 0.1 \pm 17/6.5\%$
[30-35]	$95.6 \pm 0.1 \pm 17/6.7\%$	$95.3 \pm 0.1 \pm 17/6.7\%$	$95.0 \pm 0.1 \pm 17/6.7\%$	$94.6 \pm 0.1 \pm 17/6.6\%$
[35-40]	$97.2 \pm O(0.1) \pm 9.7/4.9\%$	$97.3 \pm O(0.1) \pm 9.7/4.9\%$	$97.0 \pm O(0.1) \pm 9.7/4.8\%$	$96.5 \pm 0.1 \pm 9.6/4.8\%$
[40-50]	$98.4 \pm O(0.1) \pm 9.8/4.9\%$	$98.5 \pm O(0.1) \pm 9.9/4.9\%$	$98.3 \pm O(0.1) \pm 9.8/4.9\%$	$98.0 \pm O(0.1) \pm 9.8/4.9\%$
[50-60]	$98.9 \pm O(0.1) \pm 4.9/3.0\%$	$99.0 \pm O(0.1) \pm 5.0/3.0\%$	$98.9 \pm O(0.1) \pm 4.9/3.0\%$	$98.7 \pm O(0.1) \pm 4.9/3.0\%$
[60-70]	$99.2 \pm O(0.1) \pm 5.0/3.0\%$	$99.3 \pm O(0.1) \pm 5.0/3.0\%$	$99.2 \pm O(0.1) \pm 5.0/3.0\%$	$99.0 \pm O(0.1) \pm 5.0/3.0\%$
[70-80]	$99.5 \pm O(0.1) \pm 5.0/3.0\%$	$99.5 \pm O(0.1) \pm 5.0/3.0\%$	$99.4 \pm O(0.1) \pm 5.0/3.0\%$	$99.2 \pm 0.1 \pm 5.0/3.0\%$
$p_T > 80$	$99.5 \pm 0.1 \pm 1.0/1.0\%$			

Table 59: Muon efficiencies tables. The first and the second uncertainties are the statistical and the systematic one respectively. The shown systematic uncertainties (*syst*) corresponds to the quadratic sum of the tag-and-probe and the signal extrapolation systematic uncertainties. Two values are given corresponding to the two signal extrapolation systematic $\Delta R(\ell, \text{jet})$ ranges : [0.4-0.6] (left) / $\Delta R(\ell, \text{jet}) > 0.6$ (right) range.

- 2090 • A Z veto removing lepton pairs with $70 < m_{ll} < 100$ GeV is also applied if the two selected leptons
2091 are ee or $\mu\mu$ to bring further rejection against $Z+jets$ and $t\bar{t}Z$ events.
2092 One of the two leptons is requested to pass the signal lepton requirements (tag lepton) and the other to
2093 pass the baseline requirements (probe lepton). The two leptons are alternatively considered as possible
2094 tag with no restrictions on the lepton flavour.

2095 Validation of the method

2096 The effect of $t\bar{t}$ event selection cuts are shown in Table 60. This table shows that the W+jet events
2097 are mainly rejected by the exactly 2 leptons with $p_T > 30$ GeV requirement and the at least one b-jet
2098 requirements. On the other hand the $Z + jet$ background is rejected by the at least one b-jet, the E_T^{miss}
2099 and the m_{ll} veto requirements. After all selection cuts, the contribution from the V+jets events represents
2100 $\sim 2\%$ of the $t\bar{t}$ statistics assessing a good purity in the $t\bar{t}$ tag-and-probe events selection. VV and $t\bar{t}V$ are
2101 contributing much less due to their lower cross sections. The exactly two baseline lepton requirement is

2102 further reducing the contribution from VV and $t\bar{t}V$ by selecting events with two lepton in the final state.
 2103 The contribution from VV processes is further rejected with the at least one $b - jet$ requirement. The
 2104 contribution from $t\bar{t}Z$ processes is further reduced by the m_{ll} veto. Marginal contribution are expected
 2105 from $t\bar{t}t\bar{t}$ due to their low cross section and the at exactly two baseline lepton requirement.

Processes	$t\bar{t}$	$W+jets$	$Z+jets$
At least 2 baseline leptons	82106	38181	3519252
Exactly 2 baseline leptons with $p_T > 30$ GeV	39375 (48%)	3451 (9%)	2861459 (81%)
At least 1 b-jet	32242 (82%)	70 (2%)	36174 (1.2%)
$E_T^{miss} > 30$ GeV ($ee/\mu\mu$)	29950 (93%)	63 (90%)	9 514 (26%)
m_{ll} veto	26969 (90%)	54 (86%)	766 (8%)
Yields normalized to $t\bar{t}$ events	100%	0.06%	2%

Table 60: Expected number of events for 3 fb^{-1} computed that passes the $t\bar{t}$ tag-and-probe events cuts. The yields corresponding to the $t\bar{t}$ processes (first column) are computed using a $t\bar{t}$ Monte Carlo simulation with filter that removes all hadronic decays, the ones corresponding to the $W+jets$ processes (second column) are computed using $W \rightarrow e/\mu/\tau \nu_{e/\mu/\tau}$ Monte Carlo simulations and ones corresponding to the $Z+jets$ (third column) are computed using $Z \rightarrow ee/\mu\mu/\tau\tau$ Monte Carlo simulations. The last row corresponds to the final number of events for the different processes normalized to the number of remaining $t\bar{t}$ events.

2106 Results

2107 The distributions and the real lepton efficiencies computed with probes leptons extracted in data using
 2108 the $t\bar{t}$ tag-and-probe method have been compared to the ones from simulated $t\bar{t}$ processes. All scale
 2109 factors, the pile-up reweighing have been applied for Monte Carlo and the Monte Carlo distributions are
 2110 normalised to the data. The full 2015 data is used for those measurements which corresponds to an
 2111 integrated luminosity of $\sim 3.2 \text{ fb}^{-1}$ after good run list requirements. Figure 115 shows the comparison
 2112 between the real lepton efficiency computed with the $t\bar{t}$ tag-and-probe using data and $t\bar{t}$ simulated events.
 2113 The real efficiency is computed for different bins in p_T (top), $|\eta|$ (middle) and $\Delta R(\ell, \text{jet})$ (bottom). These
 2114 plots shows that the real lepton efficiencies computed on data agrees within the statistical errors to the ones
 2115 computed on Monte Carlo. The Monte Carlo efficiencies are very close to the Data ones. The validates
 2116 the measurement method.

2117 Comparison between Z and the $t\bar{t}$ real leptons efficiencies measurements

2118 The $t\bar{t}$ tag-and-probe method was first developed to enrich the statistics at large p_T and low $\Delta R(\ell, \text{jet})$ for
 2119 the real leptons efficiency measurements on data. Figure 116 shows the total number of probe leptons
 2120 expected to be extracted with the Z and the $t\bar{t}$ tag-and-probe method for 3fb^{-1} of collision data for different
 2121 p_T threshold. Those plots show that the number of lepton extracted from Z events are 10 times larger than
 2122 the number of lepton extracted from $t\bar{t}$ at large p_T for both muons and electrons.

2123 Figure 117 shows the $\Delta R(\ell, \text{jet})$ distribution extracted from Z and $t\bar{t}$ events normalized to 3fb^{-1} of lumin-
 2124 osity. No statistical gain is seen at low $\Delta R(\ell, \text{jet})$. This show that the statistical gain for the real lepton
 2125 efficiency measurement induced by the $t\bar{t}$ tag-and-probe is marginal.

2126

2127 Real efficiency comparisons

2128

2129 The top plots from Figure 118 show the real lepton efficiency computed with either the Z or the $t\bar{t}$
 2130 tag-and-probe method. The top plots shows the real lepton efficiency as a function the lepton p_T . The

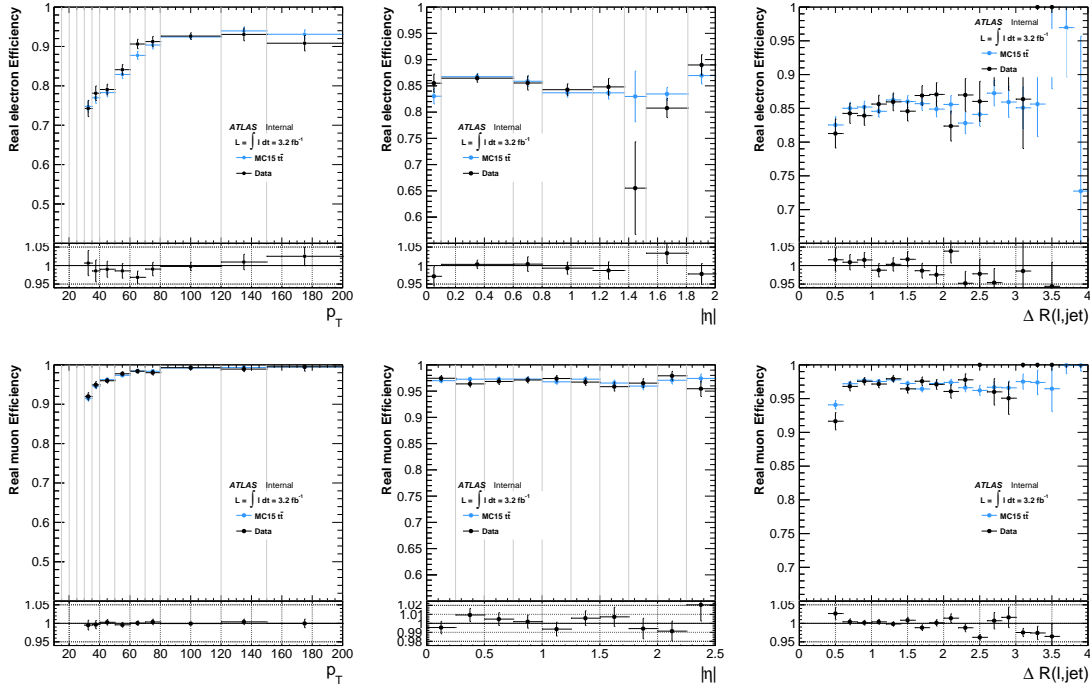


Figure 115: Real lepton efficiencies as a function of p_T (left), η (middle) and $\Delta R(\ell, \text{jet})$ (right) computed using $t\bar{t}$ probe leptons extracted from $t\bar{t}$ Monte Carlo simulations with truth match (light blue) and 2015 data (black points).

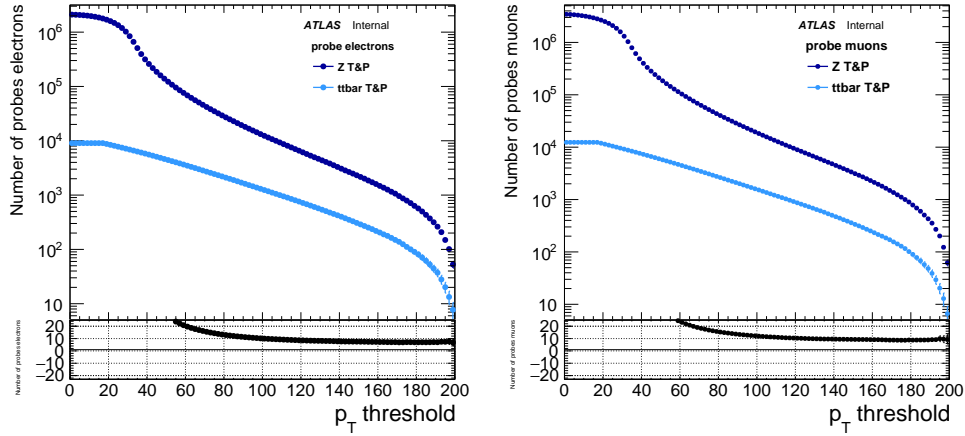


Figure 116: Total number of probe leptons normalized to 3fb^{-1} luminosity as a function of the considered p_T threshold. The leptons are extracted with the Z (dark blue) and $t\bar{t}$ (light blue) tag-and-probe method from their relevant Monte Carlo samples.

real electron efficiency computed with the $t\bar{t}$ tag-and-probe method is $\sim 4\%$ lower than the one computed with the Z tag-and-probe method for $p_T < 60$ GeV and $\sim 2\%$ lower for $p_T > 60$ GeV range. The real muon efficiency computed with the $t\bar{t}$ tag-and-probe method is $\sim 6\%$ lower than the one computed with

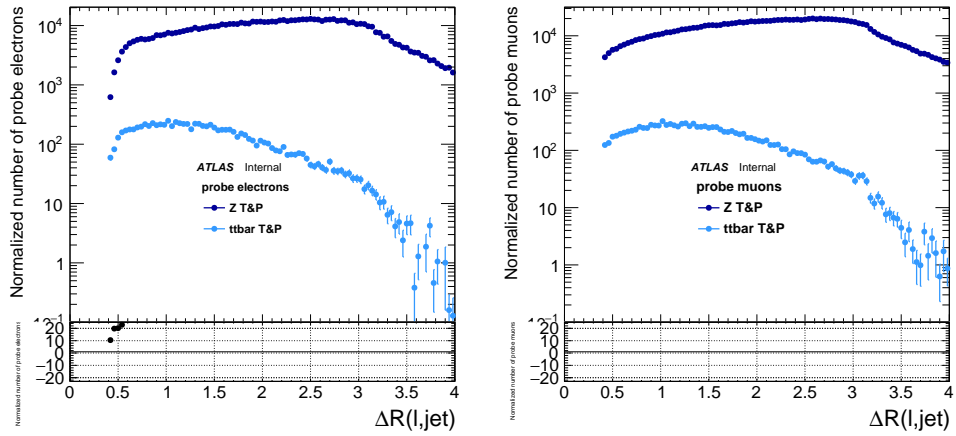


Figure 117: $\Delta R(\ell, \text{jet})$ Distribution of the probe leptons extracted with the Z and the $t\bar{t}$ tag-and-probe method from relevant Monte Carlo samples normalized to 3fb^{-1} luminosity. The left plot corresponds to the probe electrons and the right one to the probe muons.

2134 the Z tag-and-probe method in the $30 < p_T < 35$ GeV range and decreases with p_T . Almost no efficiency
2135 differences is see for the $p_T > 80$ GeV range.

2136 As the topology of the $t\bar{t}$ events is closer to the ones selected by the signal regions of the analysis than
2137 the $Z \rightarrow ll$ ones, a better estimation of the real lepton efficiency can be performed using the $t\bar{t}$ tag-
2138 and-probe method. The error bars from Figure 118 are corresponding the estimation of the statistical
2139 errors with 3 fb^{-1} of data. This shows that with 10 fb^{-1} of statistics, the statistics will be large enough
2140 for a efficiency measurement using leptons from $t\bar{t}$. This will then reduce the SUSY signal topology
2141 extrapolation systematic described in Section 16.3.

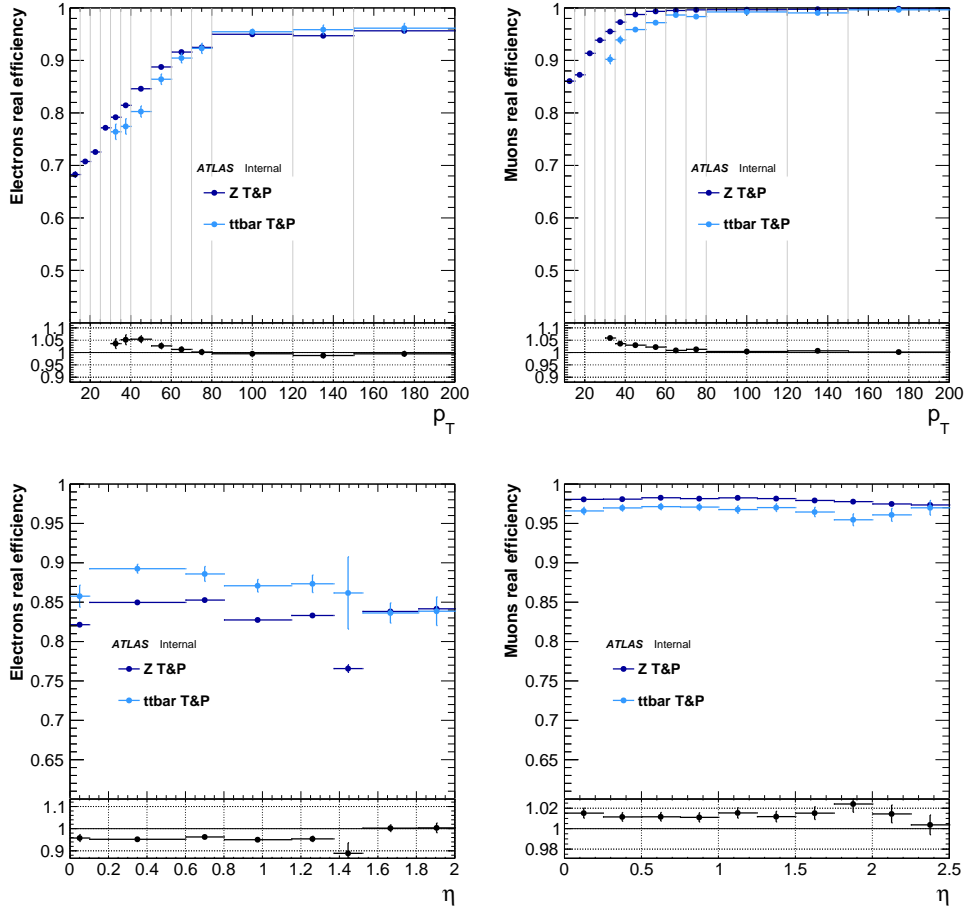


Figure 118: Real electron (left) and muon (right) efficiency efficiency computed using the Z (dark blue) and the $t\bar{t}$ (light blue) tag-and-probe method using relevant Monte Carlo samples. The top (bottom) plot shows the real lepton efficiency computed as a function p_T ($|\eta|$). The real efficiencies as a function of $|\eta|$ are computed considering only electron with $p_T > 30$ GeV. The statistical error bars are computed with the expected statistics at $3fb^{-1}$.

2142 17 Further details on background estimation

2143 **Fake electron sources close to the signal regions**

2144 Fig 119 shows the number of events and the associated statistical uncertainties for the different fake
2145 electrons, for different p_T cuts, in the relaxed signal regions defined in Table 15.

2146 Truth composition as a function of fake electron η , m_{eff} and E_T^{miss} are shown in Fig 120-122.

2147 **Fake muon sources close to the signal regions**

2148 Fig 123 shows the number of events and the associated statistical uncertainties for the different fake muon
2149 sources, for different p_T cuts, in the relaxed signal regions defined in Table 15.

2150 Truth composition as a function of fake muon m_{eff} and E_T^{miss} are shown in Fig 124-125.

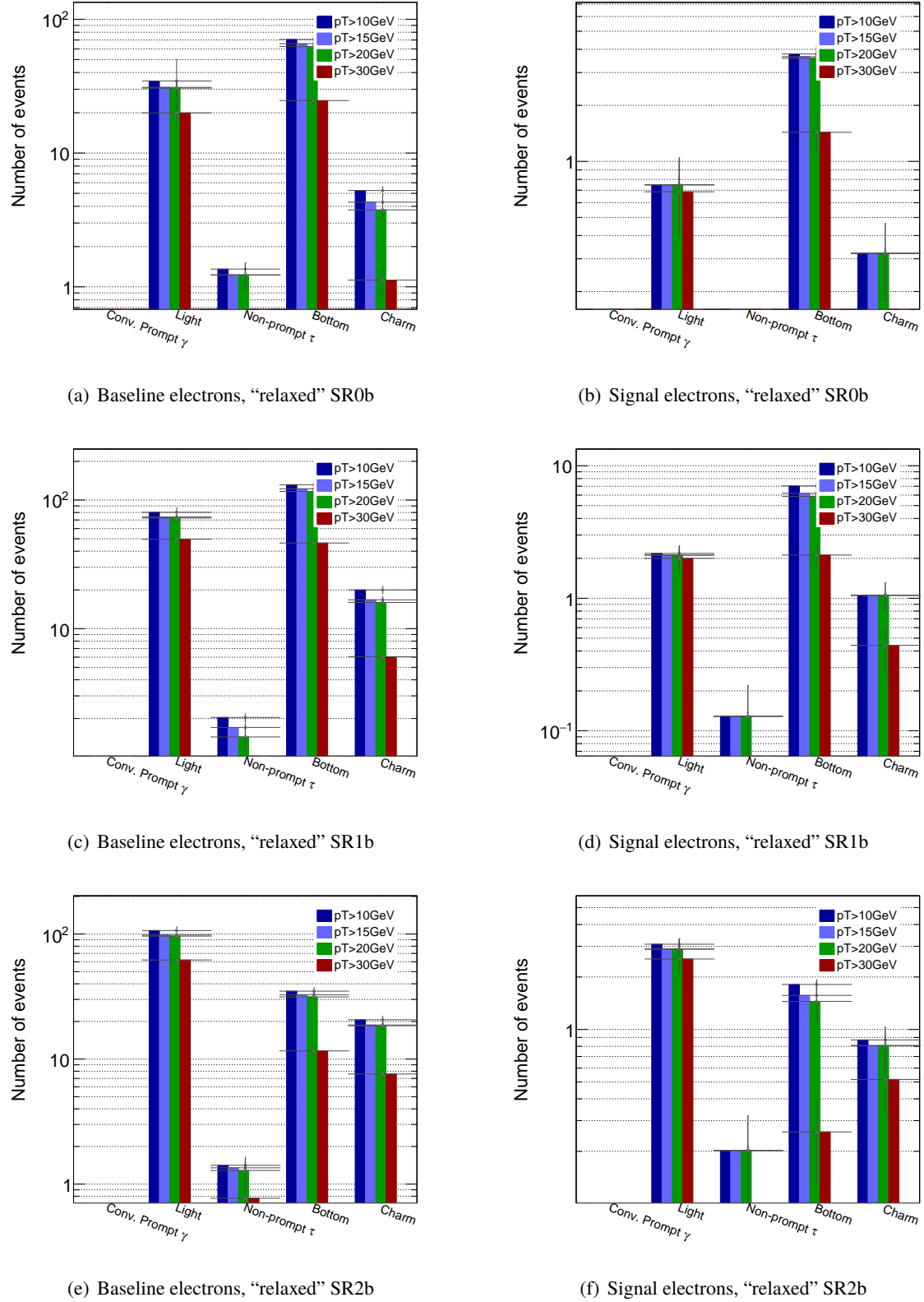


Figure 119: Sources of fake electrons as a function of the electron p_T , as predicted by MC simulations (combined $t\bar{t}$ and $V + \text{jets}$) in the relaxed signal regions defined in Table 15. The results are shown for baseline (left) or signal electrons (right). Only the statistical uncertainty are shown.

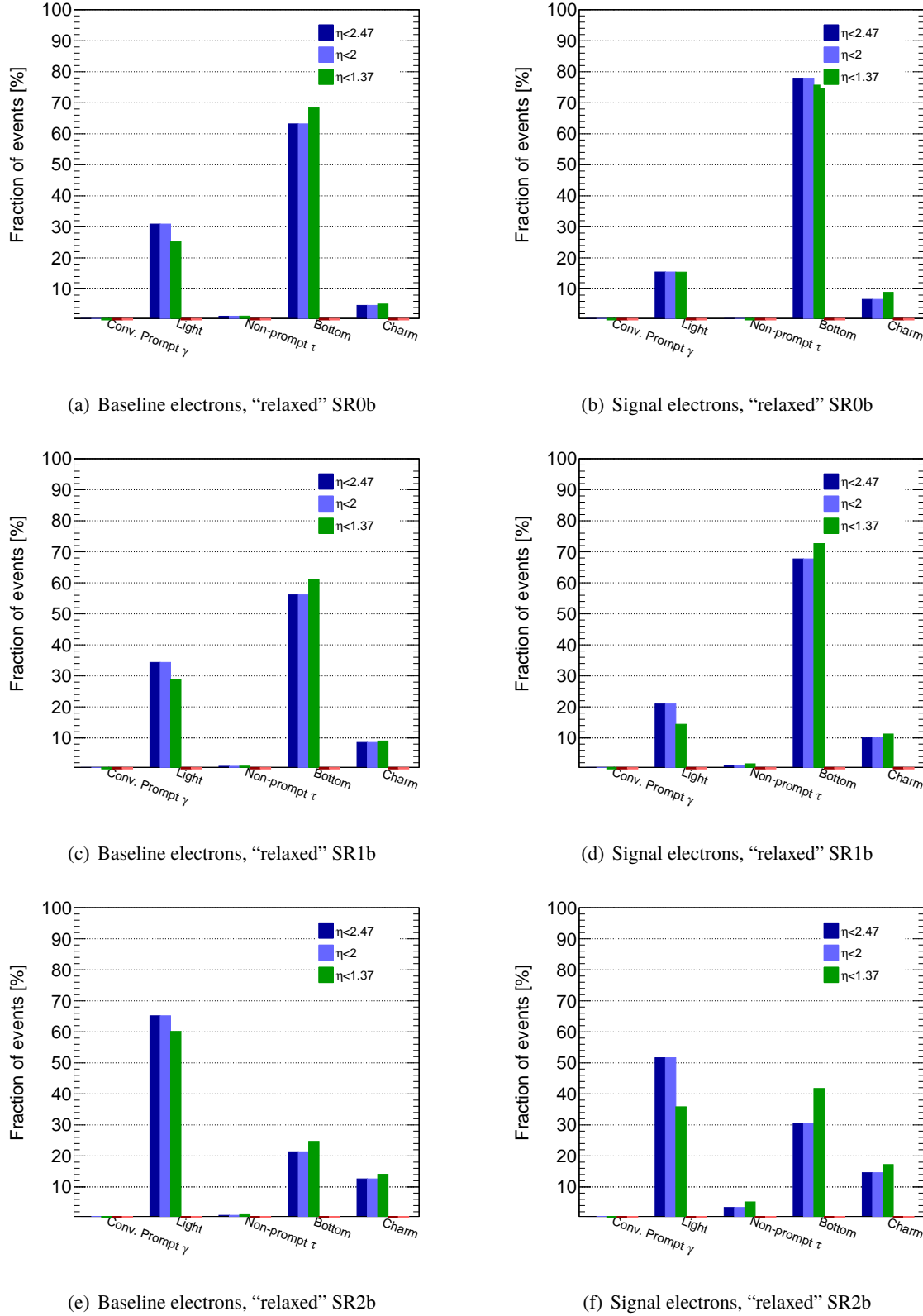


Figure 120: Sources of fake electrons as a function of the electron η , as predicted by MC simulations (combined $t\bar{t}$ and $V + \text{jets}$) in the relaxed signal regions defined in Table 15. The results are shown for baseline (left) or signal electrons (right).

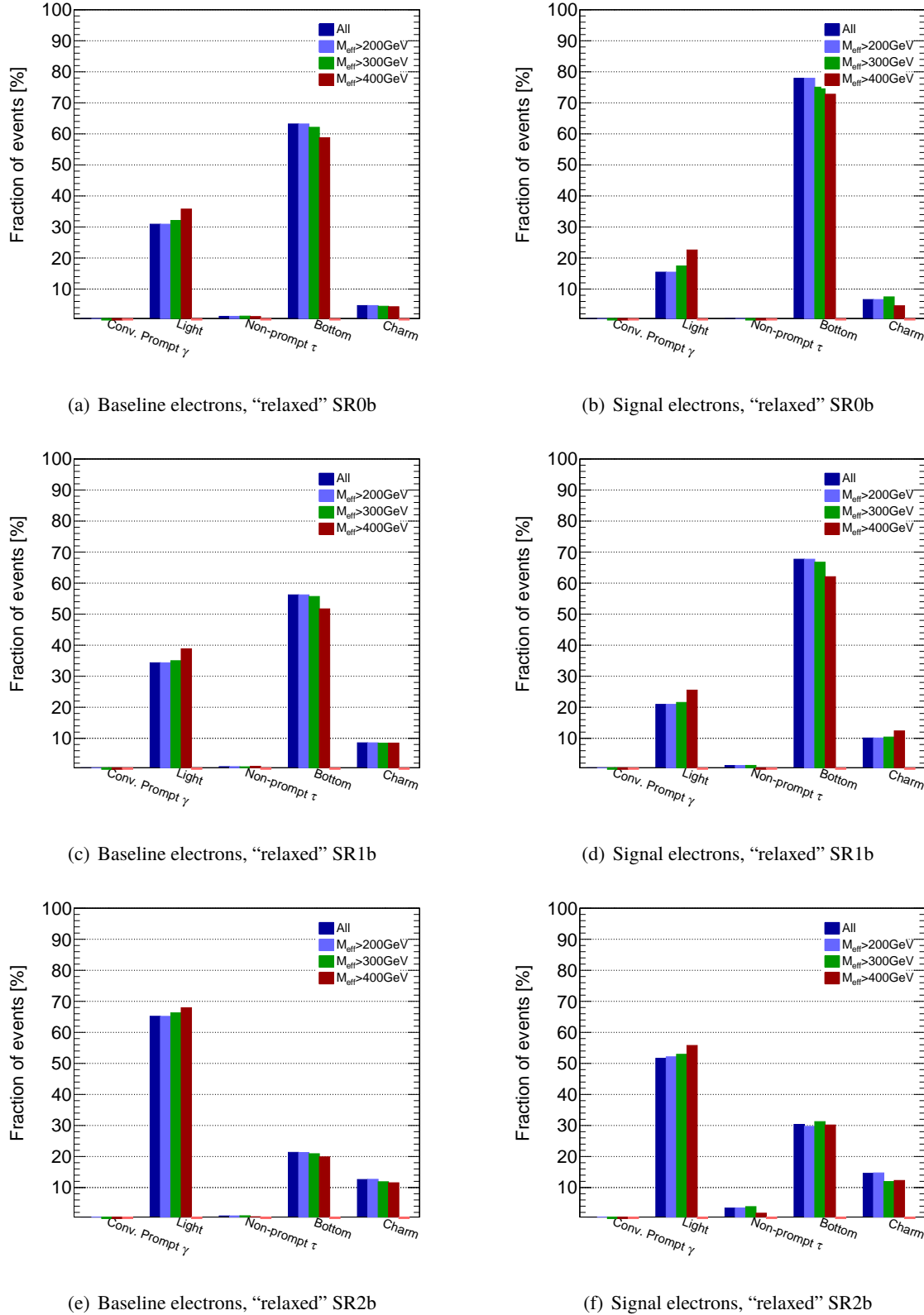


Figure 121: Sources of fake electrons as a function of m_{eff} , as predicted by MC simulations (combined $t\bar{t}$ and $V+$ jets) in the relaxed signal regions defined in Table 15. The results are shown for baseline (left) or signal electrons (right).

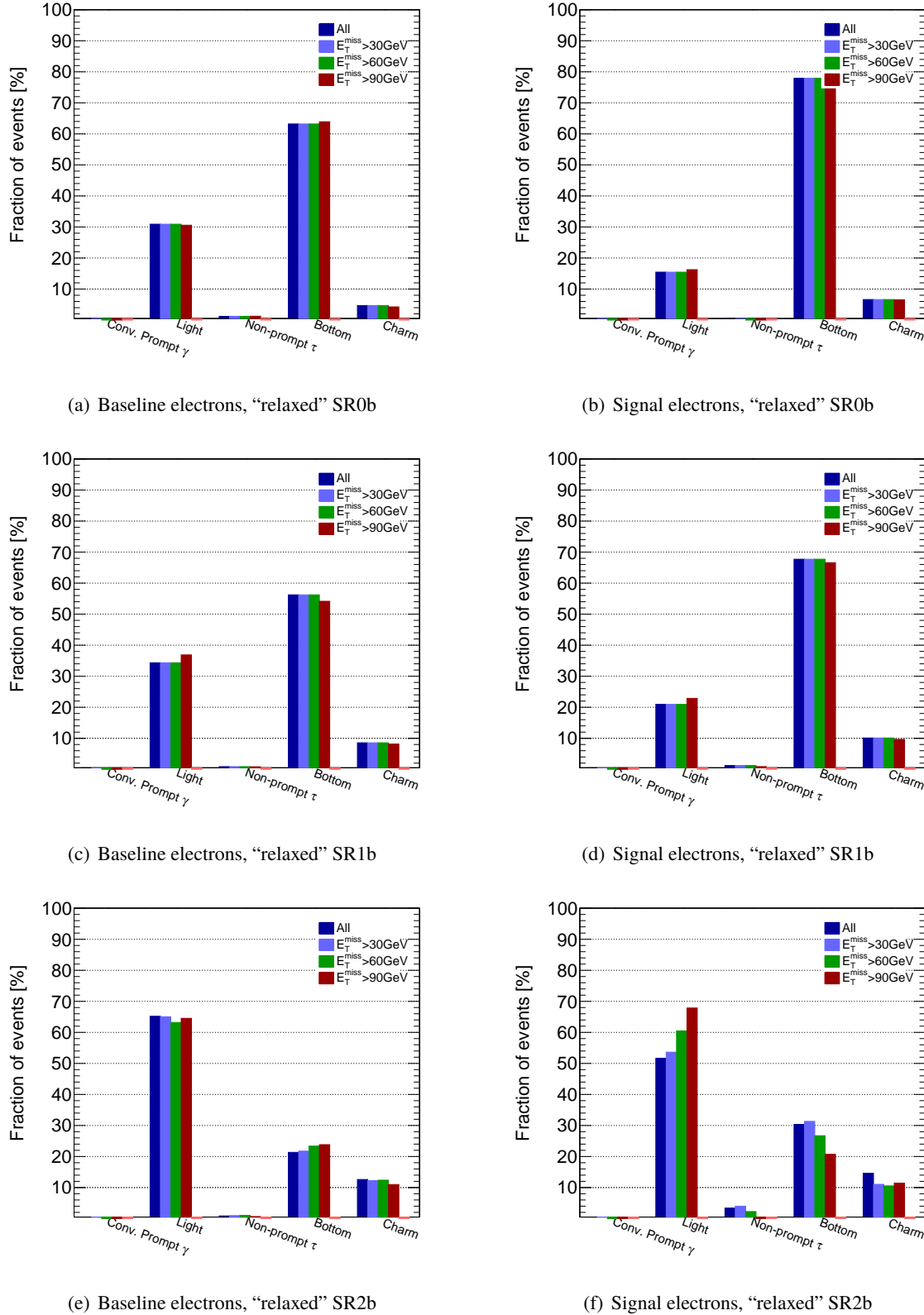


Figure 122: Sources of fake electrons as a function of E_T^{miss} , as predicted by MC simulations (combined $t\bar{t}$ and $V+$ jets) in the relaxed signal regions defined in Table 15. The results are shown for baseline (left) or signal electrons (right).

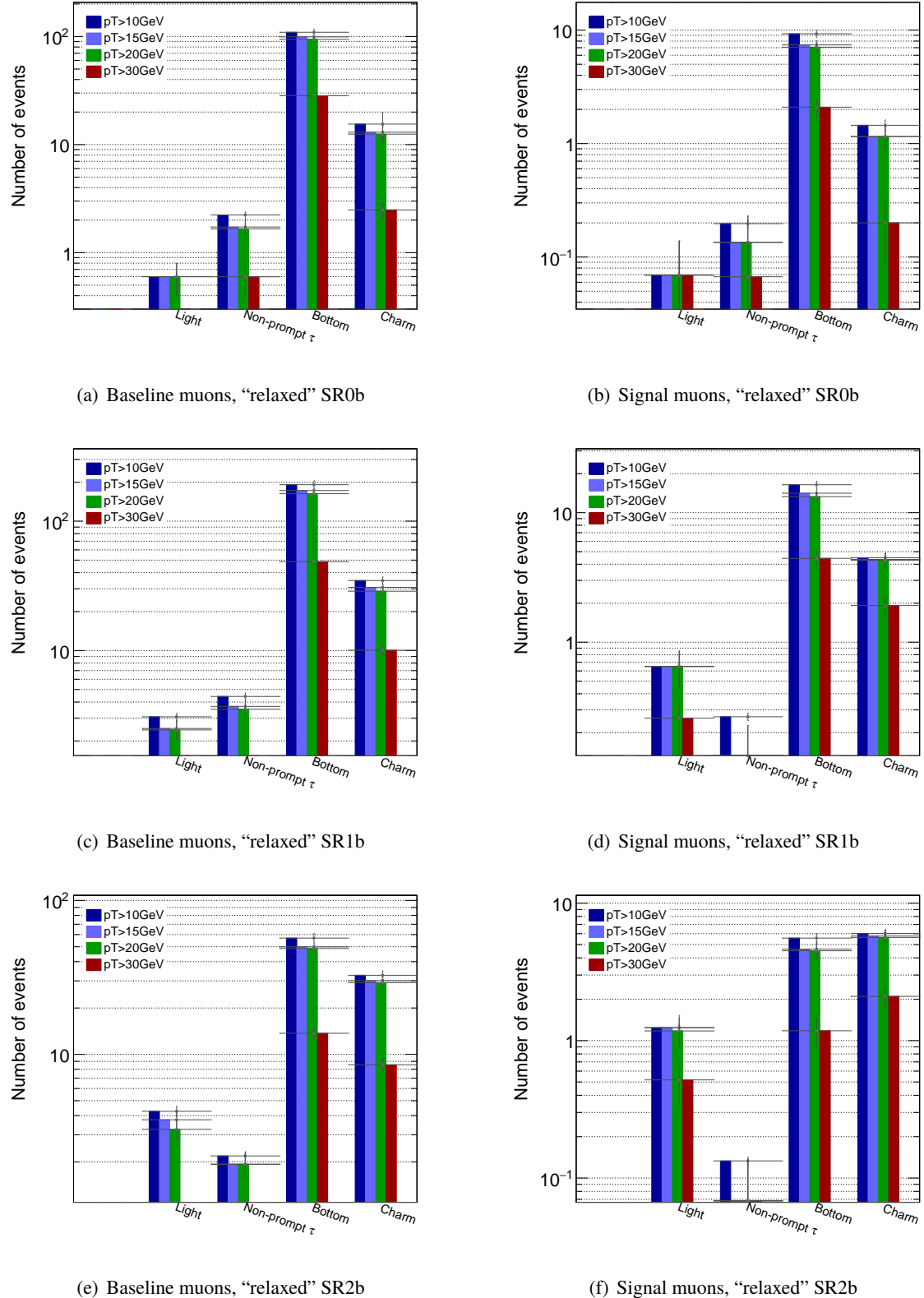


Figure 123: Sources of fake muons as a function of the muon p_T , as predicted by MC simulations (combined $t\bar{t}$ and $V + \text{jets}$) in the relaxed signal regions defined in Table 15. The results are shown for baseline (left) or signal muons (right). Only the statistical uncertainty are shown.

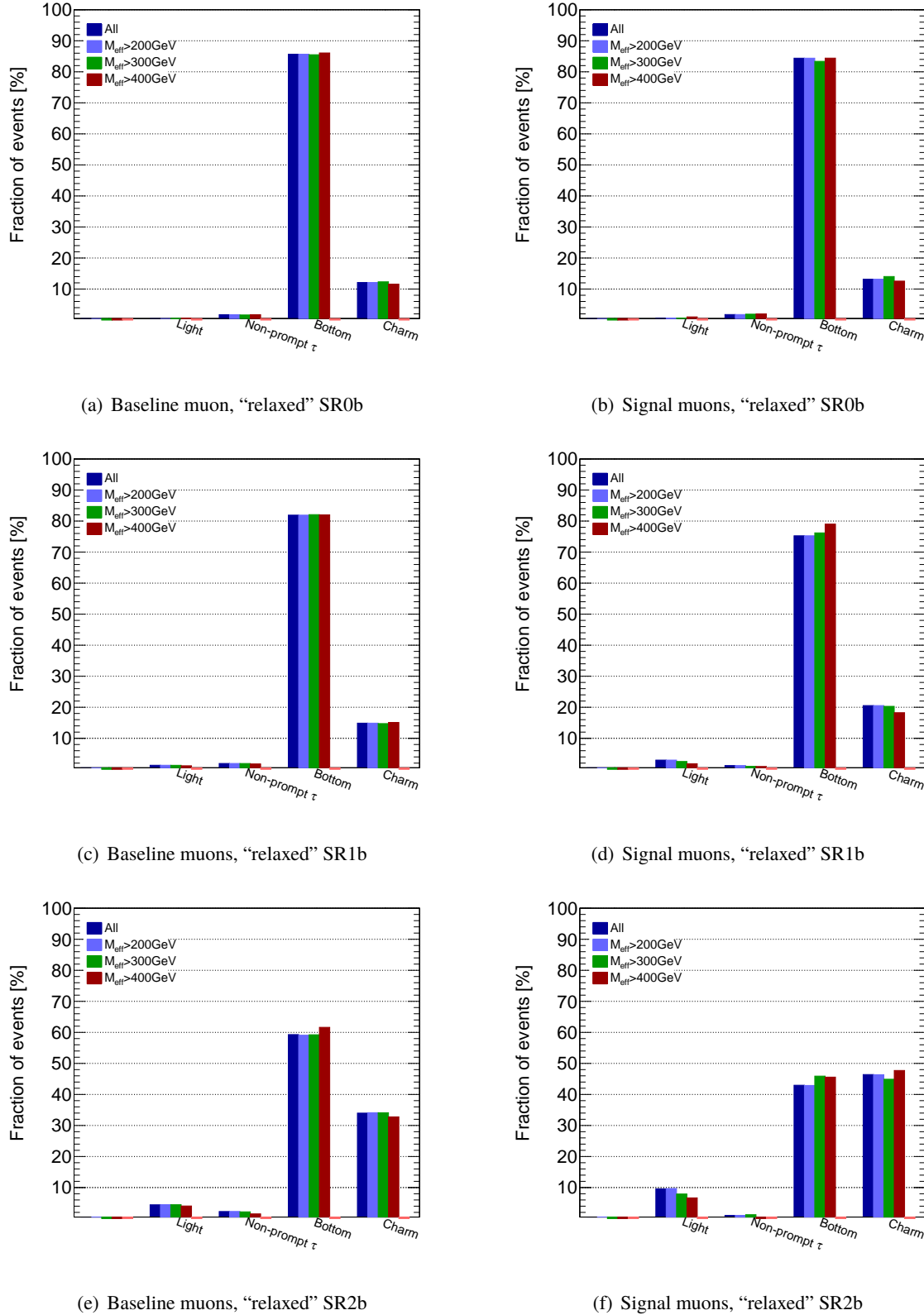


Figure 124: Sources of fake muons as a function of m_{eff} , as predicted by MC simulations (combined $t\bar{t}$ and $V + \text{jets}$) in the relaxed signal regions defined in Table 15. The results are shown for baseline (left) or signal electrons (right).

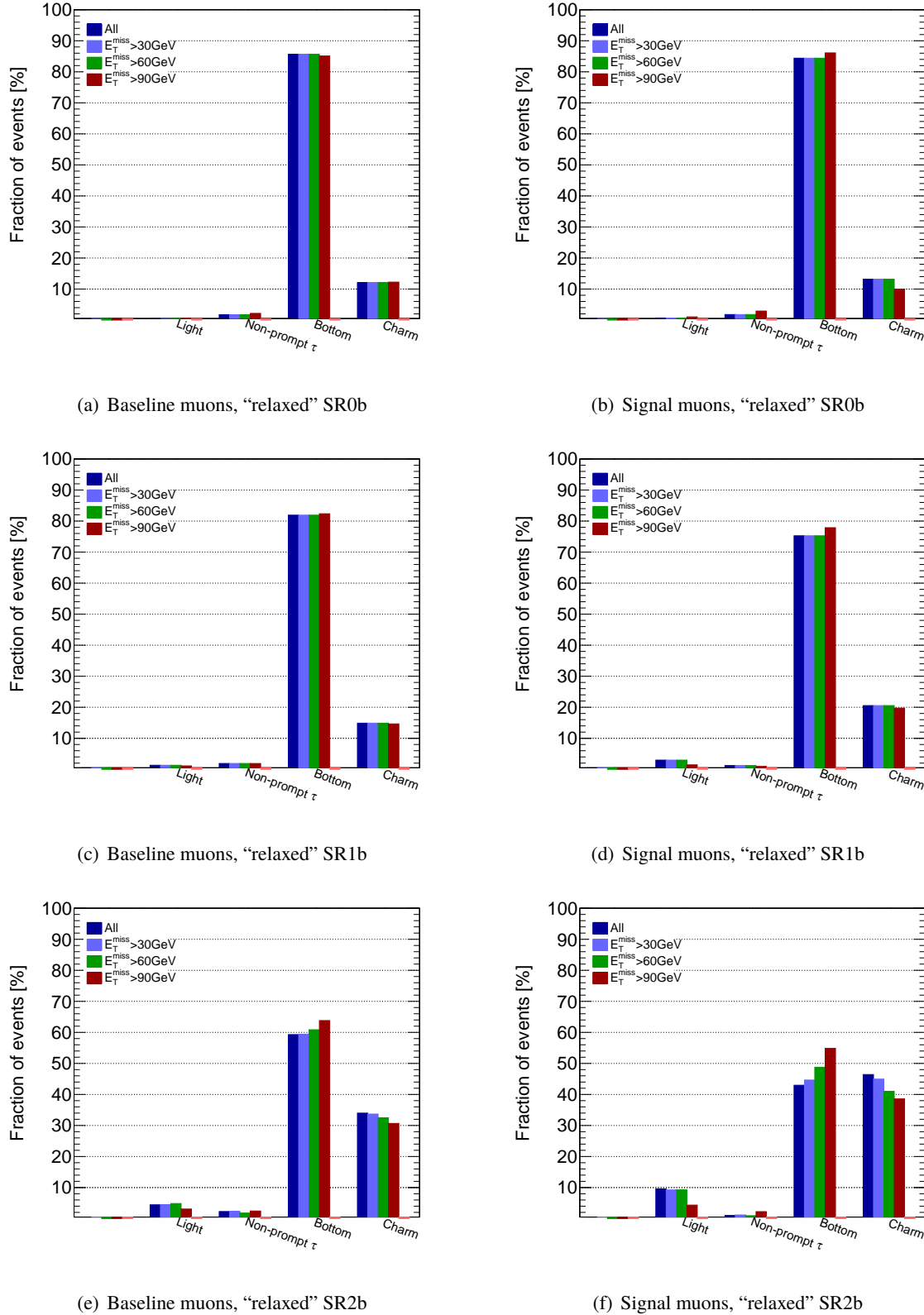


Figure 125: Sources of fake muons as a function of E_T^{miss} , as predicted by MC simulations (combined $t\bar{t}$ and $V+$ jets) in the relaxed signal regions defined in Table 15. The results are shown for baseline (left) or signal electrons (right).

2151 18 MC closure test for detector backgrounds

2152 MC clusure test for the fake leptons

2153 We did MC closure test to check if the estimated fake rate and the charge-flip rate are valid in the CRs
 2154 where $t\bar{t}$ and $V + jets$ process are dominant. In the test for the fake leptons, charge-flip background is
 2155 estimated using OS events reweighted using the charge-flip weight. The SS baseline lepton pair events are
 2156 then selected from $t\bar{t}$ and $V + jets$ sample, weighted using matrix-method weight. Events with SS signal
 2157 lepton pair are selected to make comparison with the weighted baseline-lepton pair events. The Matrix
 2158 Method weight applied to the SS events are considered respectively, with the input-fake-rate estimated
 2159 from MC and data. Also, two regions are defined for the closure test in different $b - jet$ multiplicity,
 2160 shown on Table 61. The fake-rate from MC and data are shown on Table 62 and Table 63. Number of jet
 2161 distribution was shown on figure Figure 126 for the test. Reasonable agreement is obtained in this closure
 2162 test(within 10%).

	Leptons	Jets	MET
0-bjet region	≥ 2 signal lepton $p^T > 10\text{GeV}$	exactly 0 $b - jet$ $p^T > 20\text{GeV}$	$\geq 40\text{GeV}$
1-bjet region	≥ 2 signal lepton $p^T > 10\text{GeV}$	≥ 1 $b - jet$ $p^T > 20\text{GeV}$	$\geq 40\text{GeV}$

Table 61: Lepton and $b - jets$ selection cuts of the region for fake closure test.

Table 62: The electron fake rate used in the closure test from MC.

p^T	data	MC
$10\text{GeV} < \text{pt} < 20\text{GeV}$	$0.076 \pm 0.014 \pm 0.038$	$0.047 \pm 0.001 \pm 0.023$
$\text{pt} > 20\text{GeV}$	$0.118 \pm 0.033 \pm 0.063$	$0.046 \pm 0.001 \pm 0.023$

Table 63: The muon fake rate used in the closure test from MC.

p^T	data	MC
$10\text{GeV} < \text{pt} < 15\text{GeV}$	$0.187 \pm 0.026 \pm 0.094$	$0.131 \pm 0.002 \pm 0.065$
$15\text{GeV} < \text{pt} < 20\text{GeV}$	$0.132 \pm 0.034 \pm 0.066$	$0.103 \pm 0.002 \pm 0.051$
$\text{pt} > 20\text{GeV}$	$0.117 \pm 0.035 \pm 0.059$	$0.113 \pm 0.002 \pm 0.056$

2163 Closure test for the charge-flip

2164 The charge-flip background should be subtracted in the fake-rate estimation. A closure test for the
 2165 subtraction is indispensable, as a validation of the charge-flip rate in $t\bar{t}$ and $V + jets$ sample. Two regions
 2166 in different $b - jet$ multiplicity was considered for the charge-flip closure test, definition shown on Table
 2167 64.

	Leptons	Jets
0- <i>b</i> jet region	≥ 2 signal lepton $p^T > 10\text{GeV}$	exactly 0 <i>b-jet</i> $p^T > 20\text{GeV}$
1- <i>b</i> jet region	≥ 2 signal lepton $p^T > 10\text{GeV}$	≥ 1 <i>b-jet</i> $p^T > 20\text{GeV}$

Table 64: Lepton and $b - jets$ selection cuts of the region for charge-flip closure test.

2168 SS events and OS events are selected separately in the charge-flip closure test. The OS events are applied
 2169 with charge-flip weight using rate estimated based on data or MC15 respectively. The contribution of
 2170 chage-flip lepton backround can also be estimated directly using the truth information from the SS events.
 2171 Number of jets distributions are used to perform the comparison between the two estimations of charge-
 2172 flip, shown on Figure 127. The SS distribution should be consistent with the OS distribution using MC
 2173 charge-flip rate. This is observed from the distribution, showing a good charge-flip subtraction in the
 2174 fake-rate CR.

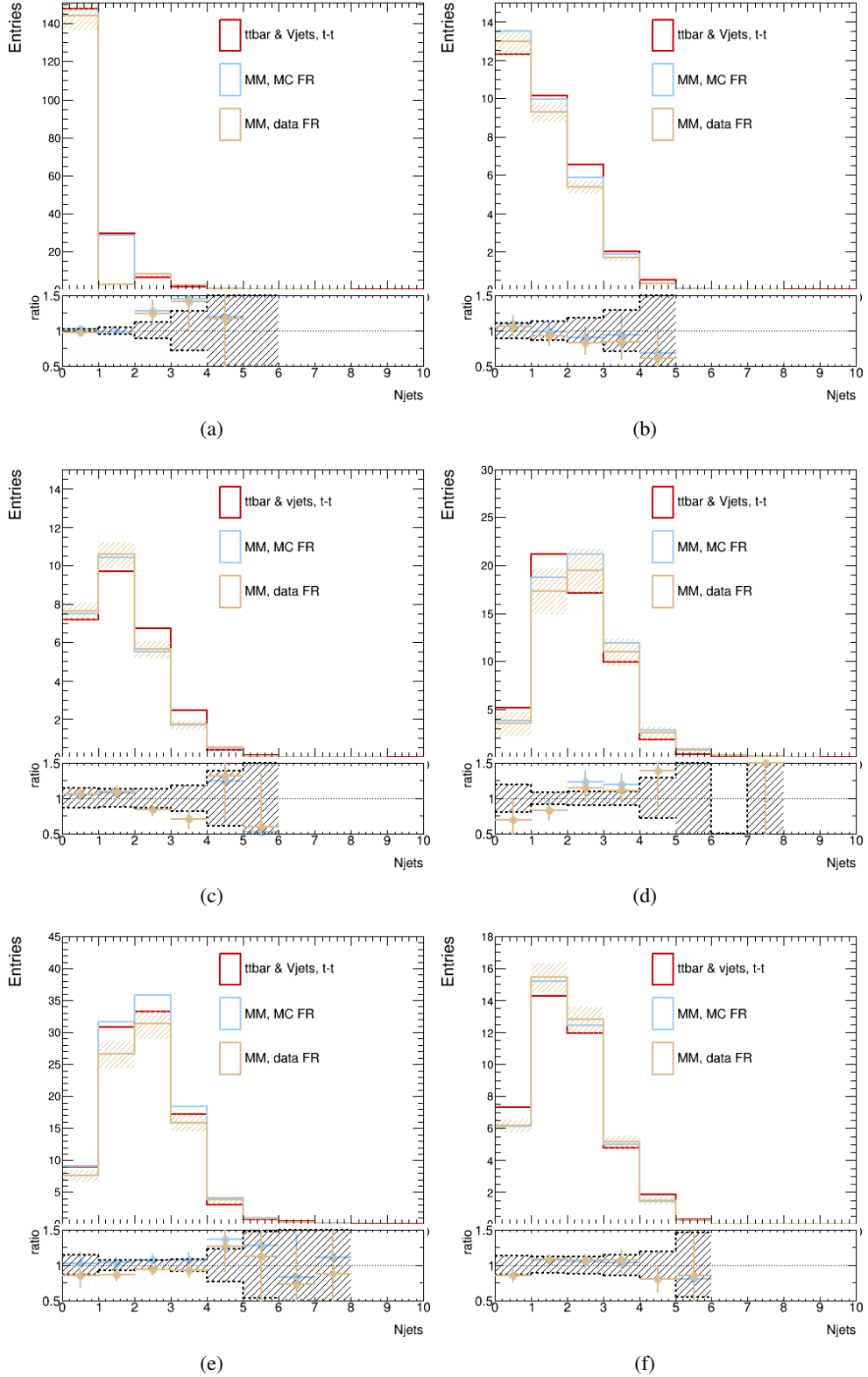


Figure 126: Distributions of number of jets for $t\bar{t}$ and $V + jets$ sample: e-e channel, region 0 – b_{jet} (a), e- μ channel, region 0 – b_{jet} (b), μ - μ channel, region 0 – b_{jet} (c), e-e channel, region 1 – b_{jet} (d), e- μ channel, region 1 – b_{jet} (e), μ - μ channel, region 1 – b_{jet} (f) Comparisons are shown among: Events with 2 same-sign leptons (red histogram); Events with 2 same-sign baseline leptons, applying Matrix-Method weight using fake-rate from MC (blue); Events with 2 same-sign baseline leptons, applying Matrix-Method weight using rate from data (golden).

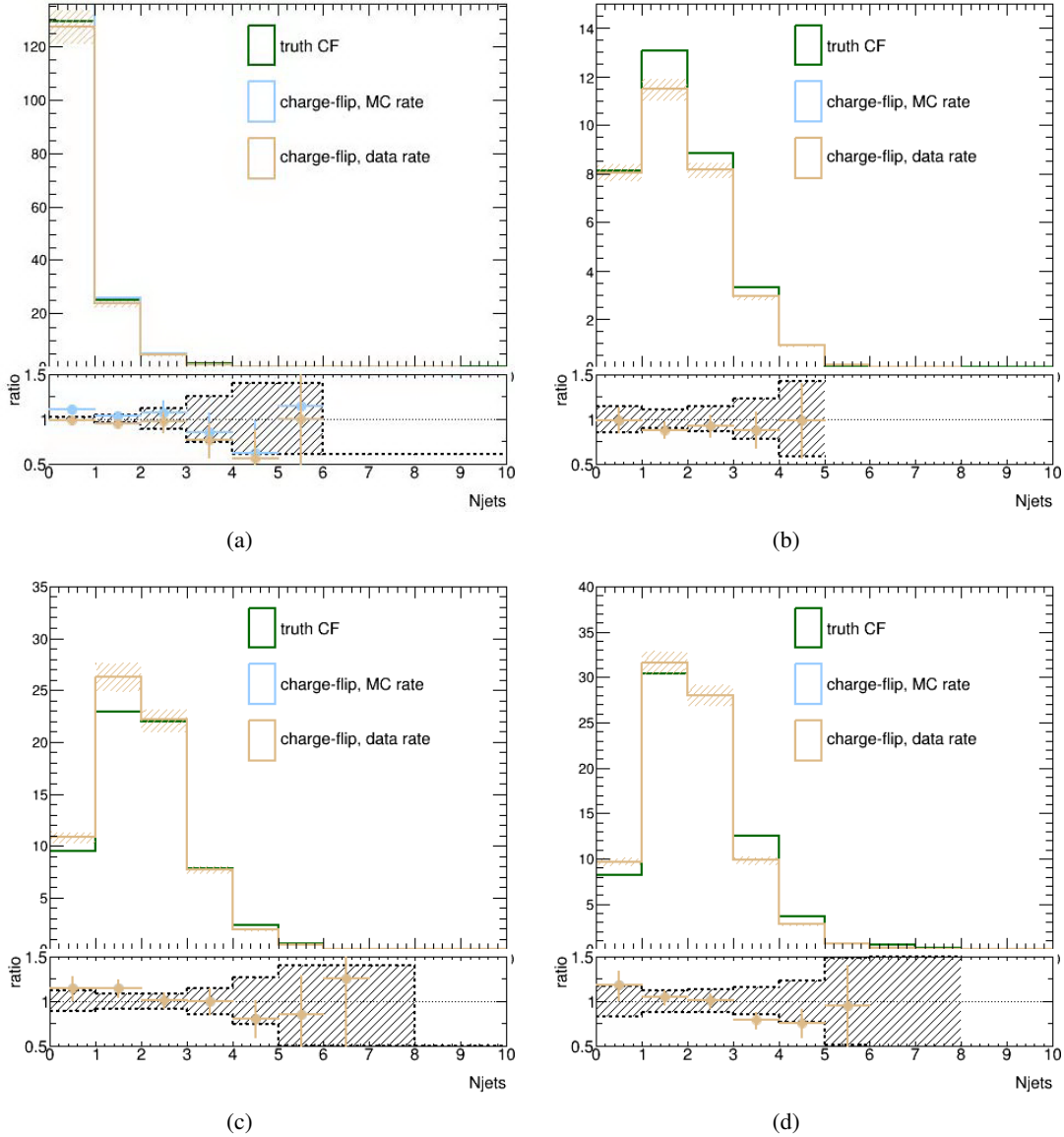


Figure 127: Distributions of number of jets for $t\bar{t}$ and $V + jets$ sample: e-e channel, region 0-bjet (a), e- μ channel, region 0-bjet (b), e-e channel, region 1-bjet (c), e- μ channel, region 1-bjet (d). Comparisons are shown among: SS charge-flip events with truth selection (green histogram); OS events with charge-flip weight using rate from MC (blue); OS events with charge-flip weight using rate from data (golden).

2175 19 Studies on the excess observed in $t\bar{t} + X$ validation regions

2176 [NOTE: These results are obtained with the the old (mc15) $t\bar{t} + V$ samples, and are not updated with the
 2177 mc15b samples, latest cross-sections and k-factors.]

2178 In this appendix we summarize the studies performed to understand the excess observed in the $t\bar{t} + Z$ and
 2179 $t\bar{t} + V$ validation regions. Results are obtained with 3.2 fb^{-1} of data and using the latest recommendations.

2180 In the tables presenting the results, the systematic uncertainty assigned to the fake lepton estimation
 2181 is obtained using the “conservative” approach (i.e it can be reduced up to a factor 2). To account for
 2182 this and for the missing sources of systematics (i.e JES, JER, etc) the discovery significance is computed
 2183 using RooStats::NumberCountingUtils::BinomialObsZ function with background uncertainty set
 2184 to stat + 50% syst.

2185 Results in $t\bar{t} + Z$ validation regions

2186 In Table 65 we recall the definition of the $t\bar{t} + Z$ validation region (ttZ 1bIncl), which is a combination
 2187 of 1b-jet exclusive (ttZ 1bExcl) and 2b-jet inclusive (ttZ 2bIncl) regions. For completeness, the results
 2188 obtained in the three regions are presented in Table 67 (combined channels) and in Table 68 (per channel).
 2189 The discovery significance of the excess in the combined channel is 0.79σ . Figure 128 (top and bottom-
 2190 left) presents the m_{eff} distribution in these regions. It can be noticed that the excess tends to be more in the
 2191 low m_{eff} region ($< 500 \text{ GeV}$). Looking separately at the ttZ 1bExcl and ttZ 2bIncl regions it is clear that
 2192 the excess is driven by the latter region selection. The discovery significance in this region is 2.08σ .

VR	$N_{\text{lept}}^{\text{signal}}$	$N_{b-\text{jets}}^{20}$	Other variables
ttZ 1bExcl	$\geq 3, p_T: (l1, l2, e3 (\mu3)) = (25, 25, 20 (10)) \text{ GeV}$	$=1$	$20 < E_T^{\text{miss}} < 150 \text{ GeV}, 100 < m_{\text{eff}} < 900 \text{ GeV}, N_{\text{jets}}^{25} \geq 4, \eta _{e1,2} < 1.37, 80 < m_{\ell\ell}^{\text{SFOS}} < 100 \text{ GeV}, !\text{SR}$
ttZ 2bIncl	$\geq 3, p_T: (l1, l2, e3 (\mu3)) = (25, 25, 20 (10)) \text{ GeV}$	≥ 2	$20 < E_T^{\text{miss}} < 150 \text{ GeV}, 100 < m_{\text{eff}} < 900 \text{ GeV}, N_{\text{jets}}^{25} \geq 3, \eta _{e1,2} < 1.37, 80 < m_{\ell\ell}^{\text{SFOS}} < 100 \text{ GeV}, !\text{SR}$

Table 65: $t\bar{t} + Z$ validation region definition (ttZ 1bIncl = ttZ 1bExcl || ttZ 2bIncl).

VR	$N_{\text{lept}}^{\text{signal}}$	$N_{b-\text{jets}}^{20}$	Other variables
ttV 2bIncl	$\geq 2, p_T: (l1, l2, l3) = (25, 25, 10) \text{ GeV}$	≥ 2	$20 < E_T^{\text{miss}} < 200 \text{ GeV}, 200 < m_{\text{eff}} < 900 \text{ GeV}, \eta _{e1,2} < 1.37, N_{\text{jets}}^{25} \geq 5 \text{ in ee and } e\mu, N_{\text{jets}}^{25} \geq 3 \text{ in } \mu\mu \text{ channels, !SR}$

Table 66: $t\bar{t} + V$ validation region definition (ttV 2bIncl).

	ttZ 1bIncl	ttZ 1bExcl	ttZ 2bIncl
Fakes	$0.65 \pm 0.60 \pm 1.88$	$0.90 \pm 0.41 \pm 0.74$	$-0.25 \pm 0.43 \pm 1.13$
ttZ	$4.38 \pm 0.08 \pm 1.31$	$1.85 \pm 0.05 \pm 0.56$	$2.52 \pm 0.06 \pm 0.76$
ttW	$0.09 \pm 0.02 \pm 0.03$	$0.02 \pm 0.01 \pm 0.01$	$0.08 \pm 0.02 \pm 0.02$
Total	$7.74 \pm 0.65 \pm 3.00$	$4.42 \pm 0.46 \pm 1.36$	$3.32 \pm 0.46 \pm 1.65$
Data	14	2	12
Significance	0.79	-1.35	2.08

Table 67: Results in ttZ 1bExcl, ttZ 1bIncl and ttZ 2bIncl regions. All channels are combined. “Total” includes the number of expected background events.

2193 Candidates in ttZ 1bIncl

2194 The observed events in data are shown in Table 69. It can be seen that all leptons are well isolated and

	ttZ 1bIncl	ttZ 1bExcl	ttZ 2bIncl
ee channel			
Fakes	$-0.44 \pm 0.24 \pm 0.36$	$-0.02 \pm 0.02 \pm 0.03$	$-0.42 \pm 0.24 \pm 0.33$
ttZ	$0.56 \pm 0.03 \pm 0.17$	$0.24 \pm 0.02 \pm 0.07$	$0.33 \pm 0.02 \pm 0.10$
ttW	$0.02 \pm 0.01 \pm 0.00$	$0.00 \pm 0.00 \pm 0.00$	$0.02 \pm 0.01 \pm 0.00$
Total	$0.42 \pm 0.26 \pm 0.46$	$0.38 \pm 0.07 \pm 0.13$	$0.05 \pm 0.25 \pm 0.36$
Data	3	0	3
Significance	1.65	-	0.90
$e\mu$ channel			
Fakes	$0.62 \pm 0.40 \pm 0.76$	$0.54 \pm 0.32 \pm 0.37$	$0.09 \pm 0.24 \pm 0.39$
ttZ	$2.06 \pm 0.06 \pm 0.62$	$0.87 \pm 0.04 \pm 0.26$	$1.19 \pm 0.04 \pm 0.36$
ttW	$0.04 \pm 0.01 \pm 0.01$	$0.00 \pm 0.00 \pm 0.00$	$0.04 \pm 0.01 \pm 0.01$
Total	$3.72 \pm 0.43 \pm 1.27$	$2.05 \pm 0.35 \pm 0.61$	$1.67 \pm 0.25 \pm 0.65$
Data	4	0	4
Significance	-0.25	-	0.87
$\mu\mu$ channel			
Fakes	$0.46 \pm 0.37 \pm 0.76$	$0.38 \pm 0.25 \pm 0.34$	$0.08 \pm 0.27 \pm 0.41$
ttZ	$1.75 \pm 0.05 \pm 0.53$	$0.75 \pm 0.03 \pm 0.22$	$1.00 \pm 0.04 \pm 0.30$
ttW	$0.03 \pm 0.01 \pm 0.01$	$0.01 \pm 0.01 \pm 0.00$	$0.02 \pm 0.01 \pm 0.01$
Total	$3.60 \pm 0.42 \pm 1.30$	$1.99 \pm 0.29 \pm 0.63$	$1.60 \pm 0.30 \pm 0.67$
Data	7	2	5
Significance	0.76	-0.39	1.33

Table 68: Results per channel in ttZ 1bExcl, ttZ 1bIncl and ttZ 2bIncl regions. “Total” includes the number of expected background events.

most of the leading leptons have a transverse momentum higher than 70-100 GeV. Such properties reduce the chance to have a hight amount of fake leptons. In this validation region only two events have 3 b -jets and 0 events have ≥ 4 b -jets; only two events have 4 leptons.

In Table 70 are shown the candidates common in ttZ and ttV 2bIncl regions. It helps to understand if the excess present in the latter region is found back in the ttZ 2bIncl VR. A total of 8 events out of 12 are found to be in both regions; the other 4 events are not passing the number of jets cut (≥ 5 in the ee and $e\mu$ channels). In ttV 2bIncl VR 19 events are observed, as shown in Tables 70 and 71. For illustration, Figure 128 (bottom) shows side by side the m_{eff} distribution in these two regions. It is clear that the tension in the $m_{\text{eff}} < 500$ GeV region diminishes with the selection proposed for ttV 2bIncl VR (2 events are not passing the N_{jets}^{25} cut).

For completeness, the background composition in these two 2bIncl regions is shown in Tables 72 and 73. Two set of results are shown : using the selection defined in Tables 65 and 66, and after adding a $m_{\text{eff}} < 500$ GeV cut.

More distributions in ttZ 2bIncl region

In order to see if this excess is localized in a certain region of the phase space or it is uniformly distributed, we look at the agreement between the background expectation and data observation in ttZ 2bIncl region by probing several kinematic variables. The distribution of the key discriminant variables are shown in Figures 129 - 131 for several selections ensuring a separation of the low m_{eff} region where the excess seems to be present. No other particular region responsible for the excess could be identified.

Very interesting is that one event has two Z-bosons (and 2 b -jets). This is illustrated in Figure 132, were we present the distribution of the **second** m_{ll} pair after requiring at least 1 b -jet (left) or at least 2 b -jets

	Run	Event Number	nLep	Leptons (p_T [GeV])	Leptons (η)	Leptons (rel trackIso)	Leptons (rel calo20Iso)	E_T^{miss} [GeV]	m_{eff} [GeV]	N_{jet}^{25}	N_{jet}^{20}
1	276329	224346343	3	$\mu-(81.71)\mu+(71.22)\mu+(24.17)$	$\mu-(1.71)\mu+(0.97)\mu+(2.12)$	$\mu-(0.00)\mu+(0.00)\mu-(0.00)$	$\mu-(0.00)\mu+(0.00)\mu-(0.00)$	60.07	453.14	4	1
2	279279	441589615	3	$\mu+(79.91)\mu-(67.23)\mu-(15.89)$	$\mu+(1.01)\mu-(0.14)\mu-(2.05)$	$\mu+(0.02)\mu-(0.00)\mu-(0.00)$	$\mu+(0.01)\mu-(0.01)\mu-(0.10)$	58.48	406.53	4	1
3	279598	791343322	3	$e-(287.20)\mu-(112.64)e+(103.26)$	$e-(0.15)\mu+(0.37)e+(0.35)$	$e-(0.00)\mu+(0.00)e-(0.00)$	$e-(0.00)\mu+(0.00)e-(0.00)$	65.46	871.03	5	2
4	282992	1402326301	3	$e-(161.82)\mu-(34.26)e+(25.24)$	$e-(0.13)\mu-(1.90)e-(0.05)$	$e-(0.00)\mu-(0.00)e+(0.00)$	$e-(0.01)\mu-(0.00)e+(0.01)$	40.19	585.40	4	2
5	280862	959305083	3	$e+(152.06)\mu-(61.63)\mu+(20.73)$	$e+(0.03)\mu-(0.73)\mu+(1.51)$	$e+(0.00)\mu-(0.00)\mu+(0.00)$	$e+(0.02)\mu-(0.00)\mu+(0.10)$	95.93	859.35	7	2
6	280873	16740141	3	$\mu+(74.86)e-(26.49)\mu-(20.46)$	$\mu+(0.16)e-(0.57)\mu-(1.62)$	$\mu+(0.00)\mu-(0.00)\mu-(0.00)$	$\mu-(0.01)\mu-(0.01)\mu-(0.01)$	97.88	436.95	4	2
7	280950	1395868892	3	$\mu+(48.45)\mu-(46.46)\mu-(21.57)$	$\mu+(0.49)\mu-(0.67)\mu-(0.61)$	$\mu+(0.00)\mu-(0.00)\mu-(0.00)$	$\mu+(0.01)\mu-(0.01)\mu-(0.03)$	58.37	333.50	3	2
8	281411	1555870149	3	$\mu-(55.92)\mu+(27.49)\mu+(1.62)$	$\mu-(0.41)\mu+(0.62)\mu+(2.33)$	$\mu-(0.00)\mu+(0.04)\mu+(0.00)$	$\mu-(0.01)\mu+(0.05)\mu+(0.01)$	93.93	332.00	3	2
9	284484	457656076	3	$\mu+(147.66)\mu-(54.04)\mu-(24.74)$	$\mu-(0.46)\mu-(1.49)\mu-(0.19)$	$\mu+(0.00)\mu-(0.00)\mu-(0.00)$	$\mu-(0.00)\mu-(0.01)\mu-(0.03)$	71.19	481.66	3	2
10	284285	3510884870	3	$e-(36.89)e+(36.73)e-(33.93)$	$e-(1.01)\mu-(0.95)e+(0.38)$	$e-(0.00)\mu+(0.00)e+(0.00)$	$e-(0.02)\mu+(0.02)e-(0.02)e+(0.00)$	32.42	382.72	3	2
11	280753	161095358	4	$\mu+(100.64)\mu+(33.89)\mu-(24.95)\mu-(15.85)$	$\mu+(0.62)\mu+(2.19)\mu-(0.37)\mu-(0.31)$	$\mu+(0.00)\mu+(0.00)\mu-(0.00)\mu-(0.00)$	$\mu+(0.01)\mu+(0.01)\mu-(0.02)\mu-(0.04)$	73.32	405.98	3	2
12	280977	330636862	4	$\mu+(1.6)\mu+(0.37)\mu-(0.48)e-(0.97)$	$\mu+(0.16)\mu+(0.37)\mu-(1.42)e-(47.89)$	$\mu+(0.00)\mu+(0.00)\mu-(0.00)e-(0.00)$	$\mu+(0.00)\mu+(0.00)\mu-(0.00)e-(0.00)$	104.09	712.46	3	2
13	280950	814383648	3	$e+(93.18)e+(36.92)e-(23.15)$	$e+(0.47)e+(1.19)e-(0.22)$	$e+(0.00)e+(0.00)e-(0.00)$	$e+(0.01)e+(0.01)e-(0.00)$	43.00	495.66	6	3
14	282992	1761706006	3	$e+(72.46)e-(36.93)e-(23.28)$	$e+(0.61)e-(0.07)e-(0.47)$	$e+(0.00)e-(0.00)e+(0.00)$	$e+(0.00)e-(0.00)e+(0.02)$	100.32	386.45	3	3

Table 69: Candidates in $t\bar{t}Z$ 1blnc validation region.

	Run	Event Number	nLep	Leptons (p_T [GeV])	Leptons (η)	Leptons (rel trackIso)	Leptons (rel calo20Iso)	E_T^{miss} [GeV]	m_{eff} [GeV]	N_{jet}^{25}	N_{jet}^{20}
3	279598	791343322	3	$e-(287.20)\mu-(112.64)e+(103.26)$	$e-(0.15)\mu+(0.37)e+(0.35)$	$e-(0.00)\mu+(0.00)e-(0.00)$	$e-(0.00)\mu+(0.00)e-(0.00)$	65.46	871.03	5	2
5	280862	959305083	3	$e+(152.06)\mu-(61.63)\mu+(20.73)$	$e+(0.03)\mu-(0.73)\mu+(1.51)$	$e+(0.00)\mu-(0.00)e-(0.00)$	$e+(0.02)\mu-(0.00)\mu+(0.10)$	95.93	859.35	7	2
7	280950	1395868892	3	$\mu+(48.45)\mu-(46.46)\mu-(21.57)$	$\mu+(0.49)\mu-(0.67)\mu-(0.61)$	$\mu+(0.00)\mu-(0.00)\mu-(0.00)$	$\mu+(0.01)\mu-(0.01)\mu-(0.03)$	58.37	333.50	3	2
8	281411	1555870149	3	$\mu-(35.02)\mu+(27.49)\mu+(1.62)$	$\mu-(0.41)\mu+(0.62)\mu+(2.33)$	$\mu-(0.00)\mu+(0.04)\mu-(0.00)$	$\mu-(0.01)\mu+(0.05)\mu+(0.01)$	93.93	332.00	3	2
9	284484	457656076	3	$\mu+(147.66)\mu-(54.04)\mu-(24.74)$	$\mu-(0.46)\mu-(1.49)\mu-(0.19)$	$\mu+(0.00)\mu-(0.00)\mu-(0.00)$	$\mu+(0.00)\mu-(0.01)\mu-(0.03)$	71.19	481.66	3	2
11	280753	161095358	4	$\mu+(100.64)\mu+(33.89)\mu-(24.95)\mu-(15.85)$	$\mu+(0.62)\mu+(2.19)\mu-(0.37)\mu-(0.31)$	$\mu+(0.00)\mu+(0.00)\mu-(0.00)\mu-(0.00)$	$\mu+(0.01)\mu-(0.01)\mu-(0.02)\mu-(0.04)$	73.32	405.98	3	2
12	280977	330636862	4	$\mu+(153.02)\mu-(0.77)\mu-(71.42)e-(47.89)$	$\mu+(0.16)\mu-(0.37)\mu-(0.48)e-(0.97)$	$\mu+(0.00)\mu+(0.00)\mu-(0.00)e-(0.00)$	$\mu+(0.00)\mu+(0.00)\mu-(0.00)e-(0.00)$	104.09	712.46	3	2
13	280950	814383648	3	$e+(93.18)e+(36.92)e-(23.15)$	$e+(0.47)e+(1.19)e-(0.22)$	$e+(0.00)e+(0.00)e-(0.00)$	$e+(0.01)e+(0.01)e-(0.00)$	43.00	495.66	6	3

Table 70: Common candidates in $t\bar{t}Z$ 2blnc validation regions.

	Run	Event Number	nLep	Leptons (p_T [GeV])	Leptons (η)	Leptons (rel trackIso)	Leptons (rel calo20Iso)	E_T^{miss} [GeV]	m_{eff} [GeV]	N_{jet}^{25}	N_{jet}^{20}
1	279685	1349229504	2	$e-(72.10)e-(58.11)$	$e-(0.47)e-(1.28)$	$e-(0.00)e-(0.00)$	$e-(0.00)e-(0.00)$	67.50	553.28	5	2
2	279867	496519944	2	$\mu+(61.08)\mu+(5.71)$	$\mu+(1.73)\mu-(0.87)$	$\mu+(0.00)\mu+(0.00)$	$\mu+(0.00)\mu+(0.00)$	120.01	561.90	5	2
3	279867	652668220	2	$e+(84.82)\mu+(50.49)$	$e+(1.08)\mu+(1.35)$	$e+(0.00)\mu+(0.00)$	$e+(0.00)\mu+(0.00)$	82.21	669.41	5	2
4	284285	425810587	2	$e-(101.85)\mu-(67.19)$	$e-(0.63)\mu-(1.78)$	$e-(0.00)\mu-(0.00)$	$e-(0.03)\mu-(0.05)$	118.19	635.59	5	2
5	284285	183826212	2	$\mu-(117.02)\mu-(77.22)$	$\mu-(1.58)\mu-(1.20)$	$\mu-(0.00)\mu-(0.00)$	$\mu-(0.00)\mu-(0.01)$	96.18	759.31	6	2
6	284213	851303151	2	$\mu+(90.96)\mu+(89.31)$	$\mu+(1.16)\mu+(1.44)$	$\mu+(0.00)\mu+(0.00)$	$\mu+(0.00)\mu+(0.00)$	74.87	674.34	6	2
7	282631	372086758	2	$e+(78.87)e+(41.47)$	$e+(1.30)e+(0.78)$	$e+(0.00)\mu+(0.00)$	$e+(0.01)\mu+(0.02)$	20.46	677.43	8	2
8	279169	1638720881	3	$\mu-(184.47)\mu-(78.34)\mu-(10.60)$	$\mu-(0.25)\mu+(1.64)\mu-(1.51)$	$\mu-(0.00)\mu+(0.00)\mu-(0.00)$	$\mu-(0.00)\mu+(0.00)\mu-(0.00)$	45.92	554.27	4	2
9	284484	612220150	3	$\mu-(58.05)\mu+(26.04)\mu+(12.14)$	$\mu-(0.68)\mu+(0.70)\mu+(0.99)$	$\mu-(0.00)\mu+(0.00)\mu+(0.00)$	$\mu-(0.00)\mu+(0.00)\mu+(0.06)$	95.23	464.64	4	2
10	282631	430599036	3	$\mu-(55.07)\mu-(52.69)\mu+(25.26)$	$\mu-(1.00)\mu-(1.42)\mu+(0.50)$	$\mu-(0.00)\mu-(0.00)\mu+(0.00)$	$\mu-(0.01)\mu-(0.01)\mu+(0.05)$	101.57	770.60	7	2
11	280950	1791881600	3	$e-(70.67)e+(31.52)\mu-(15.97)$	$e-(0.82)e+(0.50)\mu-(1.14)$	$e-(0.00)\mu+(0.00)\mu-(0.00)$	$e-(0.01)\mu+(0.03)\mu-(0.03)$	102.57	616.38	6	2

Table 71: List of the remaining candidates in $t\bar{t}V$ 2blnc validation region.

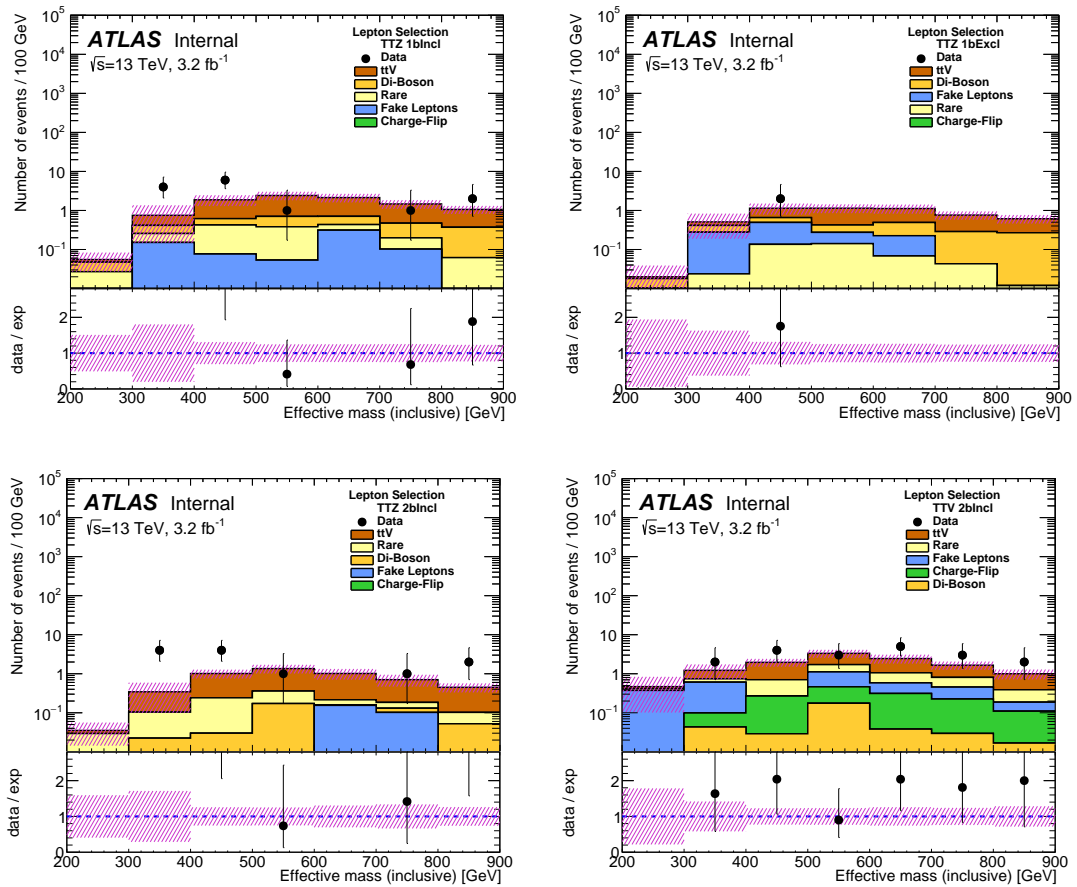


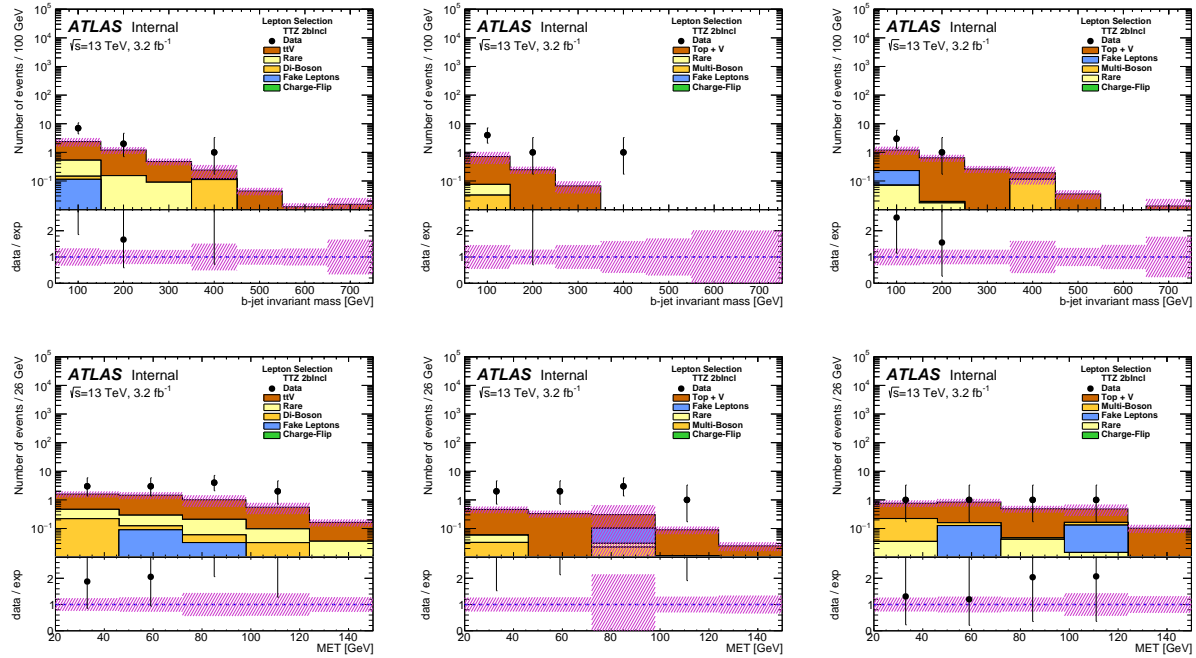
Figure 128: Effective mass distribution in $t\bar{t}Z$ 1bIncl (top-left), $t\bar{t}Z$ 1bExcl (top-right), $t\bar{t}Z$ 2bIncl (bottom-left) and $t\bar{t}V$ 2bIncl regions.

2216 (right), and at least four leptons in the event.

	ttV 2bIncl	ttZ 2bIncl
Fakes	$1.76 \pm 0.74 \pm 3.26$	$-0.25 \pm 0.43 \pm 1.13$
Charge flip	$1.14 \pm 0.06 \pm 0.30$	$0.00 \pm 0.00 \pm 0.00$
ttZ	$2.77 \pm 0.06 \pm 0.83$	$2.52 \pm 0.06 \pm 0.76$
ttW	$2.40 \pm 0.09 \pm 0.72$	$0.08 \pm 0.02 \pm 0.02$
ttH	$1.64 \pm 0.16 \pm 0.82$	$0.15 \pm 0.04 \pm 0.07$
Di-Boson	$0.33 \pm 0.13 \pm 0.10$	$0.31 \pm 0.13 \pm 0.09$
Rare	$0.60 \pm 0.06 \pm 0.28$	$0.51 \pm 0.06 \pm 0.26$
Total	$10.65 \pm 0.78 \pm 4.29$	$3.32 \pm 0.46 \pm 1.65$
Data	19	12

Table 72: Results in the ttV and ttZ 2bIncl regions.

	ttV 2bIncl	ttZ 2bIncl
Fakes	$0.57 \pm 0.49 \pm 1.33$	$-0.38 \pm 0.37 \pm 0.76$
Charge flip	$0.30 \pm 0.03 \pm 0.08$	$0.00 \pm 0.00 \pm 0.00$
ttZ	$0.74 \pm 0.03 \pm 0.22$	$0.73 \pm 0.03 \pm 0.22$
ttW	$0.81 \pm 0.05 \pm 0.24$	$0.04 \pm 0.01 \pm 0.01$
ttH	$0.40 \pm 0.08 \pm 0.20$	$0.06 \pm 0.03 \pm 0.03$
Di-Boson	$0.07 \pm 0.04 \pm 0.02$	$0.05 \pm 0.03 \pm 0.02$
Rare	$0.21 \pm 0.04 \pm 0.10$	$0.26 \pm 0.04 \pm 0.13$
Total	$3.09 \pm 0.50 \pm 1.55$	$0.77 \pm 0.37 \pm 0.86$
Data	6	8

Table 73: Results in the ttV and ttZ 2bIncl regions after adding the $m_{\text{eff}} < 500$ GeV cut.Figure 129: The invariant mass of the two most energetic b -jets (top) and the missing transverse energy (bottom) distributions in ttZ 2bIncl region. They are obtained using the nominal selection presented in Table 65 (left), after adding a $m_{\text{eff}} < 500$ GeV (instead of < 900 GeV, middle) and $m_{\text{eff}} > 500$ GeV (instead of > 100 GeV, right).

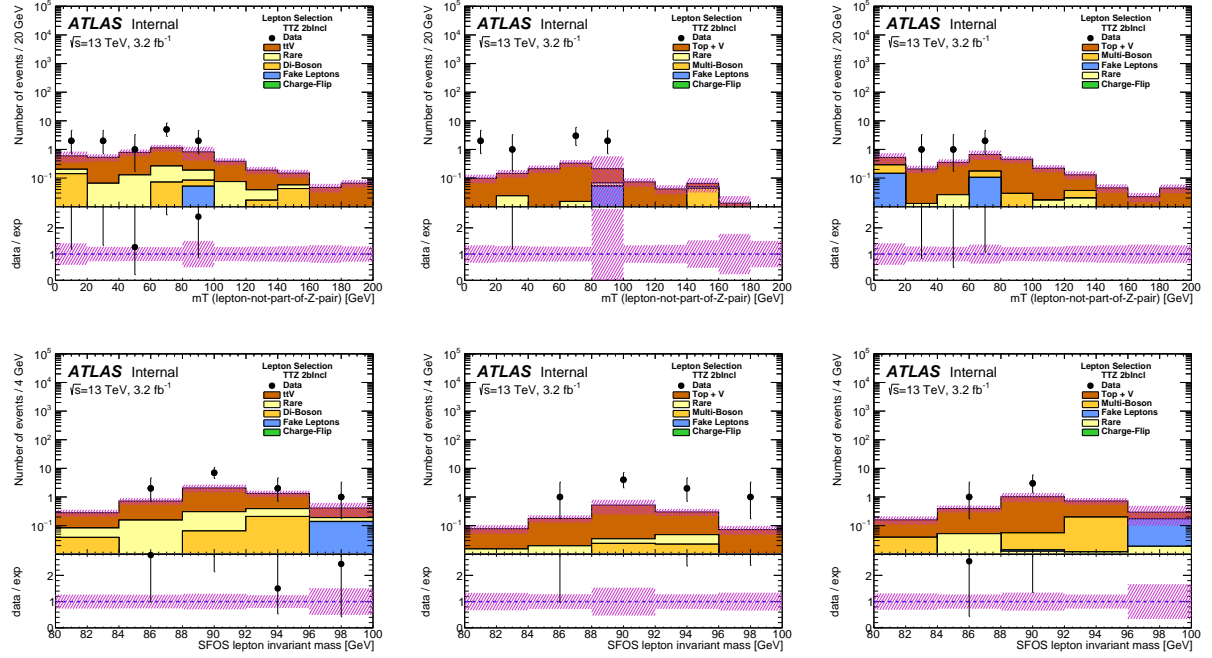


Figure 130: Transverse mass computed with the lepton not part of the Z-lepton-pair (top) and the invariant mass of the SFOS leptons pair (bottom) distributions in $t\bar{t}Z$ 2bIncl region. They are obtained using the nominal selection presented in Table 65 (left), after adding a $m_{\text{eff}} < 500$ GeV (instead of < 900 GeV, middle) and $m_{\text{eff}} > 500$ GeV (instead of > 100 GeV, right).

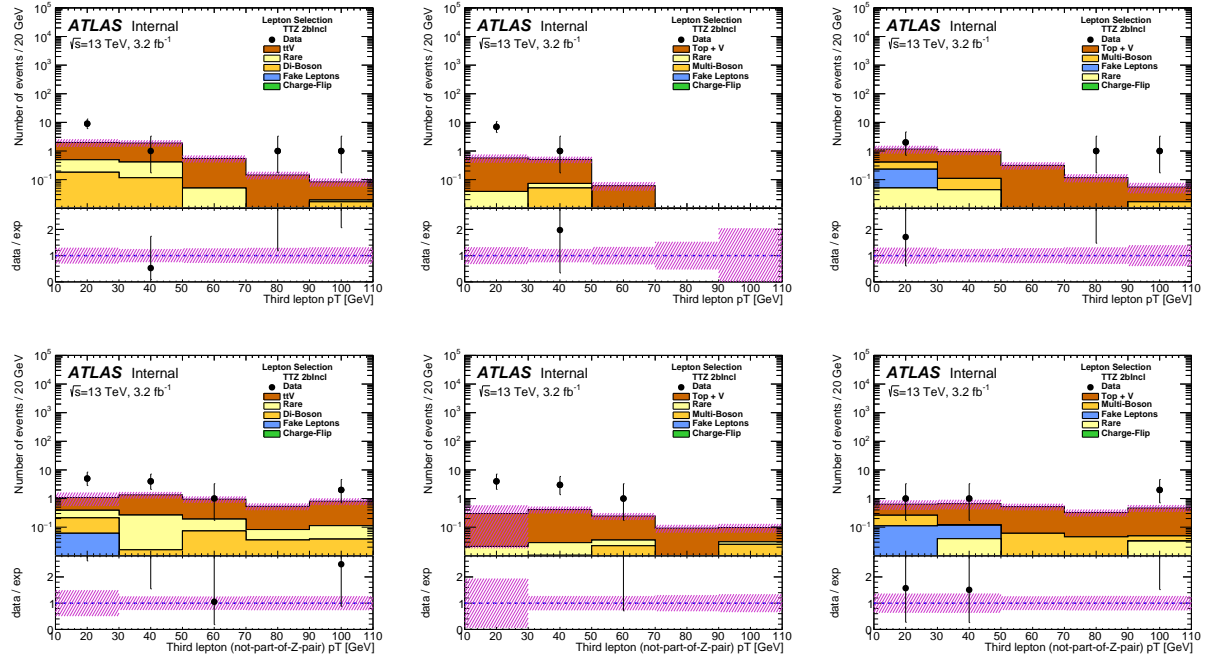


Figure 131: Third lepton p_T (top) and third lepton not part of the Z-lepton-pair p_T (bottom) distributions in $t\bar{t}Z$ 2bIncl region. They are obtained using the nominal selection presented in Table 65 (left), after adding a $m_{\text{eff}} < 500$ GeV (instead of < 900 GeV, middle) and $m_{\text{eff}} > 500$ GeV (instead of > 100 GeV, right).

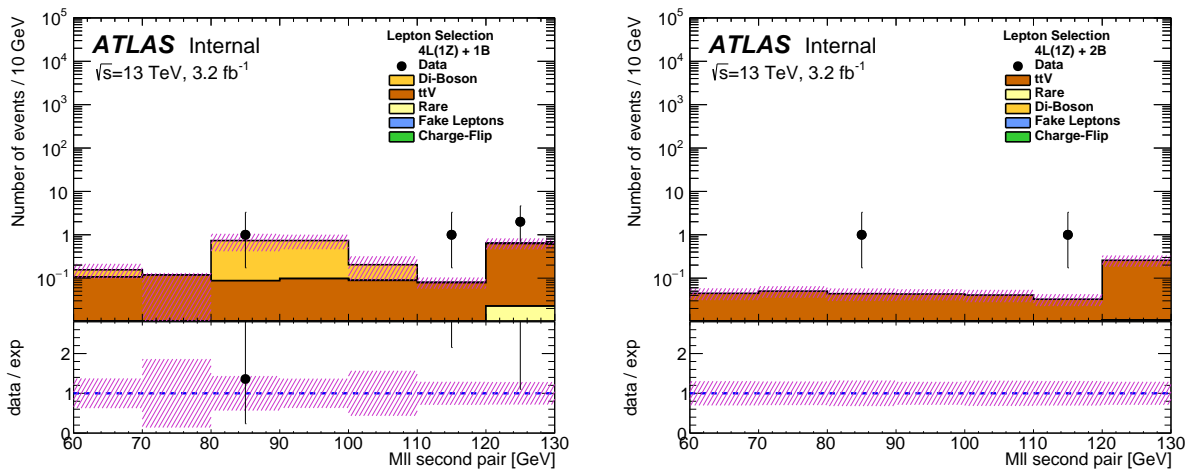


Figure 132: Distribution of the second m_{ll} pair after requiring at least 1 b -jet (left) or at least 2 b -jets (right), and at least four leptons in the event. Note that there is already one Z boson reconstructed from the other two leptons.

2217 **Results in relaxed $t\bar{t} + Z$ validation regions**

2218 In order to see if the observed excess is just a fluctuation we relax the definition of the $t\bar{t}Z$ 2bIncl region
 2219 and look at the agreement between the observed number of events and expected background. The obtained
 2220 results are presented in Table 74 and Table 75, with the considered region defined in the upper column of
 2221 the table. When using a relaxed selection, the obtained results are pointing to a fluctuation in the ee and
 2222 $e\mu$ channels, whereas, in the $\mu\mu$ channel the tension is still present (even if it is reduced when compared
 2223 to the nominal selection).

Table 74: Results in relaxed $t\bar{t}Z$ 2bIncl validation regions. The considered definitions are shown in the upper box of the table. Nominal stands for the $t\bar{t}Z$ 2bIncl VR as defined in Table 27. “Total” category includes the number of expected background events.

	Nominal	Nominal + $ \eta _{e,1,2} < 2,$	Nominal + SR, high $E_T^{\text{miss}}, m_{\text{eff}}$ $ \eta _{e,1,2} < 2,$	Nominal + $ \eta _{e,1,2} < 2, \text{ no } Z \text{ cut}$	Nominal + SR, high $E_T^{\text{miss}}, m_{\text{eff}}$ $ \eta _{e,1,2} < 2, \text{ no } Z \text{ cut}$	Nominal + $ \eta _{e,1,2} < 2, \text{ no } Z \text{ cut}, N_{\text{jets}}^{25} \geq 3$	Nominal + SR, high $E_T^{\text{miss}}, m_{\text{eff}}$ $ \eta _{e,1,2} < 2, \text{ no } Z \text{ cut}, N_{\text{jets}}^{25} \geq 3$
Fakes	$-0.25 \pm 0.43 \pm 1.13$	$-0.25 \pm 0.43 \pm 1.13$	$0.27 \pm 0.54 \pm 1.54$	$1.43 \pm 0.77 \pm 3.14$	$2.37 \pm 0.92 \pm 4.17$	$2.08 \pm 0.85 \pm 3.93$	$3.17 \pm 1.00 \pm 5.08$
$t\bar{Z}, t\bar{t}W$	$2.60 \pm 0.06 \pm 0.78$	$2.85 \pm 0.07 \pm 0.86$	$4.08 \pm 0.08 \pm 1.22$	$4.11 \pm 0.08 \pm 1.23$	$6.07 \pm 0.11 \pm 1.82$	$5.19 \pm 0.10 \pm 1.56$	$7.36 \pm 0.12 \pm 2.21$
Total	$3.32 \pm 0.46 \pm 1.65$	$3.63 \pm 0.46 \pm 1.73$	$5.62 \pm 0.57 \pm 2.34$	$7.58 \pm 0.79 \pm 3.81$	$11.16 \pm 0.95 \pm 5.16$	$9.82 \pm 0.87 \pm 4.78$	$13.80 \pm 1.03 \pm 6.27$
Data	12	12	14	17	22	20	25
Significance	2.08	1.92	1.42	1.25	1.04	1.09	0.88

SR, high $E_T^{\text{miss}}, m_{\text{eff}}$ = no cuts ensuring the orthogonality with the SRs and a small BSM contamination.

Table 75: Results per channel in relaxed $t\bar{t}Z$ 2bIncl validation regions. The considered definitions are shown in the upper box of the table. Nominal stands for the $t\bar{t}Z$ 2bIncl VR as defined in Table 27. “Total” category includes the number of expected background events.

	Nominal	Nominal + $ \eta _{e,1,2} < 2,$	Nominal + SR, high $E_T^{\text{miss}}, m_{\text{eff}}$ $ \eta _{e,1,2} < 2,$	Nominal + $ \eta _{e,1,2} < 2, \text{ no } Z \text{ cut}$	Nominal + SR, high $E_T^{\text{miss}}, m_{\text{eff}}$ $ \eta _{e,1,2} < 2, \text{ no } Z \text{ cut}$	Nominal + $ \eta _{e,1,2} < 2, \text{ no } Z \text{ cut}, N_{\text{jets}}^{25} \geq 3$	Nominal + SR, high $E_T^{\text{miss}}, m_{\text{eff}}$ $ \eta _{e,1,2} < 2, \text{ no } Z \text{ cut}, N_{\text{jets}}^{25} \geq 3$
<i>ee channel</i>							
Fakes	$-0.42 \pm 0.24 \pm 0.33$	$-0.42 \pm 0.24 \pm 0.33$	$-0.26 \pm 0.29 \pm 0.45$	$0.05 \pm 0.36 \pm 0.68$	$0.18 \pm 0.39 \pm 0.82$	$0.21 \pm 0.39 \pm 0.79$	$0.34 \pm 0.43 \pm 0.94$
$t\bar{Z}, t\bar{t}W$	$0.34 \pm 0.02 \pm 0.10$	$0.42 \pm 0.03 \pm 0.13$	$0.64 \pm 0.03 \pm 0.19$	$0.59 \pm 0.03 \pm 0.18$	$0.95 \pm 0.04 \pm 0.29$	$0.78 \pm 0.04 \pm 0.23$	$1.18 \pm 0.05 \pm 0.35$
Total	$0.05 \pm 0.25 \pm 0.36$	$0.14 \pm 0.25 \pm 0.38$	$0.56 \pm 0.29 \pm 0.52$	$0.99 \pm 0.37 \pm 0.76$	$1.65 \pm 0.40 \pm 0.97$	$1.44 \pm 0.40 \pm 0.91$	$2.15 \pm 0.44 \pm 1.13$
Data	3	3	3	3	3	3	3
Significance	0.90	1.66	1.43	0.92	0.37	0.52	0.05
<i>eμ channel</i>							
Fakes	$0.09 \pm 0.24 \pm 0.39$	$0.09 \pm 0.24 \pm 0.39$	$0.32 \pm 0.35 \pm 0.58$	$1.23 \pm 0.56 \pm 1.70$	$1.65 \pm 0.69 \pm 2.33$	$1.77 \pm 0.65 \pm 2.31$	$2.34 \pm 0.77 \pm 3.05$
$t\bar{Z}, t\bar{t}W$	$1.23 \pm 0.04 \pm 0.37$	$1.41 \pm 0.05 \pm 0.42$	$2.03 \pm 0.06 \pm 0.61$	$1.99 \pm 0.06 \pm 0.60$	$3.00 \pm 0.07 \pm 0.90$	$2.53 \pm 0.07 \pm 0.76$	$3.64 \pm 0.08 \pm 1.09$
Total	$1.67 \pm 0.25 \pm 0.65$	$1.89 \pm 0.25 \pm 0.71$	$2.88 \pm 0.36 \pm 1.01$	$4.11 \pm 0.57 \pm 1.97$	$5.84 \pm 0.70 \pm 2.73$	$5.43 \pm 0.66 \pm 2.63$	$7.43 \pm 0.79 \pm 3.50$
Data	4	4	5	6	10	7	11
Significance	0.87	0.71	0.48	0.25	0.61	0.07	0.36
<i>$\mu\mu$ channel</i>							
Fakes	$0.08 \pm 0.27 \pm 0.41$	$0.08 \pm 0.27 \pm 0.41$	$0.21 \pm 0.30 \pm 0.51$	$0.15 \pm 0.37 \pm 0.76$	$0.54 \pm 0.47 \pm 1.03$	$0.11 \pm 0.38 \pm 0.83$	$0.49 \pm 0.47 \pm 1.10$
$t\bar{Z}, t\bar{t}W$	$1.02 \pm 0.04 \pm 0.31$	$1.02 \pm 0.04 \pm 0.31$	$1.40 \pm 0.05 \pm 0.42$	$1.53 \pm 0.05 \pm 0.46$	$2.12 \pm 0.06 \pm 0.64$	$1.88 \pm 0.06 \pm 0.56$	$2.54 \pm 0.07 \pm 0.76$
Total	$1.60 \pm 0.30 \pm 0.67$	$1.60 \pm 0.30 \pm 0.67$	$2.18 \pm 0.33 \pm 0.84$	$2.48 \pm 0.40 \pm 1.12$	$3.66 \pm 0.50 \pm 1.50$	$2.95 \pm 0.41 \pm 1.31$	$4.22 \pm 0.50 \pm 1.71$
Data	5	5	6	8	9	10	11
Significance	1.33	1.33	1.25	1.65	1.23	1.86	1.42

SR, high $E_T^{\text{miss}}, m_{\text{eff}}$ = no cuts ensuring no overlap with the SRs and a small contamination in BSM signal.

2224 **Tightening the signal lepton definition**

2225 To decrease the probability of having fake muons in the $t\bar{t}Z$ 2bIncl region, we further tighten the signal
 2226 muon definition. First we use muons with “Tight” WP instead of “Medium” WP, and further we tighten
 2227 the cut on the track isolation and/or add a cut on the calorimeter isolation. For electrons, as no tighter
 2228 WP is available, we just tighten the track and the calorimeter isolation requirements. For these results the
 2229 lepton fake rate is not remeasured (i.e the nominal fake rate is used). The results are shown in Tables 76
 2230 and 77. Generally it observed that the excess is reduced when considering tighter isolation criteria (i.e a
 2231 cut value of 0.01 and adding a cut on the calorimeter isolation for muons).

2232 **Conclusions**

2233 Given all the performed cross-checks no obvious problem is found, and the tension observed in the $t\bar{t}Z$

	Nominal	e nominal $\mu_{\text{calo iso} < 0.06^* p_T}$	e nominal $\mu_{\text{track iso} < 0.01^* p_T}$	e nominal $\mu_{\text{track + calo iso} < 0.01^* p_T}$	e nominal μ_{nominal}	e track + calo iso < $0.01^* p_T$ $\mu_{\text{track iso} < 0.01^* p_T}$	e track + calo iso < $0.01^* p_T$ μ_{nominal}
Fakes	$-0.25 \pm 0.43 \pm 1.13$	$-0.30 \pm 0.37 \pm 1.00$	$-0.33 \pm 0.37 \pm 1.03$	$0.10 \pm 0.41 \pm 1.04$	$0.30 \pm 0.46 \pm 1.18$	$0.22 \pm 0.41 \pm 1.08$	$0.22 \pm 0.41 \pm 1.08$
ttZ, ttW	$2.60 \pm 0.06 \pm 0.78$	$2.36 \pm 0.06 \pm 0.71$	$2.36 \pm 0.06 \pm 0.71$	$1.54 \pm 0.05 \pm 0.46$	$1.86 \pm 0.05 \pm 0.56$	$1.46 \pm 0.05 \pm 0.44$	$1.46 \pm 0.05 \pm 0.44$
ttH	$0.15 \pm 0.04 \pm 0.07$	$0.13 \pm 0.04 \pm 0.06$	$0.13 \pm 0.04 \pm 0.07$	$0.07 \pm 0.04 \pm 0.04$	$0.11 \pm 0.04 \pm 0.05$	$0.09 \pm 0.04 \pm 0.04$	$0.09 \pm 0.04 \pm 0.04$
Di-Boson	$0.31 \pm 0.13 \pm 0.09$	$0.31 \pm 0.13 \pm 0.09$	$0.29 \pm 0.13 \pm 0.09$	$0.29 \pm 0.13 \pm 0.09$	$0.22 \pm 0.12 \pm 0.07$	$0.17 \pm 0.12 \pm 0.05$	$0.17 \pm 0.12 \pm 0.05$
Rare	$0.52 \pm 0.06 \pm 0.26$	$0.44 \pm 0.06 \pm 0.22$	$0.46 \pm 0.06 \pm 0.23$	$0.28 \pm 0.04 \pm 0.14$	$0.37 \pm 0.05 \pm 0.19$	$0.23 \pm 0.04 \pm 0.11$	$0.23 \pm 0.04 \pm 0.11$
Total	$3.33 \pm 0.46 \pm 1.66$	$2.94 \pm 0.40 \pm 1.47$	$2.91 \pm 0.41 \pm 1.50$	$2.27 \pm 0.44 \pm 1.26$	$2.86 \pm 0.48 \pm 1.46$	$2.17 \pm 0.43 \pm 1.26$	$2.17 \pm 0.43 \pm 1.26$
Data	12	10	11	7	9	8	8
Significance	2.08	1.87	2.21	1.48	1.65	1.85	1.85

Table 76: Results in relaxed $t\bar{t}Z$ 2bIncl validation regions. The changes in the signal lepton definition are shown in the upper box of the table; the electron isolation is changed only if $p_T e < 300$ GeV. Nominal stands for the $t\bar{t}Z$ 2bIncl VR as defined in Table 27. ‘‘Total’’ category includes the number of expected background events.

	e nominal μ_T nominal	e nominal μ_T calo iso < $0.06^* p_T$	e nominal μ_T track iso < $0.01^* p_T$	e nominal μ_T track + calo iso < $0.01^* p_T$	e nominal μ_T nominal	e track + calo iso < $0.01^* p_T$ μ_T nominal	e track + calo iso < $0.01^* p_T$ μ_T track iso < $0.01^* p_T$
Fakes	$-0.25 \pm 0.43 \pm 1.13$	$-0.30 \pm 0.37 \pm 1.00$	$-0.33 \pm 0.37 \pm 1.03$	$0.10 \pm 0.41 \pm 1.04$	$0.30 \pm 0.46 \pm 1.18$	$0.22 \pm 0.41 \pm 1.08$	$0.22 \pm 0.41 \pm 1.08$
ttZ, ttW	$2.36 \pm 0.06 \pm 0.71$	$2.15 \pm 0.06 \pm 0.64$	$2.14 \pm 0.06 \pm 0.64$	$1.41 \pm 0.05 \pm 0.42$	$1.65 \pm 0.05 \pm 0.49$	$1.46 \pm 0.05 \pm 0.44$	$1.46 \pm 0.05 \pm 0.44$
ttH	$0.14 \pm 0.04 \pm 0.07$	$0.11 \pm 0.04 \pm 0.06$	$0.12 \pm 0.04 \pm 0.06$	$0.06 \pm 0.03 \pm 0.03$	$0.10 \pm 0.04 \pm 0.05$	$0.09 \pm 0.04 \pm 0.04$	$0.09 \pm 0.04 \pm 0.04$
Di-Boson	$0.29 \pm 0.13 \pm 0.09$	$0.28 \pm 0.13 \pm 0.08$	$0.26 \pm 0.13 \pm 0.08$	$0.26 \pm 0.13 \pm 0.08$	$0.20 \pm 0.12 \pm 0.06$	$0.17 \pm 0.12 \pm 0.05$	$0.17 \pm 0.12 \pm 0.05$
Rare	$0.40 \pm 0.05 \pm 0.20$	$0.33 \pm 0.05 \pm 0.16$	$0.36 \pm 0.05 \pm 0.18$	$0.22 \pm 0.04 \pm 0.11$	$0.26 \pm 0.04 \pm 0.13$	$0.23 \pm 0.04 \pm 0.11$	$0.23 \pm 0.04 \pm 0.11$
Total	$2.92 \pm 0.46 \pm 1.55$	$2.57 \pm 0.40 \pm 1.38$	$2.55 \pm 0.40 \pm 1.41$	$2.05 \pm 0.43 \pm 1.22$	$2.50 \pm 0.48 \pm 1.39$	$2.17 \pm 0.43 \pm 1.26$	$2.17 \pm 0.43 \pm 1.26$
Data	12	10	11	7	9	8	8
Significance	2.32	2.11	2.36	1.63	1.88	1.85	1.85

Table 77: Results in relaxed $t\bar{t}Z$ 2bIncl validation regions. The changes in the signal lepton definition are shown in the upper box of the table; the muons passing Tight WP instead of Medium as used in this analysis; the electron isolation is changed only if $p_T e < 300$ GeV. Nominal stands for the $t\bar{t}Z$ 2bIncl VR as defined in Table 27. ‘‘Total’’ category includes the number of expected background events.

2234 1bIncl region tends to be just a fluctuation. However, it will be very interesting to study the region with
2235 at least two b -jets and low m_{eff} when more data will be available.

2236 20 Updated study on E_T^{miss} trigger

2237 In order to have the best possible acceptance of events containing leptons and missing E_T , an updated
 2238 study on the performance of the E_T^{miss} triggers has been conducted.

2239 Since the HLT_xe70 and HLT_xe80 trigger will be the lowest unprescaled missing E_T triggers in the early
 2240 RunII phase, we decided to test this triggers in addition to the di-lepton triggers to select events with
 2241 lepton pairs and high missing energy. A version of the HLT_xe80 trigger exists also using the missing
 2242 energy reconstruction based on calibrated topoclusters HLT_xe80_tc_lcw. The efficiency threshold of
 2243 these triggers was investigated in data and Monte Carlo using events preselected by the OR combination
 2244 of di-lepton triggers mentioned in the previous section. In addition, we require two offline reconstructed
 2245 leptons with $p_T > 10$ GeV in the events used for the efficiency calculation. The efficiency of the triggers
 2246 can be obtained by dividing the number of events triggered with the di-lepton and the E_T^{miss} triggers by the
 2247 events triggered only by the di-lepton triggers. Since the di-lepton triggers have an orthogonal selection
 2248 to the E_T^{miss} trigger, this allows to have an unbiased look at the efficiency evolution versus the missing
 2249 energy.

2250 The real data events used for the efficiency computation were collected during September 2015 (Run
 2251 276262 - 279928). They correspond to an integrated luminosity of 485.8 pb^{-1} . To compute the trigger effi-
 2252 ciency in simulated Monte Carlo events, a $t\bar{t}$ sample was used (MC Id: 410000, PowhegPythiaEvtGen_P2012_ttbar_h-
 2253 In both cases, we used SUSY2 DxAOD derivations produced with the derivation tag p2419 (20.1.7.1
 2254 cache). The calculation of the offline missing energy was done using the SUSYTools-00-06-24-01
 2255 package together with the AnalysisBase framework (2.3.28 branch). Leptons, photons and jets are used
 2256 for the calculation off the offline E_T^{miss} .

2257 The evolution of the trigger efficiency versus the missing E_T is shown in figure 133 for data and Monte
 2258 Carlo events. The turn-on of the trigger efficiency is in both cases faster in HLT_xe80_tc_lcw than in
 2259 HLT_xe80.

2260 The efficiency evolution for HLT_xe70 is shown in figure 134. Also a the superimposed efficiency
 2261 curves for all three triggers tested is shown there. The performance of HLT_xe70 is very similar to
 2262 HLT_xe80_tc_lcw. However, the turn-on is slithly better for HLT_xe70. Therefore, the application of
 2263 HLT_xe70 is the preferred option to select high E_T^{miss} events. If the missing energy is higher than 200
 2264 GeV, all trigger types behave similar and show an efficiency $> 90\%$. If $E_T^{\text{miss}} > 250$ GeV, the efficiency is
 2265 $> 98\%$. It should also be emphasized, that the trigger threshold is the same in data and Monte Carlo and
 2266 for both cases the triggers reach their efficiency plateaus in the same E_T^{miss} region. Further efficiency plots
 2267 can be found in Appendix 21.

2268 20.0.1 Dependency on jet requirements

2269 The several jet requirements in the signal regions of this analysis make it essential to test the trigger
 2270 efficiency also in events containing additional high p_T jets. The turn-on curves for the HLT_xe80 and
 2271 HLT_xe80_tc_lcw trigger by asking for one, two or three jets with $p_T > 50$ GeV in addition to the
 2272 missing E_T are shown in figure 135. The same plot for HLT_xe70 is shown on figure 136. This study
 2273 is only shown for $t\bar{t}$ Monte Carlo, since the selection of these events leads to lower numbers of selected
 2274 events and therefore to higher statistical uncertainties in the investigated dataset. A small dependency of

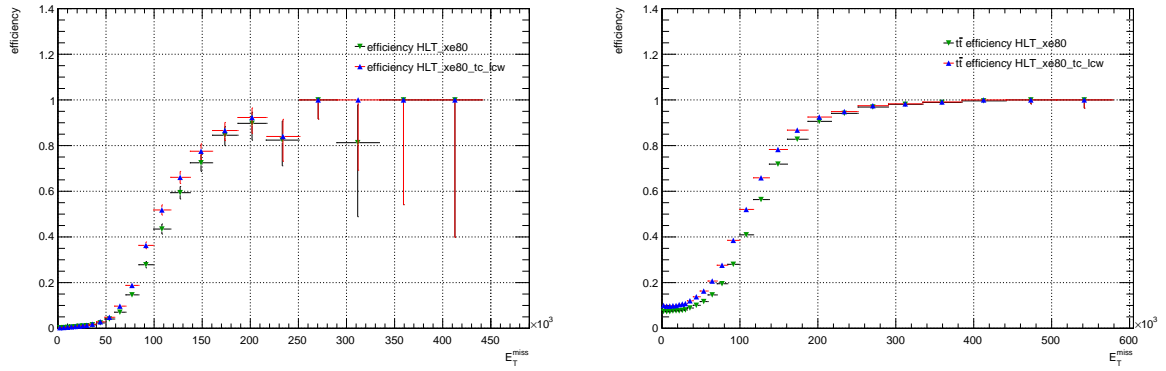


Figure 133: Trigger efficiencies for HLT_xe80 and HLT_xe80_tc_lc versus the missing energy. Shown for the real data events (left) and $t\bar{t}$ Monte Carlo (right)

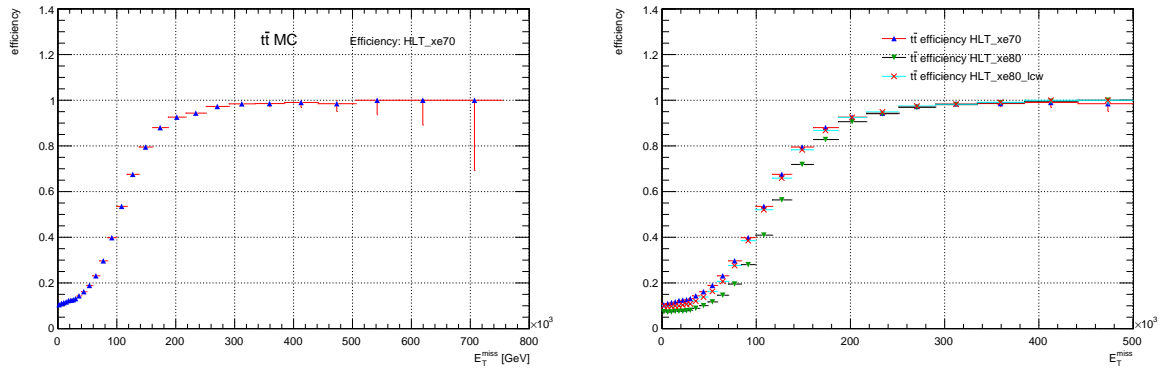


Figure 134: Trigger efficiencies for HLT_xe70 versus the missing energy (left). A direct comparison of the efficiency evolution for HLT_xe70, HLT_xe80 and HLT_xe80_tc_lc is shown on the right-hand side.

the efficiency evolution can be observed for the additional jet selection criteria. However, if the missing E_T is above 250 GeV, the effect is smaller than 5%.

20.0.2 Inefficiency issues of E_T^{miss} triggers

Both triggers show small inefficiencies for high E_T^{miss} values. A probable reason for this is that muons are not included in the L1 E_T^{miss} value used for the online trigger decision. To understand this effect, the requirement of the lepton pair with $p_T > 10$ GeV has been separated by the lepton flavor. This provides a separate measurement of efficiencies for events containing electrons and muons. The efficiencies are shown in figure 137 for $t\bar{t}$ Monte Carlo and figure 138 for data events.

It is obvious that the measurements using di-muon events show some inefficiencies with respect to the di-electron events. This supports the presumption that the missing muons at the L1 trigger E_T^{miss} are responsible for the inefficiencies observed in all E_T^{miss} triggers investigated. However, since we will combine the E_T^{miss} - and the di-lepton triggers with a logical OR for the event selection in the analysis, these events should be selected by the di-lepton triggers. Additional plots are shown in 21.

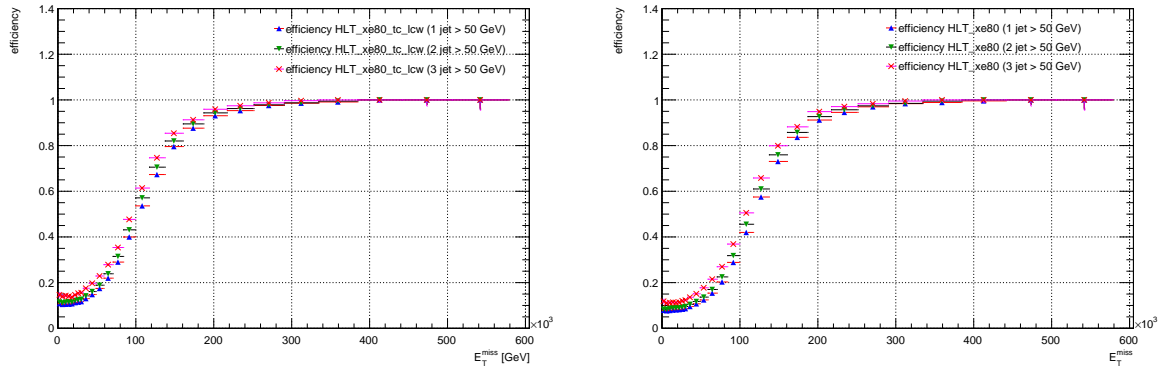


Figure 135: Trigger efficiencies for HLT_xe80_tc_lcw (left) and HLT_xe80 (right) versus the missing energy by requiring one, two or three additional jets with $p_T > 50$ GeV. Also in this case a preselection of events containing two leptons with $p_T > 10$ GeV is applied.

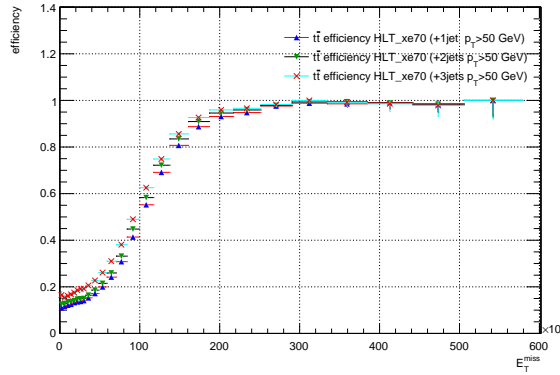


Figure 136: Trigger efficiency for HLT_xe70 versus the missing energy by requiring one, two or three additional jets with $p_T > 50$ GeV.

2288 Based on these studies and efficiency measurements, a preliminary decision for the trigger selection has
2289 been made.

- 2290 • If $E_T^{\text{miss}} < 250$ GeV, only an OR combination of di-lepton triggers is used.
2291 • If $E_T^{\text{miss}} > 250$ GeV, an OR between the di-lepton triggers and HLT_xe70 is used.

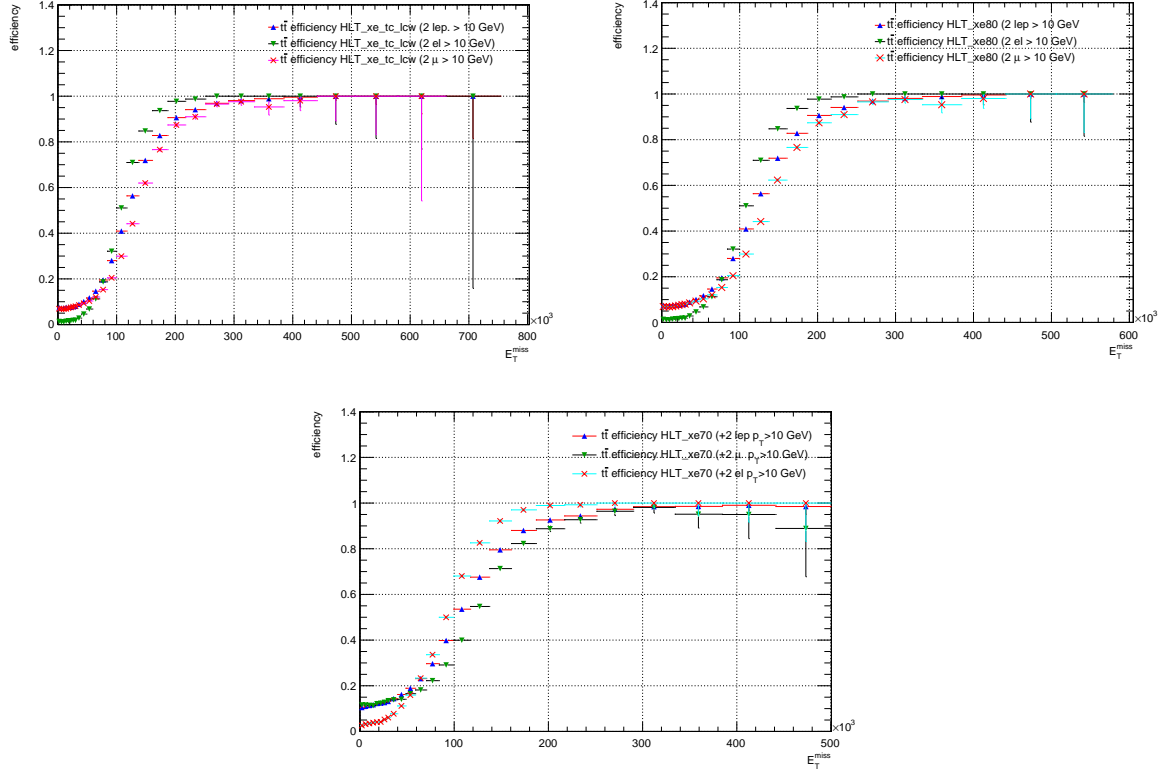


Figure 137: Trigger efficiencies for HLT_xe80_tc_lcw (top-left), HLT_xe80 (top-right) and HLT_xe80 (bottom) versus E_T^{miss} obtained from $t\bar{t}$ Monte Carlo. The different curves show the efficiency for events containing a ll , ee or $\mu\mu$ pair.

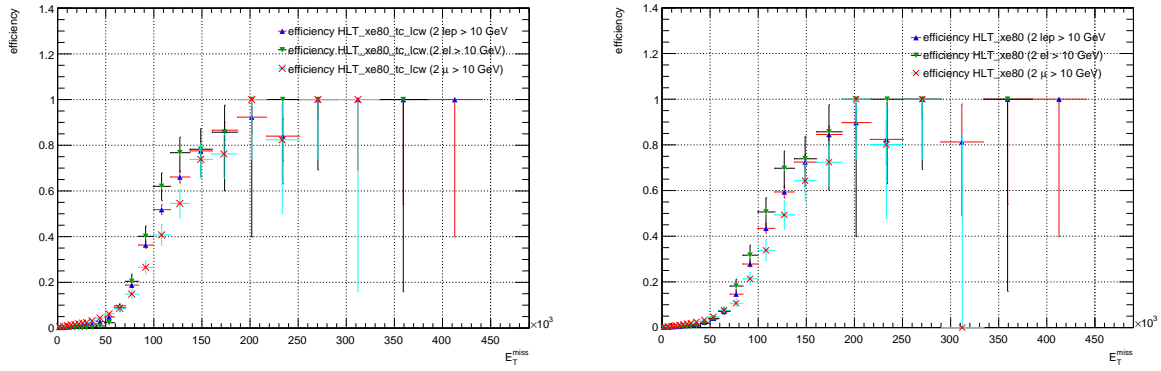


Figure 138: Trigger efficiencies in data for HLT_xe80_tc_lcw (left) and HLT_xe80 (right) versus E_T^{miss} . The different curves show the efficiency for events containing a ll , ee or $\mu\mu$ pair.

21 Selected events and efficiency plot for E_T^{miss} trigger

2293 Studies on performance and efficiency have been done for HLT_xe80 and HLT_xe80_tc_low. Efficiency
 2294 plots and histograms showing the triggered events can be found here.

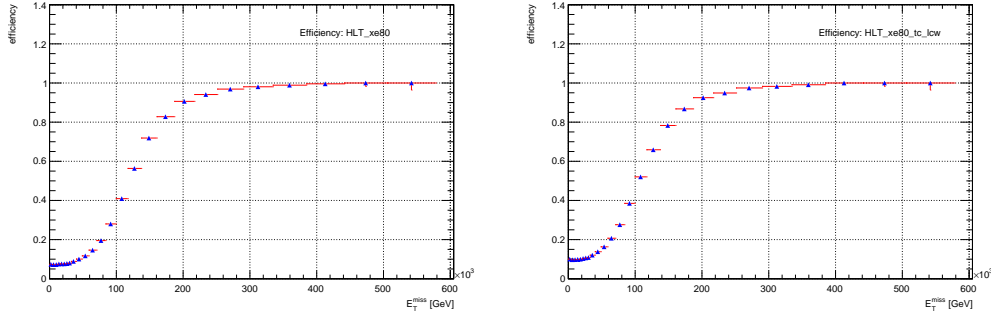


Figure 139: Efficiency of HLT_xe80 (left) and HLT_xe80_tc_low (right) versus the missing energy obtained from $t\bar{t}$ Monte Carlo

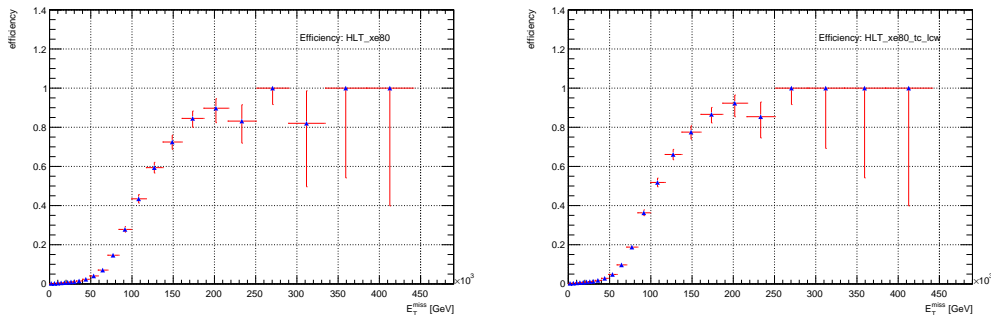


Figure 140: Efficiency of HLT_xe80 (left) and HLT_xe80_tc_low (right) versus the missing energy obtained from data

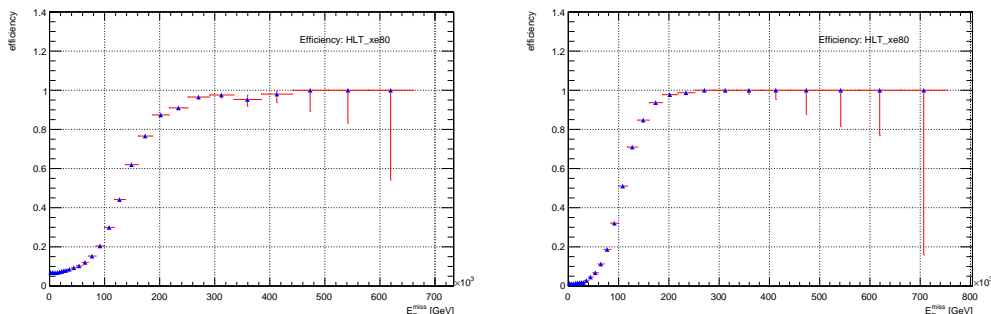


Figure 141: Efficiency of HLT_xe80 versus the missing energy. All events were preselected for a muon-pair (left) or an electron-pair (right) ($p_T > 10$ GeV).

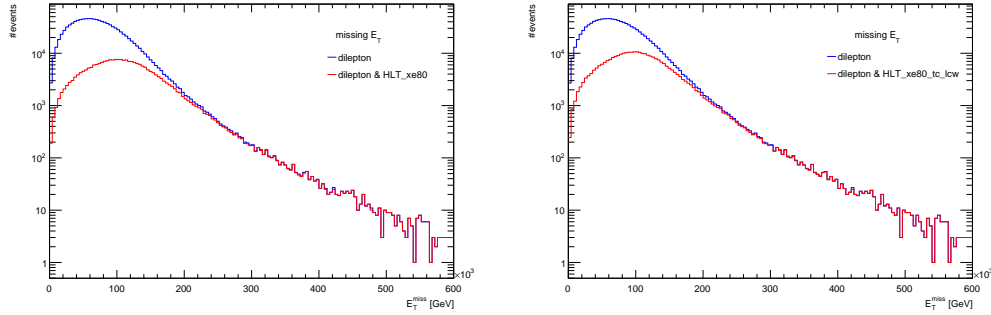


Figure 142: Events selected by di-lepton triggers only and by an AND combination of di-lepton triggers and HLT_xe80 (left), HLT_xe80_tc_1cw (right). Plotted against the missing energy.

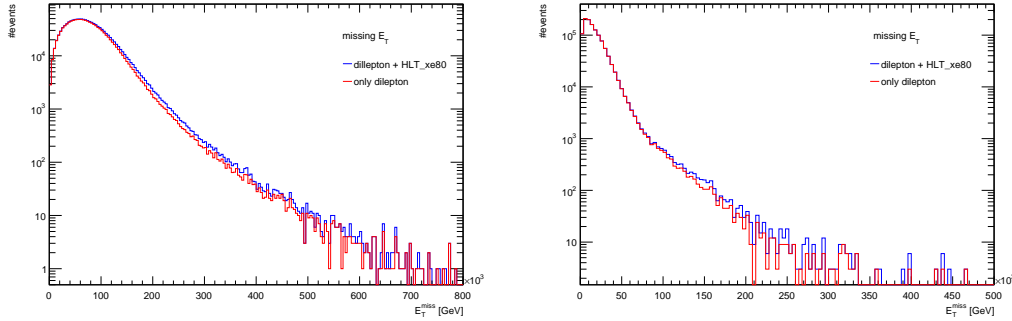


Figure 143: Events selected by di-lepton triggers only and by an OR combination of di-lepton triggers and HLT_xe80. Shown for $t\bar{t}$ Monte Carlo (left) and for real data (right).

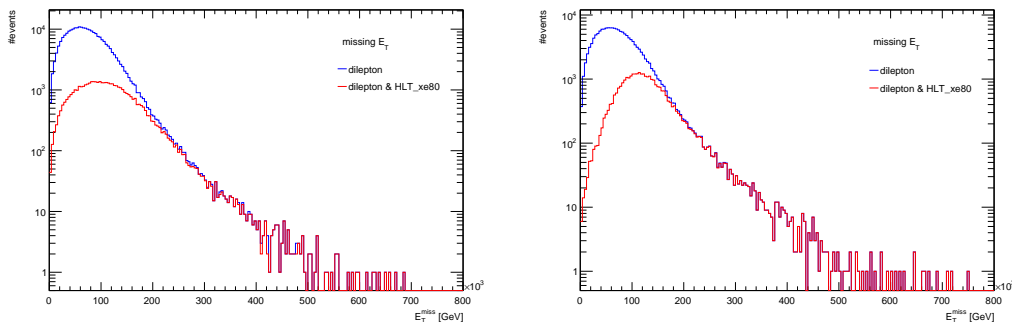


Figure 144: Events selected by di-lepton triggers only and by an AND combination of di-lepton triggers and HLT_xe80. All events were preselected for a muon-pair (left) or an electron-pair (right) ($p_T > 10$ GeV).

2295 22 Further details on the MC template method

2296 In order to validate the fitting machinery, we performed pseudo-experiments where the toy data is obtained
 2297 by randomly sampling the summed contribution from the six categories according to a Poisson distribution.
 2298 Pull plots are obtained for each fake rate as shown in Figure 145. Overall, the mean is consistent with zero
 2299 and the standard deviation is close to unity as expected.

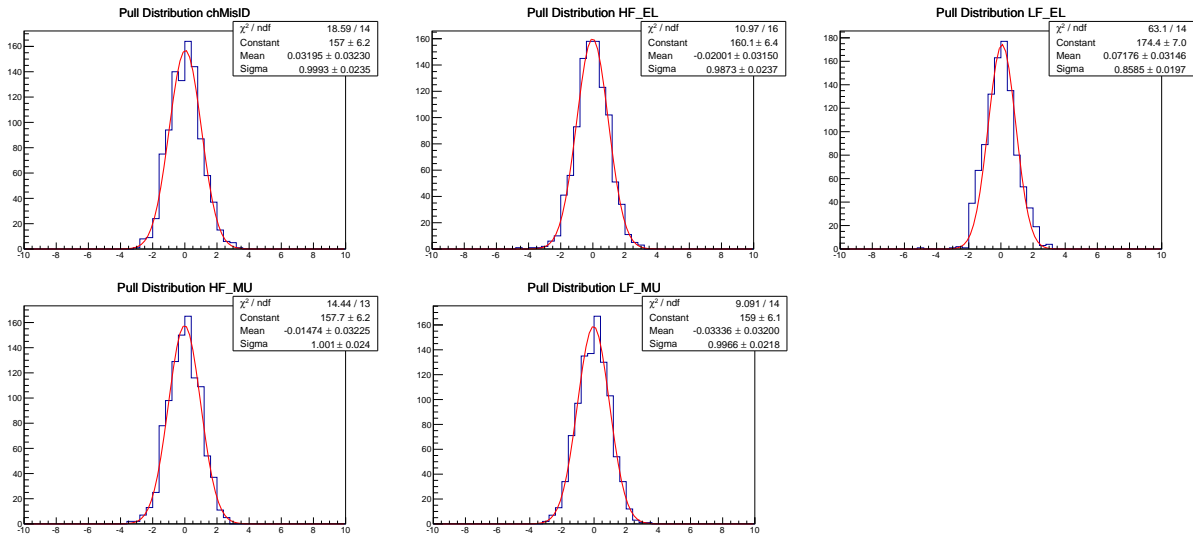


Figure 145: Pull tests for the correction factors using toy data.

2300 In our classification, we assumed that the b -tagging requirement only affects the rate of leptons coming
 2301 from b -hadrons. As a sanity check of this assumption, we also include fake leptons coming from c -hadron
 2302 decays in HF with the leptons coming from b -hadrons and re-do the fit. The comparison is shown in
 2303 Table 78 using pseudo-data which shows that there is a negligible effect in including c -jet induced
 2304 fakes.

Table 78: The fake-rate and charge flip corrections obtained in the cases where fakes from c -hadrons are categorized separate from fakes from b -hadrons and when they are categorized in the same category. A negligible effect is observed. The MC templates are normalized to 2 fb^{-1} of integrated luminosity.

Category	b -hadrons	b - or c -hadrons
Charge Flip	1.02 ± 0.11	1.02 ± 0.11
EL HF	0.99 ± 0.85	1.00 ± 0.83
EL LF	0.69 ± 0.84	0.69 ± 0.82
MU HF	1.01 ± 0.28	0.97 ± 0.24
MU LF	0.85 ± 0.84	0.92 ± 0.93

2305 23 Details on the study of the theoretical uncertainties for simulated 2306 samples

2307 This appendix describes the study performed to evaluate the theoretical uncertainties associated with
 2308 the $t\bar{t}V$ and $W^\pm W^\pm jj$ background samples. As described in section 3, the $t\bar{t}V$ processes are simulated
 2309 using using MADGRAPH and the $W^\pm W^\pm jj$ processes using Sherpa. For $W^\pm W^\pm jj$ we have compared the
 2310 nominal sample with several scale variations, listed in table 79. For $t\bar{t}V$ we have compared the nominal
 2311 MADGRAPH sample with the ones generated varying ALPSFACT as well as μ_R and μ_F by a factor of two.
 2312 In addition, for $t\bar{t}V$ we also compared the MADGRAPH prediction with the SHERPA one. The $t\bar{t}V$ samples
 are listed in table 80 and 81.

Table 79: Sherpa $W^\pm W^\pm jj$ samples. The cross section values are the ones from AMI.

Sample	cross section [pb]
mc15_13TeV.361069.Sherpa_CT10_llvjj_ss_EW4.evgen.EVNT.e3836	0.025797
mc15_13TeV.361070.Sherpa_CT10_llvjj_ss_EW6.evgen.EVNT.e3836	0.043004
mc15_13TeV.361643.Sherpa_CT10_llvjj_ss_EW4_FSFup.evgen.EVNT.e4561	0.025199
mc15_13TeV.361644.Sherpa_CT10_llvjj_ss_EW4_QSFdown.evgen.EVNT.e4561	0.026935
mc15_13TeV.361645.Sherpa_CT10_llvjj_ss_EW4_QSFup.evgen.EVNT.e4561	0.025422
mc15_13TeV.361646.Sherpa_CT10_llvjj_ss_EW4_RSFdown.evgen.EVNT.e4561	0.03369
mc15_13TeV.361647.Sherpa_CT10_llvjj_ss_EW4_RSFup.evgen.EVNT.e4561	0.021188
mc15_13TeV.361648.Sherpa_CT10_llvjj_ss_EW6_CKKWdown.evgen.EVNT.e4561	0.043657
mc15_13TeV.361649.Sherpa_CT10_llvjj_ss_EW6_CKKWup.evgen.EVNT.e4561	0.042895
mc15_13TeV.361650.Sherpa_CT10_llvjj_ss_EW6_FSFdown.evgen.EVNT.e4561	0.044477
mc15_13TeV.361651.Sherpa_CT10_llvjj_ss_EW6_FSFup.evgen.EVNT.e4561	0.042077
mc15_13TeV.361652.Sherpa_CT10_llvjj_ss_EW6_QSFdown.evgen.EVNT.e4561	0.043747
mc15_13TeV.361653.Sherpa_CT10_llvjj_ss_EW6_QSFup.evgen.EVNT.e4561	0.04359
mc15_13TeV.361654.Sherpa_CT10_llvjj_ss_EW6_RSFdown.evgen.EVNT.e4561	0.04301
mc15_13TeV.361655.Sherpa_CT10_llvjj_ss_EW6_RSFup.evgen.EVNT.e4561	0.043495
mc15_13TeV.361656.Sherpa_CT10_llvjj_ss_EW6_CKKWdown.evgen.EVNT.e4561	0.026241
mc15_13TeV.361657.Sherpa_CT10_llvjj_ss_EW4_CKKWup.evgen.EVNT.e4561	0.024757
mc15_13TeV.361658.Sherpa_CT10_llvjj_ss_EW4_FSFdown.evgen.EVNT.e4561	0.02724

Table 80: $t\bar{t}\ell\ell$ samples. The cross section values for the official samples 41011X are from AMI. The cross section for the private SHERPA sample is from the PMG documentation at <https://twiki.cern.ch/twiki/bin/viewauth/AtlasProtected/TtbarBoson>.

Sample	cross section [pb]
mc15_13TeV.410111.MadGraphPythia8EvtGen_A14NNPDF23LO_ttee_Np0.evgen.EVNT.e4265	0.0088155
mc15_13TeV.410112.MadGraphPythia8EvtGen_A14NNPDF23LO_ttee_Np1.evgen.EVNT.e4265	0.0143800
mc15_13TeV.410113.MadGraphPythia8EvtGen_A14NNPDF23LO_ttmumu_Np0.evgen.EVNT.e4265	0.0088422
mc15_13TeV.410114.MadGraphPythia8EvtGen_A14NNPDF23LO_ttmumu_Np1.evgen.EVNT.e4265	0.0143750
mc15_13TeV.410115.MadGraphPythia8EvtGen_A14NNPDF23LO_tttautau_Np0.evgen.EVNT.e4265	0.0090148
mc15_13TeV.410116.MadGraphPythia8EvtGen_A14NNPDF23LO_tttautau_Np1.evgen.EVNT.e4265	0.0146360
user.narayan.16-11-2015-sherpa2.2_tll	0.0975300

2313

2314 This study is performed at the truth level using samples in the TRUTH1 format¹⁰. The basic acceptance
 2315 criteria (momentum and pseudorapidity) are applied to leptons and jets, followed by the overlap removal
 2316 procedure. The kinematic requirements defining the signal regions and the validation regions are the same

¹⁰ The TRUTH1 samples were generated from the EVNT samples using the release 20.1.8

Table 81: $t\bar{t}W$ samples. Cross section values for the official samples are taken from AMI; for the private samples they are the ones reported by MADGRAPH. DSID scheme: xxx066=Np0, xxx067=Np1, xxx068=Np2

Sample	cross section [pb]
mc15_13TeV.410067.MadGraphPythia8EvtGen_A14NNPDF23LO_ttW_Np1.evgen.EVNT.e4111	0.140620
mc15_13TeV.410068.MadGraphPythia8EvtGen_A14NNPDF23LO_ttW_Np2.evgen.EVNT.e4111	0.136800
mc15_13TeV.410066.MadGraphPythia8EvtGen_A14NNPDF23LO_ttW_Np0.evgen.EVNT.e4111	0.176560
user.mcfayden.evnt.2015-11-04_233054.610066.13TeV_ttW_scalUp_EXT1	0.1437
user.mcfayden.evnt.2015-11-04_233147.610067.13TeV_ttW_scalUp_EXT1	0.11086
user.mcfayden.evnt.2015-11-04_233240.610068.13TeV_ttW_scalUp_EXT1	0.099048
user.mcfayden.evnt.2015-11-04_233330.710066.13TeV_ttW_scalDn_EXT1	0.24284
user.mcfayden.evnt.2015-11-04_233425.710067.13TeV_ttW_scalDn_EXT1	0.20288
user.mcfayden.evnt.2015-11-04_233522.710068.13TeV_ttW_scalDn_EXT1	0.21626
user.mcfayden.evnt.2015-11-04_233612.810066.13TeV_ttW_alpsUp_EXT1	0.1838
user.mcfayden.evnt.2015-11-04_233706.810067.13TeV_ttW_alpsUp_EXT1	0.1446
user.mcfayden.evnt.2015-11-04_233752.810068.13TeV_ttW_alpsUp_EXT1	0.13922
user.mcfayden.evnt.2015-11-04_233840.910066.13TeV_ttW_alpsDn_EXT1	0.18134
user.mcfayden.evnt.2015-11-04_233924.910067.13TeV_ttW_alpsDn_EXT1	0.14484
user.mcfayden.evnt.2015-11-04_234014.910068.13TeV_ttW_alpsDn_EXT1	0.1379

2317 ones defined in section 6. The number of b -jets used in the selection criteria is determined by emulating¹¹
 2318 the b-tagging algorithm using the typical efficiencies and mistag rates. The differences in yield between
 2319 the nominal sample and the variation samples are summarized in table 82 for $t\bar{t}V$ and in table 83 for
 2320 $W^\pm W^\pm jj$. These variations, reported in percent values, are calculated as the fractional difference in yield
 2321 for a given selection, after normalizing the inclusive samples to the same value.

2322 It should be pointed out that the uncertainties on these variations reflect the limited statistics in both the
 2323 nominal and variation samples. At the time of this writing, the number of simulated events in the variation
 2324 samples that reach the selection regions is quite limited. We expect that more events will be available
 2325 in the future, improving the accuracy of this study. In the meantime, we can observe that most of the
 2326 variations reported in this study are within the 30% being used as theoretical systematic uncertainty for
 2327 $t\bar{t}V$ and $W^\pm W^\pm jj$. The few outliers were shown to be random fluctuations: they are significantly reduced
 2328 when the selection criteria are relaxed (for example by making $sr0b5j \rightarrow sr0b4j$).

24 Detailed isolation studies

2330 Since one of the dominant background sources in the analysis is due to events with a non-prompt lepton,
 2331 dedicated lepton isolation optimization studies have been performed.

2332 For the DC14 walkthroughs in April 2015 [14], the following cuts on the isolation variables were found
 2333 to be optimal:

- 2334 • Electrons: TightLLH, $\text{ptvarcone20}/p_T < 0.06$ and $\text{topoetcone20}/p_T < 0.06$ (“FixedCutTight”)
- 2335 • Muons: $\text{ptvarcone30}/p_T < 0.06$ (“FixedCutTightTrackOnly”)

2336 Shortly after, the ATLAS isolation forum released pre-pre-recommendations for DC14 samples relying on
 2337 the ElectronIsolationSelectionTool [53]. This tool parametrizes the cuts on the isolation variables
 2338 as a function of the efficiency in $Z \rightarrow \ell\ell$ events. The pre-pre-recommendations included working

¹¹ The code used to perform this study is available at <https://github.com/gerbaudo/PMGValidation>

Table 82: Summary of the fractional variations (in percent) for the $t\bar{t}V$ samples in the relevant selection regions.

Sherpa variation		
$t\bar{t}\ell\ell$		
sr3b	-30.7 ± 12.7	
sr1b	5.8 ± 2.9	
cr2bttV	1.3 ± 2.3	
$t\bar{t}W$		
sr3b	20.1 ± 43.2	
sr1b	42.1 ± 10.6	
cr2bttV	27.6 ± 12.2	
up		down
$t\bar{t}W$		
sr3b	12.9 ± 23.3	-2.9 ± 25.5
sr1b	3.9 ± 7.0	3.4 ± 6.6
$t\bar{t}W$		
sr3b	28.8 ± 18.3	24.4 ± 19.4
sr1b	9.4 ± 6.1	-2.0 ± 6.9

Table 83: Summary of the fractional variations (in percent) for the $W^\pm W^\pm jj$ samples in the relevant selection regions.

	up	down
$WWjj$ CKKW		
sr0b5j	1.9 ± 18.6	13.6 ± 17.2
$WWjj$ FSF		
sr0b5j	16.6 ± 17.2	-9.7 ± 19.7
$WWjj$ QSF		
sr0b5j	-57.1 ± 24.3	60.1 ± 11.4
$WWjj$ RSF		
sr0b5j	0.2 ± 19.0	23.8 ± 15.5

2339 points with constant (`Tight`, `Medium`, `Loose`, `VeryLoose` and `VeryLooseTrackOnly`) or with a variable
 2340 efficiency as a function of p_T (`Gradient` and `GradientLoose`); they relied on the relative isolation
 2341 variables `topoetcone20/pT` and `ptvarcone20/pT` for electrons, and `topoetcone20/pT` and `ptvarcone30/pT`
 2342 for muons. Optimization studies considering both signal and background using the discovery significance
 2343 as figure of merit showed that the `GradientLoose` working point had a good performance for the signal
 2344 regions in this analysis.

2345 On July 2015, the MC15 isolation pre-recommendations were released by the ATLAS isolation forum [54]
 2346 which kept the definition of the `GradientLoose` working point, as well as the isolation variables used
 2347 to build it, unchanged. Figure 146 shows the isolation efficiency for non-prompt leptons in background
 2348 samples and prompt leptons in a signal sample, with a much higher fake muon efficiency compared to the
 2349 Run-1 or DC14 studies ([14]). This was traced to be due to much looser cuts applied to the `ptvarcone30/pT`

2350 inside the `IsolationSelectionTool` for low- p_T muons, as detailed in Appendix 24.

2351 Two additional custom isolation working points were defined with the same variable efficiency approach
2352 used for `Gradient` and `GradientLoose` but with much tighter settings. The isolation efficiency for these
2353 two custom working points is the following:

- 2354 • `GradientCustom`: $(0.1713 \times p_T \text{ [GeV]} + 88.71)\%$
2355 • `GradientCustomTight`: $(0.2283 \times p_T \text{ [GeV]} + 85.28)\%$

2356 The prompt and non-prompt lepton efficiency for these working points is also shown in Figure 146, and
2357 they are able to recover the rejection against non-prompt leptons to levels comparable to those in Run-1.
2358 A scan over the isolation working points in terms of discovery significance for a couple of signal models
2359 is shown in Figure 147. The significance is computed after a selection of two same-sign leptons, 4 jets
2360 with $p_T > 50 \text{ GeV}$ and $E_T^{\text{miss}} > 100 \text{ GeV}$ assuming 3 fb^{-1} of integrated luminosity and a 30% background
2361 uncertainty. As shown, `GradientLoose` is not optimal, with significances $\sim 10\%$ lower than the most
2362 performing configuration, and the customly defined working points are strongly preferred, with the simple
2363 cuts on the isolation variables used in DC14 (“eVTmT”, also referred to as “EL0p06” and “MU0p06”)
2364 providing very competitive results.

2365 The isolation working points proposed from this analysis were accepted by the ATLAS Isolation forum
2366 and implemented as officially supported working points in the `IsolationSelectionTool`. In the
2367 studies contained in this note, “`FixedCutTight`” and “`FixedCutTightTrackOnly`” are used unless otherwise
2368 stated.

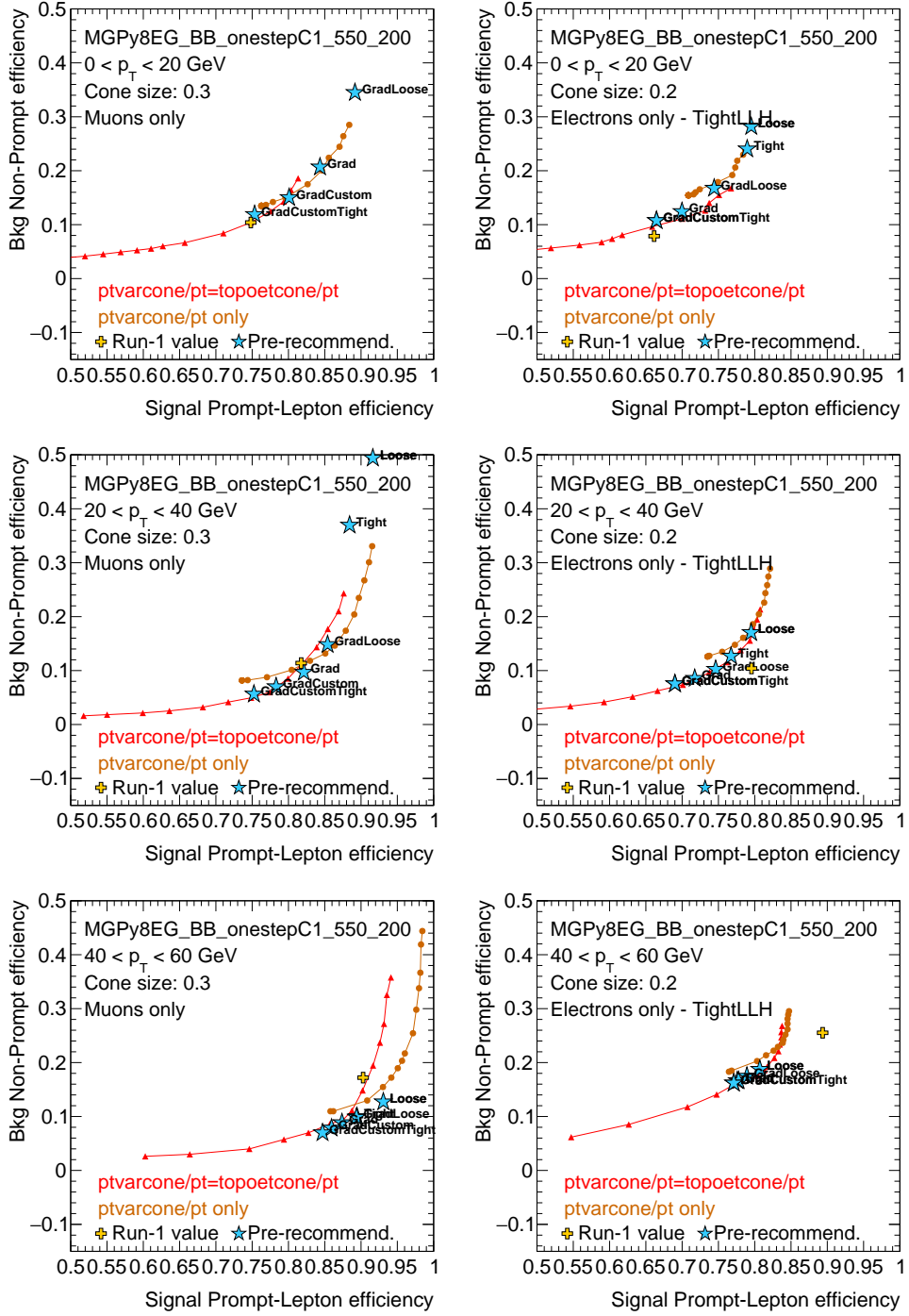


Figure 146: Isolation efficiency for background non-prompt muons as a function of the isolation efficiency for prompt muons in signal events for muons (left) and electrons (right) in different p_T bins in MC15 samples. Curves are shown for ptvarcone/ p_T alone, ptvarcone/ p_T combined with topoetcone/ p_T and the isolation pre-recommendations working points. In addition, the cross shows the value that would be obtained with settings equivalent to those used during Run-1.

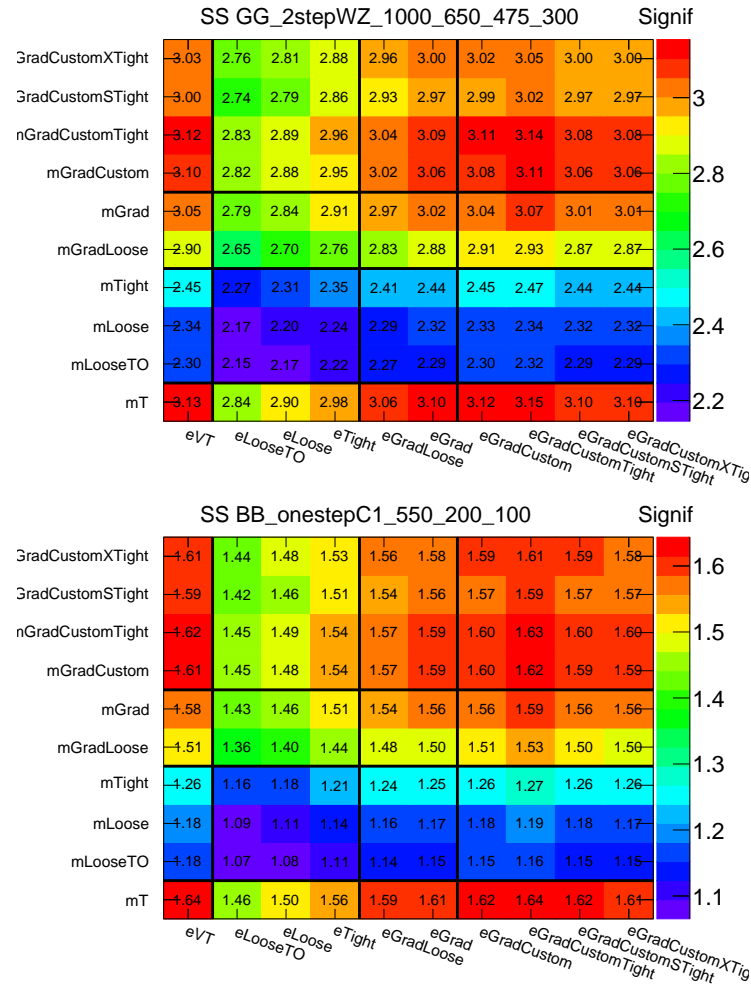


Figure 147: Discovery significance values for different isolation requirements on electrons (x-axis) and muons (y-axis) for 2 fb^{-1} .

25 Additional checks

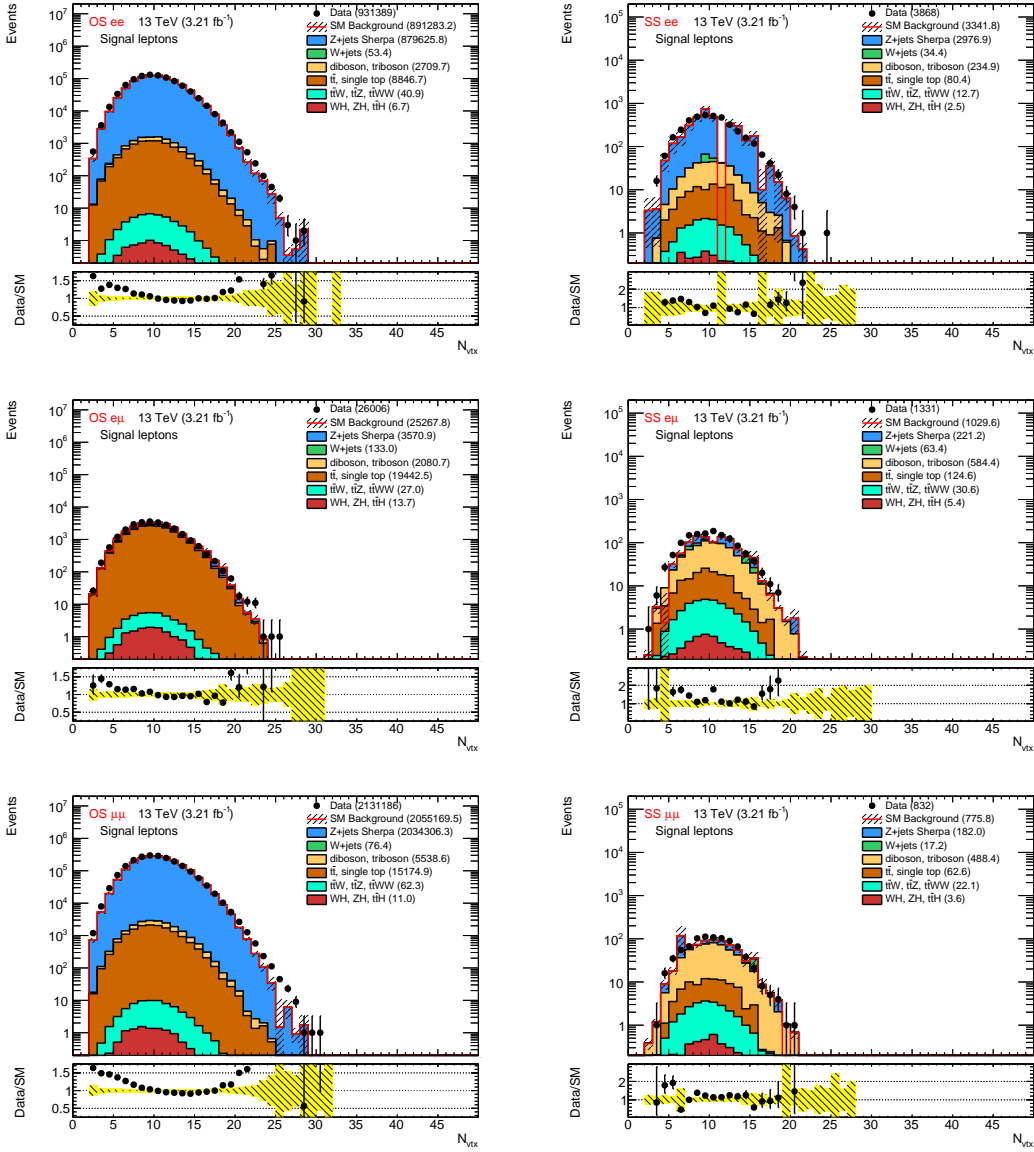


Figure 148: Distributions of the number of vertices for OS (left) and SS (right) in the ee (top), $e\mu$ (middle) and $\mu\mu$ (bottom). The background contribution is taken directly from MC with no data-driven estimation of the background with fake and non-prompt leptons or charge mis-identification. Only luminosity and MC statistical uncertainties are included. Sherpa is used to model the $Z+jets$ background.

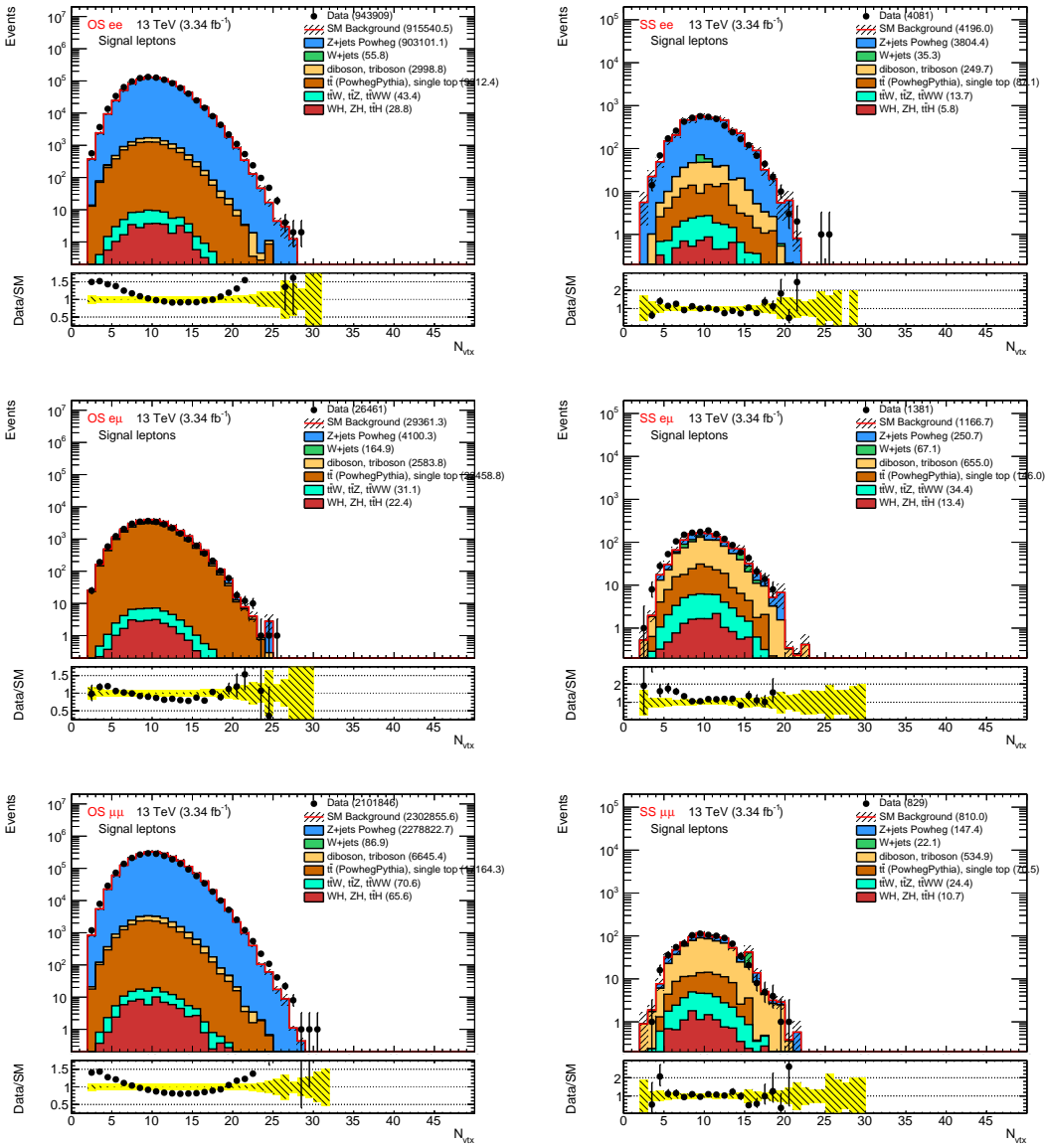


Figure 149: Distributions of the number of vertices for OS (left) and SS (right) in the ee (top), $e\mu$ (middle) and $\mu\mu$ (bottom). The background contribution is taken directly from MC with no data-driven estimation of the background with fake and non-prompt leptons or charge mis-identification. Only luminosity and MC statistical uncertainties are included. Powheg is used to model the $Z+jets$ background.

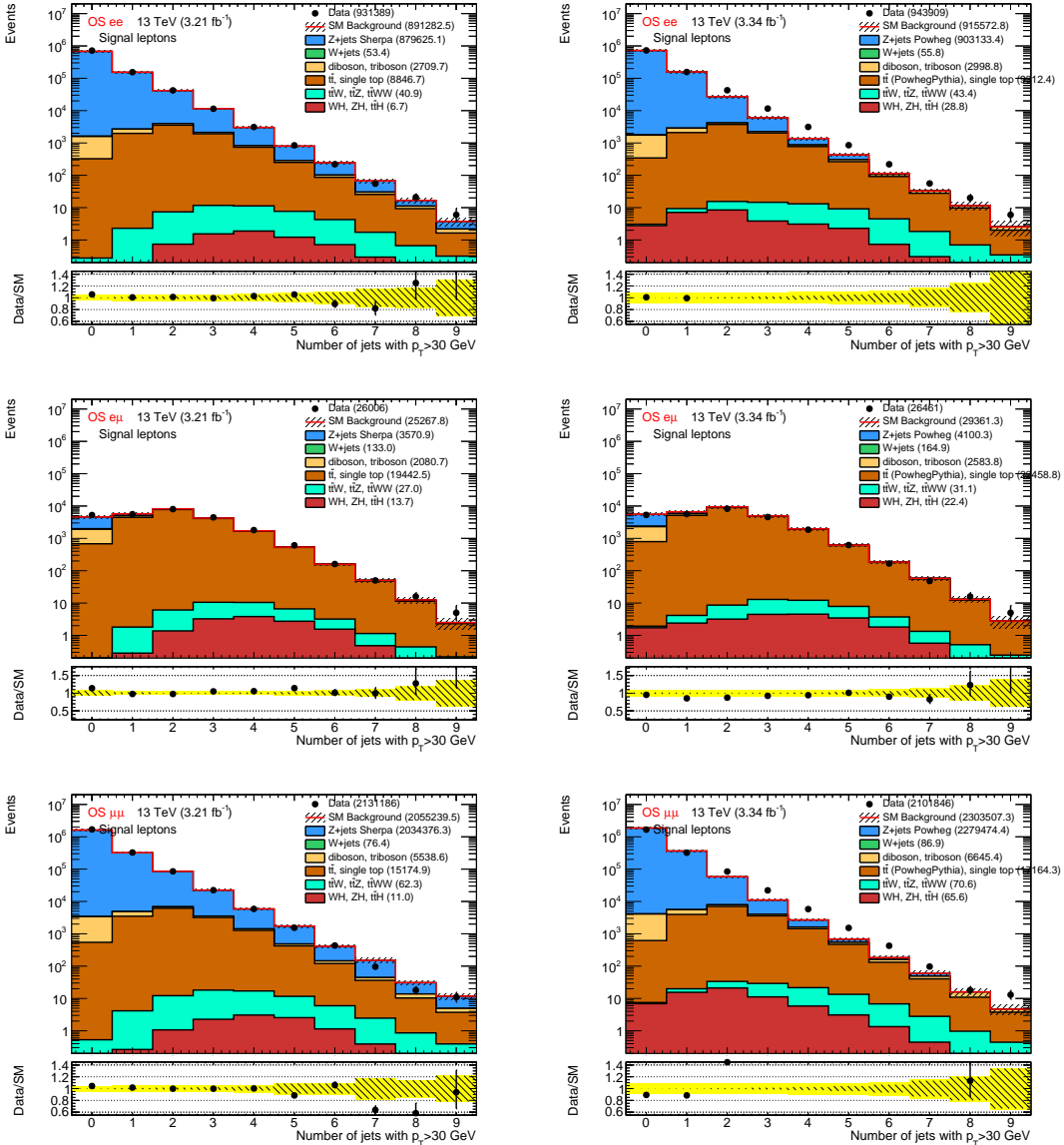


Figure 150: Distributions of the jet multiplicity for OS dilepton events in the ee (top), $e\mu$ (middle) and $\mu\mu$ (bottom). The background contribution is taken directly from MC with no data-driven estimation of the background with fake and non-prompt leptons or charge mis-identification. Only luminosity and MC statistical uncertainties are included. The Z -jets background is modeled by Sherpa (left) and Powheg (right).

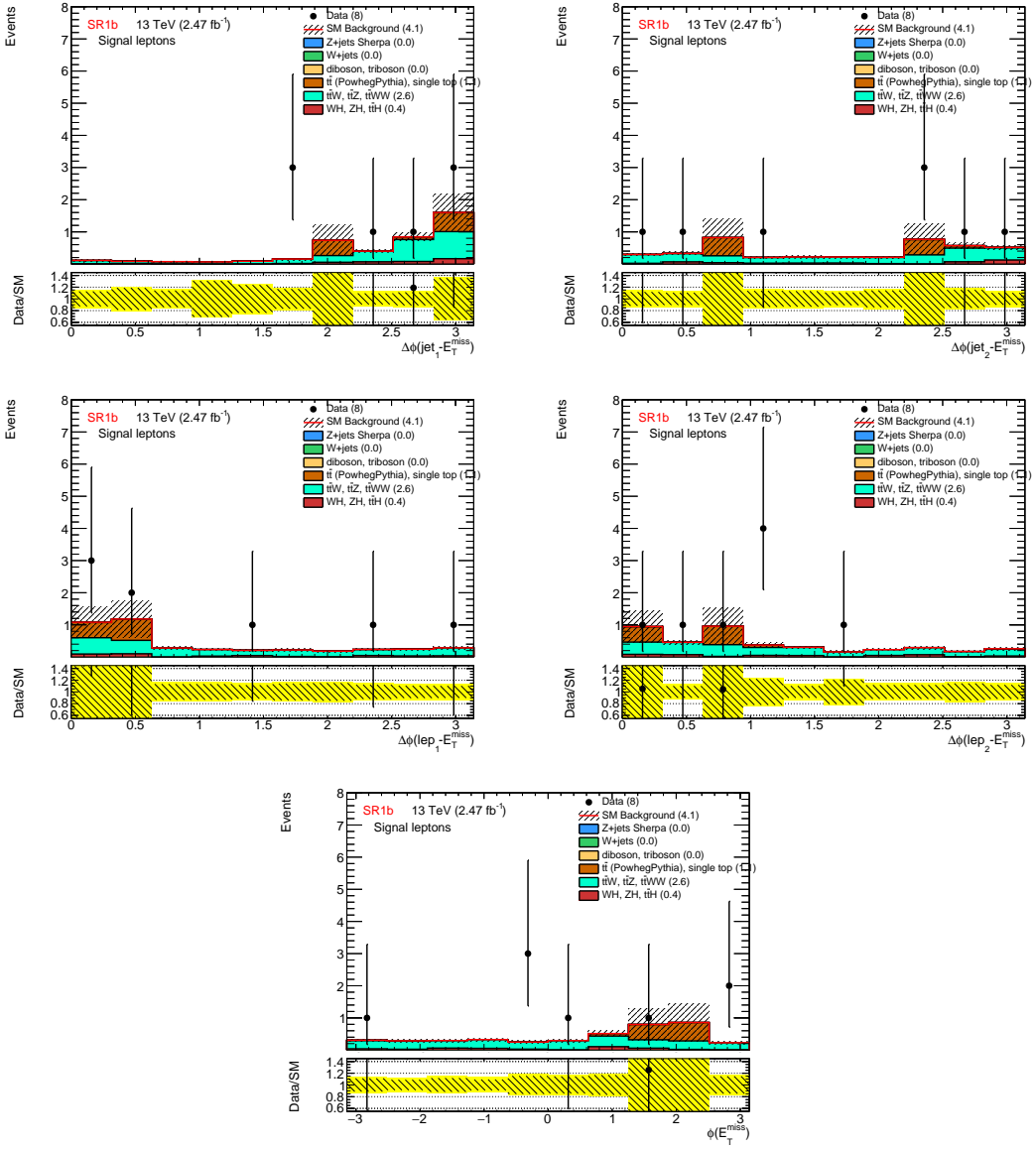


Figure 151: Distributions of $\phi(E_T^{\text{miss}})$, and its difference with the ϕ of the two leading jets and lepton for SR1b. The background contribution is taken directly from MC with no data-driven estimation of the background with fake and non-prompt leptons or charge mis-identification. Only luminosity and MC statistical uncertainties are included.

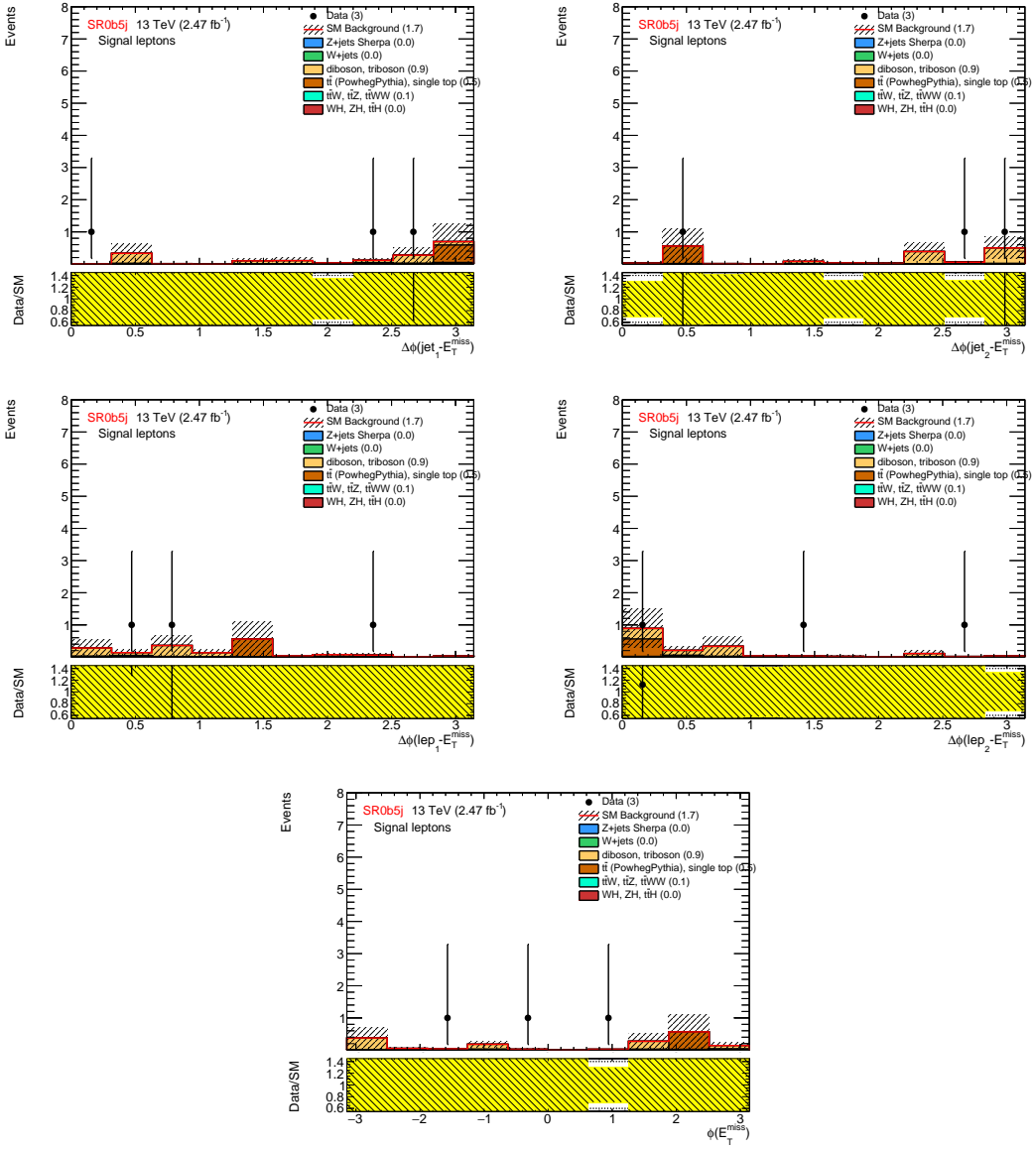


Figure 152: Distributions of $\phi(E_T^{\text{miss}})$, and its difference with the ϕ of the two leading jets and lepton for SR0b5j. The background contribution is taken directly from MC with no data-driven estimation of the background with fake and non-prompt leptons or charge mis-identification. Only luminosity and MC statistical uncertainties are included.

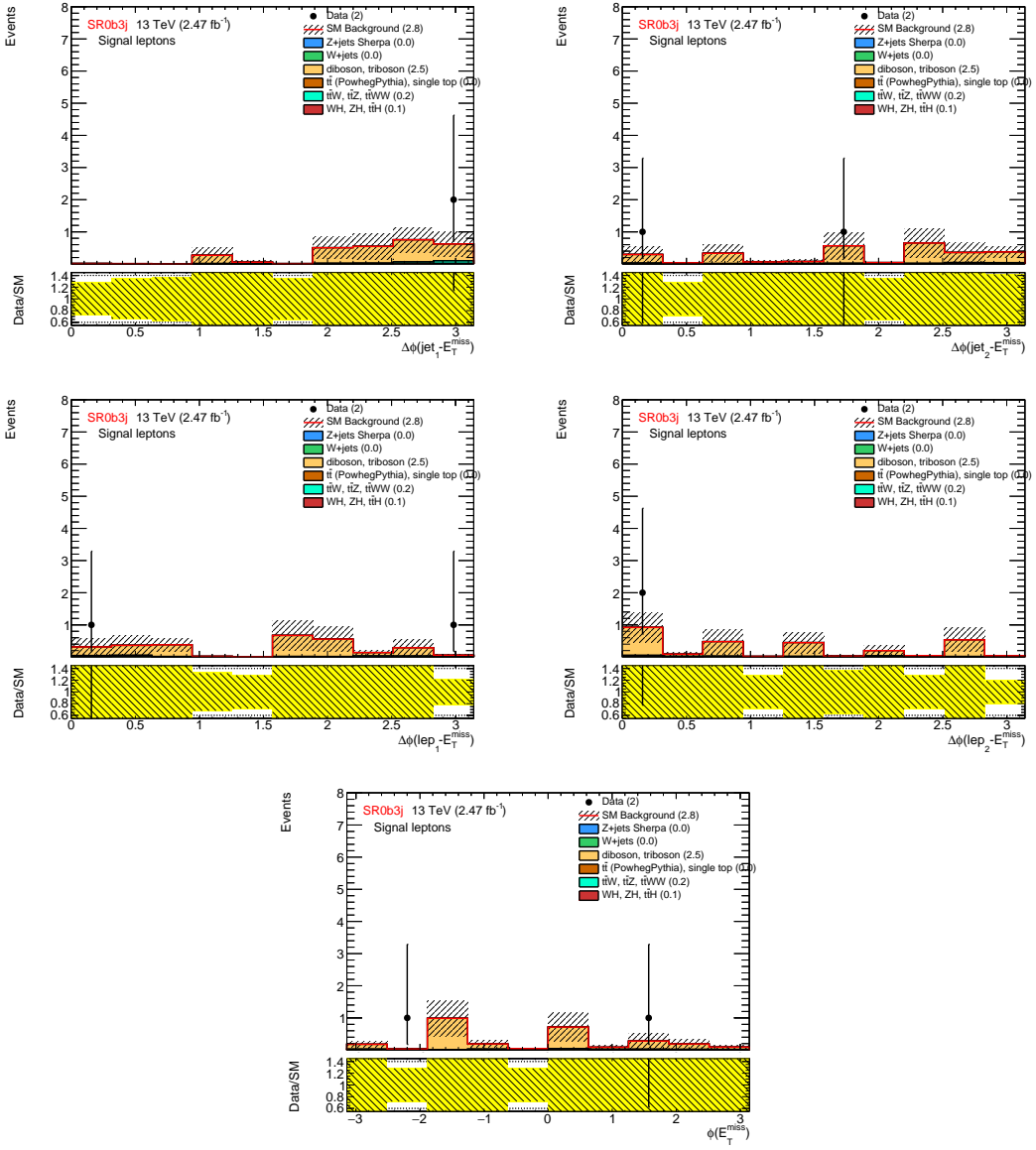


Figure 153: Distributions of $\phi(E_T^{\text{miss}})$, and its difference with the ϕ of the two leading jets and lepton for SR0b3j. The background contribution is taken directly from MC with no data-driven estimation of the background with fake and non-prompt leptons or charge mis-identification. Only luminosity and MC statistical uncertainties are included.

2370 26 List/details of candidate events in the SRs

SR	Run	Event Number	Leptons (p_T [GeV])	E_T^{miss} [GeV]	m_{eff} [GeV]	N_{jets}^{50}	N_{b-jets}^{20}	
SR0b3j	280464	785561112	$e^- (168.1)e^+(56.5)\mu^- (50.3)$	394.3	1780.9	4	0	
SR0b3j	282631	312393728	$e^+(80.2)\mu^- (60.2)e^+(42.0)$	233.1	719.1	3	0	
SR0b5j	279813	450466609	$e^- (505.5)e^- (307.5)$	299.1	1980.7	5	0	
SR0b5j	279932	1034140726	$e^- (93.6)\mu^- (76.0)$	216.6	2119.0	5	0	
SR0b5j	280520	446053391	$\mu^- (63.5)e^- (31.2)$	184.6	1148.5	5	0	
2371	SR1b	278912	193837659	$\mu^+ (62.7)e^- (41.8)e^- (16.9)$	158.7	713.2	4	2
	SR1b	279169	185693401	$\mu^+ (223.2)\mu^+ (83.1)$	322.6	1561.6	5	2
	SR1b	280231	2141228474	$\mu^+ (50.6)\mu^+ (35.0)$	181.8	818.9	4	2
	SR1b	280950	2599077443	$e^- (88.5)\mu^- (60.5)e^+(20.0)$	197.1	1076.7	5	2
	SR1b	282712	322154576	$e^- (49.3)e^- (25.9)$	154.7	784.9	4	1
2372	SR1b	283270	53340659	$\mu^+ (62.7)e^- (41.8)e^- (16.9)$	158.7	713.7	4	2
	SR1b	283429	40556465	$\mu^- (223.6)\mu^- (57.0)\mu^+ (12.8)$	223.8	1080.4	4	1

2373
2374 CAND-SR0b3j -r 280464 -lb 677 -e 785561112
2375 MET: 394.345 METphi: -2.19615 Meff: 1780.93 nJet35:4 nJet50:4 nBJet20(70%):0
2376 JET 0: pt=811.494 eta=-0.42396 phi=-0.42396 isB70=0 isB77=0 isB80=0 isB60=0
2377 JET 1: pt=118.533 eta=0.152671 phi=0.152671 isB70=0 isB77=0 isB80=0 isB60=0
2378 JET 2: pt=74.9502 eta=-0.770569 phi=-0.770569 isB70=0 isB77=0 isB80=0 isB60=0
2379 JET 3: pt=54.3096 eta=1.27342 phi=1.27342 isB70=0 isB77=1 isB80=1 isB60=0
2380 JET 4: pt=30.6546 eta=-0.978513 phi=-0.978513 isB70=0 isB77=0 isB80=0 isB60=0
2381 JET 5: pt=21.7071 eta=-0.433151 phi=-0.433151 isB70=0 isB77=0 isB80=0 isB60=0
2382 LEP 0: id=11 pt=168.141 eta=-0.449999 phi=-2.31573 ptvarcone30/pt=0 topoetcone20/pt=-0.0155184
2383 LEP 1: id=-11 pt=56.507 eta=-0.231378 phi=-2.32631 ptvarcone30/pt=0 topoetcone20/pt=0.00539259
2384 LEP 2: id=13 pt=50.2849 eta=-0.744311 phi=-2.41426 ptvarcone30/pt=0 topoetcone20/pt=0
2385 m12: 21.3771 m13: 28.6308 m23: 28.0377
2386 Trigger: 2e12:1 mu18mu8:1 e17mu14:1 xe70:1
2387
2388
2389 CAND-SR0b3j -r 282631 -lb 213 -e 312393728
2390 MET: 233.051 METphi: 1.7602 Meff: 719.112 nJet35:3 nJet50:3 nBJet20(70%):0
2391 JET 0: pt=140.798 eta=-0.974952 phi=-0.974952 isB70=0 isB77=0 isB80=0 isB60=0
2392 JET 1: pt=82.481 eta=0.0966448 phi=0.0966448 isB70=0 isB77=0 isB80=0 isB60=0
2393 JET 2: pt=80.4191 eta=0.0982909 phi=0.0982909 isB70=0 isB77=0 isB80=0 isB60=0
2394 LEP 0: id=-11 pt=80.2088 eta=-1.69559 phi=-1.596 ptvarcone30/pt=0 topoetcone20/pt=0.0017949
2395 LEP 1: id=13 pt=60.1554 eta=-0.449557 phi=1.59555 ptvarcone30/pt=0 topoetcone20/pt=0
2396 LEP 2: id=-11 pt=41.9987 eta=-0.354455 phi=-1.05441 ptvarcone30/pt=0 topoetcone20/pt=-0.00341845
2397 m12: 166.733 m13: 89.3734 m23: 97.6228
2398 Trigger: 2e12:1 mu18mu8:0 e17mu14:1 xe70:1
2399
2400
2401
2402 CAND-SR0b5j -r 279813 -lb 526 -e 450466609
2403 MET: 299.117 METphi: 1.16144 Meff: 1980.72 nJet35:5 nJet50:5 nBJet20(70%):0
2404 JET 0: pt=377.064 eta=-0.992061 phi=-0.992061 isB70=0 isB77=0 isB80=0 isB60=0
2405 JET 1: pt=149.029 eta=-0.561048 phi=-0.561048 isB70=0 isB77=0 isB80=0 isB60=0
2406 JET 2: pt=134.132 eta=1.20773 phi=1.20773 isB70=0 isB77=1 isB80=1 isB60=0
2407 JET 3: pt=90.8467 eta=1.52904 phi=1.52904 isB70=0 isB77=0 isB80=0 isB60=0
2408 JET 4: pt=64.0946 eta=-0.115875 phi=-0.115875 isB70=0 isB77=0 isB80=0 isB60=0
2409 JET 5: pt=27.7278 eta=1.07254 phi=1.07254 isB70=0 isB77=0 isB80=0 isB60=0
2410 JET 6: pt=25.8053 eta=-1.19473 phi=-1.19473 isB70=0 isB77=0 isB80=0 isB60=0
2411 LEP 0: id=11 pt=505.406 eta=-0.932194 phi=-2.83849 ptvarcone30/pt=0 topoetcone20/pt=0.0220023
2412 LEP 1: id=11 pt=307.495 eta=0.155997 phi=0.866089 ptvarcone30/pt=0 topoetcone20/pt=0.00154862

```

2413 m12: 881.244
2414 Trigger: 2e12:1 mu18mu8:0 e17mu14:0 xe70:1
2415
2416 CAND-SR0b5j -r 279932 -lb 724 -e 1034140726
2417 MET: 216.608 METphi: -1.32955 Meff: 2118.97 nJet35:5 nJet50:5 nBJet20(70%):0
2418 JET 0: pt=567.452 eta=1.42408 phi=1.42408 isB70=0 isB77=0 isB80=0 isB60=0
2419 JET 1: pt=566.44 eta=-0.665885 phi=-0.665885 isB70=0 isB77=0 isB80=0 isB60=0
2420 JET 2: pt=358.279 eta=0.667836 phi=0.667836 isB70=0 isB77=0 isB80=0 isB60=0
2421 JET 3: pt=131.565 eta=-0.33909 phi=-0.33909 isB70=0 isB77=0 isB80=0 isB60=0
2422 JET 4: pt=80.1093 eta=0.405059 phi=0.405059 isB70=0 isB77=0 isB80=0 isB60=0
2423 JET 5: pt=28.9408 eta=-1.90463 phi=-1.90463 isB70=0 isB77=0 isB80=0 isB60=0
2424 LEP 0: id=11 pt=93.5725 eta=0.538482 phi=-1.66577 ptvarcone30/pt=0 topoetcone20/pt=-0.00845377
2425 LEP 1: id=13 pt=76.0036 eta=-0.364716 phi=-0.0204372 ptvarcone30/pt=0 topoetcone20/pt=0
2426 m12: 146.594
2427 Trigger: 2e12:0 mu18mu8:0 e17mu14:1 xe70:1
2428
2429 CAND-SR0b5j -r 280520 -lb 472 -e 446053391
2430 MET: 184.625 METphi: -0.0452673 Meff: 1148.54 nJet35:5 nJet50:5 nBJet20(70%):0
2431 JET 0: pt=276.354 eta=-1.35778 phi=-1.35778 isB70=0 isB77=0 isB80=0 isB60=0
2432 JET 1: pt=273.244 eta=-0.151482 phi=-0.151482 isB70=0 isB77=0 isB80=0 isB60=0
2433 JET 2: pt=178.922 eta=1.78151 phi=1.78151 isB70=0 isB77=0 isB80=0 isB60=0
2434 JET 3: pt=84.4236 eta=-0.428144 phi=-0.428144 isB70=0 isB77=0 isB80=0 isB60=0
2435 JET 4: pt=56.2305 eta=-2.61829 phi=-2.61829 isB70=0 isB77=0 isB80=0 isB60=0
2436 LEP 0: id=13 pt=63.5164 eta=2.04941 phi=-0.768075 ptvarcone30/pt=0 topoetcone20/pt=0
2437 LEP 1: id=11 pt=31.2199 eta=0.68852 phi=-2.6408 ptvarcone30/pt=0 topoetcone20/pt=-0.0102138
2438 m12: 97.0608
2439 Trigger: 2e12:0 mu18mu8:0 e17mu14:1 xe70:1
2440
2441
2442
2443
2444 CAND-SR1b -r 278912 -lb 253 -e 193837659
2445 MET: 158.664 METphi: 1.87863 Meff: 713.655 nJet35:4 nJet50:4 nBJet20(70%):2
2446 JET 0: pt=126.555 eta=-0.386554 phi=-0.386554 isB70=1 isB77=1 isB80=1 isB60=1
2447 JET 1: pt=118.669 eta=-0.293558 phi=-0.293558 isB70=1 isB77=1 isB80=1 isB60=1
2448 JET 2: pt=84.8124 eta=-1.23533 phi=-1.23533 isB70=0 isB77=0 isB80=0 isB60=0
2449 JET 3: pt=61.8862 eta=-1.41657 phi=-1.41657 isB70=0 isB77=0 isB80=0 isB60=0
2450 JET 4: pt=20.912 eta=-1.04929 phi=-1.04929 isB70=0 isB77=0 isB80=0 isB60=0
2451 JET 5: pt=20.6413 eta=0.13547 phi=0.13547 isB70=0 isB77=0 isB80=0 isB60=0
2452 LEP 0: id=-13 pt=62.7461 eta=-0.00835671 phi=-0.366207 ptvarcone30/pt=0 topoetcone20/pt=0
2453 LEP 1: id=11 pt=41.8271 eta=0.0865255 phi=-2.7375 ptvarcone30/pt=0 topoetcone20/pt=0.00945287
2454 LEP 2: id=11 pt=16.9418 eta=0.664041 phi=-0.494687 ptvarcone30/pt=0 topoetcone20/pt=0.00313256
2455 m12: 95.0781 m13: 22.7275 m23: 50.424
2456 Trigger: 2e12:1 mu18mu8:0 e17mu14:0 xe70:0
2457
2458
2459 CAND-SR1b -r 279169 -lb 380 -e 185693401
2460 MET: 322.634 METphi: 2.83799 Meff: 1561.57 nJet35:5 nJet50:5 nBJet20(70%):2
2461 JET 0: pt=468.129 eta=0.586224 phi=0.586224 isB70=1 isB77=1 isB80=1 isB60=1
2462 JET 1: pt=146.271 eta=1.29508 phi=1.29508 isB70=0 isB77=0 isB80=0 isB60=0
2463 JET 2: pt=113.47 eta=0.428972 phi=0.428972 isB70=1 isB77=1 isB80=1 isB60=1
2464 JET 3: pt=83.6901 eta=0.404212 phi=0.404212 isB70=0 isB77=0 isB80=0 isB60=0
2465 JET 4: pt=58.0506 eta=0.222343 phi=0.222343 isB70=0 isB77=0 isB80=0 isB60=0
2466 JET 5: pt=32.396 eta=1.86307 phi=1.86307 isB70=0 isB77=0 isB80=0 isB60=0
2467 JET 6: pt=30.6691 eta=0.125955 phi=0.125955 isB70=0 isB77=0 isB80=0 isB60=0
2468 LEP 0: id=-13 pt=223.198 eta=-0.877807 phi=2.7179 ptvarcone30/pt=0 topoetcone20/pt=0
2469 LEP 1: id=-13 pt=83.0659 eta=-0.895368 phi=2.52321 ptvarcone30/pt=0 topoetcone20/pt=0

```

```

2470 m12: 26.5766
2471 Trigger: 2e12:0 mu18mu8:1 e17mu14:0 xe70:1
2472
2473
2474 CAND-SR1b -r 280231 -lb 942 -e 2141228474
2475 MET: 181.791 METphi: -0.348738 Meff: 818.942 nJet35:5 nJet50:4 nBJet20(70%):2
2476 JET 0: pt=147.076 eta=-0.484221 phi=-0.484221 isB70=0 isB77=0 isB80=0 isB60=0
2477 JET 1: pt=145.538 eta=0.197606 phi=0.197606 isB70=1 isB77=1 isB80=1 isB60=0
2478 JET 2: pt=103.247 eta=1.95611 phi=1.95611 isB70=0 isB77=0 isB80=0 isB60=0
2479 JET 3: pt=91.6692 eta=-0.445089 phi=-0.445089 isB70=0 isB77=0 isB80=0 isB60=0
2480 JET 4: pt=36.6747 eta=2.47992 phi=2.47992 isB70=0 isB77=0 isB80=0 isB60=0
2481 JET 5: pt=27.3766 eta=-2.26597 phi=-2.26597 isB70=1 isB77=1 isB80=1 isB60=0
2482 LEP 0: id=-13 pt=50.5775 eta=-1.71212 phi=-0.294339 ptvarcone30/pt=0 topoetcone20/pt=0
2483 LEP 1: id=-13 pt=34.9925 eta=1.20128 phi=0.78435 ptvarcone30/pt=0 topoetcone20/pt=0
2484 m12: 176.133
2485 Trigger: 2e12:0 mu18mu8:1 e17mu14:0 xe70:1
2486
2487
2488 CAND-SR1b -r 280950 -lb 941 -e -1695889853
2489 MET: 197.127 METphi: 0.147102 Meff: 1076.73 nJet35:6 nJet50:5 nBJet20(70%):2
2490 JET 0: pt=248.81 eta=-1.9937 phi=-1.9937 isB70=0 isB77=0 isB80=0 isB60=0
2491 JET 1: pt=117.22 eta=-0.899444 phi=-0.899444 isB70=1 isB77=1 isB80=1 isB60=1
2492 JET 2: pt=101.153 eta=0.184455 phi=0.184455 isB70=1 isB77=1 isB80=1 isB60=1
2493 JET 3: pt=80.0191 eta=-0.745511 phi=-0.745511 isB70=0 isB77=0 isB80=0 isB60=0
2494 JET 4: pt=65.0873 eta=-2.16748 phi=-2.16748 isB70=0 isB77=0 isB80=0 isB60=0
2495 JET 5: pt=36.7802 eta=0.46976 phi=0.46976 isB70=0 isB77=0 isB80=0 isB60=0
2496 JET 6: pt=34.909 eta=-2.77895 phi=-2.77895 isB70=0 isB77=0 isB80=0 isB60=0
2497 JET 7: pt=26.6185 eta=-1.41256 phi=-1.41256 isB70=0 isB77=0 isB80=0 isB60=0
2498 LEP 0: id=11 pt=88.5211 eta=0.13958 phi=0.698756 ptvarcone30/pt=0 topoetcone20/pt=-0.000882356
2499 LEP 1: id=13 pt=60.4639 eta=-2.22927 phi=1.2282 ptvarcone30/pt=0 topoetcone20/pt=0
2500 LEP 2: id=-11 pt=20.0222 eta=-0.0786426 phi=1.44109 ptvarcone30/pt=0 topoetcone20/pt=0.00285568
2501 m12: 220.119 m13: 31.8964 m23: 90.4097
2502 Trigger: 2e12:1 mu18mu8:1 e17mu14:1 xe70:1
2503
2504 CAND-SR1b -r 282712 -lb 423 -e 322154576
2505 MET: 154.682 METphi: -0.284066 Meff: 784.905 nJet35:4 nJet50:4 nBJet20(70%):1
2506 JET 0: pt=167.827 eta=-2.03598 phi=-2.03598 isB70=0 isB77=0 isB80=0 isB60=0
2507 JET 1: pt=161.197 eta=-0.0420531 phi=-0.0420531 isB70=1 isB77=1 isB80=1 isB60=1
2508 JET 2: pt=81.4767 eta=-1.12255 phi=-1.12255 isB70=0 isB77=0 isB80=0 isB60=0
2509 JET 3: pt=66.9971 eta=0.452546 phi=0.452546 isB70=0 isB77=0 isB80=0 isB60=0
2510 JET 4: pt=27.5326 eta=2.08238 phi=2.08238 isB70=0 isB77=0 isB80=0 isB60=0
2511 JET 5: pt=26.2816 eta=0.810986 phi=0.810986 isB70=0 isB77=0 isB80=0 isB60=0
2512 JET 6: pt=23.7284 eta=-2.5646 phi=-2.5646 isB70=0 isB77=0 isB80=0 isB60=0
2513 LEP 0: id=11 pt=49.3078 eta=-0.304144 phi=2.62568 ptvarcone30/pt=0 topoetcone20/pt=-4.5744e-05
2514 LEP 1: id=11 pt=25.8746 eta=-1.67588 phi=0.560547 ptvarcone30/pt=0 topoetcone20/pt=0.0385537
2515 m12: 81.017
2516 Trigger: 2e12:1 mu18mu8:0 e17mu14:0 xe70:1
2517
2518 CAND-SR1b -r 283270 -lb 26 -e 53340659
2519 MET: 262.728 METphi: 2.97717 Meff: 1329.41 nJet35:5 nJet50:5 nBJet20(70%):1
2520 JET 0: pt=333.415 eta=0.445185 phi=0.445185 isB70=0 isB77=0 isB80=0 isB60=0
2521 JET 1: pt=182.954 eta=2.33276 phi=2.33276 isB70=0 isB77=0 isB80=0 isB60=0
2522 JET 2: pt=167.08 eta=0.830914 phi=0.830914 isB70=0 isB77=0 isB80=0 isB60=0
2523 JET 3: pt=153.819 eta=0.38928 phi=0.38928 isB70=1 isB77=1 isB80=1 isB60=1
2524 JET 4: pt=55.1583 eta=0.625063 phi=0.625063 isB70=0 isB77=0 isB80=0 isB60=0
2525 JET 5: pt=28.6869 eta=-0.265669 phi=-0.265669 isB70=0 isB77=0 isB80=0 isB60=0
2526 JET 6: pt=24.341 eta=0.581841 phi=0.581841 isB70=0 isB77=0 isB80=0 isB60=0

```

```
2527 LEP 0: id=-11 pt=94.199 eta=1.03938 phi=2.55436 ptvarcone30/pt=0 topoetcone20/pt=-0.0259278
2528 LEP 1: id=-11 pt=27.0299 eta=1.79115 phi=-3.00283 ptvarcone30/pt=0 topoetcone20/pt=-0.00195136
2529 m12: 52.841
2530 Trigger: 2e12:1 mu18mu8:0 e17mu14:0 xe70:1
2531
2532 CAND-SR1b -r 283429 -lb 1436 -e 40556465
2533 MET: 223.763 METphi: -2.61501 Meff: 1080.4 nJet35:5 nJet50:4 nBJet20(70%):1
2534 JET 0: pt=169.034 eta=-0.723255 phi=-0.723255 isB70=0 isB77=0 isB80=0 isB60=0
2535 JET 1: pt=109.393 eta=-0.193642 phi=-0.193642 isB70=0 isB77=0 isB80=0 isB60=0
2536 JET 2: pt=102.062 eta=0.505164 phi=0.505164 isB70=0 isB77=0 isB80=0 isB60=0
2537 JET 3: pt=66.8916 eta=0.0271367 phi=0.0271367 isB70=0 isB77=0 isB80=0 isB60=0
2538 JET 4: pt=38.7211 eta=-1.84191 phi=-1.84191 isB70=0 isB77=0 isB80=0 isB60=0
2539 JET 5: pt=26.5674 eta=1.62338 phi=1.62338 isB70=0 isB77=0 isB80=0 isB60=0
2540 JET 6: pt=25.4032 eta=-1.13932 phi=-1.13932 isB70=0 isB77=0 isB80=0 isB60=0
2541 JET 7: pt=25.2374 eta=-0.386001 phi=-0.386001 isB70=1 isB77=1 isB80=1 isB60=1
2542 LEP 0: id=13 pt=223.551 eta=-0.746294 phi=-1.33138 ptvarcone30/pt=0 topoetcone20/pt=0
2543 LEP 1: id=13 pt=56.9659 eta=-1.33871 phi=2.65267 ptvarcone30/pt=0 topoetcone20/pt=0
2544 LEP 2: id=-13 pt=12.811 eta=-1.10118 phi=-1.25764 ptvarcone30/pt=0 topoetcone20/pt=0
2545 m12: 216.852 m13: 19.4997 m23: 50.4993
2546 Trigger: 2e12:0 mu18mu8:1 e17mu14:0 xe70:1
2547
```

27 HEPData material

2548

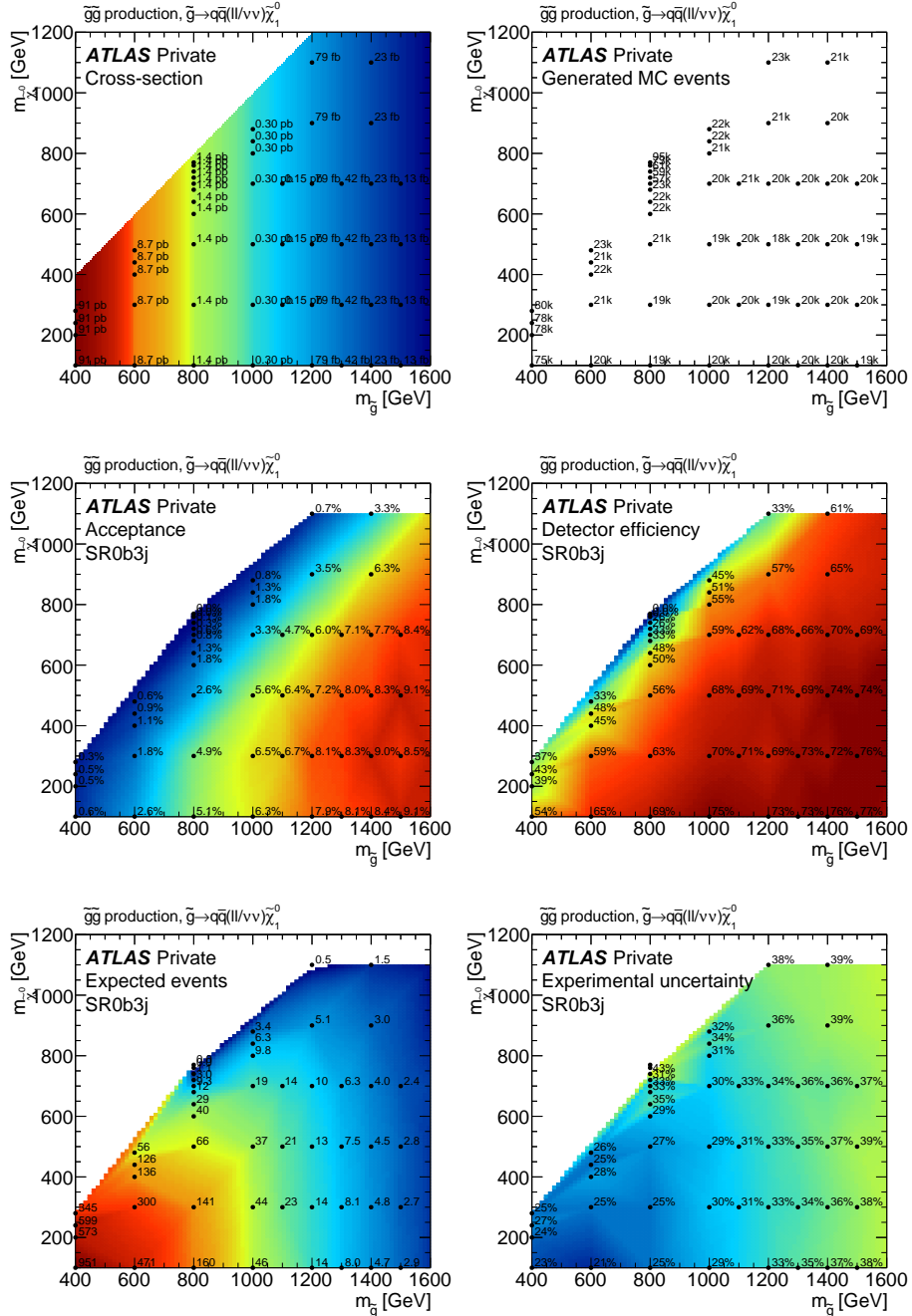


Figure 154: SUSY scenario with $\tilde{g}\tilde{g}$ production and $\tilde{g} \rightarrow q\bar{q}\ell\ell \tilde{\chi}_1^0$ decay: production cross-section (top left), number of generated MC events (top right), signal acceptance (middle left) and reconstruction efficiency (middle right) in the signal region SR0b3j, corresponding expected signal yield (bottom left) and associated uncertainty due to experimental sources (bottom right). The benchmark scenarios used to set exclusion limits are materialized by black dot markers. Acceptance and efficiency are defined as in appendix A of [55].

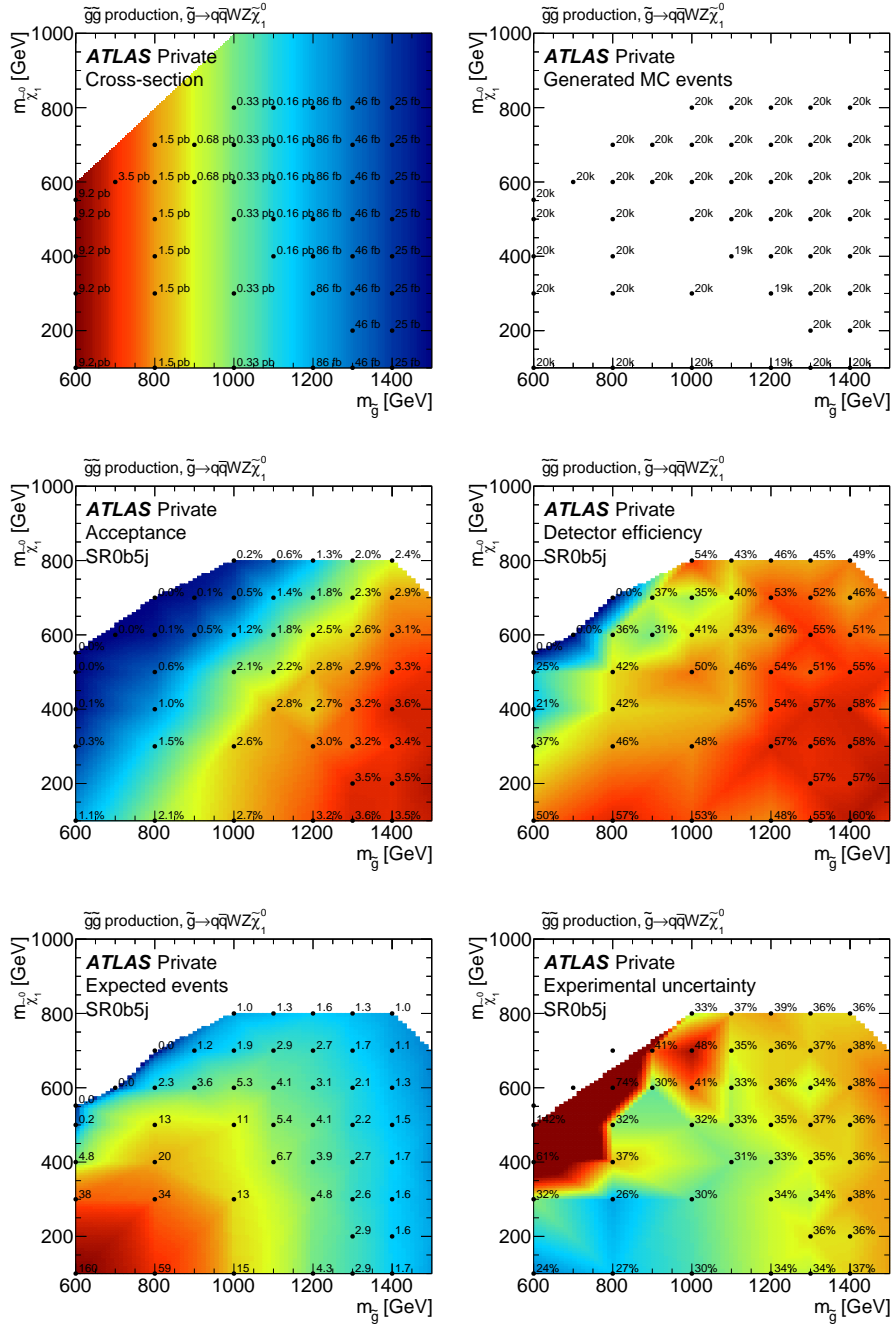


Figure 155: SUSY scenario with $\tilde{g}\tilde{g}$ production and $\tilde{g} \rightarrow q\bar{q}WZ\tilde{\chi}_1^0$ decay: production cross-section (top left), number of generated MC events (top right), signal acceptance (middle left) and reconstruction efficiency (middle right) in the signal region SR0b5j, corresponding expected signal yield (bottom left) and associated uncertainty due to experimental sources (bottom right). The benchmark scenarios used to set exclusion limits are materialized by black dot markers. Acceptance and efficiency are defined as in appendix A of [55].

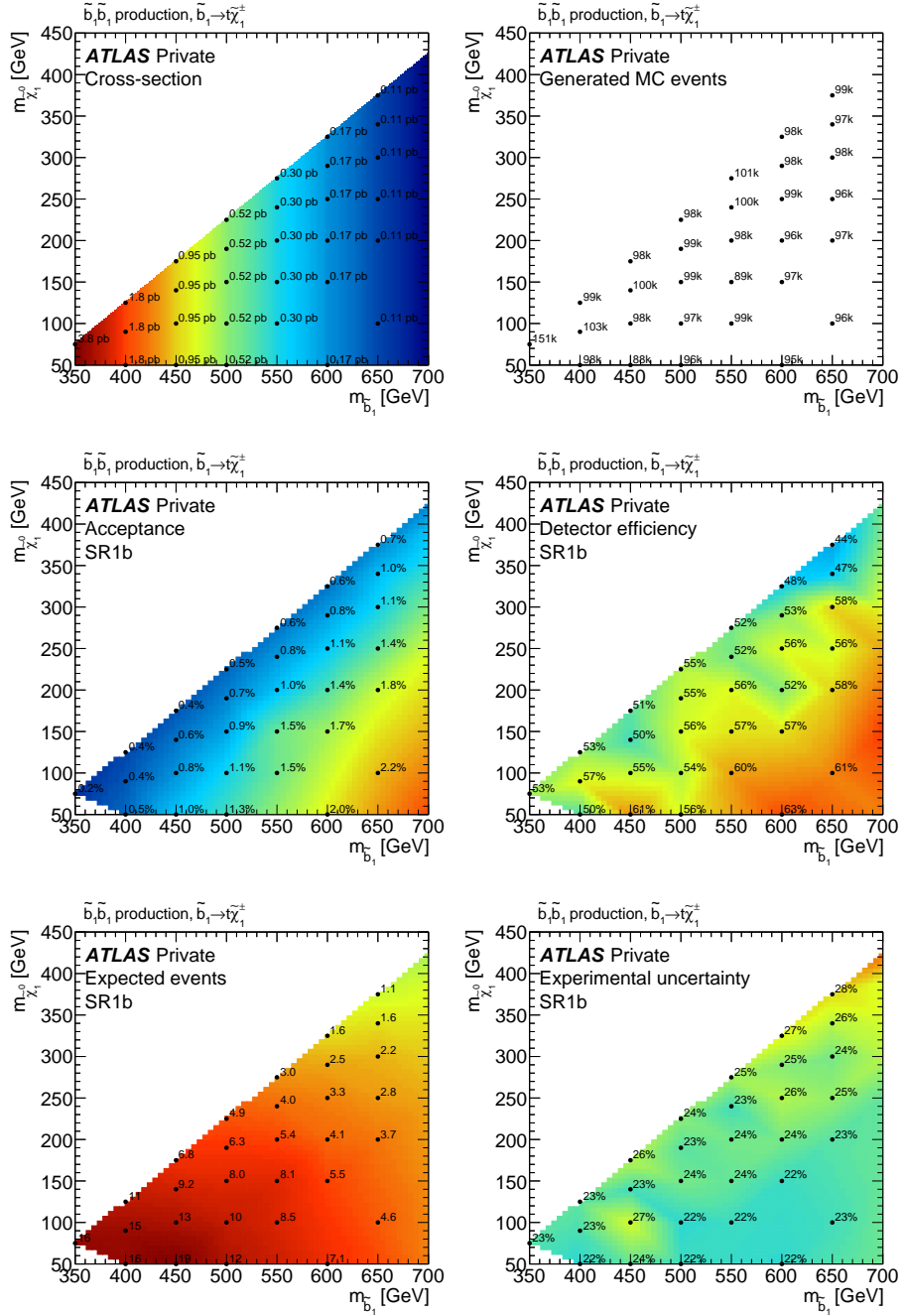


Figure 156: SUSY scenario with $\tilde{b}_1 \tilde{b}_1$ production and $\tilde{b}_1 \rightarrow tW \tilde{\chi}_1^0$ decay: production cross-section (top left), number of generated MC events (top right), signal acceptance (middle left) and reconstruction efficiency (middle right) in the signal region SR1b, corresponding expected signal yield (bottom left) and associated uncertainty due to experimental sources (bottom right). The benchmark scenarios used to set exclusion limits are materialized by black dot markers. Acceptance and efficiency are defined as in appendix A of [55].

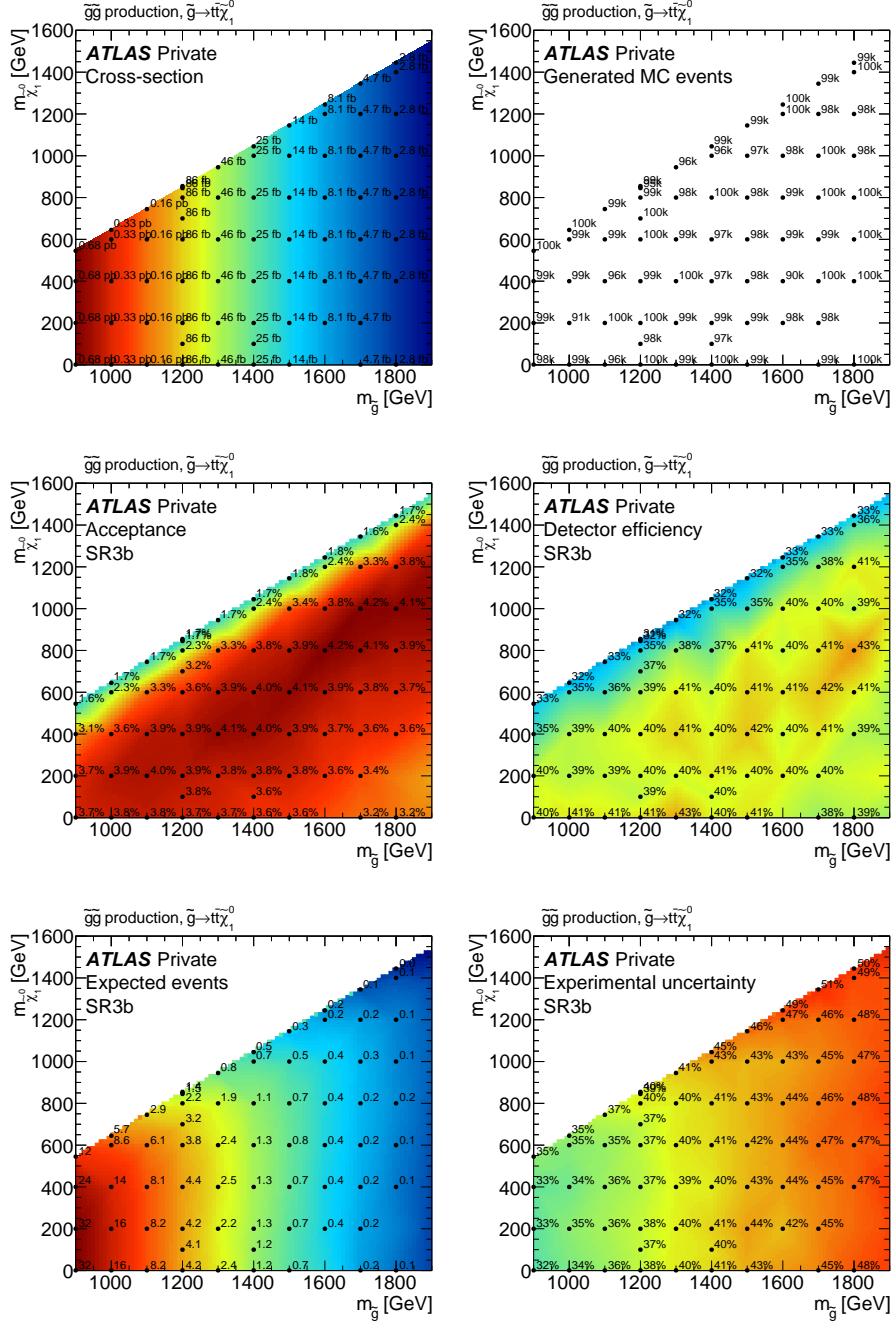


Figure 157: SUSY scenario with $\tilde{g}\tilde{g}$ production and $\tilde{g} \rightarrow t\bar{t}\tilde{\chi}_1^0$ decay: production cross-section (top left), number of generated MC events (top right), signal acceptance (middle left) and reconstruction efficiency (middle right) in the signal region SR3b, corresponding expected signal yield (bottom left) and associated uncertainty due to experimental sources (bottom right). The benchmark scenarios used to set exclusion limits are materialized by black dot markers. Acceptance and efficiency are defined as in appendix A of [55].